DISSERTATION

Titel der Dissertation

„Luminescence of Lanthanoides (Rare-earth elements) – Probes of structural variations in minerals"

Verfasser

Dipl.-Min. Christoph Lenz

angestrebter akademischer Grad

Doktor der Naturwissenschaften (Dr. rer. nat.)

Wien, März 2015

Table of contents

Appendices B – selected conference abstracts and contributions

Abstract

This cumulative PhD thesis summarises several individual studies on the luminescence of REE (rare-earth elements; i.e., trivalent lanthanoides), which are typically incorporated in accessory minerals such as zircon, titanite, monazite–(Ce) and xenotime–(Y). A main objective of these studies is to examine the powerfulness of REE^{3+} luminescence spectroscopy as structural probe. In particular, this concerns the potential use of REE^{3+} emissions in characterising structural disorder of their accessory host minerals as caused by radiation damage and/or compositional heterogeneity. Especially the former (i.e., mineral disorder due to radiation damage) is of interest to Earth and materials scientists, for instance for the understanding of changed physicochemical properties of initially crystalline materials that are affected by structural damage as caused by the radioactive decay of actinides.

Moreover, a substantial contribution of the studies presented lies in the field of basic properties of the REE^{3+} luminescence of natural accessory minerals. First, the investigations have addressed the identification of diverse REE species in diverse natural host minerals (which is done using synthetic REE-doped analogues). Second, factors that may bias the quantitative estimation of spectroscopic parameters have been studied, including effects of experimental parameters (crystal orientation and temperature) and the samples' compositional heterogeneity. The results will be particularly useful to the growing community of Earth scientists who apply REE^{3+} luminescence spectroscopy in studying geological materials.

Kurzzusammenfassung

In der vorliegenden, kumulativen Doktorarbeit sind mehrere Einzelstudien zusammengefasst, welche die Lumineszenz der Seltenenerdelemente (SEE) in den akzessorischen Mineralen Zirkon, Titanit, Monazit–(Ce) und Xenotime–(Y) thematisieren. Diese Studien sollen insbesondere die Frage klären, inwiefern die Lumineszenz der SEE^{3+} dazu verwendet werden kann strukturelle Unordnung in diesen Materialien zu charakterisieren. Strukturelle Unordnung kann einerseits maßgeblich durch Strahlenschäden und zum anderen durch eine heterogene Probenzusammensetzung verursacht werden. Ersteres ist für Geo- als auch für Materialwissenschaftler von Interesse. Schäden an der kristallinen Ordnung von Mineralen, welche durch den radioaktiven Zerfall von strukturell eingebauten Aktiniden verursacht werden, haben einen maßgeblichen Einfluss auf die physikochemischen Eigenschaften dieser Materialien.

Darüber hinaus befasst sich ein bedeutender Teil der vorliegenden Studien mit den grundlegenden, SEE-verursachten Lumineszenzeigenschaften besagter akzessorischer Minerale. Diese Voruntersuchungen galten in erster Linie der korrekten Zuordnung spezifischer Photolumineszenzbanden zum jeweiligen Element. Dies erfolgte durch Vergleich von Spektren natürlicher Proben mit ihren synthetisierten, SEE-dotierten Analoga. Desweiteren wurde der Einfluss

diverser Faktoren untersucht, welche die quantitative Bestimmung spektroskopischer Parameter erschweren. Im Speziellen sind dies messbedingte Effekte (unterschiedliche Kristallorientierungen und Umgebungstemperaturen) und der Einfluss der chemischen Zusammensetzung der Proben. Die Ergebnisse dieser Studien sind im Speziellen für die wachsende Zahl von Wissenschaftlern von Bedeutung, welche die SEE^{3+}-Lumineszenzspektroskopie zur Untersuchung von Geomaterialien verwenden.

1. Introduction

1.1. Luminescence of lanthanoides (REE^{3+})

Luminescence is defined as the ability of materials to emit photons of light in the ultraviolet (UV), visible, and/or near-infrared (NIR) spectral range after energetic excitation. The above defines the creation of photons of light through the radiative release of energy during electronic transitions. Many sources and techniques for luminescence excitation are commonly used, such as photons (photoluminescence, PL), electrons (cathodoluminescence, CL), accelerated ions (ionoluminescence, IL), to name just a few. Typical luminescence centres or activators in inorganic materials include structural defects and specific, minor or trace elements incorporated into the crystal structure (e.g., Marfunin 1979; Blasse and Grabmeier 1999). With respect to luminescence emissions of materials in general, lanthanoides are a very important group of chemical elements. This is because their luminescence characteristics are used in a wide range of modern technological applications, such as lighting, colour-television screens, solid-state lasers, phosphors, and chromophores (e.g., Belsky and Krupa 1999; Kenyon 2002; Bünzli and Piguet 2005; Liu and Jacquier 2005).

Moreover, these elements are commonly incorporated in accessory mineral phases. This is of particular interest if the lanthanoid incorporation is not homogeneous but, in contrast, shows zoning or other internal heterogeneity. Such distribution patterns within geological samples (commonly referred to as internal textures) may bear valuable information on the primary growth and the post-growth history. The lanthanoid-distribution textures are well visualised using luminescence techniques (Hanchar and Miller 1993; Rakovan and Reeder 1996; Götze 2000; Rubatto & Gebauer 2000; Edwards et al. 2007; MacRae et al. 2012, 2013).

The lanthanoides are defined as a group of 15 chemical elements, from La to Lu. They have widely similar chemical properties and, therefore, they are referred to as elements being "similar" to lanthanum from the Greek ειδής (-eides) = related/similar (compare Connelly et al. 2005). In the Earth sciences, the term "rare-earth elements" (REEs) is by far more commonly used. This term, per definition, includes all lanthanoid-group elements as well as the elements Sc and Y. The preferential use of the term "REE" in the Earth sciences is perhaps explained by the fact that lanthanoides, Sc, and Y (all belonging to the third subgroup of the periodic table) show widely similar behaviour in natural

geochemical systems. It should however be noted that "REE" is applied inconsistently in the literature; often it is wrongly used if lanthanoides are meant. For instance, an expression such as "Y, Sc and REE" (e.g., Nielson et al. 1992) is substantially incorrect, considering the definitions quoted above.

The PhD research summarized here deals with a number of lanthanoides, i.e., with selected REE not including Y and Sc. The term "lanthanoides" hence could have been used for description. However, the use of the term "REE" was preferred in the following text and the publications presented, motivated by the fact that Earth scientists are much more familiar with the latter.

The elements dealt with comprise only a sub-group of the REEs (or the lanthanoides, respectively), namely those with an incompletely filled $4f$ electronic shell (i.e., Pr^{3+} to Yb^{3+}). The luminescence of materials containing these REEs originates from intra-configurational $4f^n$ electronic transitions. Emission spectra are therefore characterised by remarkably sharp bands, in contrast to the typically broad-band luminescence of $3d$ or $4d$ elements (Blasse and Grabmaier 1994). The unique characteristics of REE^{3+} luminescence is determined by the particular electron configurations of these elements, which consists of outer filled $5s^2$ and $5p^6$ orbitals shielding the electronic transitions within non-bonding $4f$ levels. For a more detailed, comprehensive introduction see Appendix **A.1** (which contains an exemplary discussion of Nd^{3+}).

1.2. Research objectives

In the Earth sciences, one challenging task was (and still is) the detection of REEs in different host minerals using luminescence methods. A large variety of mineral systems has been studied already (Tarashchan 1978; Cesbron et al. 1995; Habermann et al. 1996; Baumer et al. 1997; Gaft et al. 1999, 2005; Götze et al. 1999; Blanc et al. 2000; Waychunas 2002; Finch et al. 2004; Nasdala et al. 2004a; Czaja et al. 2008; Friis et al. 2010; Chen & Stimets 2014). Time-resolved luminescence techniques have improved the detection of various luminescence centres utilising their different decay times (Reisfeld et al. 1996; Gaft et al. 1999, 2001). Cathodoluminescence images are commonly used to visualise internal textures of zircon and other geological materials (e.g., Vavra 1990; Hanchar and Miller 1993; Hanchar and Rudnick 1995; Rakovan and Reeder 1996; Götze 2000, 2002; Hoskin and Black 2000; Corfu et al. 2003; Götze et al. 2013).

The steady-state, laser-induced photoluminescence of REE^{3+} is commonly observed, as an analytical artefact, in Raman spectra of minerals (e.g., Nasdala et al. 2012). The laser beam that is used to induce Raman scattering is characterized by photon energies that correspond to typical absorption transitions of REE^{3+}. It may therefore excite concomitantly the PL of variable REE^{3+} centres being incorporated in the material analysed. The widths of PL bands of such elements may be as narrow as 0.1–0.3 nm at room temperature, which is on the same order as typical full-width-at-half-maximum (FWHM) values of Raman bands (i.e., a few cm^{-1}). Therefore, confusion of Raman bands with narrow PL bands of REE^{3+} emissions is found quite often in the published literature (discussed in Appendix **A.4**).

The first aim of the present PhD thesis therefore was to contribute to the PL-based identification of the REE centres that strongly affect Raman spectra, especially in the (typically REE-containing) accessory minerals zircon $ZrSiO_4$, monazite–(Ce) $CePO_4$, xenotime–(Y) YPO_4, and titanite $CaTiSiO_5$. Second, the major objective of the present PhD research was to address the question how the PL of REE^{3+} in minerals can be used as structural probe. For instance, it was studied as to which degree PL can complement applications of Raman spectroscopy, e.g., for the identification of mineral phases and to characterise effects of the real structure of geological materials (Zhang et al. 2000; Nasdala et al. 2004b; Nasdala 2012). Recently, the PL of REE^{3+} in minerals and mineral-based ceramics has been used as structural probe of order-disorder phenomena (in particular caused by the accumulation of structural damage due to irradiation). To provide a few examples, spectral parameters of Eu^{3+} emissions have been used for the characterisation of REE-substituted cation-sites in glasses and crystalline materials, to evaluate their potential use as nuclear waste forms (Ollier et al. 2003; Reisfeld et al. 2004, 2005; Ternane et al. 2005). Seydoux-Guillaume et al. (2002) and Panczer et al. (2012) have proposed that the REE-dominated luminescence emission of monazite–(Ce) may bear quantitative information on the radiation-damage accumulated by this mineral.

This thesis evaluates critically the potential of REE^{3+} photoluminescence for the estimation and visualisation of structural disorder as caused by (1) radiation damage and (2) compositional heterogeneity. The former is of interest especially to the radioactive-waste community, i.e., in the search for, and characterisation of, potentially suitable mineral-based host forms for the long-term immobilisation of spent nuclear fuel and other radioisotopes. Also, results are expected to be of interest in the fields of geochemistry/petrology and geochronology. This is because radiation damage often controls the post-growth alteration of accessory minerals that are used routinely for radiometric age dating of rocks, and whose internal textures and peculiarities are informative of the host rocks' post-growth history. In both research fields, however, a fast, reliable, and in-expensive imaging (i.e., mapping) technique would open up new opportunities in the characterisation of radiation damage in the micrometre range.

2. Summary of results

2.1. Crystal-field splitting of REE emissions – Fingerprint identification of minerals

Results of Appendix **A.4** demonstrate that steady-state laser-induced photoluminescence of REE^{3+} is a common analytical artefact in Raman spectroscopy of accessory minerals. Emissions of REE^{3+} detected in Raman spectra, however, may be advantageous in so far as specific emissions itself are indicative for the analysed mineral species and may be used as complementary fingerprint method. Specific REE^{3+} emissions appear in the similar spectral range, but REE^{3+} electronic-levels split into *sublevels* in dependence on the local structural environment of the REE^{3+} ion (*Stark level* splitting on

the order of ca. 10^2 cm^{-1}; cf. Fig. 1 in **A.1**). This crystal-field dependent splitting of $4f$ spectroscopic levels is particularly observed if PL emissions of certain REE are compared among different minerals and structure types (cf. Fig. 2 in **A.1**, and Fig. S1 in **A.4**). The crystal-field splitting depends on a variety of parameters that are related to the crystallographic environment of the REE^{3+} within the crystal structure, e.g., site symmetry, the interatomic distance to the ligands, etc. (e.g., Burns 1993). The comparison of Nd^{3+} emissions in different isotypic monazite- and zircon-type structures revealed that not only the point symmetry, but rather the charge distribution at the substitutional REE^{3+} site considerably affects the Nd^{3+} emission pattern (see Fig. 3 and discussion in **A.1**).

Many REE-related PL artefacts in Raman spectra of accessory minerals were identified by comparing natural samples with REE mono-doped analogues (which were synthesised in the course of the PhD). Differentiation of individual bands of multiple overlying REE centres is straight forward using PL spectra of the individually doped mineral equivalents (e.g., see Fig. 4 in **A.4**). Hence, the PL studies on synthetic mineral analogues provided both: (1) the materials individual sublevel splitting potentially used for a fast mineral identification (e.g., applied in igneous/metamorphic and sedimentary petrology, gemmological or mineral provenance studies; Richter et al. 2003, 2006, 2008; Fritsch et al. 2012; Andò and Garzanti 2014); and (2) an enhanced possibility to identify certain REE species in the accessory minerals discussed. The comparison of spectra of natural samples with those of singly REE-doped analogues is advantageous if the luminescence signals of multiple REE species overlap. Reference spectra may, therefore, help to discriminate individual species in steady-state PL spectra of natural specimens, and in time-resolved PL spectra with REEs having similar luminescence decay-times (cf. Gaft et al. 2000, 2001, 2005). Photoluminescence spectra and further original spectra files of REE^{3+} mono-doped accessory minerals studied were submitted to the CSIRO luminescence database (e.g., see Appendix **B.7**).

2.2. Trace-element distributions – PL mapping of REE luminescence intensities

The intensity of PL emissions of trace elements in steady-state spectra of materials depends basically on (1) the effectivity of the laser photon-energy used for their excitation, i.e., the quantum cross section of the laser and the absorption/excitation levels of the respective REE^{3+} in the crystal structure; and (2) the presence and concentration of certain PL centres in the material. Because of the latter, semi-quantitative REE distribution patterns may be easily visualised using a confocal spectrometer system with a spatial resolution of a few µm and software-controlled x-y mapping stage (see Fig. 1 below, and Fig. 2 and 7 in **A.4**). Hyperspectral PL maps in Fig. 1 show that emission intensities as caused by traces of Cr^{3+} in titanite or REE^{3+} in zircon correlate closely to concentrations of the respective elements. Intensity maps produced are found to be more sensitive to minute changes in element concentrations than panchromatic CL images that are typically used to unravel the primary formation and post-growth history of geological materials (see further discussion in "Summary and conclusions" in **A.4**).
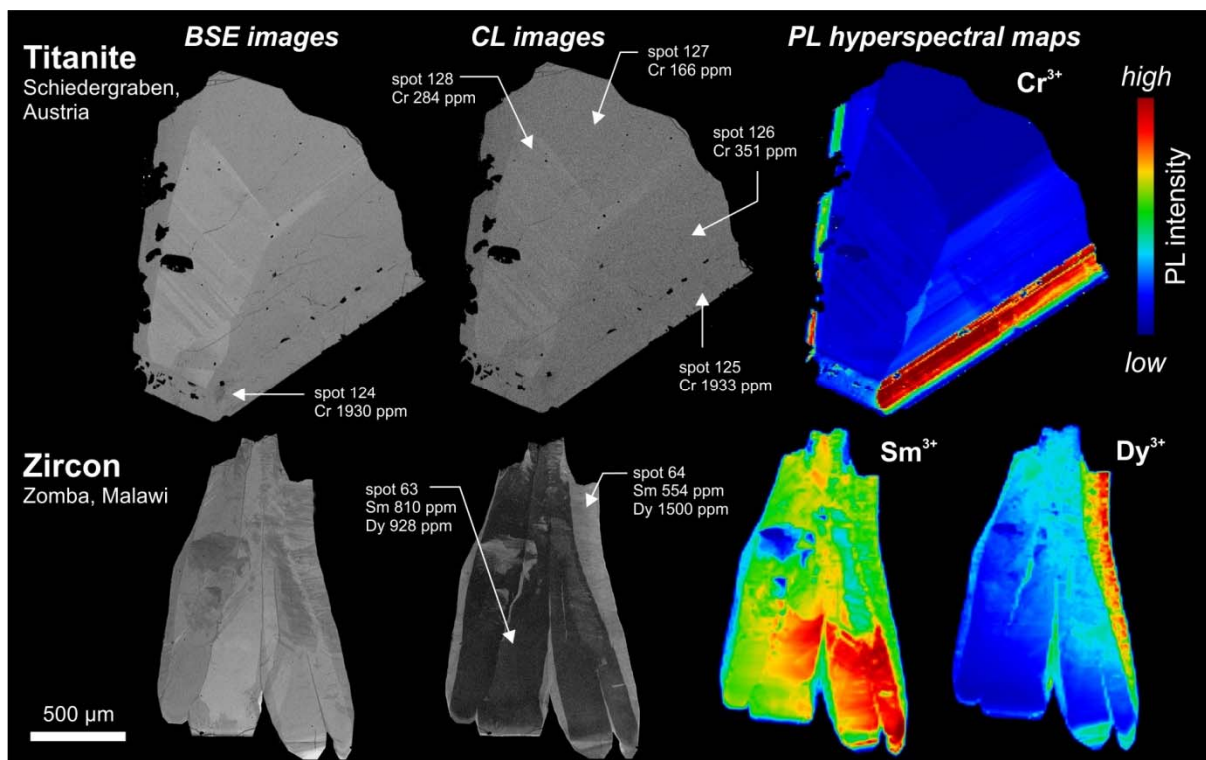
Figure 1. *Series of BSE and CL images and PL hyperspectral maps, of a titanite sample from Schiedergraben, Felbertal, Austria, and a zircon sample from Mt. Zomba, Malawi. Hyperspectral PL maps were produced using the intensity of Cr^{3+}, Sm^{3+}, or Dy^{3+} emissions. Results of LA–ICP–MS point analyses are indicated (cf. Tables 1 and 3 in Appendix A.4).*

Note, however, that luminescence imaging or mapping is of semi-quantitative character. The luminescence intensities may depend strongly on further variables such as quenching (as described for titanite; see **A.2**) and sensitizing by other elements (e.g., Marfunin 1979; Kempe and Götze 2002), effects of crystal orientation (see **A.1** and **B.1, B.2, B.3**) and the structural state/crystallinity, e.g. the accumulation of radiation damage (see **A.3**, and summary below). Although the effect of the crystal orientation on luminescence intensities is a well-known phenomenon (Owen et al. 1998; Barbarand and Pagel 2001; Finch et al. 2003), it is often neglected in luminescence studies, which may result in biased conclusions. Hence, some demonstrative examples of this effect (with particular focus on REE-related luminescence) are documented in the present thesis. The intensity of individual crystal-field split REE^{3+} bands strongly vary in dependence of the crystal orientation relative to the measuring direction (discussed in **A.1**). Further, the polarisation of the laser, as applied in PL measurements, has a strong impact (see **A.1** again). A few more examples of orientation-dependent PL of Eu^{3+}, Ho^{3+}, Dy^{3+} (see **B.1**) and Nd^{3+} emissions (see **B.2**) in xenotime–(Y) were studied.

These results suggest that relative REE^{3+}-PL intensity-differences may be comparable in PL maps of single crystals (with the crystal orientation being constant throughout mapping). In contrast, PL intensities may vary among multiple, heterogeneously-oriented grains in case of analysing polycrystalline materials (discussed in **B.3**).

2.3. Estimation and visualisation of structural disorder

2.3.1 Generalities

Structural disorder is defined here as the entity of deviations from the ideal chemical composition and the structural order (*real structure*). Common features, which contribute to structural disorder in minerals, are the presence of point defects (e.g., substitutions, vacancies, interstitials), two- and three-dimensional defects (e.g., surface defects, grain boundaries, holes). Typical effects on light-spectroscopic signals are band broadening and shifting. In optical spectroscopy, this phenomenon is commonly termed *inhomogeneous broadening* (discussed in **A.1**). Results of the present PhD thesis demonstrate that the FWHM of narrow REE^{3+} emission-bands may be used effectively to estimate quantitatively structural disorder as caused by (1) radiation damage and (2) compositional heterogeneity of minerals.

2.3.2. Structural disorder as caused by radiation damage

The long-term impact of natural radioactivity may cause severe structural damage in natural minerals. Self-irradiation induced structural damage is created mainly by the nuclear interaction (atomic "knock-ons") of heavy daughter recoil-nuclei from the decay of ^{232}Th, ^{235}U, and ^{238}U (Wasiliewski et al. 1977; Weber et al. 1990; Devanathan et al. 2006, Nasdala et al. 2013). Accessory minerals, like zircon, titanite, monazite- and xenotime-group minerals, incorporate these instable actinides in their crystal structure, whose radioactive decay creates structural damage. With progressive damage accumulation, minerals may finally be transformed to a so-called "metamict", amorphous state (e.g., Brøgger 1893; Pabst 1952; Ewing 1993).

The investigation of radiation-damaged or metamict minerals has increased appreciably over the past two decades, stimulated by the potential use of mineral-like ceramics as waste forms for the immobilisation of reprocessed spent nuclear fuel and other radioactive waste (Stefanovsky et al. 2004; Omelyanenko et al. 2007; Weber et al. 2009; Montel 2011; Ewing and Weber 2011; Vance 2012). Advances in waste form development and testing have been complemented by numerous mineralogical investigations of the analogous mineral phases in geological environments (Lumpkin 2001; Lumpkin et al. 2004). Information obtained from these studies has important implications for the validation of the long-term performance of nuclear waste forms for disposal in geological repositories.

Damage accumulation is associated with changes of physical parameters such as refraction and birefringence, hardness, density, and elastic moduli (Holland and Gottfried, 1955; Chakoumakos et al., 1991; Palenik et al., 2003), and a general decrease of the chemical resistance (Ewing et al., 1982; Balan et al., 2001; Mathieu et al., 2001; Geisler et al., 2001, 2003; Soman et al. 2010). The

generally increased susceptibility of radiation-damaged minerals to alteration processes is of enormous importance as it for instance affects negatively the ability of this mineral to immobilise radionuclides (e.g., Ewing 2011). For Earth scientists, the investigation of radiation-damaged minerals is important in so far as accessory minerals that have experienced considerable self-irradiation are more susceptible to post-growth alteration (Horie et al. 2006; Lenting et al. 2010) and the loss of radioisotopes. The latter may bias results of chemical and isotopic age determinations (Kuiper 2005; Goncalves et al. 2005; Nasdala et al. 2010a). Fission-track ages are also affected by the radiation damage of the minerals (Murakami et al. 2006; Li et al. 2011).

The impact of self-irradiation on the luminescence emission of REE^{3+} is demonstrated in Appendix **A.3**. This study deals with radiation-damage effects in zircon. Figure 2 in **A.3** shows that FWHMs of REE^{3+} PL-bands increase significantly with increasing structural damage. Band-widths of distinct levels of Dy^{3+} ($^4F_{9/2} \rightarrow {}^6H_{13/2}$) and Nd^{3+} ($^4F_{3/2} \rightarrow {}^4I_{9/2}$) emissions may be determined reliably by conventional band-fitting procedures. Band-broadening of REE-related emissions in radiation-damaged minerals is assigned to the disturbance of the structure as caused by the accumulation of defects. A complete metamictisation, hence, cause a total loss of crystal-field states (i.e., degeneration of electronic states); the respective electronic transitions are then characterised by broad humps in the luminescence spectra (see again Fig. 2 in **A.3**; and Fig. 6B in **A.4**). On the example of cut-in-half zircon samples (Fig. 3 in Appendix **A.3**), it is demonstrated that band-widths of selected REE^{3+} emission sublevels may be used to visualise the distribution of radiation-damage accumulation, as obtained from hyperspectral maps (with the FWHM of certain Stark's levels of e.g., Dy^{3+} being used as the mapping parameter). Furthermore, results of this study show that the FWHM of selected REE^{3+} luminescence sublevels of zircon is related to the amount of radiation-damage accumulated over geologic periods of time (effective α-dose). Hence, the FWHM parameter may be used to estimate quantitatively accumulated radiation-damage in accessory minerals (Fig. 5 and 7 in **A.3**).

Attempted quantifications of irradiation effects based on the study of naturally radiation-damaged minerals, however, are often biased. The latter is because of insufficient knowledge about their thermal and, hence, annealing history (see Nasdala et al. 2004b). This problem may be overcome by studying minerals that were artificially ion-irradiated in the laboratory. Within the PhD project, heavy-ion irradiations (with Au ions in the 1–12 MeV range) of zircon and monazite–(Ce) were performed to simulate the nuclear interaction of heavy daughter nuclei (that were released during α-decay events in natural minerals) with the host material (**B.4, B.5, B.6**). In nature, trajectory lengths of α-recoils do not exceed a few tens of nanometres. This is because of low momentum energies of α-recoils ranging between 0.07 to 0.16 MeV. To artificially create damage volumes with "measurable" thicknesses in the μm-range, comparably higher ion-energies in the MeV range were used in the ion-irradiation experiments. The ions irradiated (with energies in the MeV range) still have relatively short penetration depths to only a few micrometres. Consequently, irradiation of a bulk sample results in the formation of a relatively shallow radiation-damaged layer atop of a non-irradiated, still crystalline host.

An innovative aspect of the PhD project was that the majority of the irradiations were done on thin foils produced using the focused ion beam (FIB) technique (see Fig. 1 in **B.4**). The main reason behind the latter idea was that spectroscopic micro-analyses, even if done with state-of-the-art confocal systems, have a limited depth resolution. In the analysis of micrometre-thin (Picot et al. 2008; Mendoza 2010) or even thinner (~100 nm, Zhang et al. 2008) radiation-damaged layers atop of an un-irradiated host crystal, it is more than likely that the damaged layer and crystalline host are analysed simultaneously (see Fig. 2; also discussed in Nasdala et al. 2010b for Raman spectroscopic analyses). This is particularly problematic insofar as Raman or PL signals of severely damaged solids are mostly lowered appreciably in intensity; the signal of the thin damaged layer may therefore be obscured easily by the spectrum of the crystalline back (see Fig. 2 again). A relatively simple way to avoid this problem was the virtual pre-removal of the un-irradiated host behind the irradiated sample volume, by using thin foils whose thicknesses are just smaller than the maximum penetration depths of the ions irradiated. The thicknesses of these foils were adjusted carefully according to the penetration depths of the ions irradiated, which were calculated from Monte Carlo simulations (SRIM, Ziegler et al. 1984; see Fig 2a in **B.4**). This ensured on the one hand that the irradiated samples contain the majority of the structural damage produced – a presumption for quantitative estimates. On the other hand, irradiated samples do not contain any un-irradiated volumes, whose presence is likely to bias the analytical results. Most results of heavy-ion irradiation experiments done during this PhD were not published yet in peer-reviewed articles, but some preliminary results are documented in conference abstracts presented below (see Appendices **B.4**, **B.5** and **B.6**).

For zircon, Raman spectral parameters are used successfully to estimate the degree of radiation damage on a microscale (e.g., Nasdala et al. 1995), whereas this technique cannot be applied for some other mineral species (for titanite discussed by Kennedy et al. 2010); here a luminescence-based quantification is most useful. In addition to X-ray diffraction (e.g., Weber 1990; Ríos et al. 2000), several other spectroscopic techniques have been applied to quantify radiation damage accumulated in minerals. For instance, Wasilewski et al. (1973), Deliens et al. (1977), Zhang and Salje (2001) and Zhang et al. (2008) used infrared (IR) absorption spectroscopy, and Farnan et al. (2001; 2007) applied ^{29}Si nuclear magnetic resonance (NMR) spectroscopy to estimate the amorphous fraction in zircon. Advantages of using REE^{3+} luminescence spectroscopy with respect to the mentioned methods include (1) the high volume resolution (with confocal spectrometer systems, analyses can be done on a micrometre scale); (2) the possibility to visualise the distribution of structural damage in minerals/ceramics with hyperspectral mapping (a high volume resolution required); (3) the option to do non-destructive analyses without sample preparation; (4) the possibility to excite REE^{3+} luminescence emissions with various different techniques such as PL, CL, IL, etc.; and (5) to potentially analyse hazardous nuclear waste forms with remote spectrometer set-ups.
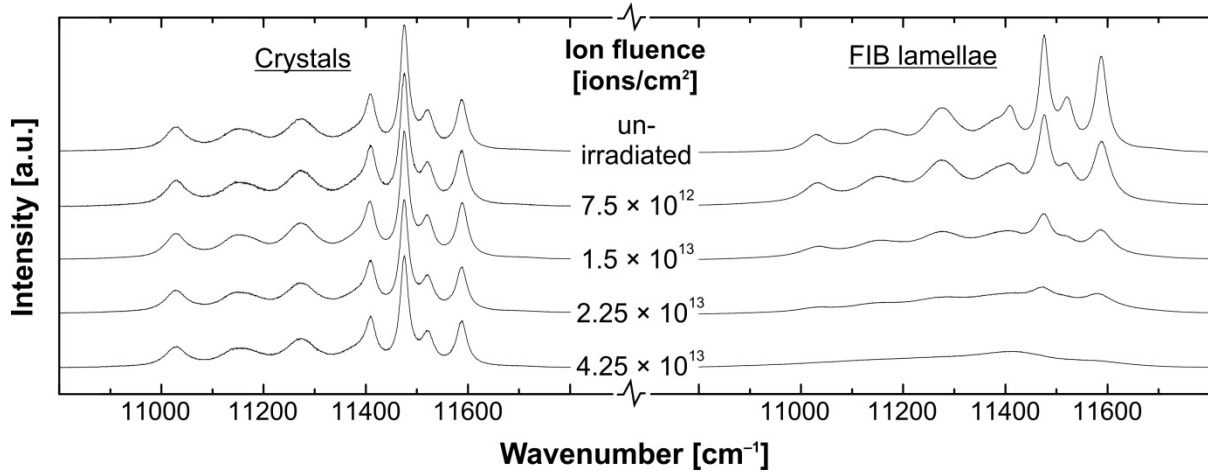
Figure 2. *Photoluminescence spectra showing the Nd^{3+} $(^4F_{3/2} \rightarrow {}^4I_{9/2})$ emission of synthetic, Nd^{3+}-doped $CePO_4$. Spectra of FIB-prepared lamellae (right) are compared with spectra obtained from simultaneously irradiated, unprepared crystals measured normal to the ion irradiated surface (left). On both sides of the figure, spectra of four samples irradiated with Au ions (1, 4, and 10 MeV) are shown along with the un-irradiated analogue. The FIB-foil spectra on the right show significant sublevel broadening with increasing irradiation doses. The sample irradiated with the highest dose (4.25×10^{13} ions/cm²) is severely radiation-damaged. It does not show any significant PL signal of crystalline $CePO_4$ anymore; crystal-field states are completely degenerate. All spectra of unprepared crystals (left) appear "undamaged". This analytical artefact is explained by the fact that spectra are dominated by intense, narrow bands originating from the un-irradiated host crystal underneath the surficial (~1.5 μm thick) damaged layer.*

2.3.3. Structural disorder as caused by compositional heterogeneity

A further aspect in the PhD project was to investigate effects which may bias the estimation of radiation-induced band broadening of REE^{3+} luminescence Stark's levels. Structural disorder as caused by compositional heterogeneity may also strongly influence PL band-widths (e.g., Panczer et al. 2012). Compositional heterogeneity is due to the incorporation of non-formula elements into the crystal structure. Consequently, the impact of compositional heterogeneity on PL band-widths is strong in minerals which are characterised by high chemical flexibility, such as the monazite (Clavier et al., 2011) or titanite crystal-structure (Higgins and Ribbe, 1976). A quantitative discrimination between compositionally-induced and irradiation-induced structural disorder is needed, however, to estimate (precisely as possible) the accumulated radiation damage in minerals of high compositional variance. For zircon, it could be demonstrated that the effect of compositionally induced disorder is

considerably small (see discussion and Fig. 4 in **A.3**). In contrast, this effect is significant in monazite–(Ce). Investigation of a suite of synthetic and natural monazite–(Ce) samples revealed that the incorporation of heterovalent ions has the strongest impact on REE^{3+}-PL band-widths, whereas the impact of homovalent substitutes is negligible relatively (see discussion in **A.1**). The impact of compositionally-induced structural disorder as caused by the incorporation of heterovalent ions may be estimated using a simple parameter which reflects the distortional behaviour of all heterovalent substituents (see Fig. 3 below, and Fig. 8 in Appendix **A.1**).

Moreover, effects of variable compositional heterogeneity on the FWHM broadening of the REE^{3+} emissions upon accumulation of radiation damage produced by heavy-ion (Au) irradiations of variable dose, have been investigated (see Appendix **B.5**). These experiments have addressed the question how compositional heterogeneity on the one hand and structural damage on the other hand contribute to changes of the REE^{3+} luminescence.
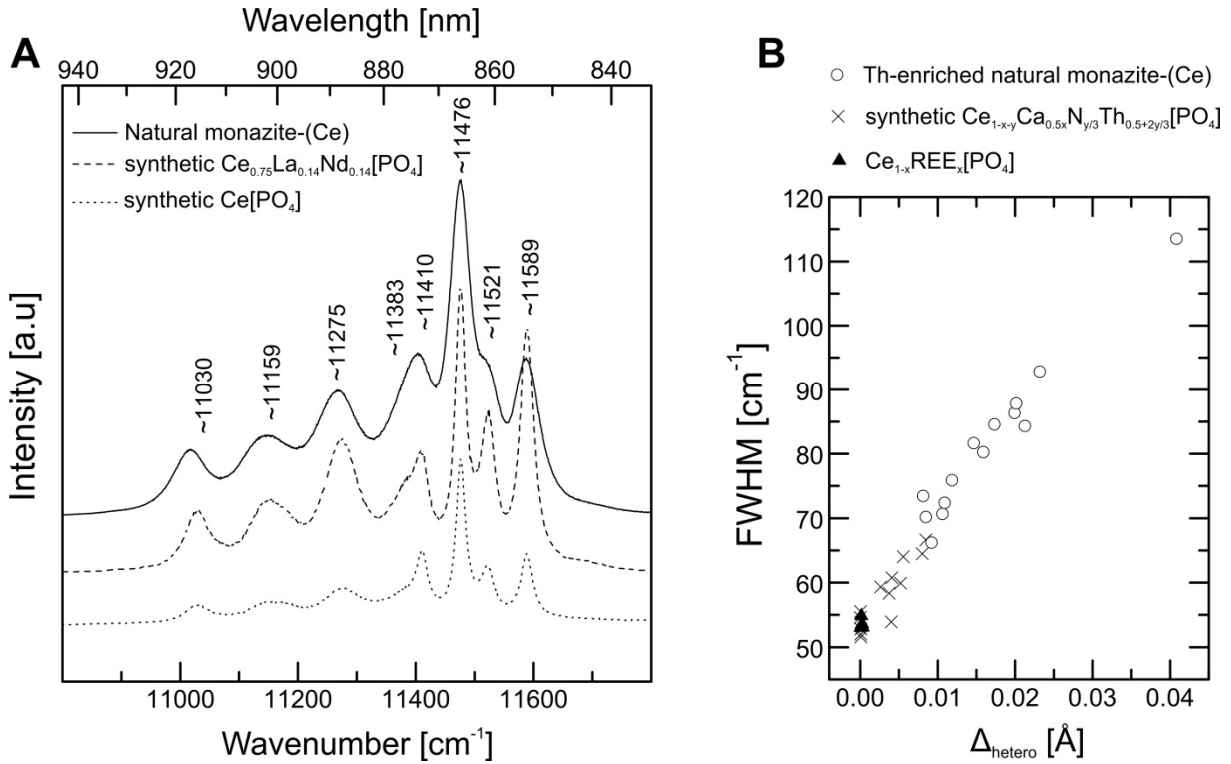
Figure 3. *Effect of chemical composition on the PL of Nd^{3+} in monazite–(Ce) (shown for the example of the ${}^4F_{3/2} \rightarrow {}^4I_{9/2}$ transition). (**A**) Spectra of an annealed monazite–(Ce) from central Australia (crystalline but compositionally impure) and pure and La-Nd-doped $CePO_4$. The incorporation of non-formula elements causes band-broadening of individual Stark's levels. (**B**) Plot of the band-broadening of the Nd^{3+} Stark's level near ~ 11030 cm^{-1} against parameter Δ_{hetero}. The latter describes the distortional impact of heterovalent, non-formula elements; it is calculated from the chemical composition of the respective sample and ionic-radii differences (cf. discussion in Appendix A.1).*

3. References

Andò, S., & Garzanti, E. (2014). Raman spectroscopy in heavy-mineral studies. Geological Society, London, Special Publications, 386(1), 395–412.

Balan, E., Neuville, D. R., Trocellier, P., Fritsch, E., Muller, J. P., & Calas, G. (2001). Metamictization and chemical durability of detrital zircon. American Mineralogist, 86(9), 1025–1033.

Baumer, A., Blanc, P., Cesbron, F., & Ohnenstetter, D. (1997). Cathodoluminescence of synthetic (doped with rare-earth elements) and natural anhydrites. Chemical Geology, 138(1), 73–80.

Barbarand, J., & Pagel, M. (2001). Cathodoluminescence study of apatite crystals. American Mineralogist, 86(4), 473–484.

Belsky, A. N., & Krupa, J. C. (1999). Luminescence excitation mechanisms of rare earth doped phosphors in the VUV range. Displays, 19(4), 185–196.

Blanc, P., Baumer, A., Cesbron, F., Ohnenstetter, D., Panczer, G., & Rémond, G. (2000). Systematic cathodoluminescence spectral analysis of synthetic doped minerals: anhydrite, apatite, calcite, fluorite, scheelite and zircon. In M. Pagel, V. Barbin, P. Blanc, and D. Ohnenstetter, D. (Eds.), Cathodoluminescence in geosciences. Springer Berlin Heidelberg, p. 127–160.

Blasse, G. & Grabmaier, B. (1994) Luminescence materials. Springer Berlin, 248 p.

Brøgger, W.C. (1893). Amorf: Salmonens store illustrerede Konversationslexikon, 1, 742–743.

Bünzli, J. C. G., & Piguet, C. (2005). Taking advantage of luminescent lanthanide ions. Chemical Society Reviews, 34(12), 1048–1077.

Burns, R.G. (1993) Mineralogical applications of crystal field theory. Cambridge Topics in Mineral Physics and Chemistry, 5, Cambridge University Press.

Cesbron, F., Blanc, P., Ohnenstetter, D., & Rémond, G. (1995). Cathodoluminescence of rare earth doped zircons. I. Their possible use as reference materials. Scanning Microscopy Supplement 9, 35–56.

Chakoumakos, B.C., Oliver, B.C., Lumpkin, G.R., & Ewing, R.C. (1991). Hardness and elastic modulus of zircon as a function of heavy-particle irradiation dose. I. In situ α-decay event damage. Radiation Effects and Defects in Solids, 118, 393–403.

Chen, H., & Stimets, R. W. (2014). Fluorescence of trivalent neodymium in various materials excited by a 785 nm laser. American Mineralogist, 99(2–3), 332–342.

Clavier, N., Podor, R., & Dacheux, N. (2011). Crystal chemistry of the monazite structure. Journal of the European Ceramic Society, 31(6), 941–976.

Czaja, M., Bodyɫ, S., Głuchowski, P., Mazurak, Z., & Strek, W. (2008). Luminescence properties of rare earth ions in fluorite, apatite and scheelite minerals. Journal of Alloys and Compounds, 451(1), 290–292.

Connelly, N.G., Damhus, T., Hartshorn, R.M., & Hutton A.T., Eds. (2005). Nomenclature of Inorganic Chemistry – IUPAC Recommendations 2005. Published for the International Union of Pure and Applied Chemistry by The Royal Society of Chemistry, Thomas Graham House, Cambridge, UK, 366 p.

Corfu, F., Hanchar, J.M., Hoskin, P.W.O., and Kinny, P. (2003). Atlas of zircon textures. In J.M. Hanchar and P.W.O. Hoskin, Eds., Zircon. Reviews in Mineralogy and Geochemistry, 53, Mineralogical Society of America, Chantilly, Virginia, p. 469–500.

Deliens, M., Delhal, J., & Tarte, P. (1977). Metamictization and U-Pb systematics—a study by infrared absorption spectrometry of Precambrian zircons. Earth and Planetary Science Letters, 33(3), 331–344.

Devanathan, R., Corrales, L. R., Weber, W. J., Chartier, A., & Meis, C. (2006). Molecular dynamics simulation of energetic uranium recoil damage in zircon. Molecular Simulation, 32(12–13), 1069–1077.

Edwards, P. R., Martin, R. W., & Lee, M. R. (2007). Combined cathodoluminescence hyperspectral imaging and wavelength dispersive X-ray analysis of minerals. American Mineralogist, 92(2–3), 235–242.

Ewing, R.C., Haaker, R.F., & Lutze, W. (1982). Leachability of zircon as a function of alpha dose. In W. Lutze, Ed, Scientific Basis for Nuclear Waste Management V., Elsevier, New York, p. 389–397.

Ewing, R.C. (1993). The metamict state: 1993 – the centennial. Nuclear Instruments and Methods in Physics Research Section B, 91, 22–29.

Ewing, R. C., & Weber, W. J. (2011). Actinide waste forms and radiation effects. In L.R. Morss, N. M. Edelstein, and J. Fuger, J., Eds., The Chemistry of the Actinide and Transactinide Elements, 6, Springer, Netherlands, p. 3813–3887.

Farnan, I., Balan, E., Pickard, C. J., & Mauri, F. (2003). The effect of radiation damage on local structure in the crystalline fraction of $ZrSiO_4$: Investigating the ^{29}Si NMR response to pressure in zircon and reidite. American Mineralogist, 88(11–12), 1663–1667.

Farnan, I., Cho, H., & Weber, W. J. (2007). Quantification of actinide α–radiation damage in minerals and ceramics. Nature, 445(7124), 190–193.

Finch, A. A., Hole, D. E., & Townsend, P. D. (2003). Orientation dependence of luminescence in plagioclase. Physics and chemistry of minerals, 30(6), 373–381.

Finch, A.A., Garcia-Guinea, J., Hole, D.E., Townsend, P.D., and Hanchar, J.M. (2004) Ionoluminescence of zircon: rare earth emissions and radiation damage. Journal of Physics D, 2795–2803.

Friis, H., Finch, A. A., Williams, C. T., & Hanchar, J. M. (2010). Photoluminescence of zircon (ZrSiO4) doped with REE^{3+} (REE= Pr, Sm, Eu, Gd, Dy, Ho, Er). Physics and Chemistry of Minerals, 37(6), 333–342.

Fritsch, E., Rondeau, B., Hainschwang, T., & Karampelas, S. (2012). Raman spectroscopy applied to Gemmology. In Eds. J. Dubessy, M.-C. Caumon and F. Rull, Raman spectroscopy applied to Earth Sciences and cultural heritage. EMU Notes in Mineralogy 12, European Mineralogical Union and Mineralogical Society of Great Britain and Ireland, London, p. 455–490.

Gaft, M., Reisfeld, R., Panczer, G., Uspensky, E., Varrel, B., & Boulon, G. (1999). Luminescence of Pr^{3+} in minerals. Optical Materials, 13(1), 71–79.

Gaft, M., Panczer, G., Reisfeld, R., & Shinno, I. (2000). Laser-induced luminescence of rare-earth elements in natural zircon. Journal of Alloys and Compounds, 300, 267–274.

Gaft, M., Panczer, G., Reisfeld, R., & Uspensky, E. (2001). Laser-induced time-resolved luminescence as a tool for rare-earth element identification in minerals. Physics and Chemistry of Minerals, 28(5), 347–363.

Gaft, M., Reisfeld, R., & Panczer, G. (2005). Modern luminescence spectroscopy of minerals and materials. Springer, Berlin, 356 p.

Geisler, T., Ulonska, M., Schleicher, H., Pidgeon, R. T., & van Bronswijk, W. (2001). Leaching and differential recrystallization of metamict zircon under experimental hydrothermal conditions. Contributions to Mineralogy and Petrology, 141(1), 53–65.

Geisler, T., Trachenko, K., Ríos, S., Dove, M. T., & Salje, E. K. (2003). Impact of self-irradiation damage on the aqueous durability of zircon (ZrSiO4): implications for its suitability as a nuclear waste form. Journal of Physics: Condensed Matter, 15(37), 597–605.

Götze, J., Habermann, D., Neuser, R. D., & Richter, D. K. (1999). High-resolution spectrometric analysis of rare earth elements-activated cathodoluminescence in feldspar minerals. Chemical Geology, 153(1), 81–91.

Götze, J. (2000) Cathodoluminescence microscopy and spectroscopy in applied mineralogy. Freiberger Forschungshefte C485, TU Bergakademie Freiberg, 128 p.

Götze, J., Schertl, H. P., Neuser, R. D., Kempe, U., & Hanchar, J. M. (2013). Optical microscope-cathodoluminescence (OM–CL) imaging as a powerful tool to reveal internal textures of minerals. Mineralogy and Petrology, 107(3), 373–392.

Goncalves, P., Williams, M. L., & Jercinovic, M. J. (2005). Electron-microprobe age mapping of monazite. American Mineralogist, 90(4), 578–585.

Habermann, D., Neuser, R. D., & Richter, D. K. (1996). REE-activated cathodoluminescence of calcite and dolomite: high-resolution spectrometric analysis of CL emission (HRS–CL). Sedimentary Geology, 101(1), 1–7.

Hanchar, J.M. & Miller, C.F. (1993) Zircon zonation patterns as revealed by cathodoluminescence and backscattered electron images: implications for interpretation of complex crustal histories. Chemical Geology, 110, 1–13.

Hanchar, J.M. & Rudnick, R.L. (1995) Revealing hidden structures: the application of cathodoluminescence and back-scattered electron imaging to dating zircons from lower crustal xenoliths. Lithos, 36, 289–303.

Higgins, J. B., & Ribbe, P. H. (1976). The crystal chemistry and space groups of natural and synthetic titanites. American Mineralogist, 61(9–10), 878–888.

Holland, H.D. and Gottfried, D. (1955). The effect of nuclear radiation on the structure of zircon. Acta Crystallographica, 8, 291–300.

Horie, K., Hidaka, H., & Gauthier-Lafaye, F. (2006). Elemental distribution in zircon: Alteration and radiation-damage effects. Physics and Chemistry of the Earth, Parts A/B/C, 31(10), 587–592.

Hoskin, P. W. O., & Black, L. P. (2000). Metamorphic zircon formation by solid-state recrystallization of protolith igneous zircon. Journal of metamorphic Geology, 18(4), 423–439.

Kempe, U., & Götze, J. (2002). Cathodoluminescence (CL) behaviour and crystal chemistry of apatite from rare-metal deposits. Mineralogical Magazine, 66(1), 151–172.

Kenyon, A. J. (2002). Recent developments in rare-earth doped materials for optoelectronics. Progress in Quantum Electronics, 26(4), 225–284.

Kennedy, A. K., Kamo, S. L., Nasdala, L., & Timms, N. E. (2010). Grenville skarn titanite: potential reference material for SIMS U–Th–Pb analysis. Canadian Mineralogist, 48(6), 1423–1443.

Kuiper, Y. D. (2005). Isotopic age constraints from electron microprobe U-Th-Pb dates, using a three-dimensional concordia diagram. American Mineralogist, 90(4), 586–591.

Lenting, C., Geisler, T., Gerdes, A., Kooijman, E., Scherer, E. E., & Zeh, A. (2010). The behavior of the Hf isotope system in radiation-damaged zircon during experimental hydrothermal alteration. American Mineralogist, 95(8–9), 1343–1348.

Li, W., Wang, L., Lang, M., Trautmann, C., & Ewing, R. C. (2011). Thermal annealing mechanisms of latent fission tracks: Apatite vs. zircon. Earth and Planetary Science Letters, 302(1), 227–235.

Liu, G., & Jacquier, B. (2005). Spectroscopic properties of rare earths in optical materials. Springer, Berlin Heidelberg, 550 p.

Lumpkin, G.R. (2001): Alpha-decay damage and aqueous durability of actinide host phases in natural systems. Journal of Nuclear Materials, 289, 136–166.

Lumpkin, G.R., Smith, K.L., Gieré, R., Williams, C.T. (2004): Geochemical behavior of host phases for actinides and fission products in crystalline ceramic nuclear waste forms. In R. Gieré, P. Stille, Eds., Energy, Waste, and the Environment: a Geochemical Perspective, Geological Society of London Special Publications 236, p. 89–111.

Marfunin, A.S. (1979). Spectroscopy, luminescence, and radiation centers in minerals, Springer, Berlin, Heidelberg, New York, 352 p.

Mathieu, R., Zetterström, L., Cuney, M., Gauthier-Lafaye, F., & Hidaka, H. (2001). Alteration of monazite and zircon and lead migration as geochemical tracers of fluid paleocirculations around the Oklo–Okélobondo and Bangombé natural nuclear reaction zones (Franceville basin, Gabon). Chemical Geology, 171(3), 147–171.

MacRae, C. M., Wilson, N. C., Torpy, A., & Davidson, C. J. (2012). Hyperspectral cathodoluminescence imaging and analysis extending from ultraviolet to near infrared. Microscopy and Microanalysis, 18(6), 1239.

MacRae, C.M., Wilson, N.C., & Torpy, A. (2013). Hyperspectral cathodoluminescence. Mineralogy and Petrology, 107, 429–440.

Mendoza, C. (2010). Caractérisation et comportement sous irradiation de phases powellites dopées terres rares – Application au comportement à long terme des matrices de confinement des déchets. Ph.D. thesis, Universite Claude Bernard – Lyon 1.

Nielsen, R. L., Gallahan, W. E., & Newberger, F. (1992). Experimentally determined mineral-melt partition coefficients for Sc, Y and REE for olivine, orthopyroxene, pigeonite, magnetite and ilmenite. Contributions to Mineralogy and Petrology, 110(4), 488–499.

Montel, J. M. (2011). Minerals and design of new waste forms for conditioning nuclear waste. Comptes Rendus Geoscience, 343(2), 230–236.

Murakami, M., Yamada, R., & Tagami, T. (2006). Short-term annealing characteristics of spontaneous fission tracks in zircon: A qualitative description. Chemical Geology, 227(3), 214–222.

Nasdala, L., Irmer, G., & Wolf, D. (1995). The degree of metamictization in zircons: a Raman spectroscopic study. European Journal of Mineralogy, 7(3), 471–478.

Nasdala, L., Smith, D.C., Kaindl, R. & Ziemann, M. (2004a). Raman spectroscopy: Analytical perspectives in mineralogical research. In A. Beran and E. Libowitzky, Eds., Spectroscopic methods in mineralogy, EMU Notes in Mineralogy, 6, European Mineralogical Union, p. 281–343.

Nasdala, L., Reiners, P. W., Garver, J. I., Kennedy, A. K., Stern, R. A., Balan, E., & Wirth, R. (2004b). Incomplete retention of radiation damage in zircon from Sri Lanka. American Mineralogist, 89(1), 219–231.

Nasdala, L., Hanchar, J. M., Rhede, D., Kennedy, A. K., & Váczi, T. (2010a). Retention of uranium in complexly altered zircon: an example from Bancroft, Ontario. Chemical Geology, 269(3), 290–300.

Nasdala, L., Grötzschel, R., Probst, S., & Bleisteiner, B. (2010b). Irradiation damage in monazite–(Ce): an example to establish the limits of Raman confocality and depth resolution. The Canadian Mineralogist, 48(2), 351–359.

Nasdala, L., Beyssac, O., Schopf, J.W., and Bleisteiner, B. (2012) Application of Raman-based images in the Earth sciences. In A. Zoubir, Ed., Raman imaging – Techniques and applications, Springer Series in Optical Sciences, 168, Springer, Berlin, Heidelberg, p. 145–187.

Nasdala, L., Grambole, D., & Ruschel, K. (2013). Review of effects of radiation damage on the luminescence emission of minerals, and the example of He-irradiated $CePO_4$. Mineralogy and Petrology, 107(3), 441–454.

Ollier, N., Concas, G., Panczer, G., Champagnon, B., & Charpentier, T. (2003). Structural features of a Eu^{3+} doped nuclear glass and gels obtained from glass leaching. Journal of Non-Crystalline Solids, 328(1), 207–214.

Omel'yanenko, B. I., Livshits, T. S., Yudintsev, S. V., & Nikonov, B. S. (2007). Natural and artificial minerals as matrices for immobilization of actinides. Geology of Ore Deposits, 49(3), 173–193.

Owen, J. J., Cheetham, A. K., & McFarlane, R. A. (1998). Orientation-dependent fluorescence studies and spectroscopic analysis of doped barium yttrium fluoride upconversion laser crystals ($BaY_{2-x-y}Yb_xTm_yF_8$). Journal of the Optical Society of America B–Optical Physics, 15(2), 684–693.

Pabst, A. (1952). The metamict state. American Mineralogist, 37, 137–157.

Palenik, C. S., Nasdala, L., & Ewing, R. C. (2003). Radiation damage in zircon. American Mineralogist, 88, 770–781.

Panczer, G., De Ligny, D., Mendoza, C., Gaft, M., Seydoux-Guillaume, A., & Wang, X. (2012). Raman and fluorescence. In J. Dubessy, M.-C. Caumon & F. Rull, Eds., Raman Spectroscopy applied to Earth sciences and cultural heritage. EMU Notes in Mineralogy 12, European Mineralogical Union, p. 61–82.

Picot, V., Deschanels, X., Peuget, S., Glorieux, B., Seydoux-Guillaume, A. M., & Wirth, R. (2008). Ion beam radiation effects in monazite. Journal of Nuclear Materials, 381(3), 290–296.

Rakovan, J., & Reeder, R. J. (1996). Intracrystalline rare earth element distributions in apatite: Surface structural influences on incorporation during growth. Geochimica et Cosmochimica Acta, 60(22), 4435–4445.

Reisfeld, R., Gaft, M., Boulon, G., Panczer, C., & Jørgensen, C. K. (1996). Laser-induced luminescence of rare-earth elements in natural fluor-apatites. Journal of luminescence, 69(5), 343–353.

Reisfeld, R., Zigansky, E., & Gaft, M. (2004). Europium probe for estimation of site symmetry in glass films, glasses and crystals. Molecular Physics, 102(11–12), 1319–1330.

Reisfeld, R. (2005) Spectroscopy of rare earth ions. In A. Vaseashta, D. Dimova-Malinovska, J.M. Marshall, Eds., Nanostructured and advanced materials for applications in sensor, optoelectronic and photovoltaic technology, Nato Sci Ser II Math 204, Springer Berlin Heidelberg, p. 77–100.

Richter, D. K., Götte, T., Götze, J., & Neuser, R. D. (2003). Progress in application of cathodoluminescence (CL) in sedimentary petrology. Mineralogy and Petrology, 79(3–4), 127–166.

Richter, D. K., Krampitz, H., Görgen, P., Götte, T., & Neuser, R. D. (2006). Xenotime in the lower buntsandstein of central europe: evidence from cathodoluminescence investigation. Sedimentary Geology, 183(3), 261–268.

Richter, D. K., Görgen, P., & Götte, T. (2008). Monazite cathodoluminescence – A new tool for heavy mineral analysis of siliciclastic sedimentary rocks. Sedimentary Geology, 209(1), 36–41.

Rios, S., Salje, E. K., Zhang, M., & Ewing, R. C. (2000). Amorphization in zircon: evidence for direct impact damage. Journal of Physics: Condensed Matter, 12(11), 2401.

Rubatto, D., & Gebauer, D. (2000). Use of cathodoluminescence for U-Pb zircon dating by ion microprobe: some examples from the Western Alps. In M. Pagel, V. Barbin, P. Blanc, and D. Ohnenstetter, D. (Eds.), Cathodoluminescence in geosciences. Springer Berlin Heidelberg, p. 373–400.

Seydoux-Guillaume, A. M., Wirth, R., Nasdala, L., Gottschalk, M., Montel, J. M., & Heinrich, W. (2002). An XRD, TEM and Raman study of experimentally annealed natural monazite. Physics and Chemistry of Minerals, 29(4), 240–253.

Soman, A., Geisler, T., Tomaschek, F., Grange, M., & Berndt, J. (2010). Alteration of crystalline zircon solid solutions: a case study on zircon from an alkaline pegmatite from Zomba–Malosa, Malawi. Contributions to Mineralogy and Petrology, 160(6), 909–930.

Stefanovsky, S. V., Yudintsev, S. V., Gieré, R., & Lumpkin, G. R. (2004). Nuclear waste forms. Geological Society, London, Special Publications, 236(1), 37–63.

Tarashchan, A. (1978). Luminescence of minerals. Naukova Dumka, Kiev, 296 p.

Ternane, R., Ferid, M., Panczer, G., Trabelsi-Ayadi, M., & Boulon, G. (2005). Site-selective spectroscopy of Eu^{3+}-doped orthorhombic lanthanum and monoclinic yttrium polyphosphates. Optical Materials, 27(12), 1832–1838.

Vance, E.R. (2012) Ceramic Waste Forms, In R.J.M. Konings, Ed., Comprehensive Nuclear Materials Vol. 5, Elsevier, Oxford, p. 485–503.

Vavra, G. (1990). On the kinematics of zircon growth and its petrogenetic significance: a cathodoluminescence study. Contributions to Mineralogy and Petrology, 106(1), 90–99.

Waychunas, G. A. (2002). Apatite luminescence. Reviews in mineralogy and geochemistry, 48(1), 701–742.

Wasilewski, P.J., Senftle, F.E., Vaz, J.E., Thorpe, A.N., and Alexander, C.C. (1973). A study of the natural α-recoil damage in zircon by infrared spectra. Radiation Effects, 17, 191–199.

Weber, W. J. (1990). Radiation-induced defects and amorphization in zircon. Journal of Materials Research, 5, 2687–2697.

Weber, W.J., Navrotsky, A., Stefanovsky, S., Vance, E.R., and Vernaz, E. (2009): Materials science of high-level nuclear waste immobilization. MRS Bull., 34, 46–53.

Zhang, M., Salje, E. K., Farnan, I., Graeme-Barber, A., Daniel, P., Ewing, R. C., Clark, A.M. & Leroux, H. (2000). Metamictization of zircon: Raman spectroscopic study. Journal of Physics: Condensed Matter, 12(8), 1915.

Zhang, M., & Salje, E. K. (2001). Infrared spectroscopic analysis of zircon: Radiation damage and the metamict state. Journal of physics: Condensed matter, 13(13), 3057.

Zhang, M., Boatner, L. A., Salje, E. K., Ewing, R. C., Daniel, P., Weber, W. J., Zhang Y. & Farnan, I. (2008). Micro-Raman and micro-infrared spectroscopic studies of Pb-and Au-irradiated $ZrSiO_4$: Optical properties, structural damage, and amorphization. Physical Review B, 77(14), 144110.

Ziegler, J.F., Biersack, J.P., & Littmark, U. (1985). The stopping and range of ions in solids. Pergamon Press, New York.

Appendix A.1

Factors affecting the Nd^{3+} (REE^{3+}) luminescence of minerals

Lenz, C., Talla, D., Ruschel, K., Skoda, R., Götze, J. & Nasdala, L. (2013)

Mineralogy and Petrology, 107, 415–428 (published)

ORIGINAL PAPER

Factors affecting the Nd^{3+} (REE^{3+}) luminescence of minerals

**Christoph Lenz · Dominik Talla · Katja Ruschel ·
Radek Škoda · Jens Götze · Lutz Nasdala**

Abstract In this paper, possibilities and limits of the application of REE^{3+} luminescence (especially the Nd^{3+} $^4F_{3/2} \rightarrow$ $^4I_{9/2}$ emission) as structural probe are evaluated. Important factors controlling the Nd^{3+} luminescence signal are discussed, including effects of the crystal-field, crystal orientation, structural state, and temperature. Particular attention was paid to the study of the accessory minerals zircon ($ZrSiO_4$), xenotime–(Y) (YPO_4), monazite–(Ce) ($CePO_4$) and their synthetic analogues. Based on these examples we review in short that (1) REE^{3+} luminescence can be used as non-destructive phase identification method, (2) the intensities of certain luminescence bands are strongly influenced by crystal orientation effects, and (3) increased widths of REE^{3+}-related emission bands are a strong indicator for structural disorder. We discuss the potential of luminescence spectroscopy, complementary to Raman spectroscopy, for the quantitative estimation of chemical (and potentially also radiation-induced) disorder. For the latter, emissions of Nd^{3+}-related centres are found to be promising candidates.

C. Lenz (✉) · D. Talla · K. Ruschel · L. Nasdala
Institut für Mineralogie und Kristallographie, Universität Wien,
Althanstraße 14, 1090 Wien, Austria
e-mail: christoph.lenz@univie.ac.at

D. Talla · R. Škoda
Institute of Geological Sciences, Masaryk University, Kotlářská 2,
61137 Brno, Czech Republic

J. Götze
Institut für Mineralogie, TU Bergakademie Freiberg,
Brennhausgasse 14, 09596 Freiberg, Germany

Introduction

The luminescence emission of rare-earth elements (REEs) in general is well-studied, stimulated by their importance in various modern technological applications such as lighting, colour-television screens, solid-state lasers, phosphors, and chromophores in different host materials (e.g., Belsky and Krupa 1999; Kenyon 2002; Bünzli and Piguet 2005; Liu and Jacquier 2005). In the Earth sciences, one challenging task is the detection of REEs in different host minerals using luminescence methods; a large variety of mineral systems have been studied already (Tarashchan 1978; Ohnenstetter et al. 1991; Habermann et al. 1996; Gaft et al. 1999; Götze et al. 1999; Blanc et al. 2000; Waychunas 2002; Nasdala et al. 2004; Gaft et al. 2005; Czaja et al. 2008). Synthetic minerals individually- or multi-doped with REEs have also been studied routinely, aiming at a better understanding of the luminescence in their natural analogues. For the example of zircon and synthetic $ZrSiO_4$, such investigations have been done by Cesbron et al. (1993, 1995), Blanc et al. (2000), Hanchar et al. (2001), and Friis et al. (2009). Time-resolved luminescence techniques have improved the detection of various luminescence centres utilizing their different decay times (Reisfeld et al. 1996; Gaft et al. 1999; Gaft et al. 2001). Furthermore, unravelling the internal zoning of the REE distribution within crystals, especially of accessory minerals, may provide valuable information on their primary formation and post-growth history. Such patterns are visualised easily using luminescence techniques (Hanchar and Miller 1993; Hanchar and Rudnick 1995; Rakovan and Reeder 1996; Götze 2000, 2002; see also the review chapter by Götze et al. in this special issue).

In addition to traditional direct imaging, the luminescence of crystals and other geological samples is studied increasingly using (hyperspectral) mapping techniques (see the review

🖉 Springer

chapter by MacRae et al. in this special issue). The need four sound spectral interpretation in reducing such hyperspectral data sets has increased the interest in a detailed understanding of REE luminescence features (Nasdala et al. 2004; MacRae et al. 2005). For a number of minerals, luminescence-intensity based quantifications of trace REEs have been proposed (Barbarand and Pagel 2001; Habermann 2002; Richter et al. 2003; MacRae et al. 2005; 2012). Moreover, traces of REE^{3+} in minerals and mineral-based ceramics are used as structural probes studied with respect to order–disorder phenomena, in particular the accumulation of structural damage as caused by irradiation. For instance, spectral parameters of Eu^{3+} emissions have been used for the characterisation of REE-substituted cation-sites in glasses and crystalline materials in process of evaluation of potential nuclear waste forms (Ollier et al. 2003; Reisfeld et al. 2004; Reisfeld 2005; Ternane et al. 2005). Seydoux-Guillaume et al. (2002) and Panczer et al. (2012) proposed that the REE-dominated luminescence emission of monazite–(Ce) may bear quantitative information on the accumulated radiation-damage in this mineral.

In accordance to the finding of the latter authors, we consider the luminescence signal of Nd^{3+} as particularly promising structural probe. The $^4F_{3/2} \rightarrow {}^4I_{9/2}$ electronic transition of Nd^{3+} causes luminescence emission in the near-infrared (NIR) spectral range between 10,600 and 11,800 cm^{-1} (830–940 nm). This emission is a promising candidate because : (1) the luminescence signal can be collected with standard Si-based detectors; (2) it is effectively excited by standard lasers, e.g., Ar$^+$ (488 nm, 514 nm) as well as via accelerated electrons (cathodoluminescence, CL); (3) other luminescence emissions in the respective wavenumber range are rare; and (4) it has been identified in many mineral hosts, especially in REE-bearing accessory minerals. The application of Nd^{3+} (REE^{3+}) luminescence as a structural probe requires a detailed understanding of the influencing factors and their calibration, respectively. Here we discuss the basic effects of (1) the crystal field environment;

(2) crystal orientation; (3) structural disorder; and (4) temperature on the Nd^{3+} luminescence as representative example. Similar to Nd^{3+}, other appropriate REE^{3+} can be used, e.g., Pr^{3+}, Sm^{3+}, Eu^{3+}, but are not discussed in this work. In this study, the Nd^{3+} hosts zircon, xenotime–(Y) and monazite–(Ce) and their synthetic analogues have been studied in detail.

Samples & methods

Samples and preparation

Luminescence investigations were performed on a large variety of specimens including monazite–(Ce), Zircon and xenotime–(Y) and/or their synthetic analogues (see Table 1). An overview of the chemically homogeneous, natural monazite–(Ce) samples measured here, including their origins and ages, is given in Ruschel et al. (2012). Only samples of these authors that were annealed in air to reconstitute their crystalline state were chosen for the study of chemical-induced disorder, to avoid biases of the results due to effects of self-irradiation damage on the luminescence parameters obtained. In addition, a range of flux-grown, synthetic samples were studied, including Ce$_{1-x}$LREE$_x$PO$_4$ (with LREE = La, Nd, Gd) of Ruschel et al. (2012) and CePO$_4$ samples with predominant *cheralite* (2 REE^{3+} ↔ Ca^{2+} + Th^{4+}) or *huttonite* (P^{5+} + REE^{3+} ↔ Si^{4+} + Th^{4+}) substitution (synthesised in this study; see below).

The orientation-dependence of the luminescence was studied for Nd-doped YPO$_4$ samples synthesised by Talla et al. (2011), and Nd-doped ZrSiO$_4$ crystals produced in this study (see sub-chapter "Details on synthesis procedures" below). An overview of the samples investigated is given in Table 1.

Doubly polished thin sections (thicknesses ~30 μm) attached to a glass slide were prepared with respect to the crystallographic orientation (xenotime and zircon samples),

Table 1 Overview of samples studied in detail

Samples		Substitution type	Reference
Monazite-(Ce)	natural	huttonite + cheralite	all homogeneous, dry-annealed monazite–(Ce) samples from Ruschel et al. (2012)
	synthetic	Ce$_{1-x}$REE$_x$[PO$_4$] substitution	Nd-, Gd- and/or La-containing homogeneous samples from Ruschel et al. (2012)
	synthetic	cheralite + "Na-Th substitution" Ce$_{1-x-y}$Ca$_{0.5x}$Na$_{y/3}$Th$_{0.5+2y/3}$[PO$_4$]	this study; see in "Details on synthesis procedures"
Zircon	synthetic	almost pure crystals doped with trace Nd^{3+} without charge compensation	this study; see in "Details on synthesis procedures"
	synthetic	almost pure crystals doped with trace Nd^{3+} incorporated via xenotime substitution, Zr$_{1-x}$Nd$_x$[Si$_{1-x}$P$_x$O$_4$]	this study; see in "Details on synthesis procedures"
Xenotime-(Y)	synthetic	crystals doped with Nd^{3+} incorporated via Y$_{1-x}$Nd$_x$[PO$_4$] substitution	Talla et al. (2011)

or as randomly cut slabs (monazite samples from Ruschel et al. 2012). For electron microprobe and cathodoluminescence analysis the sections were coated with carbon.

Details on synthesis procedures

Synthetic monazite–(Ce) crystals with predominant cheralite or huttonite substitution were produced by a flux method using the slow-cooling technique. Sodium polyphosphate was preferentially used as flux material because of its good solubility in water, making the extraction of the resulting product straightforward (and fast in comparison with $Pb_2P_2O_7$, commonly used for REE phosphate syntheses; Boatner 2002; Talla et al. 2011). Platinum crucibles with a volume of 100 cm^3 were used as reaction vessels. For each batch, 10 grams of $NaPO_3$ were used as flux material and mixed with $CeCl_3.7H_2O$, setting the molar ratio Ce/(Ce+Na) in the melt to 0.12 (Talla et al. 2011). A total of five samples of Th-doped monazite–(Ce) were produced using $Th(NO_3)_4.5H_2O$. In the first three, Th was added in varying amounts, the weight ratio Th/(Th+Ce) in the melt being 400, 2,000 and 10,000 ppm. Charge balance was provided using the *cheralite substitution* mechanism (2 REE^{3+} ↔ Ca^{2+} + Th^{4+}) with $CaCO_3$ (analytical grade) as source of Ca. A fourth, un-doped sample was also produced for comparison (blank). In the fifth sample, the *huttonite substitution* (P^{5+} + REE^{3+} ↔ Si^{4+} + Th^{4+}) was used as the mechanism for introducing Th into monazite–(Ce) with silica as source of Si. The weight fraction Si/(Si+Ce+Th) in the melt was adjusted to 0.02. All reagents were of analytical grade except for $NaPO_3$ and the cerium chloride. Preliminary tests showed that pollutant

trace Nd present in the commercial $CeCl_3.7H_2O$ results in minute concentrations of Nd in the $CePO_4$ samples grown, which, however, yield easily measurable Nd^{3+}-luminescence emissions. A separate Nd source was therefore not added to the crucible. After being filled, the Pt crucibles were capped by a loose lid. Crucibles were first heated to a peak temperature of 1,170 °C, at a rate of 230 K per hour. This temperature was kept for 2 hours, and reduced afterwards to 900 °C, at a rate of −1.35 K per hour. The furnace was then switched off, and it was not opened until samples had cooled down slowly to room temperature. The crystals produced were about 0.3–1.0 mm in size. Their colours range from light green (low-Th syntheses) to colourless (elevated Th content). The total amount of crystals produced was much smaller when higher concentrations of heterovalent substituents were present. A detailed microchemical characterisation of these synthetic samples is given in Table 2.

Synthesis of zircon crystals (up to 1.5 mm) was accomplished by a flux technique similar to that described by Cesbron et al. (1993, 1995) and Hanchar et al. (2001) with an adjusted synthesis route combining the evaporation of the highly volatile MoO_3 with a rapid cooling rate. This allowed us to use an alkali-free mixture of 0.53 g ZrO_2 with 0.26 g SiO_2 and 10 g MoO_3, preventing the incorporation of Li$^+$ into the zircon crystals (Hanchar et al. 2001). Preliminary test runs showed that the resulting ratios of 0.07 mol% (Zr+Si)/(Zr+Si+Mo) and 1:1 Zr/Si resulted in the growth of larger, well-developed crystals. To produce Nd-doped $ZrSiO_4$, a minor amount of Nd was added. This was done in two different ways, first by adding Nd_2O_3 without any additional charge-

Table 2 Chemical formulae of synthetic Th-doped monazite-(Ce) samples in atomic percent per formula unit (apfu), calculated from average electron-microprobe data of different chemically heterogeneous zones. The distortional behaviour of all substituents (Δ) and heterovalent substituents (Δ$_{hetero}$) are approximated with a weighted ionic radii difference between the predominant cation/anion [Ce/P in monazite–(Ce)] and each substituent (see Eq. 1)

| Sample | Point | Chemical formula (apfu) | | | | | | | | Δ | Δ$_{hetero}$ |
		Ce	Nd	Na	Ca	Th	U	P	Si		
C1 *(blank)*	1	0.999	0.001	bdl	bdl	bdl	bdl	0.999	bdl	0.00012	0.00009
C2	2	0.998	0.001	bdl	0.001	bdl	bdl	0.999	bdl	0.00011	0.00008
C3	3	0.997	0.002	bdl	bdl	bdl	bdl	0.999	bdl	0.00015	0.00008
	4	0.939	0.001	0.010	0.013	0.037	0.001	0.997	bdl	0.00405	0.00023
	5	0.941	0.001	0.009	0.014	0.036	0.001	0.999	bdl	0.00377	0.00374
	6	0.915	0.001	0.015	0.018	0.051	0.001	0.999	bdl	0.00522	0.00520
C4	7	0.864	0.001	0.023	0.029	0.083	0.001	0.999	bdl	0.00850	0.00847
	8	0.931	0.001	0.012	0.015	0.040	0.001	1.000	bdl	0.00410	0.00407
	9	0.997	0.001	0.001	0.001	bdl	bdl	0.999	bdl	0.00010	0.00004
CSi	10	0.987	0.012	bdl	bdl	0.001	bdl	1.000	bdl	0.00044	0.00002
	11	0.960	bdl	0.010	0.001	0.001	bdl	0.999	bdl	0.00266	0.00264
	12	0.867	bdl	0.040	0.002	0.089	0.001	0.999	bdl	0.00805	0.00803
	13	0.909	bdl	0.027	0.002	0.061	bdl	0.999	0.001	0.00556	0.00554

compensating species, and second by adding $NdPO_4$ ensuring charge balance via the *xenotime substitution* ($Zr^{4+} + Si^{4+} \leftrightarrow REE^{3+} + P^{5+}$). The molar ratio Nd/(Nd+Zr) in the melt was adjusted to 0.6 mol%. The temperature path consisted of heating the loosely capped Pt crucibles to 1,100 °C, at a rate of 216 K per hour. Without a soaking interval, the temperature was then reduced to 700 °C, at a rate of −26.5 K per hour. Afterwards, samples were left in the furnace to cool slowly. Crystals were extracted manually (i.e., without the need to use any chemical reagents) from the crucible without problems. It was found that the size of the crystals grown was influenced strongly by the evaporation surface of the melt during the experiment. A small evaporation surface prevents rapid vaporisation of Mo-flux, the solvent of all reagents. Therefore, thinner crucibles result in the formation of larger single-crystals.

Analytical methods

Electron microprobe analyses were performed using a Cameca SX100 electron microprobe with the following measurement conditions: accelerating voltage 15 kV, beam current 20 nA, and 8 μm beam diameter. A defocused beam was in order to minimize the loss of Na during analysis. The peak counting times were 20 s for major elements and 40 to 60 s for minor and trace elements; counting times for the background (measured on both, the high- and low-energy side) were set to half of the respective peak counting-time. The following natural and synthetic standards were used: $Si_{K\alpha}$-natural sanidine, Eifel; $Na_{K\alpha}$-natural albite, Amelia; $P_{K\alpha}$-LaPO$_4$; $Ca_{K\alpha}$,$Th_{M\alpha}$-synthetic CaTh(PO$_4$)$_2$; $Ce_{L\alpha}$-synthetic CePO$_4$; $Nd_{L\beta}$-synthetic NdPO$_4$; $U_{M\beta}$-synthetic U. The raw data were corrected using the PAP routine (Pouchou and Pichoir 1991). Elemental X-ray maps were acquired at following conditions: accelerating voltage 15 kV, beam current 60 nA, and <1 μm beam diameter. Signals of $Na_{K\alpha}$, $P_{K\alpha}$, $Ce_{L\alpha}$, $Nd_{L\beta}$, and $Th_{M\alpha}$, and backgrounds for each element were collected. The data were acquired in stage moving mode, with 1 μm step width and 50 ms dwell time. The collected peak intensities were corrected for the background intensities and converted to absolute concentrations. Finally colour-coded element distribution maps were produced to visualize internal distribution patterns for certain chemical components.

Cathodoluminescence (CL) spectroscopy was performed using a hot cathode luminescence microscope (HC1-LM) with a high-vacuum chamber (< 10^{-6} bar). Spectral acquisition was done with an Acton Spectra Pro 2300i spectrometer with a charge-coupled device (CCD) detector, which is attached to the CL microscope by a silica-glass fibre-guide. Measurements were taken with a 100 μm slit, a 150 s line grid, an accelerating voltage of 14 kV and a current of 0.2 mA with a current density of approximately 10 μA mm^{-2}. Calibration was done with the mercury vapour discharge emission. The optical aperture produces a spot size of 30 μm. Cathodoluminescence examinations

were carried out on polished thin sections that are coated with carbon to prevent any build-up of electrical charge during CL operation (further details in Neuser et al. 1995).

Room-temperature laser-induced photoluminescence measurements were carried out by means of a Horiba Jobin Yvon LabRam-HR (high resolution) system equipped with an Olympus BX41 optical microscope, a grating with 600 grooves per millimetre, and a Si-based, Peltier-cooled CCD detector. Luminescence spectra were excited using the continuous 532 nm emission of a frequency-doubled Nd:YAG laser (34 mW on the sample surface). With the system operated in confocal mode and an Olympus 100× objective (numerical aperture=0.9), the lateral resolution was better than 1.5 μm, and the depth resolution (with the laser beam focused at the sample surface) was approximately 3 μm. The spectral resolution in the NIR was determined to be ~2 cm^{-1}. Wavenumber calibration was done using the Rayleigh line and Ne lamp emissions; the wavenumber accuracy was better than 0.5 cm^{-1}. Temperature-dependent measurements were done adding a Linkam FTIR 600 liquid-nitrogen cooling stage. The temperature accuracy was better than 2 K. Photoluminescence (hyperspectral) maps were obtained using a software-controlled x–y stage, with a step width of 3 μm.

Luminescence bands were fitted assuming Lorentzian-Gaussian (pseudo-Voigt) band shapes. Background correction turned out to be unnecessary.

Fingerprints of Nd^{3+} luminescence emission: generalities

Luminescence emissions are generated through the (radiative) release of energy during electronic transitions. Emission spectra of REE^{3+} in crystalline hosts are characterised by very sharp bands in contrast to the luminescence of 3d or 4d elements (Blasse and Grabmaier 1994). This unique characteristic of REE^{3+} luminescence is determined by their particular electron configuration. Trivalent rare earth ions (Ce^{3+} to Yb^{3+}) have an incompletely filled 4f shell which is shielded by outer filled 5s^2 and 5p^6 orbitals. In consequence, the influence from ligands in the host matrix is small (but of crucial importance). The narrow luminescence bands originate from intra-configurational 4f^n electronic transitions. The distinct 4f^n energy levels result from different electronic interactions. The four kinds of electronic interactions are illustrated in Fig. 1 for the example of Nd^{3+} with 4f^3 electron configuration. The energetic state of 4f^n electrons in free REE^{3+} ions splits into spectroscopic *terms* due to the repulsion of unpaired 4f electrons (*electron–electron interaction*). In REE^{3+} ions, this term-splitting is on the order of ca. 10^4 cm^{-1} (Marfunin 1979). While the possible influence of negative charges from ligands is low, these terms further split into spectroscopic *levels* due to their *spin-orbit coupling* (on the order of ca. 10^3 cm^{-1}). Note that the separation of energy levels by these interactions applies to free REE^{3+} ions.
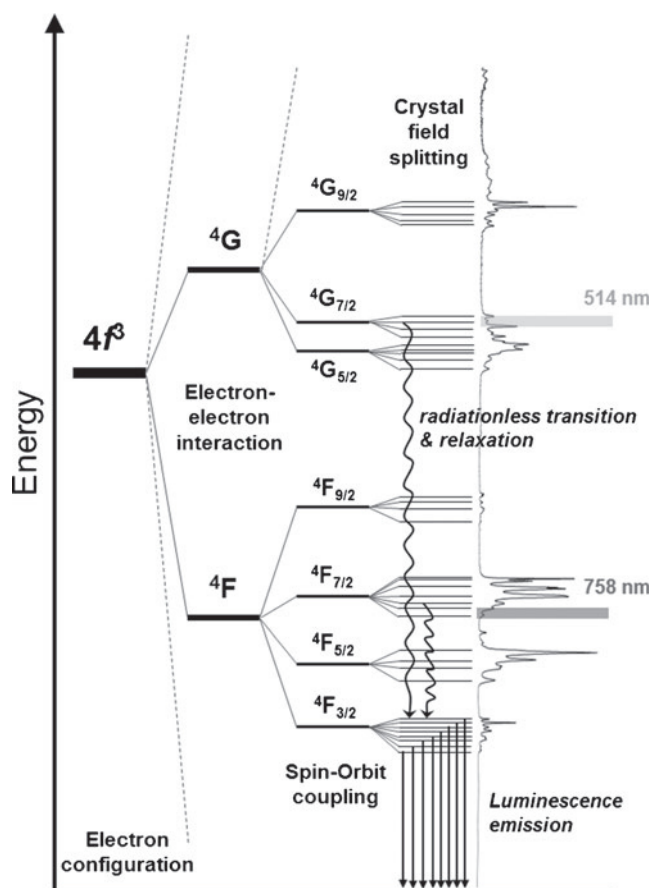
Fig. 1 Schematic illustration of the generation of electronic states for the example of Nd^{3+} with $4f^3$ electronic configuration. As examples for typical photoluminescence excitations, energies of photons of 514 and 758 nm laser light are marked on the right. After various excitation and subsequent relaxation processes, electrons eventually reach the lowest excited level ($^4F_{3/2}$). The transition from this level to the ground state is typically a radiative process that results in the emission of light, observed in the near-infrared range of the electromagnetic spectrum

An important result is that REE^{3+} optical transitions appear at similar energy ranges in very different host materials. A complete diagram of possible energy levels for each REE^{3+} is given in Carnall et al. (1989). If REE^{3+} ions are further surrounded by ligands e.g., in molecules (*ligand field*) or solids (*crystal field*), the electronic levels split into *sublevels* (*Stark level* splitting on the order of ca. 10^2 cm^{-1}; cf. Fig. 1). According to the *crystal field theory* (cf. Burns 1993) ligand-directed orbitals experience an energy destabilization due to repulsion with the negative charge of the ligand. Non-directed orbitals are stabilized, as their potential energy drops. The crystal field splitting depends on a variety of parameters connected to the site of the REE^{3+} within the crystal structure, e.g., site symmetry, the interatomic distance to the ligands, charge of ligands etc. Given the different characteristics of cation sites among minerals, REE^{3+} spectra may provide site-specific information on the short-range order.

Figure 2 exemplifies the Nd^{3+} photoluminescence of five different hosts: the accessory minerals xenotime–(Y), monazite–(Ce), titanite, and synthetic cubic zirconia (YCZ) and Yttrium-aluminium garnet (YAG). In all hosts the Nd^{3+}-related ($^4F_{3/2} \rightarrow {}^4I_{9/2}$) luminescence emission can be detected within the spectral range between 10,600 and 11,800 cm^{-1} (940–840 nm). Yttrium-stabilized zirconia (fluorite structure type, *Fm3m*) and YAG (garnet structure type, *Ia3d*) are well known synthetic gemstones, both with cubic symmetry. Xenotime–(Y) crystallizes in the tetragonal space group *I4$_1$/amd*. Monazite (*P2$_1$/n*) and titanite (*P2$_1$/a*) have monoclinic crystal structures. The completely different crystal field around the Nd^{3+}-centre is reflected by strongly differing photoluminescence spectra (Fig. 2). Note that in many minerals probably more than one substitutional REE-site exists (e.g., apatite, Czaja et al. 2009). In these cases standard steady-state luminescence techniques obtain the luminescence signal from all potential sites possibly differing from sample to sample. Time-resolved luminescence spectroscopy or site-selective spectroscopy may offer differentiation possibilities (Dexpert-Ghys et al. 1984; Dexpert-Ghys et al. 1996; Gaft et al. 1997; Piriou et al. 2001).

Comparing the isostructural minerals monazite–(Ce) (CePO$_4$) and gasparite–(Ce) (CeAsO$_4$), both with C_1 cation site symmetry, reveals a comparatively close Nd^{3+}-luminescence pattern with only minor band shifts (Fig. 3a). Note that the band width is strongly influenced by chemical heterogeneity and intensity ratios by the crystal orientation (in more detail discussed below).

The minerals xenotime–(Y) (YPO$_4$) and chernovite–(Y) (YAsO$_4$) are isostructural with zircon (ZrSiO$_4$). All crystallize in space group *I4$_1$/amd* with D_{2d} cation site symmetry.
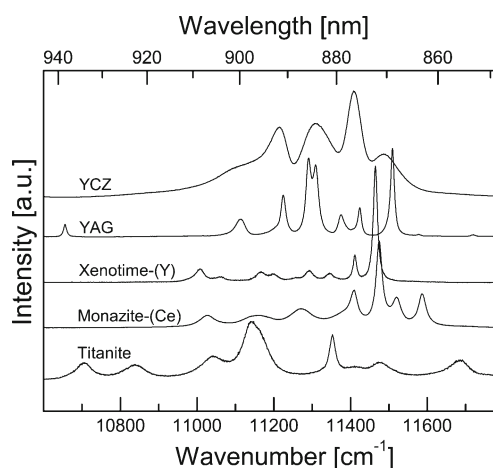
Fig. 2 Photoluminescence spectra (532 nm excitation) of Nd^{3+} ($^4F_{3/2} \rightarrow {}^4I_{9/2}$) in different host minerals: Yttrium-stabilized cubic zirconia (YCZ), yttrium-aluminium garnet (YAG), xenotime–(Y), monazite–(Ce), and titanite. Different cationic environments of the substituted Nd^{3+} cause dissimilar crystal field splittings and hence fingerprint-like luminescence patterns
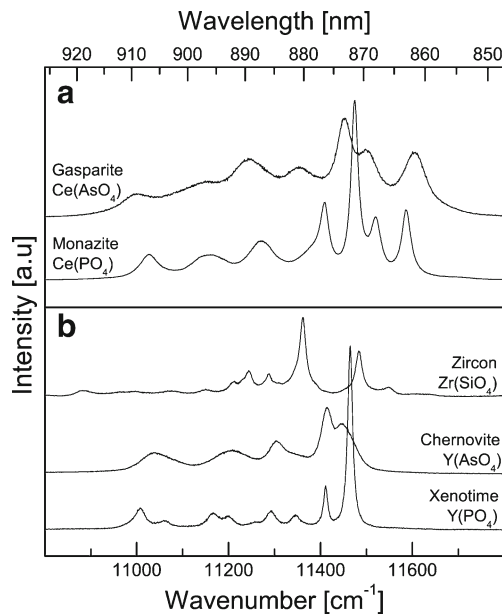
Fig. 3 Photoluminescence spectra (532 nm excitation) of Nd^{3+} ($^4F_{3/2} \rightarrow$ $^4I_{9/2}$) in two groups of isostructural minerals. **a** Gasparite–(Ce) and monazite–(Ce) with cation site-symmetry C_1. **b** Zircon, chernovite–(Y), and xenotime–(Y) with cation site-symmetry D_{2d}

Whereas xenotime–(Y) and chernovite–(Y) show similarities in the Nd^{3+}-luminescence spectra, zircon differs remarkably, despite having the same site symmetry (Fig. 3b). Synthetic Nd^{3+}:ZrSiO$_4$ charge-balanced with P^{5+} and without, as well as reference zircons from various locations were compared; their Nd^{3+} luminescence shows a similar pattern to that of synthetic Nd^{3+}:ZrSiO$_4$ shown in Fig. 3b. This example demonstrates the impact of a modified *electronic* structure on the luminescence pattern: xenotime–(Y) and chernovite–(Y) have an isotypic crystal structure with chemically related elements; both have trivalent Y^{3+} on the cationic and $P^{5+}/As^{5+}O_4$ on the anionic position. Zircon is different, having tetravalent Zr^{4+} at the cation and $Si^{4+}O_4$ at the anion sites, respectively. A different charge distribution at the substitutional REE^{3+} site remarkably affects the crystal field splitting, and therefore the REE^{3+} luminescence signal.

Luminescence studies on synthetic mineral analogues provide both: (1) a better identification of a REE in a specific host since the luminescence signal of many REE^{3+} overlap and a discrimination is complicated in natural specimens (e.g., Sm^{3+}–Pr^{3+}); and (2) a fast mineral identification when the individual sublevel splitting is known, potentially applied to igneous/metamorphic or sedimentary petrology (Richter et al. 2008).

Orientation-dependence of REE^{3+} luminescence

As mentioned above, the crystal-field splitting depends on the site symmetry of the REE^{3+}-substituted cation site. A direct

consequence is that the luminescence intensity of sublevels depends on the orientation of the measuring direction to certain symmetry elements of the crystal structure. Even though being a well-known luminescence phenomenon (Owen et al. 1998; Barbarand and Pagel 2001; Finch et al. 2003), the orientation-dependence of REE^{3+} emissions is often neglected, which may result in biased conclusions. To give two examples: Czaja et al. (2009) proposed to use the intensity ratio of emissions related to Pr^{3+} and Sm^{3+} to determine Pr/Sm ratios in apatite. Habermann (2002) applied REE-cathodoluminescence intensity for a semi-quantitative estimation of REE trace element concentration in calcite. In those papers, however, authors failed to consider possible luminescence intensity differences due to the orientation-dependence of the emissions analysed. For this reason, the orientation dependence of REE^{3+} luminescence on the example of Nd^{3+} is exemplified here for the sake of completeness (cf. Cesbron et al. 1995, Gaft et al. 2005).

Depending on the luminescence technique applied, different aspects of orientation effects can be discerned. In laser-induced photoluminescence studies the polarisation of the incident laser has to be considered, because most standard apparatus provide a strongly linear-polarised beam due to polarising effects of optical components (e.g., resonator, mirrors). The coupled interaction of the laser-beam polarisation and the orientation of the crystal leads to four independent variables: (1) the direction of the laser beam relative to the crystal [e.g., $x(yy)y$, cf. Porto notation in Porto and Krishnan (1967)]; (2) the polarisation of the laser beam relative to the crystal [$y(xy)y$)]; (3) the polarisation of the luminescence emission relative to the crystal [$y(yx)y$], and (4) the direction of luminescence emission detected relative to the crystal [$y(yy)x$]. Most spectrometer systems used in geoscientific research are coupled to microscopes, in which the laser beam and the emission detected proceed in opposite direction through the observing objective lens ($x(yy)\overline{x}$, quasi-backscattering set-up). Hence, the latter variable cannot be analysed separately using such a system set-up. Figure 4 shows the other three aspects with the example of laser-induced photoluminescence spectra of Nd^{3+} ($^4F_{3/2}$ $\rightarrow$ $^4I_{9/2}$) in synthetic tetragonal Nd^{3+}:YPO$_4$ (xenotime structure type, $I4_1/amd$). Please note that the measurement conditions, e.g., laser power, measurement point on the sample, accumulation time etc., were kept strictly identical. Figure 4a demonstrates the effect of a polarised laser beam with the electric field vector (E) aligned along different crystallographic directions; here the laser beam is directed along the crystallographic x axes; the polarisation of the electric field vector is aligned in y and z, respectively. The polarisation of the emission is neglected (no polarisation filters), all intensity of the randomly polarised signal in plane $z - y$ is detected. Changing the polarisation direction of the laser beam causes intensity ratios of the luminescence sublevels to vary significantly. The main sublevel band at 11,467 cm^{-1} is most strongly affected.
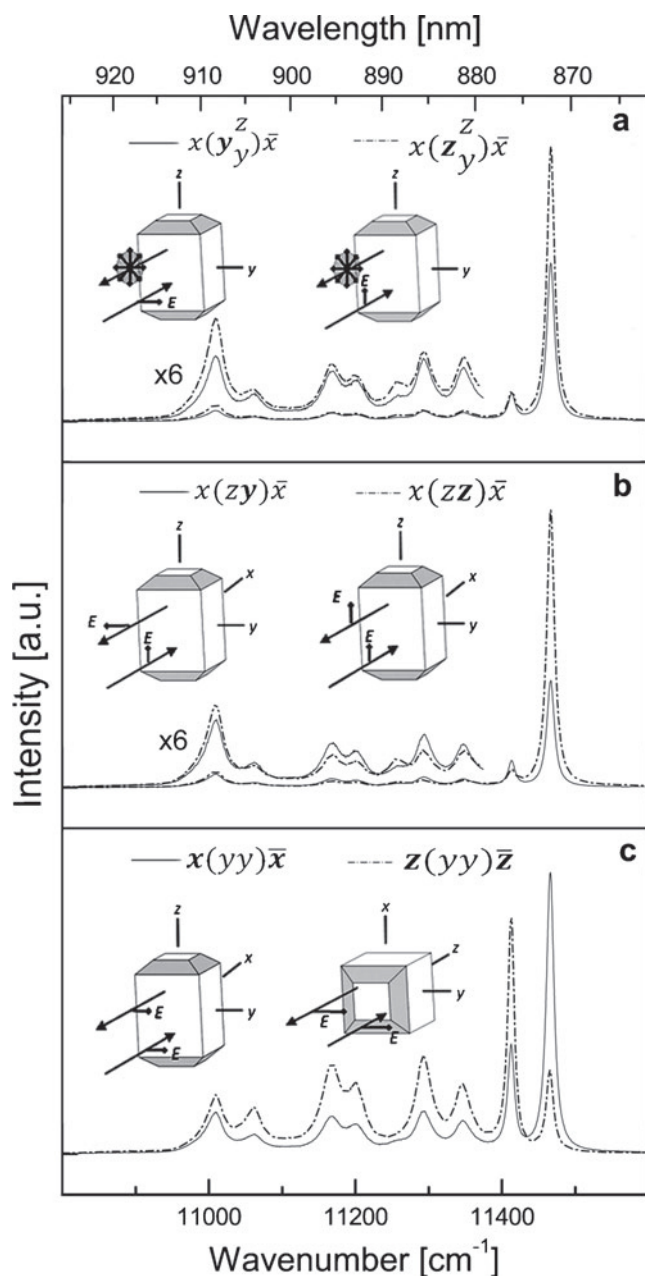
Fig. 4 Orientation-dependence of the laser-induced PL (532 nm excitation) of Nd^{3+} ($^4F_{3/2} \rightarrow {}^4I_{9/2}$) in synthetic tetragonal Nd^{3+}:YPO₄ (xenotime; $I4_1/amd$). Note that all spectra have the same vertical scaling, intensities are therefore directly comparable. **a** Effect of the polarization of the incident laser beam. **b** Effect of the polarization of the luminescence emission. **c** Effect of the direction (relative to the crystal) of the excitation/emission analysed. Small schematic sketches are inserted for better illustration of the Porto notation quoted above

A polarisation filter placed in the emission path-way reveals that the luminescence emission itself is polarised (Fig. 4b). Analysing the luminescence emission with polarisation filters in different directions leads to significant variations of intensity ratios. Turning the sample perpendicular to its tetragonal main axis (z), with the laser polarization direction and the

polarization direction of the analysed emission held constant, results in intensity increases in all other sublevel bands relative to the main at 11,467 cm⁻¹ (Fig. 4c).

In contrast to laser-induced photoluminescence, the effect of beam polarisation is without significance using an unpolarised electron or ion beam with cathode-/ionoluminescence techniques. The polarisation of the luminescence emission is of importance especially if the signal is analysed with polarisation filters, which is commonly not done in CL measurements. In Fig. 5 the cathodoluminescence spectra of synthetic xenotime–(Y) and zircon crystals are presented. Although the luminescence was excited with an unpolarized electron beam there are significant effects of different analysing directions relative to the crystal. A potential semi-quantitative estimation of trace elements via cathodoluminescence intensity, as for instance applied to apatite, therefore needs a broad range of carefully calibrated conditions, e.g., standard material, system stability, system response (Cesbron et al. 1993; Barbarand and Pagel 2001). Moreover, other effects, e.g., concentration quenching, quenching/sensitizing by other impurities (Kempe and Götze 2002) and, in particular, the analysing direction relative to the crystal, have to be considered (cf. Barbarand and Pagel 2001).

Effects of the real structure on Nd³⁺ luminescence: the example of monazite–(Ce)

Real structure is defined as the entity of deviations from the ideal chemical composition and structure. A common feature
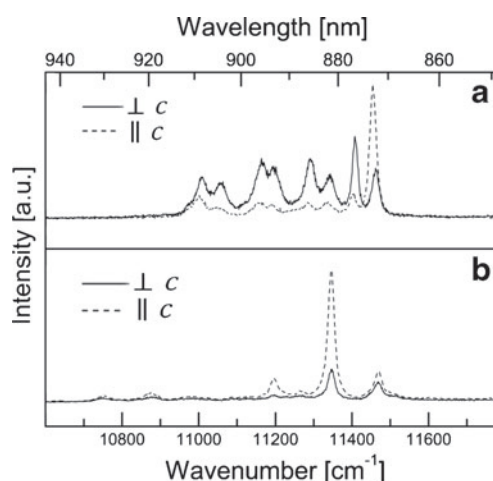
Fig. 5 Orientation dependence of the CL emission of Nd³⁺ ($^4F_{3/2} \rightarrow {}^4I_{9/2}$). **a** Synthetic Nd³⁺:YPO₄ (xenotime). **b** Synthetic Nd³⁺:ZrSiO₄ (zircon). Note that all spectra have the same vertical scaling, intensities are therefore directly comparable. The emitted CL light was obtained in directions perpendicular and parallel to the c-axis of the respective crystal. Note that intensity ratios among sublevel bands vary appreciably

is the presence of defects, including point (e.g., substitutions, vacancies, interstitials), line, or three-dimensional defects (e.g., holes, surface defects, grain boundaries). Typical effects on light-spectroscopic signals are band broadening and shifting. In optical spectroscopy this phenomenon is commonly termed *inhomogeneous broadening* (cf. Macfarlane 1990; cf. Skinner and Moerner 1996). The sharpness of optical transitions, observed either in absorption or emission processes, depends theoretically on the lifetime of the excited electronic state. This is due to the quantum-mechanical uncertainty and includes both radiative and non-radiative processes (Blasse and Grabmaier 1994). For excited states of the f^n configuration, radiative rates are typically in the millisecond and sub-millisecond time scale. This is because these transitions are parity-forbidden and often spin-forbidden as well (Blasse and Grabmaier 1994; Gaft et al. 2001; Liu and Jacquier 2005). At hypothetical ideal conditions, absorption and emission bands of REE have very narrow Lorentzian shapes. These conditions include: REE substituents of the same type with no cross-interaction, a perfect crystal without defects/strain, and without any lattice vibrations (phonons) achieved at very low temperature (ideally 0 K with hypothetically no vibronic coupling). The observed absorption/emission band is considered as superposition of all electronic transitions of a certain number of REE substituents in the area analysed (*homogeneous broadening*, Fig. 6a). However, effects of the real structure (Fig. 6b) perturb the local environment of the REE centre. As a consequence, the crystal field around the REE cations is randomly distorted to a certain amount and electronic transition energies shift slightly. The observed spectral profiles can then be considered as a broad envelope over much narrower homogeneous lines introducing a Gaussian character to the band shape (schematically illustrated in Fig. 6b).

To illustrate the effect of the real structure on REE luminescence, we use the example of chemically induced disorder in monazite–(Ce) for three reasons: First of all, almost all natural monazite-group minerals contain Nd^{3+} and show Nd-luminescence. Second of all, the monazite structure has an extremely broad range of chemical compositions, so that a variety of substitution mechanisms can be studied. Third, Ruschel et al. (2012) have recently studied the structural disorder of monazite–(Ce) using Raman spectroscopy (band broadening of the symmetric stretching vibration of PO_4 tetrahedrons; A_{1g} mode). This was done with the basic objective to investigate, and distinguish among, disturbing effects of the chemical composition and/or structural damage as caused by self-irradiation due to the incorporation of actinide elements. Panczer et al. (2012) showed that the incorporation of non-formula elements affects the sharp sublevel luminescence bands of Nd^{3+} as well. In the present paper we address the question whether Nd^{3+}-luminescence spectroscopy can be used for a quantitative estimation of the chemically induced structural disorder.
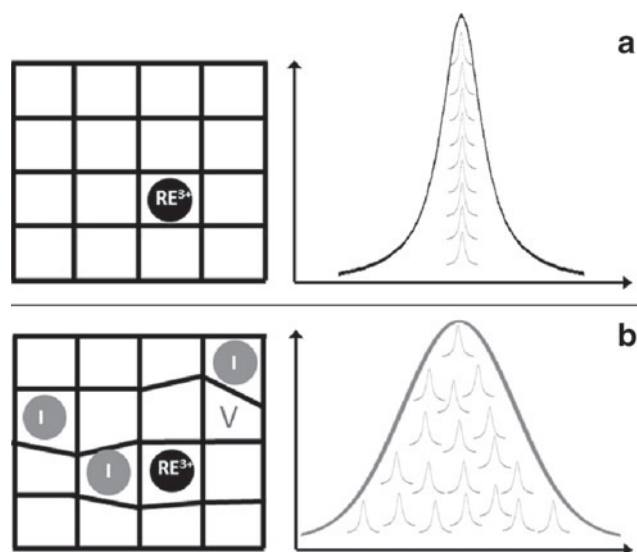
Fig. 6 Schematic illustration (simplified) of the band broadening related to optical transitions as affected by the sample's real structure (modified after Skinner and Moerner 1996). **a** Nearly "ideal" crystal (merely doped with low levels of an individual REE), assuming the absence of notable amounts of defects and strain. The observed absorption or emission band, respectively, is considered as superposition of all electronic transitions of a certain number of REE substituents in the area analysed (*homogenous broadening*). **b** "Real" crystal with notable amounts of defects such as impurities (I), vacancies (V), and non-formula constituents, resulting in notable lattice strain. Here, the crystal field around the REE site is perturbed randomly. The observed spectral profile is a broad envelope over much narrower homogenous lines (*inhomogeneous broadening*)

Monazites are monoclinic orthophosphates with the general formula $LREE[PO_4]$. These minerals have an extremely broad range of chemical compositions with Ce being the predominant cation in naturally occurring species. Solid solutions with other minerals of the monazite group allow extensive substitutions of Ce by other LREEs (especially La, Nd, Sm). In addition to the more limited incorporation of heavy REEs, significant amounts of the actinide elements Th and U, and to much lesser extent radiogenic Pb, may also be present (Williams et al. 2007). The incorporation of non-REE ions in the wt% range is commonly explained by the two coupled substitutions: (1) $2REE^{3+} \leftrightarrow Ca^{2+} + Th^{4+}$ (*cheralite substitution*) and (2) $P^{5+} + REE^{3+} \leftrightarrow Si^{4+} + Th^{4+}$ (*huttonite substitution*). The continuity in the monazite-huttonite series extends to a maximum of 30 at% huttonite in natural monazites (Della Ventura et al. 1996; Kucha 1980; Förster and Harlov 1999). The substitution mechanisms for Th^{4+} can be applied to U^{4+}, also. For details on the crystal chemistry of the monazite structure the reader is referred to reviews by Kolitsch and Holstam (2004) and Clavier et al. (2011).

Here we present Nd^{3+} luminescence data for three different sample sets reflecting different substitution mechanisms: (1) a series of homogeneous synthetic $Ce_{1-x}LREE_xPO_4$ crystals doped with large amounts of other REEs, forming

a solid solution with LREE = La, Nd, Gd (for detailed characterisation see Ruschel et al. 2012); (2) synthetic samples doped with Th^{4+} compensated with Ca^{2+} and/or Na$^+$ (see details in the sample description above); and (3) homogeneous natural monazite–(Ce) samples reflecting combined substitution mechanisms in nature including the huttonite substitution with charge compensation by Si^{4+} on anionsites (for detailed characterisation see Ruschel et al. 2012).

Figure 7 shows that the exclusive substitution of homovalent REE^{3+} for Ce^{3+} on the cation-site causes only minor band broadening. Monazites–(Ce) with heterovalent substitutions, such as Th^{4+}, Ca^{2+} on cation and Si^{4+} on the anion site, show stronger band broadening and shifting (Fig. 7). In this case, the FWHM (full width at half maximum) of the sublevel bands lowers the probability of a precise deconvolution/fitting due to an effective band overlap. Hence, the less affected out of the eight distinctive sublevel bands at ca. 11,030 abs. cm^{-1} is chosen for the interpretation of the FWHM hereafter.

To describe chemically induced disorder we introduce a *distortion parameter* (Δ) which reflects the distortional behaviour of every substituent on regular cation and anion sites. This is approximated with a summation of the weighted ionic radii difference between the predominant cation/anion (Ce/P in monazite–Ce) and each substituent:

$$\Delta = \sum_{cs} c_{cs} * |r_c - r_{cs}| + \sum_{as} c_{as} * |r_a - r_{as}| \qquad (1)$$

where c is the concentration of cation (c_{cs}) or anion substituents (c_{as}) in atomic percent per formula unit (apfu), and
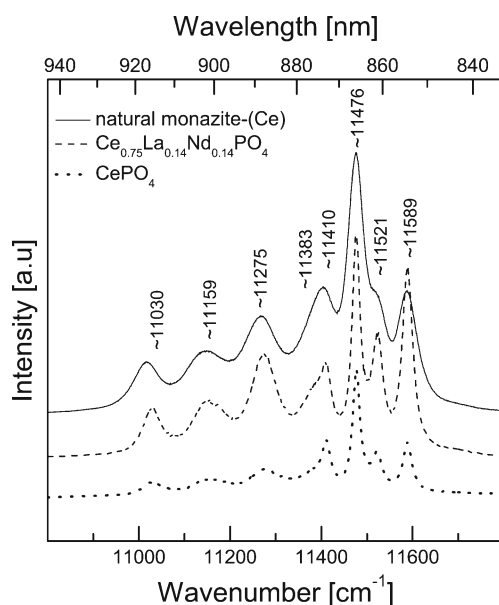

Fig. 7 Photoluminescence spectra (532 nm excitation) of Nd^{3+} ($^4F_{3/2} \rightarrow$ $^4I_{9/2}$) of annealed, Th-rich natural monazite-(Ce) from Central Australia (sample ECA6 of Ruschel et al. 2012) in comparison with La,Nd-doped and un-doped CePO$_4$. Band positions are quoted for un-doped CePO$_4$

r the ionic radius of the predominant cation (r_c) or anion (r_a), and of the cation (r_{cs}) or anion substituent (r_{as}), respectively. For monazite–(Ce), the cationic radii in 9-fold and anionic radii of P and Si in 4-fold coordination after Shannon (1976) are used. This formalism takes into account that large ionic radii differences between predominant and substitutional ions should have much more distortional impact than smaller. Additionally, this impact is weighted with the concentration of each ion providing an effective distortional impact which is summed over all substitutional ions present.

Figure 8 shows the effects of chemical substitution on spectral parameters of the Nd^{3+} ($^4F_{3/2} \rightarrow$ $^4I_{9/2}$) luminescence emission. An increase of the distortion parameter (Δ), calculated from chemical data of all investigated monazite–(Ce) samples (i.e., Table 2), causes a band shift to lower wavenumbers. In this case, the band shift is linear to the total sum of weighted radii differences of all substituents (Δ). This indicates that the substitution of smaller ions than Ce causes a reduced cell volume. Clavier et al. (2011) summarized data suggesting a complete solid solution in the synthetic system LaPO$_4$–ThSiO$_4$ with linearly decreasing cell parameters with increasing Th content. Alike, unit cell parameters decrease linearly with the substitution ratio in the La$_x$Gd$_{1-x}$PO$_4$ monazite solid solution (Clavier et al. 2011).

Interestingly, the FWHM of the Nd^{3+}-luminescence bands is mainly controlled by heterovalent substituents (Figs. 7 and 8b). The Δ_{hetero} parameter in Fig. 8b was calculated applying Eq. 1 only to heterovalent substituents present in the samples analysed. The comparison of spectral parameters of the Ce$_{1-x}$ REE$_x$[PO$_4$] solid solution (filled triangle, Fig. 8) gives an illustrative example: The extensive substitution of homovalent REE^{3+} causes large band shifts (Fig. 8a), but have no effect on the FWHM (Fig. 8b). Heterovalent substitutions appear to have a much higher impact on the electronic structure and therefore on the perturbation of electronic states than homovalent ones (see the discussion on the crystal field above). Hence, the FWHM of luminescence bands is rather a measure of the perturbed electronic structure which is in this case connected to chemically induced disorder via substitution of heterovalent ions.

The estimation of structural disorder by radii differences applied above is based upon a rigid hard-sphere model of ions and cannot take into account lattice distortion by other real-structure defects, e.g., vacancies. Nevertheless, the good fit to a linear trend suggests that the inferred disorder is mainly controlled by the different chemical substitution mechanisms in the synthetic and natural monazites analysed in this study. Panczer et al. (2012) correlate the FWHM of Nd-luminescence bands of natural monazites with the thorium content (wt%) without regarding other heterovalent substitutions. For comparison, we show a similar correlation of our samples in Fig. 8c. The variance of FWHM among the natural
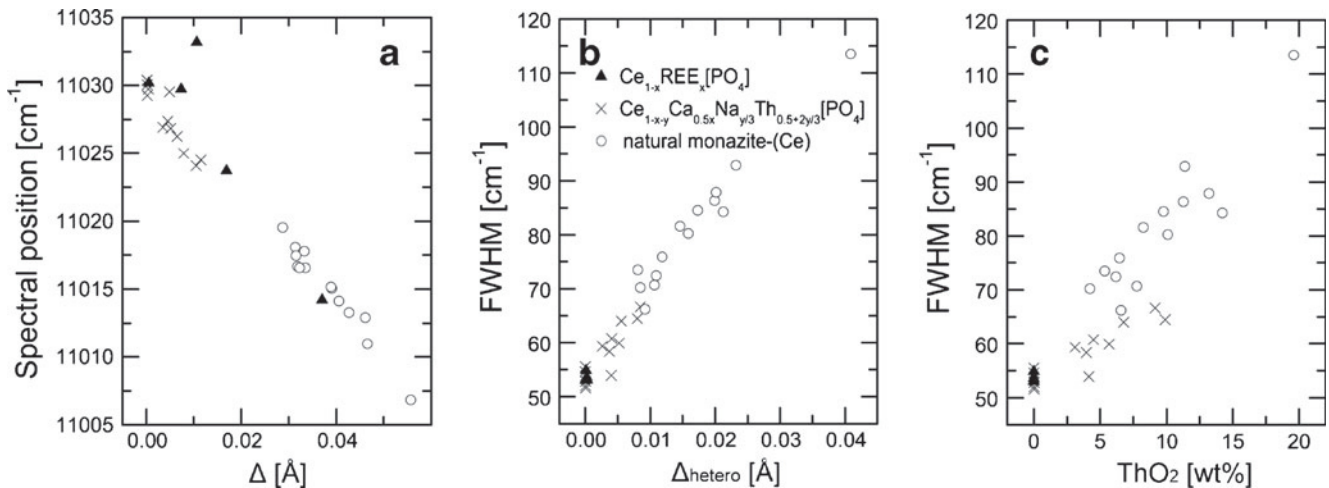
Fig. 8 Effects of chemical substitutions in various natural and synthetic monazite samples on spectral parameters of the Nd^{3+} ($^4F_{3/2} \rightarrow$ $^4I_{9/2}$) luminescence emission, shown for the ~11,030 cm^{-1} sublevel band (see Fig. 7). **a** The increase of the distortion parameter Δ (see text and Eq. 1) causes a band shift to lower wavenumbers. **b** The increase of the heterovalent distortion parameter Δ_{hetero} (see text) causes a linear increase of the band FWHM. **c** Band FWHM and ThO_2 content show a less pronounced correlation, making potential estimates of the chemically induced structural disorder from the ThO_2 content alone rather imprecise

samples (open dots) is greater than for the correlation in Fig. 8b. The FWHMs of synthetic multi-doped monazite samples (cross, Fig 8) show an individual correlation with the ThO_2 content. Therefore, the correlation of the FWHM – as potential estimation of structural disorder – with the ThO_2 content alone is imprecise if variable substitution mechanisms determine the chemical composition.

In this study, potential effects of corpuscular self-irradiation on the structural disorder are excluded by using synthetic or annealed samples. The estimation of the chemical impact on the REE-luminescence band widths is of major importance for the discrimination and quantification of irradiation-induced disorder by REE-luminescence spectroscopy (see the review chapter of Nasdala et al. in this special issue). The irradiation-induced disorder accumulated in geologic timescales can be quantified if the chemical-dependent contribution is known. Hence, REE-luminescence spectroscopy may be a complementary technique to Raman spectroscopy, especially for minerals where distinctive Raman bands are absent (e.g., titanite or pyrochlore).

Furthermore, information on the chemically induced structural disorder derived from REE-luminescence data may help to study the dynamics in solid solutions and the interpretation of zoning patterns. This is illustrated in Fig. 9, which presents
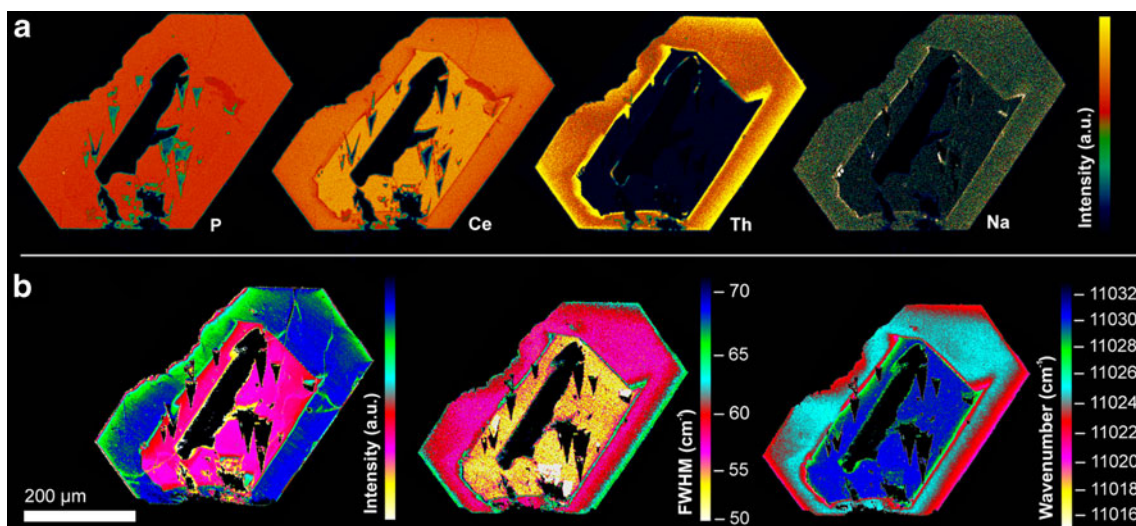
Fig. 9 Element distribution maps (**a**) and hyperspectral Nd^{3+} maps (**b**) of a synthetic Th-doped monazite single crystal. The latter shows distributions of spectral parameters of the ~11,030 cm^{-1} sub-band of the $^4F_{3/2} \rightarrow {}^4I_{9/2}$ electronic transition of Nd^{3+}. Irregularities in the inner zone (i.e. black triangular areas) are flux inclusions and outbreaks from polishing. Note that changes in Nd-luminescence parameters (especially the FWHM) correlate closely with changes in the incorporation of non-formula elements

element distribution (Fig. 9a) and hyperspectral Nd-luminescence maps (Fig. 9b) of a synthetic Th-doped monazite–(Ce). The single crystal shown is characterised by two major zones of significantly different chemical composition. The inner area consists of $CePO_4$ with extremely low amounts of trace elements below the EPMA detection limits, and represents an early stage of crystal growth in the flux. The outer zone (ca. 30–70 μm in width) contains elevated amounts of Th, Ca, and Na and is hence depleted in Ce (average chemical formula $Ce_{0.854}Th_{0.084}Ca_{0.039}Na_{0.023}PO_4$). The rim of the crystal (i.e. the outermost ca. 5–10 μm of the outer zone) is strongly enriched in Th. Note that the Th-doped synthetic samples contain well-detectable amounts of Na (Table 2), which we assign to their growth in a sodium-polyphosphate flux (cf. description of synthesis details above). Table 2 presents element quantities (quoted in apfu) of several measurement points on the synthetic Th-doped monazite–(Ce) samples. It was observed for all individual analyses that after subtraction of the respective Th amount related to the cheralite component ($2REE^{3+} \leftrightarrow Ca^{2+} + Th^{4+}$; Ca:Th = 1:1), the ratio of the remaining Na–to–Th is close to 1:2. This suggests a substitution mechanism according to

$$Na^+ + 2Th^{4+} \leftrightarrow 3Ce^{3+} \qquad (2)$$

To the best of our knowledge, this Na–Th substitution has not been described for natural monazite–(Ce) thus far.

The Nd-luminescence parameters are very sensitive to the structural disorder as introduced by the presence of non-formula elements (cf. again Fig. 9b). The FWHM of the ~11,030 cm^{-1} sublevel band broadens from 53 cm^{-1} in the case of nearly pure $CePO_4$ (inner area) up to 65 cm^{-1} near the Th-rich rim of the crystal, accompanied by a shift of the band position from 11,031 cm^{-1} to 11,022 cm^{-1}. In all interior regions and zones, the concentration of Nd was below the EPMA detection sensitivity. We speculate that Nd may be slightly enriched in the outer zone, coupled to the other substituents; this is concluded from the generally higher Nd-luminescence intensity in this area. Other potential causes of lateral differences in the Nd-emission intensity – such as quenching and/or sensitizing (e.g., Marfunin 1979) or effects of structural disorder (e.g., Nasdala et al. 2006) – can be excluded in our case of synthetic, mildly Nd-contaminated specimens.

Temperature dependence

An additional important factor affecting the REE-luminescence band width (and marginally the band position) is temperature. Increasing temperature enhances the extent of lattice vibrations (phonons). Lattice vibrations induce an oscillation of interatomic distances at the luminescence

centre within the crystal structure. In consequence, the potential energy of electronic states and thus the transition energy of corresponding optical phenomena are distributed around an equilibrium value. The observed band shape is again a sum of all constituent transitions over a specific time interval in the analysed area. Luminescence measurements are commonly done at very low temperatures to avoid this additional perturbation (vibronic coupling). In general, lowering the temperature allows an improved separation of the obtained luminescence features, but also enables transitions from excited levels, which have previously been depopulated via phonons (non-radiative transitions). The temperature effect on REE band widths is comparatively small compared with d-d or d-f transitions, where absorption and luminescence band widths are much larger. This is because f-electrons and their inter-transitions are well shielded by the outermost filled $5s^2 5p^6$ orbitals, so that the interaction with the ligands is small.

Figure 10 illustrates the effect of temperature on the Nd^{3+} luminescence with the monazite–(Ce) example discussed above: The FWHMs of all the eight observed sublevel bands of the Nd^{3+} ($^4F_{3/2} \rightarrow {}^4I_{9/2}$) emission increase with increasing temperature. The FWHM of broad sublevel bands increases much more than those of the thinner ones (Fig. 10). Similarly, broad bands show the strongest positional shift. However, the shift of the broadest band at 11,159 cm^{-1} does not exceed 9 cm^{-1} (0.7 nm) from 80 K to 300 K. The low sensitivity of the band position to higher temperature is a useful feature for high temperature experiments with diamond anvil cells (DAC), where optical-luminescence pressure-gauges are used successfully. Datchi et al. (1997; 2007) promote the distinct luminescence emission of Sm^{2+} (intra $4f^{-6}$; $^5D_0 \rightarrow {}^7F_0$) doped SrB_4O_7 as viable temperature-
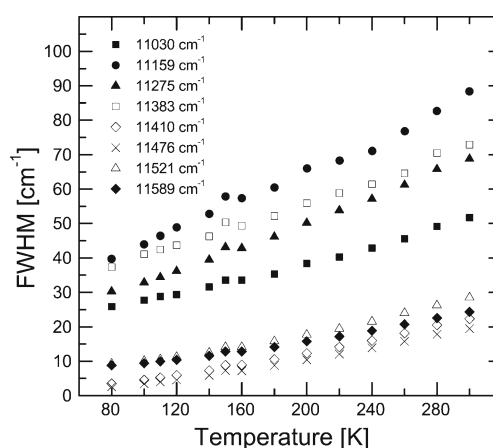
Fig. 10 Effect of temperature on the FWHM of eight distinctive luminescence sublevel bands (Nd^{3+}, $^4F_{3/2} \rightarrow {}^4I_{9/2}$) of synthetic $CePO_4$. Temperature increase causes general broadening of sublevel bands, with broader bands showing stronger absolute increase of their FWHM, compared to narrower bands

insensitive alternative to the Cr^{3+} (R-lines) luminescence of ruby (Cr^{3+}:Al_2O_3).

The prediction of FWHMs and shifts of REE bands cannot be deduced from first principles. The temperature not only affects the electronic interaction within the luminescent REE^{3+} ion, but also the surrounding ligands of the crystal field. An anisotropic thermal expansion of the crystal structure stresses the cation site (Mogilevsky et al. 2007; Jardin et al. 2008; Li et al. 2009) and results in a anisotropic crystal field splitting, which is further influenced by local defects. This consideration is of crucial importance for the evaluation of band widths for the quantification of chemically induced (see above) or radiation-induced disorder (see the review chapter of Nasdala et al. in this special issue). Figure 11 shows the FWHM of the 11,030 cm^{-1} Nd-sublevel band of different monazite–(Ce) samples with various chemical compositions. Chemically induced disorder not only causes higher FWHMs but also influences the impact of the temperature effect. High chemical disorder inhibits the effect of temperature broadening, possibly due to structural relaxation induced by the presence of non-formula elements. Measuring the FWHMs for the quantification of e.g., chemically induced disorder gives different absolute values at different temperatures, whereby the relative significance is not changed drastically. Hence, an absolute FWHM correlation with effects connected to structural disorder should be done at constant temperature, which is done throughout this study. All luminescence spectra presented in the sections above are recorded at room temperature (298 K), because low temperature measurements using cooling stages or other liquid-nitrogen set-ups entail considerable effort; especially for measurements with high lateral resolution for hyperspectral luminescence maps (cf. Fig. 9).
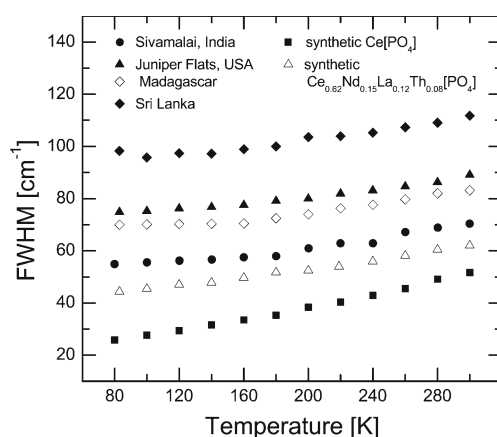

Fig. 11 Influence of the chemical composition on the FWHM-temperature dependence, for the example of the ~11,030 cm^{-1} Nd^{3+} sublevel. Chemically induced disorder not only causes FWHM increases (cf. Fig. 8a) but also decreases the effect of temperature on the band broadening, possibly due to structural relaxation by the substituents

Concluding remarks

First of all, the luminescence emission of REE^{3+} in minerals depends on the type of incorporated REEs. The energetic positions of their spectroscopic levels determine the luminescence emission pattern (a chart of spectroscopic levels of all REE^{3+} was given by Carnall et al. 1989). Commonly, natural samples contain more than one type of REE^{3+}, often resulting in extensively overlapping luminescence patterns. Due to electronic shielding of the outermost $5s^2$ and $5p^6$ orbitals, the influence on the $4f$ transitions of the crystal field is weak and a specific optical transition of a REE^{3+} appears with comparable spectral energies in very different mineral hosts (Fig. 2). Nevertheless, the crystal field splits spectroscopic levels into sublevels depending on the distribution of the electron density at the substituted lattice site (Fig. 2). Luminescence investigations of REE^{3+} in minerals hence provide first the opportunity to identify REEs in a specific host mineral. Second, they enable fast mineral identification, provided the individual sublevel splitting of a specific REE^{3+} in the mineral under investigation is known. With respect to the latter, the luminescence emission of Nd^{3+} was found to be a promising candidate because (1) the luminescence signal can be traced with standard Si-based detectors, (2) it is effectively excited by standard lasers as well as via cathodoluminescence, (3) other luminescence emissions in the respective spectral energy range are rare, and (4) a low number of sublevels simplifies the data reduction (i.e., fitting/deconvolution).

Even minute amounts of REE^{3+} cause detectable luminescence signals and can potentially be used for the qualitative identification of trace REEs. In contrast to optical absorption spectroscopy, the quantitative estimation of REEs concentrations via luminescence intensity is difficult for several reasons (see detailed discussions above). In particular, this study shows once more that the relative luminescence intensity of certain sublevels may depend strongly on the crystal orientation (Fig. 4). Furthermore, both the polarisation of the incident laser (in the case of laser-induced photoluminescence) and the polarisation of the luminescence signal are of importance when comparing relative luminescence intensities.

The FWHM of REE^{3+} luminescence sublevel bands contains information on the crystal-structural state and provides great opportunities to study different types of structural disorder with luminescence techniques (Fig. 9). In this study, the effect of chemically induced disorder on the luminescence signal of monazite–(Ce) has been described with a simple model based on ionic radii. The discrimination between chemically induced (Fig. 8) and irradiation-induced structural disorder is possible, however, when the influence of measurement temperature (Fig. 10 and 11) is considered.

References

Barbarand J, Pagel M (2001) Cathodoluminescence study of apatite crystals. Am Mineral 86:473–484

Belsky A, Krupa J (1999) Luminescence excitation mechanisms of rare earth doped phosphors in the VUV range. Displays 19:185–196

Blanc P, Baumer A, Cesbron F, Ohnenstetter D, Panczer G, Rémond G (2000) Systematic cathodoluminescence spectral analysis of synthetic doped minerals: anhydrite, apatite, calcite, fluorite, scheelite and zircon. In: Pagel M, Barbin V, Blanc P, Ohnstetter D (eds) Cathodoluminescence in geosciences. Springer, Berlin, pp 127–160

Blasse G, Grabmaier B (1994) Luminescence materials. Springer, Berlin, 248 p

Boatner LA (2002) Synthesis, structure, and properties of monazite, pretulite, and xenotime. Rev Mineral Geochem 48:87–121

Bünzli JCG, Piguet C (2005) Taking advantage of luminescent lanthanide ions. Chem Soc Rev 34:1048–1077

Burns RG (1993) Mineralogical applications of crystal field theory, Cambridge University Press

Carnall W, Goodman G, Rajnak K, Rana R (1989) A systematic analysis of the spectra of the lanthanides doped into single crystal LaF. J Chem Phys 90:3443–3457

Cesbron F, Ohnenstetter D, Blanc P, Rouer O, Sichere MC (1993) In corporation des terres rares dans des zircons de synthèse: étude par cathodoluminescence. C R Acad Sci II 316:1231–1238

Cesbron F, Blanc P, Ohnenstetter D, Rémond G (1995) Cathodoluminescence of rare earth doped zircons. I. Their possible use as reference materials. Scanning Microscopy Suppl 9:35–56

Clavier N, Podor R, Dacheux N (2011) Crystal chemistry of the monazite structure. J Eur Ceram Soc 31:941–976

Czaja M, Bodył S, Głuchowski P, Mazurak Z, Strek W (2008) Luminescence properties of rare earth ions in fluorite, apatite and scheelite minerals. J Alloy Compd 451:290–292

Czaja M, Bodył S, Lisiecki R, Mazurak Z (2009) Luminescence properties of Pr^{3+} and Sm^{3+} ions in natural apatites. Phys Chem Miner 37:425–433

Datchi F, LeToullec R, Loubeyre P (1997) Improved calibration of the SrB4O7:Sm2+ optical pressure gauge: advantages at very high pressures and high temperatures. J Appl Phys 81:3333–3339

Datchi F, Dewaele A, Loubeyre P, Letoullec R, Le Godec Y, Canny B (2007) Optical pressure sensors for high-pressure–high-temperature studies in a diamond anvil cell. High Press Res 27:447–463

Della Ventura G, Mottana A, Parodi GC, Raudsepp M, Bellatreccia F, Caprilli E, Rossi P, Fiori S (1996) Monazite-huttonite solid-solutions from the vico volcanic complex, Latium, Italy. Mineral Mag 60:751–758

Dexpert-Ghys J, Faucher M, Caro P (1984) Site selective spectroscopy and structural analysis of yttria-doped zirconias. J Solid State Chem 54:179–192

Dexpert-Ghys J, Mauricot R, Faucher M (1996) Spectroscopy of Eu^{3+} ions in monazite type lanthanide orthophosphates LnPO$_4$, Ln= La or Eu. J Lumin 69:203–215

Finch A, Hole D, Townsend P (2003) Orientation dependence of luminescence in plagioclase. Phys Chem Miner 30:373–381

Förster H, Harlov D (1999) Monazite–(Ce)-huttonite solid solutions in granulite-facies Metabasites from the Ivrea-Verbano Zone, Italy. Mineral Mag 63:587–594

Friis H, Finch AA, Williams CT, Hanchar JM (2009) Photoluminescence of zircon (ZrSiO4) doped with REE^{3+} (REE = Pr, Sm, Eu, Gd, Dy, Ho, Er). Phys Chem Miner 37:333–342

Gaft M, Reisfeld R, Panczer G, Shoval S, Champagnon B, Boulon G (1997) Eu^{3+} Luminescence in high-symmetry sites of natural apatite. J Lumin 72:572–574

Gaft M, Reisfeld R, Panczer G, Uspensky E, Varrel B, Boulon G (1999) Luminescence of Pr^{3+} in minerals. Opt Mater 13:71–79

Gaft M, Panczer G, Reisfeld R, Uspensky E (2001) Laser-induced time-resolved luminescence as a tool for rare-earth element identification in minerals. Phys Chem Miner 28:347–363

Gaft M, Reisfeld R, Panczer G (2005) Luminescence spectroscopy of minerals and materials. Springer, Berlin, 372 p

Götze J (2000) Cathodoluminescence microscopy and spectroscopy in applied mineralogy. Freiberger Forschungsheft C 485, TU Bergakademie Freiberg, 128 p

Götze J (2002) Potential of cathodoluminescence (CL) microscopy and spectroscopy for the analysis of minerals and materials. Anal Bioanal Chem 374:703–708

Götze J, Habermann D, Neuser RD, Richter DK (1999) High-resolution spectrometric analysis of rare earth elements-activated cathodoluminescence in feldspar minerals. Chem Geol 153:81–91

Habermann D (2002) Quantitative cathodoluminescence (CL) spectroscopy of minerals: possibilities and limitations. Miner Petrol 76:247–259

Habermann D, Neuser RD, Richter DK (1996) REE-activated cathodoluminescence of calcite and dolomite: high-resolution spectrometric analysis of CL emission (HRS-CL). Sediment Geol 101:1–7

Hanchar J, Miller C (1993) Zircon zonation patterns as revealed by cathodoluminescence and backscattered electron images: implications for interpretation of complex crustal histories. Chem Geol 110:1–13

Hanchar J, Rudnick R (1995) Revealing hidden structures: the application of cathodoluminescence and back-scattered electron imaging to dating zircons from lower crustal xenoliths. Lithos 36:289–303

Hanchar JM, Finch RJ, Hoskin PWO, Watson EB, Cherniak DJ, Mariano AN (2001) Rare earth elements in synthetic zircon: part 1. Synthesis, and rare earth element and phosphorus doping. Am Mineral 86:667–680

Jardin R, Pavel CC, Raison PE, Bouëxière D, Santa-Cruz H, Konings RJM, Popa K (2008) The high-temperature behaviour of PuPO4 monazite and some other related compounds. J Nucl Mater 378:167–171

Kempe U, Götze J (2002) Cathodoluminescence (CL) behaviour and crystal chemistry of apatite from rare-metal deposits. Mineral Mag 66:151–172

Kenyon A (2002) Recent developments in rare-earth doped materials for optoelectronics. Prog Quant Electron 26:225–284

Kolitsch U, Holtstam D (2004) Crystal chemistry of REEXO4 compounds (X= P, as, V). II. Review of REEXO4 compounds and their stability fields. Eur J Mineral 16:117–126

Kucha H (1980) Continuity in the monazite-huttonite series. Mineral Mag 43:1031–1034

Li H, Zhang S, Zhou S, Cao X (2009) Bonding characteristics, thermal expansibility, and compressibility of RXO4 (R = rare earths, X = P, as) within monazite and zircon structures. Inorg Chem 48:4542–4548

Liu G, Jacquier B (2005) Spectroscopic properties of rare earths in optical materials. Springer, Berlin, 550 p

🦋 Springer

Macfarlane R (1990) Inhomogeneous broadening of spectral lines in doped insulators. J Lumin 45:1–5

MacRae CM, Wilson NC, Johnson SA, Phillips PL, Otsuki M (2005) Hyperspectral mapping –combining cathodoluminescence and X-ray collection in an electron microprobe. Microsc Res Techniq 67:271–277

MacRea CM, Wilson NC, Torpy A, Davidson CJ (2012) Hyperspectral cathodoluminescence imaging and analysis extending from ultra-violet to near infrared. Microsc Microanal 18:1239–1245

Marfunin AS (1979) Spectroscopy, Luminescence, and Radiation Centers in Minerals. Springer, Berlin Heidelberg, New York, p 352

Mogilevsky P, Boakye E, Hay R (2007) Solid solubility and thermal expansion in a $LaPO_4$-YPO_4 system. J Am Ceram Soc 90:1899–1907

Nasdala L, Götze J, Hanchar J, Gaft M, Krbetschek M (2004) Luminescence techniques in earth sciences. In: Beran A, Libowitzky E (eds) Spectroscopic methods in mineralogy, vol 6, Eur mineral union notes in mineralogy. Eötvös Univ Press, Budapest, pp 43–91

Nasdala L, Kronz A, Hanchar JM, Tichomirova M, Davis DW, Hofmeister W (2006) Effects of natural radiation damage on back-scattered electron images of single crystals of minerals. Am Mineral 91:1739–1746

Neuser R, Bruhn F, Götze J, Habermann D, Richter D (1995) Kathodolumineszenz: methodik und anwendung. Zbl Geo Pal I 1995(1/2):287–306

Ohnenstetter D, Cesbron F, Rémond G, Caruba R, Claude JM (1991) Emission de cathodoluminescence de deux populations de zircons naturels: tentative d'interprétation. C R Acad Sci II 313:641–647

Ollier N, Concas G, Panczer G, Champagnon B, Charpentier T (2003) Structural features of a Eu^{3+} doped nuclear glass and gels obtained from glass leaching. J Non-Cryst Solids 328:207–214

Owen JJ, Cheetham AK, McFarlane RA (1998) Orientation-dependent fluorescence studies and spectroscopic analysis of doped barium yttrium fluoride upconversion laser crystals ($BaY_{2-x-y}Yb_xTm_yF_8$). J Opt Soc Am B 15:684–693

Panczer G, De Ligny D, Mendoza C, Gaft M, Sexdoux-Guillaume A, Wang X (2012) Raman and fluorescence. In: Dubessy J, Caumon M-C, Rull F (eds) Applications of Raman spectroscopy to Earth sciences and cultural heritage. Eur Mineral Union Notes in Mineralogy, vol 12. Eur Mineral Union and Mineral Soc of Great Britain and Ireland, pp 61–82

Piriou B, Elfakir A, Quarton M (2001) Site-selective spectroscopy of Eu^{3+}-doped sodium lead phosphate apatite. J Lumin 93:17–26

Porto S, Krishnan R (1967) Raman effect of corundum. J Chem Phys 47:1009–1013

Pouchou J-L, Pichoir F (1991) Quantitative analysis of homogeneous or stratified microvolumes applying the method "PAP". In: Heinrich KFJ, Newbury DE (eds) Electron probe quantitation. Plenum Press, New York, pp 31–75

Rakovan J, Reeder RJ (1996) Intracrystalline rare earth element distri-butions in apatite: surface structural influences on incorporation during growth. Geochim Cosmochim Ac 60:4435–4445

Reisfeld R (2005) Spectroscopy of rare earth ions. In: Vaseashta A, Dimova-Malinovska D, Marshall JM (eds) Nanostructured and advanced materials for applications in sensor, optoelectronic and photovoltaic technology, Nato Sci Ser II math, vol 204. Springer, Berlin, pp 77–100

Reisfeld R, Gaft M, Boulon G, Panczer C, Jørgensen C (1996) Laser-induced luminescence of rare-earth elements in natural fluor-apatites. J Lumin 69:343–353

Reisfeld R, Zigansky E, Gaft M (2004) Europium probe for estimation of site symmetry in glass films, glasses and crystals. Mol Phys 102:1319–1330

Richter D, Götte T, Götze J, Neuser R (2003) Progress in application of cathodoluminescence (CL) in sedimentary petrology. Miner Petrol 79:127–166

Richter D, Gorgen P, Götte T (2008) Monazite cathodoluminescence – a new tool for heavy mineral analysis of siliciclastic sedimentary rocks. Sediment Geol 209:36–41

Ruschel K, Nasdala L, Kronz A, Hanchar JM, Többens DM, Škoda R, Finger F, Möller A (2012) A Raman spectroscopic study on the structural disorder of monazite–(Ce). Miner Petrol 105:41–55

Seydoux-Guillaume AM, Wirth R, Nasdala L, Gottschalk M, Montel JM, Heinrich W (2002) An XRD, TEM and Raman study of experimentally annealed natural monazite. Phys Chem Miner 29:240–253

Shannon R (1976) Revised effective ionic radii and systematic studies of interatomic distances in halides and chalcogenides. Acta Crystallogr A 32:751–767

Skinner J, Moerner W (1996) Structure and dynamics in solids as probed by optical spectroscopy. J Phys Chem 100:13251–13262

Talla D, Beran A, Škoda R, Losos Z (2011) On the presence of OH defects in the zircon-type phosphate mineral xenotime, (Y, REE)PO_4. Am Mineral 96:1799–1808

Tarashchan AN (1978) Luminescence of minerals. Naukova Dumka, Kiev, 296 p (in Russian)

Ternane R, Ferid M, Panczer G, Trabelsi-Ayadi M, Boulon G (2005) Site-selective spectroscopy of Eu^{3+}-doped orthorhombic lantha-num and monoclinic yttrium polyphosphates. Opt Mater 27:1832–1838

Waychunas GA (2002) Apatite luminescence. In: Kohn ML, Rakovan J and Hughes JM (eds) Rev Mineral Geochem, vol 48. Mineral Soc Am, Washington DC, 701–742

Williams ML, Jercinovic MJ, Hetherington CJ (2007) Microprobe monazite geochronology: understanding geologic processes by integrating composition and chronology. Annu Rev Earth Planet Sci 35:137–175

Appendix A.2

Photoluminescence of synthetic titanite-group pigments: A rare quenching effect

Nasdala, L., Lyubenova, T.S., Gaft, M., Wildner, W., Diegor, W., Petautschnig, C., Talla, D., Lenz, C. (2014).

Chemie der Erde – Geochemistry, 74, 419–424. (published)
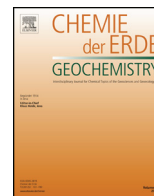
Photoluminescence of synthetic titanite-group pigments: A rare quenching effect

Lutz Nasdala [a,*], Teodora Stoyanova Lyubenova [b], Michael Gaft [c], Manfred Wildner [a], Wilfredo Diegor [d], Christian Petautschnig [a], Dominik Talla [e], Christoph Lenz [a]

[a] Institut für Mineralogie und Kristallographie, Universität Wien, Althanstr. 14, A-1090 Wien, Austria
[b] Departament de Química Inorgànica i Orgànica, University Jaume I, 12071 Castellón de la Plana, Spain
[c] OLDS Laser Distance Spectrometry Ltd., Petah-Tikva 49528, Israel
[d] Department of Earth Sciences, Memorial University of Newfoundland, St. John's, NL A1B 3X5, Canada
[e] Institute of Geological Sciences, Masaryk University, 61137 Brno, Czech Republic

ARTICLE INFO

ABSTRACT

Chromium-doped titanite and malayaite samples, which were synthesised to evaluate their performance as ceramic pigments, show remarkable photoluminescence behaviour. Emissions of centres related to traces of trivalent rare-earth elements (REE) are observed exclusively from chromium-free samples. Their Cr-doped analogues (containing the same REEs on the same concentration levels), in contrast, only show broad-band Cr^{3+} emission whereas all REE emissions are suppressed. This behaviour is assigned to quenching of REE emissions by chromium centres (i.e., $REE^{3+} \rightarrow Cr^{3+}$ energy transfer).

© 2014 Elsevier GmbH. All rights reserved.

1. Introduction

Minerals of the titanite group (general formula $CaX[O/SiO_4]$, with X = Ti, Sn, V; space group $C2/c$) have been studied extensively. Whilst titanite ($CaTi[O/SiO_4]$; Speer and Gibbs, 1976) is an ubiquitous accessory component in many igneous and metamorphic rocks, the tin silicate malayaite ($CaSn[O/SiO_4]$; Alexander and Flinter, 1965) occurs less commonly, typically in skarns (Higgins and Ribbe, 1977). The third group-member known to date is the rare mineral vanadomalayaite (Basso et al., 1994). Takenouchi (1971) has shown that at high temperatures there exists a complete solid solution between titanite and malayaite. Both of the two minerals are characterised by an excellent thermal stability and chemical resistance. For these reasons, and stimulated by their ability to incorporate a wide range of non-formula elements in their crystal lattices, synthetic analogues of titanite-group minerals have been proposed as potential host materials for the immobilisation of radioactive waste from nuclear power stations (Lutze and Ewing, 1988).

Both titanite and malayaite are colourless if chemically pure, however they become coloured when being doped with transition metal ions, which then act as chromophores. Especially Cr-doped malayaite, due to its intense colouration, is used commonly as a pink ceramic pigment. Correspondingly, there are many papers addressing in detail the absorption of chromium and other chromophores in titanite-group minerals, and the use of these phases as thermally stable pigments (e.g., Stefani et al., 1997; Bartis et al., 2007; Hajjaji et al., 2010; Borcanescu et al., 2013). The luminescence of titanite-group minerals, in contrast, has been investigated in very few studies only, even though "titanite may be a very interesting luminescent material" (Gaft et al., 2005). Undoped titanite shows weak green luminescence (broad band with maximum at 520 nm wavelength) under ultraviolet (UV) excitation, which is assigned to the "intrinsic" emission of TiO_6 polyhedrons (Blasse et al., 1988). A similar, Ti^{4+}-related broad-band emission was observed from synthetic, Ti-activated malayaite ($CaSn_{0.97}Ti_{0.03}SiO_5$; Abe et al., 2010). The emission of natural titanite, in contrast, may in some cases be most complex, comprising numerous narrow and broad bands assigned to rare-earth elements (REE, including Sm^{3+}, Eu^{3+}, Pr^{3+}, Nd^{3+}, Tm^{3+}, Er^{3+}) and transition metals (especially Cr^{3+}; Gaft et al., 2003; Kennedy et al., 2010).

During a recent research project addressing oxidation states and lattice sites of chromophore ions in such titanite-group pigments, which was conducted at University Jaume I, Castellón de la Plana, Spain, several suites of titanite and malayaite samples with different levels of Cr-doping were produced and characterised

in detail (see Stoyanova Lyubenova et al., 2008, 2009a,b; Cruciani et al., 2009). In the course of a systematic spectroscopy study of these pigments that involved optical absorption, vibrational, and emission spectroscopy, we made the puzzling observation that only Cr-free samples always show emissions of minute levels of pollutant REEs. In Cr-doped samples, by contrast, REE emissions are virtually absent. In the present study we have studied the apparently unusual behaviour for REE centres in titanite-group minerals.

2. Samples and experimental

2.1. Synthesis and preparation of samples

The Cr-doped titanite and malayaite pigments and their undoped analogues were prepared by traditional ceramic method (i.e., solid-state reaction of oxide precursors). The raw materials were mixed and homogenised with water by stirring. The powders were then dried ($100 \pm 5\,°C$) and further calcined at 1200, 1300 and 1400 °C (heating rate of 3°/min, and 4 h soaking time) in mullite crucibles. More details are described elsewhere (Stoyanova Lyubenova et al., 2009a,b); for generalities of the ceramics-type synthesis technique see Cordoncillo et al. (1998).

To eliminate the hypothetical possibility that the observed emission behaviour of trace REEs is an artefact caused by peculiarities of the ceramic-type pigment-synthesis process, additional flux syntheses of titanite samples (doped with Nd, and with and without Cr) were done. These samples were grown in a sodium-tetraborate flux (duration 10 days, peak temperature 1130 °C). The experiments corresponded mainly to the procedure described by Mazdab (2009); however we used a starting material with 1:1 molar ratio of CaO and TiO_2 (with excess of SiO_2). To extract titanite from the crucible, remnants of the flux were dissolved using HNO_3 (30 wt%).

For X-ray fluorescence (XRF) analysis, pigment samples were ground in a tungsten carbide mill for $2\times$ 30 s, to produce fine powders. The sample material was mixed with wax as a binder (1:10) and then pressed (with 150 kN for 10 s) in an aluminium cup on a layer of boric acid as stabilising substrate. For laser ablation inductively coupled plasma mass spectrometry (LA–ICP–MS) analysis, pigment samples were finely powered and homogenised with a pestle in a mortar under ethanol. After drying, the samples were mixed up with "White neutral pH adhesive" (Lineco, University Products, Inc.). After mixing, the samples were dried in air for several hours, cut into squares (ca. 5 mm × 5 mm) and then mounted on double-sided tape. The adhesive used is extremely pure and introduces essentially no chemical impurities to the LA–ICP–MS measurements. The only impurity elements that were detected in concentrations greater than 1 μg/g were Si (10 μg/g), P (2 μg/g), and Ca (37 μg/g) from an average of 10 analyses of the adhesive. For back-scattered electrons imaging, samples were embedded in araldite epoxy and ground and polished; these sample mounts were also used for Raman spectroscopy. Unprepared samples were used for optical absorption and emission spectroscopy.

2.2. Analytical techniques

The major-element composition of pigment samples was determined, rather semi-quantitatively, by XRF analysis and X-ray diffraction (XRD) refinement. The XRF analyses were done by means of a Bruker S4 Pioneer dispersive XRF spectrometer operated at 60 kV and 66 mA. A LiF analyser and the standardless MultiRes programme were used. For XRD details, the reader is referred to Cruciani et al. (2009) and Stoyanova Lyubenova et al. (2009a).

The low levels of trace-REEs in the pigments were measured by LA–ICP–MS analysis. A Finnigan Element XR, high resolution double focusing magnetic sector ICP–MS, coupled to a GeoLas 193 nm Excimer laser system, was used. The ablated material was transported to the ICP–MS using He gas with a flow rate of 1.25 l/min, with additional argon make-up gas added after the ablation cell. Laser spot sizes of 40 μm (reference materials) and 59 μm (ceramics) were used. The energy density was ca. $5\,J/cm^2$ with a laser repetition rate of $8\,s^{-1}$. Time resolved intensity data were acquired by peak-jumping in a combination of pulse-counting and analogue modes, depending on signal strength, with one point measured per peak. The average values for CaO determined by the XRF analyses were used as an internal standard to normalise counts to concentrations. Elements in high abundance were analysed in analogue mode, whereas true trace elements were analysed using digital pulse counting mode. For external independent reference materials, NIST 610 and NIST 612 glasses (Pearce et al., 1997) and USGS standard BCR–2G (Jochum et al., 2005) were used for calibration. Data were reduced using the Iolite software package (Paton et al., 2011). For more experimental details on the LA–ICP–MS trace-element analysis routine at the Department of Earth Sciences, Memorial University of Newfoundland, the reader is referred to Dorais and Tubrett (2008) and Rodríguez et al. (2011).

Diffuse reflectance spectra of the titanite pigment samples were measured at room temperature in the spectral range 26,000–6000 cm^{-1} on a Bruker IFS66v/S Fourier-transform infrared (FTIR) spectrometer using a Perkin-Elmer diffuse reflectance accessory unit. A tungsten light source, a quartz beam-splitter, and silicon (26,000–10,000 cm^{-1}) and germanium detectors (10,000–6000 cm^{-1}), respectively, were used to cover the desired spectral range. Standard spectra were obtained from MgO powder. Standard and sample spectra were each averaged from 512 scans. The spectral resolution was 10 cm^{-1} for both detector setups. Sub-spectra were aligned in absorbance for perfect match, if necessary.

Steady-state photoluminescence (PL) spectra in the visible and near-infrared range (i.e., spectral range 21,000–10,600 cm^{-1}) were obtained by means of two dispersive spectrometer systems. First, spectra with 488 nm Ar^+ excitation (8 mW at the sample surface) were recorded using a Renishaw RM1000 system equipped with Leica DMLM microscope and a diffraction grating with 1200 grooves/mm in the optical pathway. Second, a Horiba Jobin Yvon LabRam–HR spectrometer with Olympus BX41 optical microscope and a diffraction grating with 1800 grooves/mm, was used to record PL spectra excited with the 473 nm emission of a diode laser (3 mW). Both systems were equipped with Si-based, Peltier-cooled charge-coupled device (CCD) detector. A $50\times$ objective (NA = 0.55) was used in both cases. Spectra were calibrated using emission lines of a neon lamp. The wavenumber accuracy was better than 0.5 cm^{-1}, and the spectral resolution was determined at ∼3–4 cm^{-1} (RM1000) and better than 1 cm^{-1} (LabRam–HR), respectively. The latter system was used also to obtain Raman spectra for phase identification.

Time-resolved PL spectra were obtained with pulsed laser excitation (second harmonic of a Nd:YAG laser at 532 nm wavelength; pulse durations 5–10 ns). Spectra were obtained in 90° geometry, by means of an intensified Andor iStar CCD detector synchronised to the laser pulses. The setup used enabled us to perform measurements in selectable "time windows" that are determined by the delay time D (time period between the end of the laser pulse and the beginning of the measurement) and the gate width G (duration between beginning and end of the measurement). With a diffraction grating with 600 grooves/mm in the beam path, the spectral resolution was on the order of 8–10 cm^{-1} (or ca. 0.4 nm wavelength) in the red range.
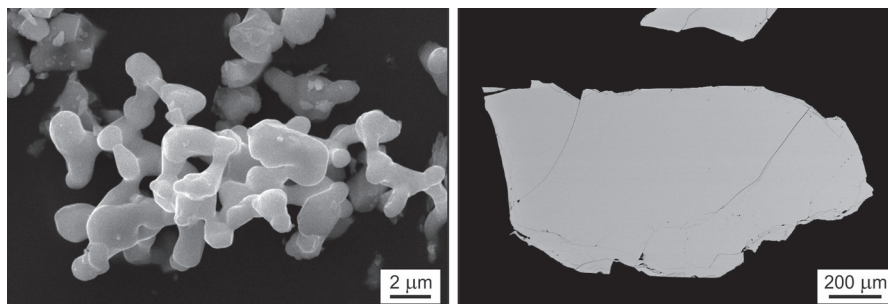
Fig. 1. Two representative electron microscope images of Cr-doped titanite samples. (a) Secondary electrons image of a Cr-doped titanite pigment after heating at 1200 °C. (b) Back-scattered electrons image of a polished Cr- and Nd-doped titanite grown by flux synthesis.

3. Results and discussion

3.1. Generalities and optical absorption

The titanite and malayaite pigment samples are fine-grained, with crystal sizes on the order of a few micrometres (Fig. 1a). Additional titanite references that were grown by the flux technique are larger, up to one millimetre in size (Fig. 1b). All samples were found to be remarkably homogeneous, that is, no growth zoning or other internal texture was observed in back-scattered electrons images (Fig. 1b).

Titanite and malayaite samples, respectively, were cleaned mechanically by hand-picking under a powerful binocular microscope, and phase identity was then confirmed by XRD and Raman spectroscopy. In all cases, only X-ray diffraction lines and Raman bands of titanite or malayaite were found, without any indication for the presence of additional phases. Depending on their chemical compositions, colours of titanite samples vary between nearly colourless (Cr-free), light ochre (low-Cr), and dark ochre- to reddish-brown (high-Cr). Macroscopic colours of malayaite samples depend similarly strongly on the Cr content, ranging from nearly colourless to light grey (Cr-free) and pale pinkish (low-Cr) to intense pink (high-Cr), respectively.

Chemical compositions of the pigment samples are listed in Table 1. Values quoted for the major oxides (SiO_2, CaO, TiO_2, SnO_2) are means of XRF and XRD results (note that XRD results for two samples have already been published by Cruciani et al., 2009; Stoyanova Lyubenova et al., 2009a). The CrO_2 concentrations quoted are means including our LA–ICP–MS results also. Chemical formulae of the three titanite pigments can be simplified to $CaTiSiO_5$, $Ca(Ti_{0.98}Cr_{0.02})SiO_5$, and $Ca(Ti_{0.80}Cr_{0.20})SiO_5$. Analogously, simplified formulae of the three malayaite pigments are $Ca(Sn_{1.00-x}Cr_x)SiO_5$ ($x = 0$, $x = 0.02$, and $x = 0.20$). The Cr per formula unit (for instance "$Cr_{0.02}$") is used to label the samples in Table 1 and the figures.

Representative optical absorption spectra (as obtained by diffuse reflectance spectroscopy) of Cr-free and Cr-doped titanite pigments are shown in Fig. 2. While the Cr-free sample lacks any significant absorption features in the visible and near-infrared (NIR) spectral ranges, the Cr-doped samples are characterised by steadily increasing absorbance in the visible range towards the ultraviolet (UV). The absorption pattern consists of several broad bands, located roughly around 20,000, 17,500, and 13,100 cm^{-1}, and further absorption bands in the NIR at around 10,700 and 8800 cm^{-1}. The latter is not visible in Fig. 2 but has been reported by Stoyanova Lyubenova et al. (2008; see Fig. 7 in that paper). The resulting absorption minimum lies in the NIR at ~12,000 cm^{-1} (Fig. 2). In the visible range, the Cr-doping has resulted in a general increase in absorbance by a factor of 5–6.

These absorption features, resulting in brown colouration of the calcinated Cr-doped titanite powders, have been attributed by

Table 1
Chemical compositions as determined by XRF/XRD and LA–ICP–MS (normed to 100% total).

Constituent (unit)	Malayaite samples			Titanite samples		
	Cr-free	$Cr_{0.02}$	$Cr_{0.20}$	Cr-free	$Cr_{0.02}$	$Cr_{0.20}$
MgO (wt%)	0.13	0.10	0.11	0.10	0.10	0.19
Al_2O_3 (wt%)	0.30	0.18	0.09	0.30	0.46	0.27
SiO_2 (wt%)	22.5	22.7	23.4	30.5	30.4	30.1
P_2O_5 (wt%)	(bdl)	0.17	0.17	0.26	0.28	0.89
SO_3 (wt%)	0.28	(bdl)	(bdl)	(bdl)	(bdl)	0.09
K_2O (wt%)	(bdl)	(bdl)	(bdl)	0.05	0.04	0.05
CaO (wt%)	20.9	20.7	21.7	28.6	27.9	21.7
TiO_2 (wt%)	(bdl)	(bdl)	0.26	40.0	39.6	30.0
CrO_2 (wt%)[a]	(bdl)	0.85	8.30	(bdl)	0.91	9.88
Fe_2O_3 (wt%)	0.51	0.08	0.11	0.07	0.12	0.20
ZnO (wt%)	(bdl)	(bdl)	(bdl)	(bdl)	0.09	(bdl)
SrO (wt%)	0.05	0.04	(bdl)	(bdl)	(bdl)	(bdl)
ZrO_2 (wt%)	(bdl)	0.04	(bdl)	(bdl)	(bdl)	(bdl)
SnO_2 (wt%)	55.3	55.1	45.9	(bdl)	(bdl)	(bdl)
WO_3 (wt%)[b]	(bdl)	(bdl)	(bdl)	0.06	0.02	(bdl)
Pr (µg/g)	0.6	0.5	0.3	0.9	0.9	0.7
Nd (µg/g)	18.8	13.9	7.4	5.7	8.6	4.1
Sm (µg/g)	0.4	0.5	0.1	0.8	0.8	0.5
Eu (µg/g)	0.1	0.1	0.5	0.1	0.4	0.2
Er (µg/g)	0.2	0.3	0.2	0.4	0.4	0.2

bdl: Not detected, or results below the 3σ detection limit.

[a] Chromium is quoted as CrO_2 because in the samples studied, chromium is predominantly present as Cr^{4+}, replacing Sn^{4+} (cf. Cruciani et al., 2009) or Ti^{4+} (Stoyanova Lyubenova et al., 2009a,b), respectively. Values quoted are means of XRF, XRD, and LA–ICP–MS results.

[b] Tungsten is a contaminant resulting from the grinding process.
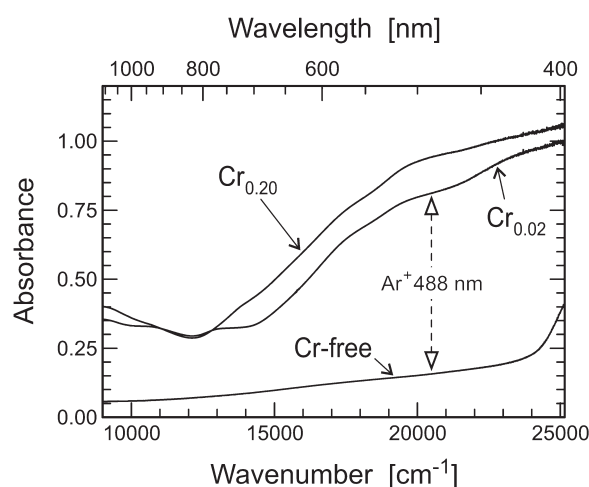

Fig. 2. Optical absorption spectra of the three titanite pigments. Note that the Cr-doping has resulted in ca. 5–6-fold increase of the absorption of the blue laser light (see grey arrow) used to excite the PL spectra presented in Fig. 3.
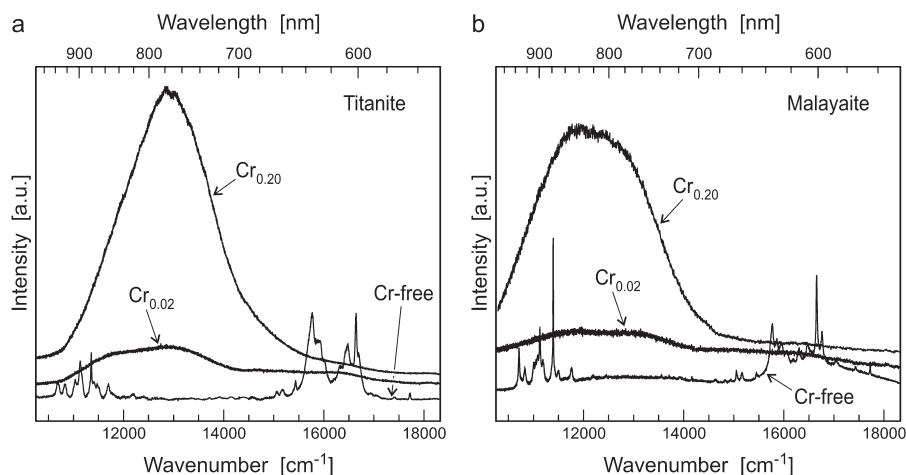
Fig. 3. Steady-state PL spectra of synthetic pigments (Ar⁺ 488 nm excitation; a, titanite samples; b, malayaite samples) showing how effectively the presence of chromium controls the appearance or absence of REE-related emissions.

Stoyanova Lyubenova et al. (2008) to co-actions of crystal-field transitions of Cr^{3+} ions in octahedral, and Cr^{4+} ions in octahedral as well as tetrahedral sites; and we adopt their interpretation to the discernible bands and shoulders in Fig. 2. However, we propose that in the visible spectral range these crystal-field bands are superposed on the low-energy wing of a UV absorption edge (or pre-edge band), probably caused by ligand-metal charge-transfer of Cr^{6+} cations replacing Si^{4+} in the tetrahedral sites of the titanite structure. It has been shown that tetrahedrally oxygen-coordinated Cr^{6+}, even if only present in trace amounts, may cause a significant red-shift of the fundamental absorption edge or a broad charge-transfer pre-edge band (e.g. Talla et al., 2013). The widely similar ionic radii of Cr^{6+} and Si^{4+} in tetrahedral coordination (Shannon, 1976) might also facilitate a partial oxidation of $(Cr^{4+})^{[4]}$ to $(Cr^{6+})^{[4]}$ at high calcination temperatures. This hypothesis seems to be in accordance with observations of Stoyanova Lyubenova et al. (2008) who reported a colour change from yellow to brown colour for Cr-doped titanite pigments after calcination at ≥1000 °C.

3.2. Photoluminescence

Steady-state PL spectra obtained under blue laser excitation are presented in Fig. 3. Spectra of undoped titanite and malayaite pigments do not show any significant "intrinsic" feature but, instead, groups of narrow emission bands in the orange-red to NIR region of the electromagnetic spectrum. The absence of "intrinsic" emissions corresponds to the results of Abe et al. (2010) who did not observe any emission from pure $CaTiSiO_5$ and $CaSnSiO_5$. The observation is also consistent with the results of Blasse et al. (1988): These authors reported that the green "intrinsic" broad-band emission of titanite is excited by mid-range UV light (excitation maximum reported at 290 nm wavelength) but not under long-wave UV or visible excitation. The groups of narrow emission bands are assigned to REEs, in particular Pr^{3+} and Sm^{3+} (perhaps also Er^{3+}) in the orange-red, and Nd^{3+} (and ancillary Er^{3+}) in the NIR. As pigment samples have not been doped intentionally, the origins of these REEs are assigned to minute pollutions of the starting oxides.

The REEs, whose emissions are observed in PL spectra, are interpreted as incorporated in the titanite and malayaite lattice, respectively, rather than forming separate phases. In the case of titanite samples, this interpretation is supported strongly by the fact that groups of REE^{3+} emission bands show fine-structures that are typical of REEs in titanite (compare spectra published by Gaft et al., 2003; Kennedy et al., 2010). In contrast, if REE-bearing phases other than titanite were present (i.e. if emitting REEs were

incorporated in different solids), different crystal-field effects would result in notably different fine-structures of electronic transitions (Gaft et al., 2005; Lenz et al., 2013). To the best of our knowledge, no appropriate references for the REE–PL of malayaite have been published thus far. However, the remarkable similarity of fine-structures of REE emissions of malayaite samples compared to those of titanite samples (see Fig. 3), supports REE incorporation in the malayaite lattice (which is iso-structural with titanite).

As expected, Cr-doped samples show the typical broad-band emission of Cr^{3+} whose intensity seems to correlate well with the Cr concentration (Fig. 3). Note that only a small fraction of the chromium is present as Cr^{3+} whereas the majority of this element is tetravalent (Cruciani et al., 2009; Stoyanova Lyubenova et al., 2008, 2009a); nevertheless the absolute quantity of the trivalent fraction of chromium is sufficient to cause intense PL emission. The PL emission of tetrahedrally coordinated Cr^{4+} has been observed in synthetic apatite (Gaft and Panczer, 2013), but to the best of our knowledge not in natural minerals thus far. Even if there was Cr^{4+} emission from our pigment samples, it would be rather irrelevant for our PL spectra: This emission, if present, is to be expected at low quantum energies of ca. 0.9–1.0 eV (ca. 1.3 μm wavelength; Gaft et al., 2005), which is far off the sensitivity range of the Si-based CCD detectors in the spectrometers used here.

Most remarkably, the narrow REE emission lines have disappeared completely in all Cr-doped samples. There are two hypothetically feasible reasons for this. First, the presence of chromium in the crucible could hinder the incorporation of trace-REEs into titanite/malayaite lattice. The absence of REE lines in the spectra would then be due to the absence of REE centres. Second, if the REEs are not excluded during crystal growth but present in the lattice, the simultaneous presence of sufficient amounts of Cr could suppress REE emissions. It was therefore crucial to measure concentrations of trace-REEs in all pigment samples. Results are quoted in the lower part of Table 1. As more or less uniform REE contents were measured in all samples, the former hypothesis can be excluded, and the observed emission behaviour is assigned to quenching of REE^{3+} emissions by Cr^{3+} centres (compare Reisfeld and Jørgensen, 1977).

To verify the above quenching effect, which was first observed from mildly REE-contaminated pigment samples, a suite of additional titanite samples, intentionally doped with REEs, were grown in a sodium-borate flux. Photoluminescence spectra of two Nd-doped samples are shown in Fig. 4. In the spectrum of Nd-doped Cr-free titanite (nearly colourless sample; lower spectrum in Fig. 4) it can be seen that the starting Nd_2O_3 was somehow impure and
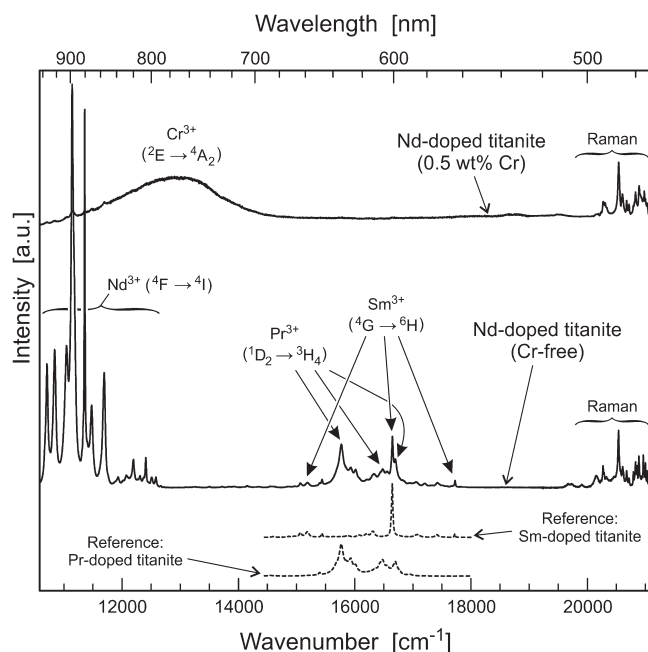
Fig. 4. Steady-state PL spectra of two flux-grown titanite samples (473 nm excitation). Dashed graph, Cr-free sample containing 520 µg/g Nd; solid graph, Cr-bearing sample containing 340 µg/g Nd. Spectra are shown with vertical offset for more clarity.

contained low levels of pollutant Sm and Pr (interpretation verified by reference spectra of Sm- and Pr-doped titanite), causing emissions in the orange to red spectral range. The fact that Sm^{3+} and Pr^{3+} emissions, in spite of their trace concentration, are relatively strong in intensity, is assigned to the particular effectiveness of the blue laser to excite these centres and the much higher sensitivity of Si-based CCDs in the visible range, compared to the NIR. This consideration is supported by the spectrum of Cr-free titanite in Fig. 3a: The emissions of Pr and Sm (15,500–17,000 cm^{-1}) are much higher in intensity than the emission of Nd (below 11,500 cm^{-1}), even though Nd is present in much higher quantity (see Table 1).

The upper spectrum in Fig. 4 was obtained from Nd-doped titanite containing 0.5 wt% Cr (dark olive-brown coloured sample). It is dominated by the broad emission band of Cr^{3+}. Emissions of REEs

are either reduced considerably (the Nd^{3+} emission in the NIR is reduced to ca. 2% of its intensity in the Cr-free sample, even though the concentrations are on the same order of magnitude) or extinct (Pr^{3+} and Sm^{3+}). This shows that, again, the presence of a sufficient amount of chromium suppresses the emission of REEs. Obviously, broad Cr^{3+} and narrow REE emissions are observed simultaneously (see Fig. 2 of Gaft et al., 2003, and Fig. 3B of Kennedy et al., 2010) only for samples with comparably moderate Cr concentration and virtual "REE excess" (compare Table 1 of Gaft et al., 2003).

A small selection of time-resolved PL spectra of titanite pigments are presented in Fig. 5. The spectrum of the undoped sample (Fig. 5a) is dominated by narrow emission lines assigned to REE centres. The decay time (τ) of the Nd^{3+} emission near 11,000–11,500 cm^{-1} (ca. 900 nm wavelength) was determined at 150–200 µs, which is about one order of magnitude longer than the typical decay time of the $^4F_{3/2} \rightarrow ^4I_{9/2}$ Nd^{3+} emission in natural titanite ($\tau \sim$10–30 µs; see also Gaft et al., 2003). In analogy to the steady-state PL spectra discussed above, time-resolved PL spectra of Cr-doped titanite pigments do not show REE emissions but only the broad $^2E \rightarrow ^4A_2$ emission of Cr^{3+} (Fig. 5b,c). The spectra indicate the presence of two different types of Cr^{3+} emission centres, characterised by slightly different maxima and decay times. They are assigned to Cr^{3+} ions in positions with weaker and stronger crystal field, respectively. Variable occupation of these Cr sites may also explain variations in the spectral position of the Cr^{3+} emission band in steady-state PL spectra (compare for instance $Cr_{0.02}$ and $Cr_{0.20}$ in Fig. 3a).

The general disappearance of REE emission lines accompanying the incorporation of notable chromium concentrations is quite unusual, and difficult to explain. The relatively long decay time of Nd^{3+} points to the possibility in the Cr-free pigments, REEs (or at least a part of the REE centres present) are not excited directly but through non-radiative energy transfer via (an)other centre(s) with relatively long decay time. In Cr-bearing pigments, in contrast, the REEs do not emit; rather, the excitation energy is preferentially transferred to trivalent chromium. This may be due partially to the enhanced absorption of the exciting laser light by chromium; however a ca. 5–6-fold increase in absorption (Fig. 2) alone is unable to cause a decrease in REE emissions by more than two orders of magnitude (Fig. 3). It appears much more likely that in Cr-bearing samples, the Cr^{3+} centres present quench the REE^{3+} emissions, that is, energy migrates from REE centres to Cr^{3+} by non-radiative mechanisms. The (re)absorption of potential REE emissions by Cr^{3+} needs

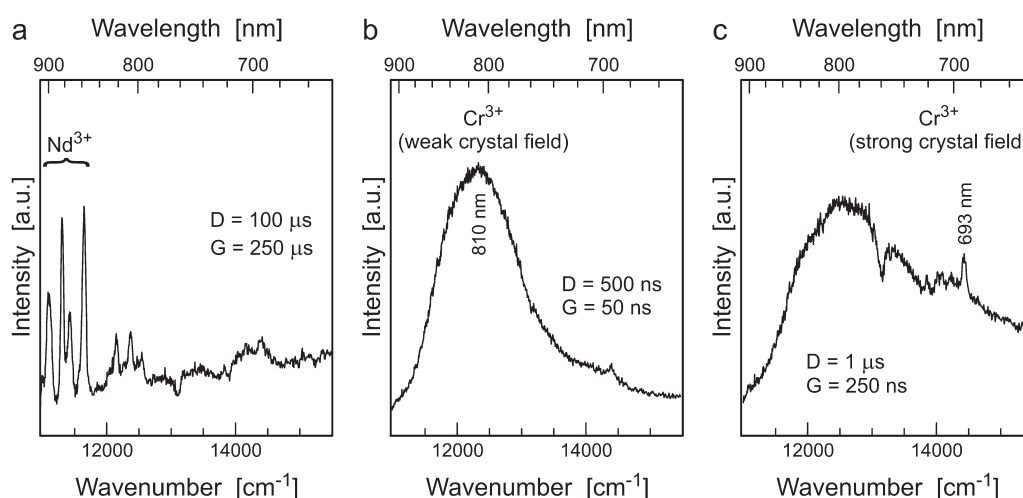**Fig. 5.** Time-resolved PL spectra of synthetic pigments in the red and near-infrared region (532 nm excitation). (a) Cr-free titanite pigment showing narrow REE-related bands (assigned mainly to the $^4F_{3/2} \rightarrow ^4I_{9/2}$ transition of Nd^{3+}). (b,c) Cr-rich titanite pigment (sample $Cr_{0.20}$). There are two chromium-related emissions with different spectral positions and decay times.

to be considered also. Quenching of REE luminescence by trivalent chromium has already been discussed by Reisfeld and Jørgensen (1977) who presented several examples. To the best of our knowledge, REE → Cr energy transfer has however not been reported for titanite-structured minerals thus far.

Remarkably, this process affects REE emissions with lower (e.g., Nd^{3+} at <1.4 eV) as well as REE emissions with higher energy (e.g., Pr^{3+} at ∼2 eV), compared to the ca. 1.46–1.61 eV transition of Cr^{3+} in titanite (see again Figs. 3 and 4). This suggests that evidently there is a – quite effective – energy migration from excited states of the REEs to an excited state of trivalent chromium.

Acknowledgements

References

Abe, S., Yamane, H., Yoshida, H., 2010. Synthesis and photoluminescence of Ca–(Sn,Ti)–Si–O compounds. Mater. Res. Bull. 45, 367–372.

Alexander, J.B., Flinter, B.H., 1965. A note on varlamoffite and associated minerals from the Batang Padang district, Perak, Malaya, Malaysia. Mineral. Mag. 35, 622–627.

Bartis, T., Lazau, R.I., Becherescu, D., Lazau, I., Pacurariu, C., Matea, O., 2007. Synthesis of some pink malayaite pigments and study of their behavior in ceramic glazes. Rev. Rom. Mater. 37, 113–121.

Basso, R., Lucchetti, G., Zefiro, L., Palenzona, A., 1994. Vanadomalayaite, CaVOSiO₄, a new vanadium analog of titanite and malayaite. Neues Jb. Miner. Monat. 11, 489–498.

Blasse, G., Dirksen, G.J., Tanaka, I., Kojima, H., 1988. The luminescence of titanite (CaTiSiO₅). Mater. Res. Bull. 23, 1727–1730.

Borcanescu, S., Lazau, I., Lazau, R.I., Pacurariu, C., 2013. Malayaite pink pigments behaviour in colouring some tableware faience glazes. Rev. Rom. Mater. 43, 90–95.

Cordoncillo, E., del Rio, F., Carda, J., Llusar, M., Escribano, P., 1998. Influence of some mineralizers in the synthesis of sphene-pink pigments. J. Eur. Ceram. Soc. 18, 1115–1120.

Cruciani, G., Dondi, M., Ardit, M., Stoyanova Lyubenova, T., Carda, J.B., Matteucci, F., Costa, A.L., 2009. Malayaite ceramic pigments: a combined optical spectroscopy and neutron/X-ray diffraction study. Mater. Res. Bull. 44, 1778–1785.

Dorais, M.J., Tubrett, M., 2008. Identification of a subduction zone component in the Higganum dike, Central Atlantic Magmatic Province: A LA-ICPMS study of clinopyroxene with implications for flood basalt petrogenesis. Geochem. Geophys. Geosyst. 9, Q10005.

Gaft, M., Panczer, G., 2013. Laser-induced time-resolved luminescence spectroscopy of minerals: a powerful tool for studying the nature of emission centres. Mineral. Petrol 107, 363–372.

Gaft, M., Nagli, L., Reisfeld, R., Panczer, G., 2003. Laser-induced time-resolved luminescence of natural titanite CaTiOSiO₄. Opt. Mater. 24, 231–241.

Gaft, M., Reisfeld, R., Panczer, G., 2005. Modern Luminescence Spectroscopy of Minerals and Materials. Springer, Berlin Heidelberg, New York, 356 pp.

Hajjaji, W., Zanelli, C., Seabra, M.P., Dondi, M., Labrincha, J.A., 2010. Cr-doped titanite pigment based on industrial rejects. Chem. Eng. J. 158, 167–172.

Higgins, J.B., Ribbe, P.H., 1977. The structure of malayaite, CaSnOSiO₄, a tin analog of titanite. Am. Mineral. 62, 801–806.

Jochum, K.P., Nohl, U., Herwig, K., Lammel, E., Stoll, B., Hofmann, A.W., 2005. GeoReM: a new geochemical database for reference materials and isotopic standards. Geostand. Geoanal. Res. 29, 333–338.

Kennedy, A.K., Kamo, S.L., Nasdala, L., Timms, N.E., 2010. Greenville skarn titanite: potential reference material for SIMS U–Th–Pb analysis. Can. Mineral. 48, 1423–1443.

Lenz, C., Talla, D., Ruschel, K., Škoda, R., Götze, J., Nasdala, L., 2013. Factors affecting the Nd³⁺ (REE³⁺) luminescence in minerals. Miner. Petrol. 107, 415–428.

Lutze, W., Ewing, R.C., 1988. Summary and evaluation of waste forms. In: Lutze, W., Ewing, R.C. (Eds.), Radioactive Waste Forms for the Future. North-Holland Physics Publishing, Amsterdam, pp. 699–740.

Mazdab, F., 2009. Characterization of flux-grown trace-element-doped titanite using the high-mass-resolution ion microprobe (SHRIMP–RG). Can. Mineral. 47, 813–831.

Paton, C., Hellstrom, J.C., Paul, B.T., Woodhead, J.D., Hergt, J.M., 2011. Iolite: Freeware for the visualisation and processing of mass spectrometric data. J. Anal. Atom. Spectrom. 26, 2508–2518.

Pearce, N.J.G., Perkins, W.T., Westgate, J.A., Gorton, M.P., Jackson, S.E., Neal, C.R., Chenery, S.P., 1997. A compilation of new and published major and trace element data for NIST SRM 610 and NIST SRM 612 glass reference materials. Geostandards Newslett. 21, 115–144.

Reisfeld, R., Jørgensen, C.K., 1977. Lasers and Excited States of Rare Earths. Springer, Berlin Heidelberg, pp. 226p.

Rodríguez, H.B., Lozano, D.O., Martínez, Y.A.R., Pérez, A.G.A., Balogh, A.G., Cabri, J.L., 2011. Quantification of refractory gold in grains of pyrite and arsenopyrite from the El Diamante gold mine in Nariño–Colombia. Revista Tumbaga 6, 153–164.

Shannon, R.D., 1976. Revised effective ionic radii and systematic studies of interatomic distances in halides and chalcogenides. Acta Cryst. A32, 751–767.

Speer, J.A., Gibbs, G.V., 1976. The crystal structure of titanite, CaTiSiO₅, and the domain textures of natural titanites. Am. Mineral. 61, 238–247.

Stefani, R., Longo, E., Escribano, P., Cordonciollo, E., Carda, J.B., 1997. Developing a pink pigment for glazes. Am. Ceram. Soc. Bull. 76, 61–64.

Stoyanova Lyubenova, T., Ocaña, M., Carda, J., 2008. Brown ceramic pigments based on chromium(III)-doped titanite obtained by spray pyrolysis. Dyes Pigments 79, 265–269.

Stoyanova Lyubenova, T., Matteucci, F., Costa, A.L., Dondi, M., Ocaña, M., Carda, J., 2009a. Synthesis of Cr-doped CaTiSiO₅ ceramic pigments by spray drying. Mater. Res. Bull. 44, 918–924.

Stoyanova Lyubenova, T., Matteucci, F., Costa, A.L., Dondi, M., Carda, J., 2009b. Ceramic pigments with sphene structure obtained by both spray- and freeze-drying techniques. Powder Technol. 193, 1–5.

Takenouchi, S., 1971. Hydrothermal synthesis and consideration of the genesis of malayaite. Miner. Deposita 6, 335–347.

Talla, D., Wildner, M., Beran, A., Škoda, R., Losos, Z., 2013. On the presence of hydrous defects in differently coloured wulfenites (PbMoO₄): an infrared and optical spectroscopic study. Phys. Chem. Miner. 40, 757–769.

Appendix A.3

A photoluminescence study of REE^{3+} emissions in radiation-damaged zircon

Lenz, C. and Nasdala, L. (2015)

American Mineralogist (in press)

Appendix A.3

A photoluminescence study of REE^{3+} emissions in radiation-damaged zircon† ⌀

Christoph Lenz[1],* and Lutz Nasdala[1]

[1]Institut für Mineralogie and Kristallographie, Universität Wien, Althanstrasse 14, 1090 Wien, Austria

Abstract

A series of natural zircon samples (with U concentrations of 140–2600 ppm and ranging from well crystalline to severely radiation damaged) were investigated by means of REE^{3+} photoluminescence spectroscopy. We found systematic changes in REE^{3+} emissions depending on the accumulated radiation damage expressed by the effective time-integrated α-dose of zircon samples. Structural reconstitution as caused by dry annealing resulted in intensity gains and decreases of half-widths of REE^{3+} emissions. The band half-widths of distinct luminescence Stark's levels of the $^4F_{9/2} \rightarrow {}^6H_{13/2}$ transition of Dy^{3+} (~17250 cm^{-1}; ~580 nm wavelength) and the $^4F_{3/2} \rightarrow {}^4I_{9/2}$ transition of Nd^{3+} (~11300 cm^{-1}; ~885 nm wavelength) were found to correlate sensitively with the degree of radiation damage accumulated. These REE^{3+} emissions are proposed as potential measure of the irradiation-induced structural disorder of zircon. The two emissions are considered particularly suitable because (1) they are commonly detected in PL spectra of natural zircon, and (2) they are hardly biased by other emissions or Stark's levels. Preliminary calibration curves that relate band-width increases to the α dose were established using a suite of well-characterized Sri Lankan zircon. Band broadening upon increasing corpuscular self-irradiation is assigned to increasing structural destruction, i.e., the increasing perturbation of REE^{3+} cationic lattice sites. Possible advantages of REE^{3+} luminescence spectroscopy, complementary to Raman spectroscopy, as method to quantify structural radiation damage are discussed.

Keywords: Radiation damage, rare-earth elements (REE), photoluminescence spectroscopy, hyperspectral PL mapping, zircon

Introduction

Structural disorder in U- and Th-containing minerals is caused predominantly by α-decay events, in particular comprising atomic displacements created by recoils of heavy daughter nuclei. The α particles, in constrast, have minor contribution to the total bulk damage (ca. 10–15%; Nasdala et al. 2001), whereas β and γ radiation are considered insignificant for the creation of permanent structural damage. The transformation of initially crystalline minerals into an amorphous state, through accumulation of recoil clusters over geologic periods of time, is commonly referred to as "metamictization" (e.g., Brøgger 1893; Pabst 1952; Ewing 1993).

Zircon, ZrSiO$_4$, is a widespread accessory mineral that occurs in many igneous, metamorphic, and sedimentary rocks. Zircon incorporates the actinides U^{4+} and Th^{4+} that substitute for Zr^{4+} in dodecahedral coordination (D$_{2d}$; Finch et al. 2001). Concentrations of the two actinides lie predominantly in the range 10–4000 ppm. As much as several weight percent have however been reported in some cases (for instance reported by Törnroos 1985; Rubin et al. 1989; Geisler et al. 2005). The accumulation of structural damage as caused by the radioactive decay of U and Th and their instable daughter nuclei, results in dramatic changes of solid-state properties. This includes changes of physical parameters such as refraction and birefringence, hardness, density, and elastic moduli (Holland and Gottfried 1955; Chakoumakos et al. 1991; Palenik

et al. 2003), and a general decrease of the chemical resistance (Balan et al. 2001; Mathieu et al. 2001; Geisler et al. 2003a). The generally increased susceptibility of radiation-damaged zircon to alteration in potential post-growth processes is of enormous importance as it for instance affects negatively the ability of this mineral to immobilize radioactive elements (storage of nuclear waste; e.g., Ewing 2001) or to retain radiogenic nuclei (bias of U–Pb geochronology results; Geisler et al. 2003b).

In addition to X-ray diffraction (e.g., Weber 1990; Ríos et al. 2000), several spectroscopic techniques have been applied to quantify radiation damage accumulated in zircon. For instance, Wasilewski et al. (1973), Deliens et al. (1977), Zhang et al. (2008), and Zhang and Salje (2001) used infrared (IR) absorption spectroscopy, and Farnan and Salje (2001) and Farnan et al. (2007) applied ^{29}Si nuclear magnetic resonance (NMR) spectroscopy for the estimation of the amorphous fraction in radiation-damaged zircon. Raman spectroscopy was introduced by Nasdala et al. (1995) as a method to quantify the degree of radiation-induced structural disorder in zircon. This technique has opened up new opportunities for studying the structural state of heterogeneous zircon crystals and for investigating relationships between α-doses, age, and the annealing history of geothermal events on a micrometer-scale (cf. Nasdala et al. 2001). The present study has been performed with the objective to test the applicability of REE^{3+} luminescence spectroscopy for the very same purpose, i.e., to check if the proposed method may be used, complementary to Raman spectroscopy, to characterize and estimate non-destructively the radiation-induced disorder of zircon.

Zircon typically incorporates traces of—mainly heavy—trivalent rare-earth elements (REE) into the structure, which is explained commonly by the coupled, xenotime-type substitution (Hanchar et al. 2001)

$$(REE^{3+}, Y^{3+}) + P^{5+} \rightarrow Zr^{4+} + Si^{4+} \qquad (1)$$
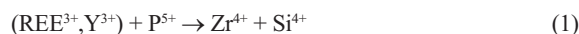
The emissions of REE^{3+} of zircon have been studied with differing luminescence techniques based on differing excitation mechanisms, such as photoluminescence (PL, e.g., Friis et al. 2010), cathodoluminescence (CL, e.g., Blanc et al. 2000), ionoluminescence (IL, e.g., Yang et al. 1994; Finch et al. 2004), thermally induced luminescence (TL, e.g., Vaz and Senftle 1971; Van Es et al. 2002), etc. Among them, CL imaging is the most widespread technique within the Earth sciences. Intensity-based imaging of CL emissions is commonly used to visualize internal textures of zircon, which provide valuable information on primary formation and post-growth history (e.g., Vavra 1990; Hanchar and Miller 1993; Hanchar and Rudnick 1995; Rakovan and Reeder 1996; Götze 2000, 2002; Corfu et al. 2003; Götze et al. 2013). Luminescence spectroscopy of REE emissions was (and still is) used successfully to detect traces of different REE species in zircon (e.g., Nicholas 1967; Yang et al. 1992; Götze et al. 1999; Kempe et al. 2000; Gaft et al. 2001). Synthetic zircon individually or multi-doped with REEs have also been studied routinely, aiming at a better understanding of the luminescence in their natural analogs (e.g., Cesbron et al. 1995; Blanc et al. 2000; Karali et al. 2000; Hanchar et al. 2001; Friis et al. 2010).

More recently, the luminescence of REE^{3+} was used as structural probe for the characterization of REE-substituted lattice sites in minerals and mineral-based ceramics. For instance, spectral parameters of Eu^{3+} emissions have been used for the characterization of REE-substituted cation-sites in glasses and crystalline materials in process of evaluation of potential nuclear waste forms (Ollier et al. 2003; Reisfeld et al. 2004; Ternane et al. 2005).

It has been found that REE^{3+} emission-band widths are influenced significantly by the real structure, i.e., deviations from the ideal chemical composition and structural state. In particular, it has been observed that individual REE emissions broaden appreciably, and decrease in intensity, upon (1) increasing incorporation of non-formula elements (e.g., Lenz et al. 2013), and (2) increasing radiation damage (e.g., Jazmati and Townsend 2000; Nasdala et al. 2002, 2013; Ruschel et al. 2010; Panczer et al. 2012).

In the present study we review briefly the REE^{3+} photoluminescence typical of natural zircon samples, and effects of radiation damage on the REE^{3+} luminescence pattern of zircon. The potential of hyperspectral luminescence mapping, e.g., to visualize radiation damage patterns on a micrometer scale, is demonstrated by comparing well-characterized, cut zircon crystal halves (with on half annealed through heat treatment and the other left in the natural radiation-damaged state, Nasdala et al. 2006). Finally, we show that the FWHM of selected REE^{3+} luminescence sublevels of zircon is related to the amount of radiation-damage accumulated over geologic periods of time (α-dose). The latter aspect provides an alternative possibility to estimate the quantity of radiation damage present in unknown zircon samples by measuring the FWHM of REE luminescence Stark's levels.

SAMPLES AND METHODS

The effects of radiation damage on the REE^{3+} luminescence were first studied using four zoned samples of natural, accessory zircon single crystals (lengths ranging from 150 to 350 μm, U–Pb ages scattering between Archean and Neogene), which have been characterized in detail by Nasdala et al. (2006). In that study, single crystals were cut in two halves, along their c-axes. One half each was then subjected to heat treatment in air to anneal the radiation damage, whereas the other half remained in its natural, radiation-damaged state. Both, the annealed and naturally radiation-damaged half-crystal, of each sample were then embedded in epoxy, and prepared in close proximity to each other in one polished mount. These four zircon samples originated from the following lithologies and localities: (1) a potassium-rich leuco-granite located near Dannemora, Adirondack Mountains, New York [sample A1; age ~1045–1050 Ma; (J.M. Hanchar and M.J. Whitehouse, personal communication); for rock description cf. McLelland et al. 2001], (2) the Bluffpoint quartz diorite, Atikwa Lawrence Batholith, Ontario [sample 81A; age 2732 ± 1 Ma; (D.W. Davis, personal communication); for rock description cf. Davis and Edwards 1985], (3) a gabbro from the Mulcahy Lake intrusion, Ontario (sample 31E; age 2733 ± 1 Ma; Morrison et al. 1985), and (4) a rhyolite tuff from the Gyulakeszi formation near Pécs, Hungary (sample M2; age 19.6 ± 1.4 Ma; Harangi 2001). An overview of the samples studied, and results of electron probe micro-analysis (EPMA), are given in Table 1 (compare also Nasdala et al. 2006).

Second, we have investigated large, homogeneous, gem-quality zircon samples. These included 13 mildly to severely radiation-damaged stones from gem gravels in the Ratnapura area, Sri Lanka (U–Pb ages in the range 522–572 Ma; Nasdala et al. 2004a, 2008), and one well-crystalline stone from the Ban Lung area, Ratanakiri, Cambodia (age 1.2 ± 0.3 Ma, P.C. Piilonen, personal communication; for sample description see Wittwer et al. 2013, and references therein). Uranium and thorium concentrations, ages, α-doses and spectroscopic data of the gem samples are listed in Table 2.

To identify specific REE^{3+} emissions in natural zircon, PL spectra of synthetic REE-doped $ZrSiO_4$ single crystals up to millimeters in size were obtained as internal references. Those materials have been synthesized in earlier studies using flux techniques; details are described elsewhere (Hanchar et al. 2001; Lenz et al. 2013).

Photoluminescence measurements in the visible to near infrared (NIR) range (single spectra and hyperspectral maps) were made using a Horiba LabRAM HR Evolution-dispersive spectrometer. The spectrometer system was equipped with an Olympus BX41 optical microscope, two diffraction gratings with 600 and 1800 grooves per millimeter, and a Si-based, Peltier-cooled charge-coupled device detector. Photoluminescence was excited using a 473 nm diode-pumped solid-state laser (9 mW at the sample surface) and the 532 nm emission of a frequency-doubled Nd^{3+}:YAG laser (10 mW at the sample surface). An Olympus 100× objective (numerical aperture 0.9) was used. The system was operated in the confocal mode (confocal aperture and entrance slit set at 100 μm); the resulting lateral resolution was ~1 μm, and the depth resolution (with the beam being focused at the sample surface) was ~2–3 μm. The spectral resolution for visible light was 0.8–1.1 cm⁻¹ with the 1800/mm grating (used for low-T measurements). The hyperspectral PL maps, consisting typically of 60000–80000 single spectra, were obtained using a software-controlled x–y stage. Color-coded PL maps (here, distribution patterns of the FWHM of individual Stark's levels) were then produced after appropriate data reduction, which included background correction and band-fitting assuming combined Lorentzian-Gaussian band shapes. Any mathematical correction of measured FWHMs for the system's spectral resolution (in detail discussed by Nasdala et al. 2001) turned out to be unnecessary. This is because spectrometer-related artificial broadening of Stark's level bands detected (FWHMs ≥12 cm⁻¹ at room temperature) was negligibly small, owing to the high spectral resolution of the spectrometer. Low-temperature photoluminescence-measurements of homogeneous, gem-quality zircon samples were done using a long-distance, 50× objective (numerical aperture 0.55; free working distance 10.6 mm) and a Linkam FTIR-600 liquid-nitrogen cooling stage. The temperature accuracy was better than ±2 K.

RESULTS AND DISCUSSION

Photoluminescence spectra

Figure 1 shows the laser-induced (λ_{exc} = 473 nm) REE^{3+} photoluminescence spectrum of sample M2. This spectrum can be considered typical of spectra of well-crystallized natural zircon. It is dominated by groups of narrow emission bands. In contrast, broad-band yellow and blue emissions (which are more often detected in CL spectra; e.g., Götze et al. 1999) were observed

TABLE 1. Electron probe microanalysis results for cut-in-half zircon samples (data from Nasdala et al. 2006)

Zone[a]	BSE Intensity	EPMA data (wt% oxide)										
		ZrO_2	SiO_2	HfO_2	P_2O_5	Y_2O_3	Dy_2O_3	Er_2O_3	Yb_2O_3	ThO_2	UO_2	Total
		Sample A1 (Adirondacks leucogranite, Fig. 3a)										
N1	middle	66.6	32.0	1.31	0.04	0.10	<0.04	0.04	<0.05	<0.02	0.04	100.1
N2	bright	66.8	32.1	1.27	<0.03	0.04	<0.04	<0.04	<0.05	<0.02	0.12	100.3
N3	very bright	65.0	31.7	0.98	0.13	0.79	0.04	0.15	0.16	0.08	0.19	99.2
A1	low	66.7	32.2	1.26	0.05	0.13	<0.04	0.04	<0.05	<0.02	0.05	100.4
A2	low	65.6	32.5	1.26	<0.03	0.03	<0.04	<0.04	<0.05	0.02	0.10	99.5
		Sample 81A (Bluffpoint quartz diorite, Fig. 3b)										
N1	very bright	67.3	32.6	1.13	0.04	0.07	<0.04	0.04	<0.05	0.02	0.02	101.3
N2	middle	67.3	32.7	0.86	<0.03	0.05	<0.04	0.04	<0.05	<0.02	<0.02	100.9
N3	bright	67.1	32.6	0.81	0.05	0.17	<0.04	0.04	<0.05	<0.02	0.03	100.7
A1	low	67.1	32.6	1.11	0.03	0.06	<0.04	<0.04	<0.05	<0.02	<0.02	100.9
A2	low	67.0	32.5	0.87	0.03	0.05	<0.04	<0.04	<0.05	<0.02	<0.02	100.6
A3	low	67.0	32.6	0.84	0.06	0.17	<0.04	<0.04	<0.05	<0.02	<0.02	100.8
		Sample 31E (Mulcahy Lake gabbro, Fig. 3c)										
N1	very bright	67.1	32.3	0.79	0.05	0.14	<0.04	<0.04	<0.05	<0.02	0.02	100.5
N2	low	67.6	32.3	0.54	<0.03	<0.03	<0.04	0.04	0.05	<0.02	<0.02	100.6
A1	low	67.0	32.4	0.82	0.06	0.17	<0.04	0.05	<0.05	<0.02	0.02	100.4
A2	low	66.9	32.6	0.63	<0.03	<0.03	<0.04	<0.04	<0.05	<0.02	<0.02	100.2
		Sample M2 (Hungary rhyolite tuff, Fig. 4)										
N1	middle	66.7	32.8	0.96	0.27	0.11	<0.04	0.05	<0.05	<0.02	0.03	100.8
N2	very bright	65.5	32.5	1.30	0.12	0.48	0.05	0.12	0.14	0.12	0.32	100.7
A1	low	66.7	32.6	0.89	0.05	0.18	<0.04	<0.04	<0.05	<0.02	<0.02	100.6
A2	bright	65.2	32.5	1.23	0.15	0.52	0.04	0.13	0.13	0.21	0.54	100.7

Notes: Al, Ca, Fe, and Ho have also been analysed. Data are not reported here because these elements were in most cases below the detection limit of the EPMA.
[a] N = naturally, damaged un-annealed zircon sample; A = annealed zircon sample. Number after letter A or N refers to different zones of the zircon grain.

TABLE 2. Uranium and thorium concentrations, ages, α-doses and spectroscopic data for zircon samples from Sri Lanka and Ratanakiri, Cambodia

Sample	U[a] (ppm)	Th[a] (ppm)	$^{206}Pb/^{238}U$ age[a] (Ma)	α-dose[b] (×10^18 α/g)	effective α-dose[c] (×10^18 α/g)	Dy^{3+} (I) FWHM (cm^{-1})	Dy^{3+} (II) FWHM (cm^{-1})	Nd^{3+} FWHM (cm^{-1})	Raman $v_3(SiO_4)$ FWHM[a]
M144	436 ±7	140 ± 3	552 ± 6	0.86–0.91	0.47–0.50	27.0 ± 1.4	27.0 ± 1.4	27.0 ± 2.7	7.2 ± 0.5
CZ3	550 ± 10	30 ± 2	563.9 ± 1.1	1.05–1.10	0.58–0.61	28.3 ± 1.4	27.2 ± 1.4	30.8 ± 3.1	8.2 ± 0.5
B188	556 ± 24	59 ± 4	559 ± 8	1.03–1.15	0.57–0.63	29.3 ± 1.5	27.0 ± 1.4	30.0 ± 3.4	8.5 ± 0.5
BR1	796 ± 13	39 ± 1	558 ± 13	1.47–1.60	0.81–0.88	37.5 ± 1.9	31.4 ± 1.6	34.2 ± 3.4	10.9 ± 0.8
BR231	772 ± 10	109 ± 2	571 ± 4	1.53–1.59	0.84–0.87	43.5 ± 2.2	32.4 ± 1.6	34.6 ± 3.5	11.0 ± 0.8
M257	840 ± 27	235 ± 20	561.3 ± 0.3	1.66–1.78	0.91–0.98	41.7 ± 2.1	32.8 ± 1.6	35.4 ± 3.5	11.7 ± 1.0
BR266	909 ± 17	201 ± 7	559.0 ± 0.3	1.77–1.88	0.97–1.03	44.0 ± 2.2	36.8 ± 1.8	38.0 ± 3.8	13.3 ± 1.0
M146	923 ± 17	411 ± 9	567 ± 4	1.92–2.03	1.06–1.12	47.2 ± 2.4	33.3 ± 1.7	37.0 ± 3.7	13.6 ± 1.0
M127	923 ± 23	439 ± 11	524.3 ± 0.4	1.78–1.88	0.98–1.03	50.8 ± 2.5	36.1 ± 1.8	39.7 ± 4.0	14.1 ± 1.2
OR1	1490 ± 70	279 ± 18	522 ± 3	2.62–2.92	1.44–1.61	65.2 ± 3.3	41.1 ± 2.1	42.8 ± 4.3	20.7 ± 1.5
G168	1499 ± 33	257 ± 9	547 ± 3	2.83–3.00	1.56–1.65	67.5 ± 3.4	39.6 ± 2.0	40.6 ± 4.1	24.5 ± 2.0
G4	2355 ± 84	330 ± 12	564 ± 5	4.48–4.91	2.46–2.70	81.2 ± 4.1	65.5 ± 3.3	49.6 ± 5.0	28.1 ± 2.0
G3	2572 ± 96	585 ± 34	542 ± 5	4.77–5.25	2.62–2.89	86.7 ± 4.3	67.2 ± 3.4	51.2 ± 5.1	30.4 ± 2.5
Rata	140 ± 100	90 ± 80	1.2 ± 0.3	± 0	± 0	11.8 ± 0.6	19.7 ± 1.0	14.3 ± 1.4	1.8 ± 0.3

Notes: Errors quoted are estimates that include errors of individual measurements and sample heterogeneity (scatter among multiple analyses).
[a] Sources for U and Th concentrations, ages, α-doses, and Raman-band FWHMs: Nasdala et al. (2008) for M257, Nasdala et al. (unpublished) for M127, Piilonen et al. (personal communication) and Wittwer et al. (2013) for Rata, and Nasdala et al. (2004a, and references therein) for all other samples.
[b] α-doses were calculated from U–Pb age and U and Th concentrations (Holland and Gottfried 1955; Murakami et al. 1991; Nasdala et al. 2001).
[c] Effective α-doses were estimated for zircon samples from Sri Lanka to account for incomplete damage retention by multiplying the α-dose value by a correction factor of 0.55 (for details see Nasdala et al. 2004a).

only occasionally in PL. Note that the sharpness of individual REE^{3+} emission lines (with FWHMs as small as 12 cm^{-1} at ambient temperature) may often causes confusion with Raman signals (for a detailed discussion see Nasdala et al. 2012).

Comparison of the PL spectrum of zircon M2 with spectra of synthetic REE-doped $ZrSiO_4$ (Fig. 1) reveals that the former comprises the principal transitions of traces of Dy^{3+} and Sm^{3+} in the visible to NIR spectral range. The most intense emissions are assigned to electronic transitions of Dy^{3+}, namely $^4F_{9/2} \rightarrow {}^6H_{15/2}$ near ~20 700 cm^{-1} and $^4F_{9/2} \rightarrow {}^6H_{13/2}$ near ~17 250 cm^{-1}. They are accompanied by several transitions of Sm^{3+} (Fig. 1; compare, e.g., Cesbron et al. 1995; Blanc et al. 2000; Karali et al. 2000; Gaft et al. 2001; Friis et al. 2010). In addition, low-intensity PL of Tm^{3+} and Nd^{3+} (in the NIR near ~11 400 cm^{-1}; assigned to the $^4F_{3/2} \rightarrow {}^4I_{9/2}$ transition) was observed. Assignments of electronic transitions and Russel-Saunders terms in Figure 1 have been extracted from

"Dieke" energy-level diagrams (e.g., Dieke and Crosswhite 1963; Reisfeld and Jørgensen 1977; Wegh et al. 2000).

All electronic transitions detected show crystal-field splitting into sharp sublevel bands (which are commonly referred to as Stark's levels). This is caused by a non-isotropic electronegative, crystallographic environment of REE^{3+} ions (crystal field splitting; e.g., reviewed in Burns 1993). As one consequence, REE^{3+} emissions show notable orientation dependence, i.e., individual Stark's levels of a given transition may be detected with variable relative intensities, depending on crystal orientation (compare, for example, relative intensities of individual peaks in the main Dy^{3+} emissions of zircon M2 and Dy^{3+}-doped $ZrSiO_4$ in Fig. 1).

The predominance of Dy^{3+} bands in REE^{3+} luminescence spectra of natural zircon has been well documented already in CL (Mariano 1989; Rémond et al. 1992; Hanchar and Rudnick 1995; Götze et al. 1999) and IL studies (Yang et al. 1994; Finch
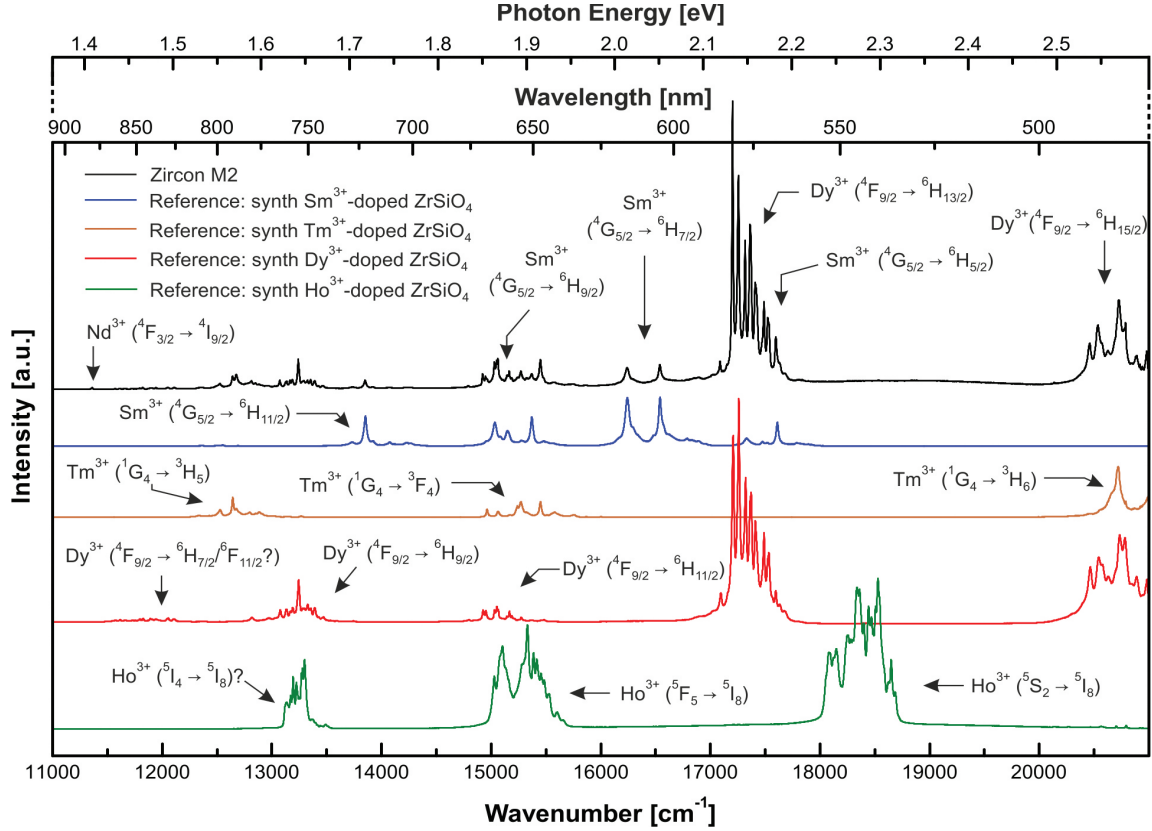
FIGURE 1. Typical laser-induced PL spectrum (λ_{exc} = 473 nm) of well-crystallized zircon in the visible to NIR spectral range (here sample M2; Pécs, Hungary). Comparison with spectra of synthetic REE-doped ZrSiO$_4$ (corresponding transitions are marked with arrows and labeled) reveals the dominance of Dy^{3+} and Sm^{3+} emissions in the natural sample, whereas the main transitions of Ho^{3+} were not observed. Minor emission signal of Nd^{3+} was observed in the NIR near ~11 400 cm^{-1}.

et al. 2004). In contrast, emissions of Ho^{3+} (cf. spectrum of Ho^{3+}-doped ZrSiO$_4$ in Fig. 1) were not detected in any steady-state PL spectrum obtained from the natural zircon samples studied here, neither with 473 nm nor with 532 nm laser-excitation. This is remarkable insofar as some of the samples have Ho and Dy concentrations of comparable magnitude. For instance, zircon M275 contains 12.6 ± 0.8 ppm Dy and 4.4 ± 0.3 ppm Ho (Nasdala et al. 2008) and M127 contains 57 ± 6 ppm Dy and 21 ± 2 ppm Ho (D. Frei, personal communication); however both samples showed intense Dy emission but no notable Ho emission bands. This observation seems to support results of the IL study of Finch et al. (2004) who concluded that Ho^{3+} emissions may be suppressed in the presence of Dy^{3+}.

Moreover, it is worthy of note that PL spectra strongly depend on the excitation wavelength. None of the PL spectra of natural zircon samples, including M257, obtained in the present study (with 473 nm and 532 nm laser excitation) showed emissions of Er^{3+} with significant intensity. In contrast, Er^{3+} emissions have been readily detected in PL spectra of zircon M275 obtained with 488 nm excitation (Nasdala et al. 2008). The contradiction is however only apparent, because selective excitation of REE emissions is well-known in steady-state laser-induced PL (e.g., Blasse and Grabmaier 1994). Strong excitation bands of Er^{3+} centered at 490 nm ($^4I_{15/2} \rightarrow {}^4F_{7/2}$) have been reported for synthetic zircon (Friis et

al. 2010). These may allow PL excitation with a nearby 488 nm, but not with a 473 nm laser.

Low-intensity emissions of Er and Ho, as well as emissions of other REEs in zircon (including Eu, Tb, Pr, Tm, Ce), which are hardly or not detectable with steady-state luminescence techniques, can however be measured using time-resolved laser-induced spectroscopy (cf. Gaft et al. 2001).

Hyperspectral PL mapping

Reliable estimation of spectral parameters (i.e., band fitting to determine FWHMs of individual REE^{3+} sublevels) is possible only if the emission detected consists of well-separated, distinct peaks. This is not the case for Sm^{3+} (and, similarly, not for Er^{3+} and Ho^{3+} emissions) in synthetic ZrSiO$_4$ whose emissions show numerous Stark's levels that strongly superimpose each other (Fig. 2A). In contrast, Stark's levels of the $^4F_{9/2} \rightarrow {}^6H_{13/2}$ transition of Dy^{3+} (especially those two in the range 17 240–17 260 cm^{-1}) can be identified and fitted without bias, as there are intense and not obscured by other bands (Fig. 2B). Dy^{3+} Stark's level I (Fig. 2B) is therefore used exemplarily in the present study, for the creation of PL maps based on the distribution of this band's FWHM.

Figure 3 shows BSE images, CL images and hyperspectral PL maps of pairs of halves of heterogeneous zircon crystals, whereas one half is naturally radiation-damaged, the other one an-
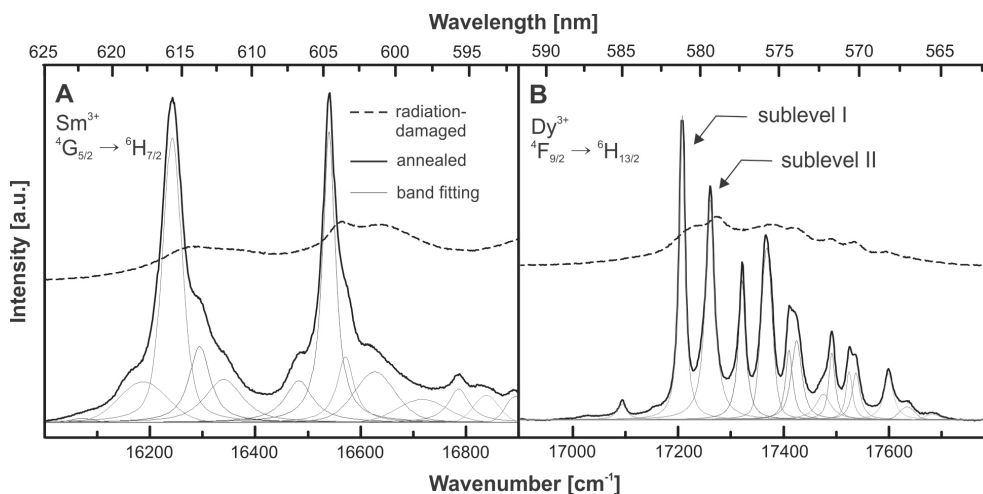
FIGURE 2. Pairs of PL spectra (λ_{exc} = 473 nm) obtained from the unannealed and annealed halves of zircon sample A1 (Adirondack Mts.). The two measurements were placed at corresponding locations, i.e., within the altered interior region of the crystal (cf. Fig. 3a). Spectra are shown with normalized maximum intensities and with vertical offset for clarity. (**A**) Emission related to the $^4G_{5/2} \rightarrow {}^6H_{7/2}$ transition of trace Sm^{3+}. (**B**) Emission related to the $^4F_{9/2} \rightarrow {}^6H_{13/2}$ transition of trace Dy^{3+}. Graphical results of least-square band fitting (assuming Lorentzian-Gaussian band shapes) are shown for spectra of annealed halves.

nealed. The PL maps show color-coded distribution patterns of the FWHM of sublevel I of the $^4F_{9/2} \rightarrow {}^6H_{13/2}$ transition of Dy^{3+}. Corresponding PL spectra and the respective Stark's levels used for mapping are presented in Figure 2B.

Figure 3 shows that accumulation of self-irradiation damage causes significant BSE increase and CL intensity decrease, as revealed by opposite trends upon structural reconstitution by dry annealing (Fig. 3). Nasdala et al. (2006) attempted to explain the BSE increase with increasing damage by electron channeling contrast (cf. Mitchell and Day 1998), and the CL-intensity loss upon damage accumulation was discussed by Nasdala et al. (2002). A similarly close, inverse correlation was observed also for the total PL emission, whose intensity decreases appreciably with increasing U concentration and radiation damage (see Fig. 2 again). The hypothesis that the presence of U is the main reason for the decreased PL emission (this effect was proposed for CL by Poller et al. 2001) is disproved by the fact that annealed halves have the same U concentrations as their unannealed counterparts but yield much more intense PL. Also, ion-irradiation of synthetic and natural zircon samples done by Finch et al. (2004) showed that REE^{3+} emissions observed in IL strongly decrease with increasing radiation damage. Finch et al. (2004) explained their observation by increasing defect concentrations upon increasing structural damage created, which give rise to non-radiative transitions and cause a reduced possibility of energy migration through the crystal.

In addition the general intensity loss of PL bands increasing radiation damage results in clear increases in FWHMs of individual bands (see also, e.g., Nasdala et al. 2013). Hyperspectral PL maps (Fig. 3) show that in naturally radiation-damaged zircon, the FWHM of Dy^{3+} sublevel I is broadened particularly in zones with high uranium concentrations and, hence, with more extensive radiation damage. In contrast, zones with low uranium concentrations (with corresponding lower levels of accumulated radiation damage) are characterized by narrow Dy^{3+} Stark's level bands (for instance see overgrowth rim of sample 31E, Fig. 3c). De-

pending on the degree of radiation damage of particular interior regions, the Dy^{3+} sublevel near 17 200 cm^{-1} yielded FWHMs of up to >40 cm^{-1}, whereas predominantly values close to 12 cm^{-1} were obtained after annealing. Distribution patterns of the FWHM of certain REE-emission sublevels (here, Dy^{3+} sublevel I) are hence virtual distribution patterns of radiation damage or crystallinity, respectively.

It should be noted that, in contrast to FWHM or band position, the band intensity and intensity-related spectral parameters such as the area integral are not suitable to estimate directly the degree of disorder. This is because luminescence intensity strongly depends on further variables, such as the absolute concentration of the respective REE^{3+}, effects of quenching/sensitizing by other elements (e.g., Marfunin 1979; Kempe and Götze 2002), and effects of crystal orientation (e.g., Lenz et al. 2013). The present study was, hence, not focused merely on intensity-based REE distributions (e.g., MacRae et al. 2012, 2013), but based on the interpretation of band widths of REE emissions.

The dependence of the broadening of the PL emission on the structural damage, rather than on the U concentration, is supported by the observation that annealed halves (containing the same amounts of U as their unannealed counterparts; Table 1) show narrow Dy^{3+} sublevel-bands. Furthermore, clustering of REE centers potentially may also result in PL band broadening. The similarity of our PL maps and Raman maps for the same pairs of crystal-halves (presented by Nasdala et al. 2006) rather supports the dependence of PL broadening on the defect accumulation upon increasing radiation damage. Both show the very same distribution patterns, which are in the case of Raman maps caused predominantly by the radiation damage accumulated.

In addition to effects of structural damage on the PL broadening, however, minor effects of the chemical composition cannot be neglected. An example is the PL map in Figure 3a. The annealed half-zircon of sample A1 still shows a slightly heterogeneous FWHM distribution pattern. Nasdala et al. (2006) discussed their
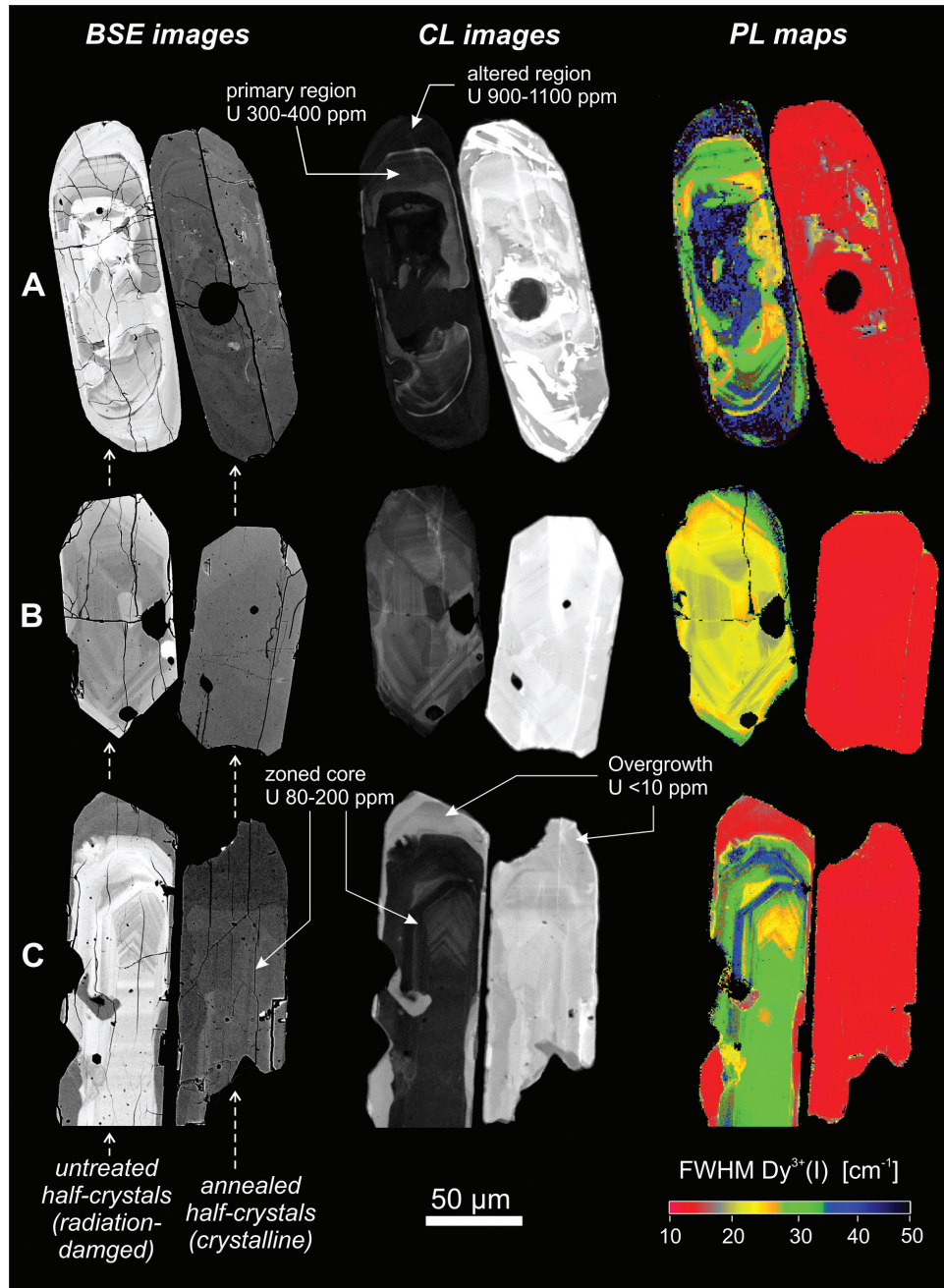
FIGURE 3. Images of cut zircon crystals from three different lithologies, with the heat-treated crystal half always shown in close proximity to its unannealed counterpart. (**a**) Zircon from a leucogranite, Adirondack Mountains, New York (sample A1). (**b**) Zircon from the Bluffpoint quartz diorite, Ontario (sample 81A). (**c**) Grain from the Mulcahy Lake intrusion, Ontario (sample 31E). In all three cases, a sequence of BSE and CL images (modified after Nasdala et al. 2006) and PL map is shown. The PL maps (λ_{exc} = 473 nm) were generated from the FWHM of the Dy^{3+} emission sublevel near 17 200 cm^{-1} (sublevel I; compare Fig. 2).

similar Raman observation for the very same sample as possible indication of incomplete structural reconstitution during the heat treatment (four days at 1300 °C). As an alternative interpretation we consider the possibility that minor heterogeneity in their Raman map, and our PL map, may be due to minor heterogeneity of the chemical composition (i.e., FWHM increase due to the elevated presence of non-formula elements). These heterogeneous areas are

characterized by slightly, but significantly, elevated concentrations of P_2O_5, REE_2O_3, and U/ThO_2 (see EPMA measurement point N3 from the sample A1 in Table 1).

The impact of compositional heterogeneity on the FWHM is supported also by the PL map of the very mildly radiation-damaged zircon M2 (Fig. 4), whose internal FWHM variations (between 14 and 25 cm^{-1} in the natural and between 12 and 15 cm^{-1} in the
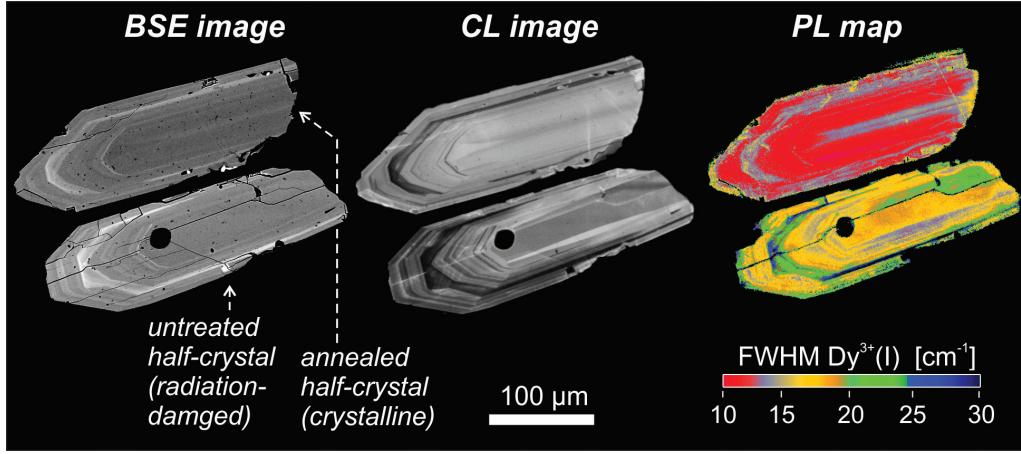
FIGURE 4. Series of BSE and CL image (modified after Nasdala et al. 2006) and PL map (λ_{exc} = 473 nm) of a cut zircon from a rhyolite tuff from the Gyulakeszi formation near Pécs, Hungary (sample M2). Note the different color-coding scale compared to the three PL maps in Figure 3. The non-uniformity of the BSE intensity within the annealed crystal half indicates that slight FWHM variations of the PL might be due to moderate chemically induced band broadening.
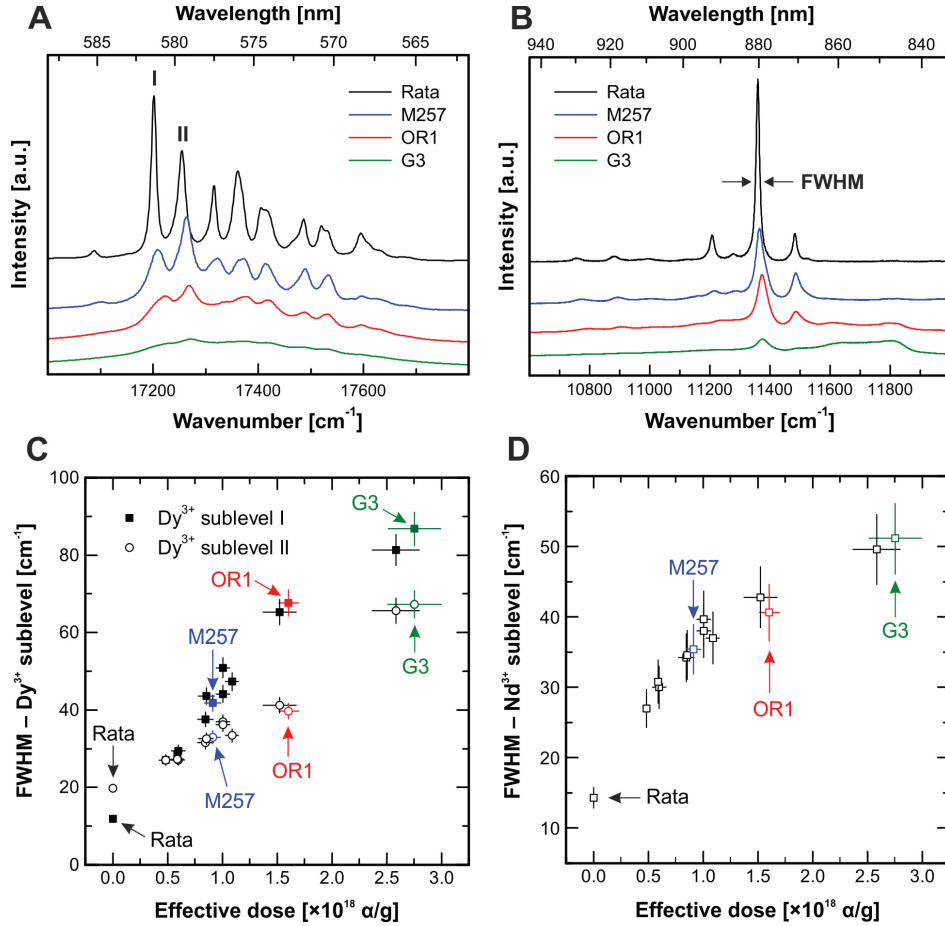
FIGURE 5. Effect of radiation damage on PL spectral parameters, obtained at room temperature, of gem-quality zircon samples. (**a** and **b**) Photoluminescence spectra (**a**, λ_{exc} = 473 nm; **b**, λ_{exc} = 532 nm) of samples whose degrees of radiation damage range from well crystalline (Rata) to severely damaged (G3). (**c**) Plot of the FWHM of two Dy^{3+} ($^4F_{9/2} \rightarrow {}^6H_{13/2}$) sublevels (which are indicated in **a**) against calculated effective α-doses. Note the clear FWHM-dose correlations, which however show different slopes. Data plotted were extracted from Table 1. (**d**) Plot of the FWHM of the ~11 350 cm^{-1} sublevel of Nd^{3+} ($^4F_{3/2} \rightarrow {}^4I_{9/2}$; marked in **b** with arrows) against calculated effective α-doses.

annealed half-crystal) are assigned in part to chemical heterogeneity. First, FWHMs are not uniform in the annealed crystal half (as it should be expected if FWHM broadening was solely due to structural damage). Second, the bright-BSE growth zone is characterized by both elevated concentrations of UO_2, ThO_2, and REE_2O_3 (Table 1) and the strongest PL band broadening (Fig. 4). Note that, due to its Neogene age (Harangi 2001), sample M2 has accumulated much less radiation damage compared to the zircon samples shown in Figure 3. Effects of radiation damage on the PL are hence less extensive in sample M2, and, correspondingly, the (minor) effects of the chemical composition on band FWHMs are detected because they are less obscured.

Effects of compositional-induced structural-disorder have been well documented already for the Nd^{3+} luminescence of monazite–(Ce) (e.g., PL study of Lenz et al. 2013). Note, however, that natural monazite–(Ce) typically has much higher compositional variability, when compared to natural zircon, which hence affects the FWHMs of PL emissions of monazite–(Ce) to much higher magnitudes. The impact of chemical heterogeneity on the FWHM of REE^{3+} Stark's levels in natural zircon is, therefore, comparably low.

Reference zircon spectra: Estimation of radiation damage

Effects of radiation damage on the Dy^{3+} and Nd^{3+} luminescence of zircon are visualized and determined more quantitatively by PL data obtained from a suite of gem-zircon samples from Ratnapura, Sri Lanka, and Ratanakiri, Cambodia (Fig. 5). Note that the Sri Lankan zircon samples represent various degrees of radiation damage, ranging from moderately (M144) to strongly damaged (G3; see Table 2; compare also Nasdala et al. 2004a). The Ratanakiri zircon, in contrast, is characterized by a remarkably low degree of self-irradiation damage (Wittwer et al. 2013), which is mainly due to the sample's young age of 1.2 ± 0.3 Ma (P.C. Piilonen,

personal communication). Note also that the Sri Lanka zircon has experienced partial structural reconstitution in its geological history, which is why α-doses calculated based on the time period since the Neoproterozoic to Cambrian closure of the U–Pb system overestimate the radiation damage present (for details Nasdala et al. 2004a). To account for the annealing, "effective α-doses" were corrected applying a correction factor of 0.55 to the calculated total α-doses, as elucidated by Nasdala et al. (2004a).

In accordance to our findings described above, band widths of Dy^{3+} and Nd^{3+} luminescence sublevels show a marked increase that is closely related to the self-irradiation dose (Fig. 5). Note that the particular extent of the dose-related FWHM increase for a given Stark's level band is not necessarily uniform but may vary appreciably among emission centers and even among individual sublevels of a single transition. As an example, FWHMs of two sublevels belonging to the $^4F_{9/2} \rightarrow {}^6H_{13/2}$ transition of Dy^{3+} (labeled I and II in Fig. 5a), show divergent band-broadenings upon increasing α-doses (Fig. 5c). Dysprosium sublevel I [FWHM increase from 12 cm^{-1} (Rata) to 87 cm^{-1} (G3)] obviously is more sensitive to radiation-induced structural disorder, compared to Dy^{3+} sublevel II [FWHM increase from 20 cm^{-1} (Rata) to 68 cm^{-1} (G3)] and the ~11 350 cm^{-1} sublevel of Nd^{3+} ($^4F_{3/2} \rightarrow {}^4I_{9/2}$) [FWHM increase from 14 cm^{-1} (Rata) to 51 cm^{-1} (G3)], respectively (Fig. 5d). Consequently, for each single Stark's level that is intended to be used as measure of the radiation damage, a separate calibration of the FWHM-dose dependence needs to be available.

The FWHM increase of REE-related emissions in mildly to strongly radiation-damaged (but not yet fully amorphous) zircon is assigned to disturbance of the structure as caused by the accumulation of defects. These defects are considered to perturb the local crystallographic environment of the REE^{3+} centers. As a consequence, the crystal field around REE cations is distorted, and PL bands may shift slightly in spectral position. The spectral
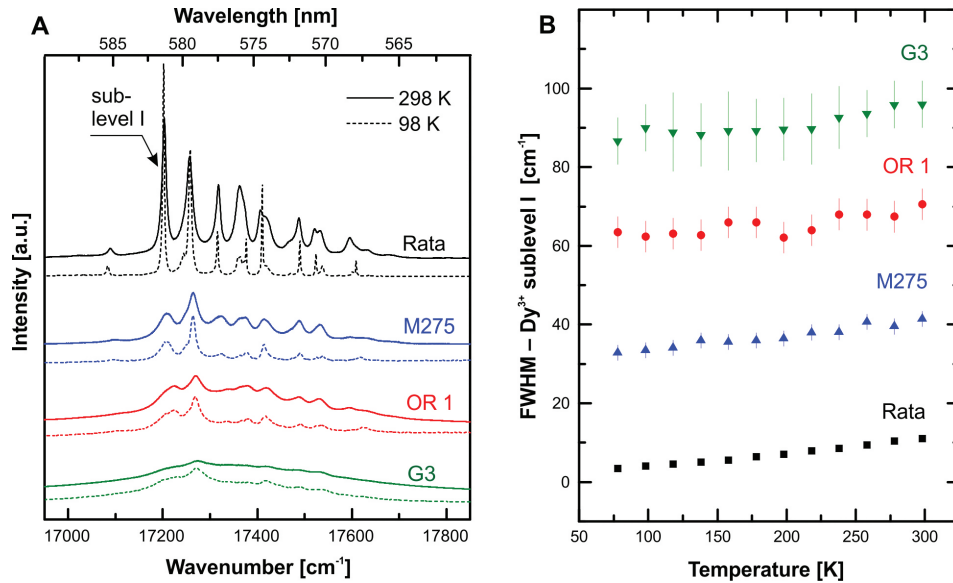
FIGURE 6. Effect of temperature on the PL spectra of various gem-quality zircon samples ranging from well crystallized to severely radiation damaged. (**a**) Pairs of spectra showing the Dy^{3+} emission ($^4F_{9/2} \rightarrow {}^6H_{13/2}$) at ambient and low temperature. (**b**) Plot of the FWHM of Dy^{3+} sublevel I (see arrow in **a**) against temperature. Note that FWHMs of Dy^{3+} Stark's levels depend strongly on the sample's degree of radiation damage (cf. Fig. 5), whereas temperature has moderate effects.
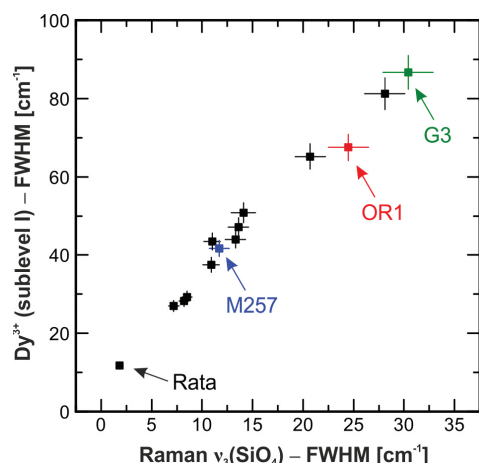
FIGURE 7. Plot of the FWHM of sublevel I of the Dy^{3+} $^4F_{9/2} \rightarrow {}^6H_{13/2}$ PL emission against the FWHM of the $\nu_3(SiO_4)$ Raman band (B_{1g} mode; antisymmetric stretching of SiO_4 tetrahedrons). Data pairs of the four gem-quality zircon samples, whose PL spectra are shown in Figure 5, are labeled and marked with arrows.

band detected may then be regarded as superposition of a multitude of single levels arising from variably distorted crystallographic sites within the spatially resolved area analyzed (e.g., Skinner and Moerner 1996; Lenz et al. 2013).

Completely metamict $ZrSiO_4$, and amorphous volumes in moderately damaged zircon, are in contrast characterized by randomly perturbed cation sites, which results in the entire degeneration of REE^{3+} crystal-field states. This in turn leads to the total loss of fine structure of electronic transitions, i.e., no more distinct Stark's levels but broad single bands are observed in PL spectra. Analogous effects are observed in PL spectra of glasses produced by melt quenching; see for instance the PL spectra of Dy-doped $CaTiSiO_5$ glass (degenerate transitions) and crystal (Stark fine-split transitions) in Figure 15 of Nasdala et al. (2004b). Consequently, the broadened (but still split) Stark's level bands obtained from zircon samples studied here are assigned to the crystalline fraction present, whereas amorphous clusters (for a general description of the damage-accumulation process see Murakami et al. 1991) are virtually "PL-invisible" at low self-irradiation doses. At elevated radiation damage, fitting of individual Stark's level bands is feasible as long as a minimum of remnant (even though strongly stressed) crystalline volume units contribute to the luminescence emission, and provided the REE signal originating from the amorphous volume fraction does not hamper too much the background.

Note, however, that FWHMs of luminescence bands also depend on temperature. In general, low-temperature luminescence studies are conducted to improve the sharpness of individual bands (for the narrowing of REE^{3+} emissions at low temperatures see, e.g., Reisfeld and Jørgensen 1977; Marfunin 1979; Blasse and Grabmaier 1994; Lenz et al. 2013). Figure 6a shows an exemplary low-temperature series of PL spectra of Dy^{3+} in zircon samples representing various degrees of radiation damage. The plot of FWHMs against temperature (Fig. 6b) however indicates that FWHMs of Dy^{3+} sublevels differ appreciably among variably

radiation-damaged samples. In contrast, the effect of temperature on the FWHMs (i.e., narrowing with lowered temperature) is comparably low. The band FWHMs decrease by approximately about -8 cm^{-1} from ambient temperature to 78 K (virtually independent from the degree of the sample's radiation damage).

The effect of temperature on widths of REE^{3+} emissions (i.e., $4f$ elements) is hence comparably small when compared with d-d or d-f transitions. This is because f-electrons and their inter-transitions are well shielded by the outermost filled $5s^25p^6$ orbitals (Blasse and Grabmaier 1994). Low-temperature PL measurements are, therefore, of insignificant usefulness to increase the reliability of FWHM estimates for strongly radiation-damaged zircon (see data for samples OR1 and G3 in Fig. 6b). The effective temperature-induced narrowing of Stark's levels of these two samples does not exceed significantly the statistical error of the FWHM estimates. In addition, low temperature measurements performed by using cooling stages or other liquid-nitrogen setups entail considerable effort; especially for measurements with high lateral resolution such as for hyperspectral PL mapping. Therefore, all reference luminescence spectra presented in the sections above are recorded at room temperature (298 K) as this study promotes the application of REE^{3+} luminescence spectroscopy being used potentially for various other techniques as well (such as CL coupled to EPMA). Nevertheless, for unbiased quantitative estimates, it needs to be ensured that luminescence analyses are done at room temperature or, alternatively, at the same temperature as the calibration measurements. Consequently, uncontrolled sample heating, such as due to intense local absorption of the incident laser light, must be avoided.

IMPLICATIONS

The REE^{3+} luminescence of zircon was found once again to be very sensitive to structural disorder caused by corpuscular self-irradiation. The emission intensity generally decreases, and band FWHMs increase, possibly accompanied by minor band shifts, with increasing structural damage. Our results show that the band-widths of distinct sublevels of Dy^{3+} ($^4F_{9/2} \rightarrow {}^6H_{13/2}$) and Nd^{3+} ($^4F_{3/2} \rightarrow {}^4I_{9/2}$) emissions (1) can be determined reliably by conventional band-fitting procedures and (2) is strongly related to the amount of radiation-damage accumulated (the latter being expressed by the effective time-integrated α-dose; Fig. 5). We propose the use of the FWHM of the Stark's level at $\sim$17 200 cm^{-1} of the $^4F_{9/2} \rightarrow {}^6H_{13/2}$ transition of Dy^{3+} (here described as sublevel I; see again Fig. 5c) and the dominant Stark's level of Nd^{3+} near 11 350 cm^{-1} (Figs. 5b and 5d) as most suitable means of estimating quantitatively the radiation-induced structural disorder of zircon on a micrometer-scale.

Estimation of the crystallinity based on REE-band FWHMs may open up new opportunities to characterize the structural state of radiation-damaged zircon, complementary to the use of Raman-band FWHMs for this purpose (Nasdala et al. 1995, 2001). This is supported by Figure 7, which shows that the radiation-damage induced FWHM increase of the Dy^{3+} sublevel I is related to that of the $\nu_3(SiO_4)$ Raman band of zircon. Potential advantages of using REE^{3+} luminescence spectroscopy include (1) the high-volume resolution (with confocal spectrometer systems, analyses can be done on a micrometer scale), (2) the

option to do non-destructive analyses without sample preparation, and (3) the possibility to obtain the FWHM of Stark's levels of multiple REE^{3+} centers simultaneously (e.g., Dy^{3+} and Nd^{3+}). The latter (i.e., choosing another center or transition) may be advisable if a Stark's level under analysis should be obscured by other phenomena (e.g., defect-related broad-band emissions created upon corpuscular irradiation; Götze et al. 1999; Finch et al. 2004; Nasdala et al. 2013). The proposed PL of Dy^{3+} sublevel I may be used widely in studying zircon, because according to our experience, trace-Dy is virtually omnipresent in natural zircon, and even minute quantities yield well-measurable luminescence signals. Finally, similar to FWHMs of SiO_4-related Raman bands, FWHMs of the Dy^{3+} (and Nd^{3+}) signals studied here were found to depend predominantly on the degree of radiation damage present, whereas chemical effects, which may be much more extensive in minerals that typically are compositionally variable, are almost negligible in the case of (unaltered igneous or metamorphic) zircon.

ACKNOWLEDGMENTS

REFERENCES CITED

Balan, E., Neuville, D.R., Trocellier, P., Fritsch, E., Muller, J.P., and Calas, G. (2001) Metamictization and chemical durability of detrital zircon. American Mineralogist, 86, 1025–1033.

Blanc, P., Baumer, A., Cesbron, F., Ohnenstetter, D., Panczer, G., and Rémond, G. (2000) Systematic cathodoluminescence spectral analysis of synthetic doped minerals: anhydrite, apatite, calcite, fluorite, scheelite and zircon. In M. Pagel, V. Barbin, P. Blanc, and D. Ohnenstetter, Eds., Cathodoluminescence in Geosciences, 127–160. Springer, Berlin.

Brøgger, W.C. (1893) Amorf: Salmonens store illustrerede Konversationslexikon, 1, 742–743.

Burns, R.G. (1993) Mineralogical applications of crystal field theory. Cambridge Topics in Mineral Physics and Chemistry, 5, Cambridge University Press.

Blasse, G., and Grabmaier, B. (1994) Luminescence Materials, 248 p., Springer, Berlin.

Cesbron, F., Blanc, P., Ohnenstetter, D., and Rémond, G. (1995) Cathodoluminescence of rare earth doped zircons. I. Their possible use as reference materials. Scanning Microscopy Supplement, 9, 35–56.

Chakoumakos, B.C., Oliver, B.C., Lumpkin, G.R., and Ewing, R.C. (1991) Hardness and elastic modulus of zircon as a function of heavy-particle irradiation dose. I. In situ a-decay event damage. Radiation Effects and Defects in Solids, 118, 393–403.

Corfu, F., Hanchar, J.M., Hoskin, P.W.O., and Kinny, P. (2003) Atlas of zircon textures. In J.M. Hanchar and P.W.O. Hoskin, Eds., Zircon, 53, p. 469–500. Reviews in Mineralogy and Geochemistry, Mineralogical Society of America, Chantilly, Virginia.

Davis, D.W., and Edwards, G.R. (1985) The petrogenesis and metallogenesis of the Atikwa-Lawrence volcanic-plutonic terrain. Grant 179, Ontario Geological Survey Miscellaneous Publication, 127, 101–111.

Deliens, M., Delhal, J., and Tarte, P. (1977) Metamictization and U-Pb systematics – a study by infrared absorption spectrometry of Precambrian zircons. Earth and Planetary Science Letters, 33, 331–344.

Dieke, G.H., and Crosswhite, H.M. (1963) The spectra of the doubly and triply ionized rare earths. Applied Optics, 2, 675–686.

Ewing, R.C. (1993) The metamict state: 1993—the centennial. Nuclear Instruments and Methods in Physics Research Section B, 91, 22–29.

——— (2001) The design and evaluation of nuclear-waste forms: clues from mineralogy. Canadian Mineralogist, 39, 697–715.

Farnan, I., and Salje, E.K.H. (2001) The degree and nature of radiation damage in zircon observed by ^{29}Si nuclear magnetic resonance. Journal of Applied Physics, 89, 2084–2090.

Farnan, I., Cho, H., and Weber, W.J. (2007) Quantification of actinide α-radiation damage in minerals and ceramics. Nature, 445, 190–193.

Finch, R.J., Hanchar, J.M., Hoskin, P.W.O., and Burns, P.C. (2001) Rare-earth elements in synthetic zircon: Part 2. A single-crystal X-ray study of xenotime substitution, American Mineralogist, 86, 681–689.

Finch, A.A., Garcia-Guinea, J., Hole, D.E., Townsend, P.D., and Hanchar, J.M. (2004) Ionoluminescence of zircon: rare earth emissions and radiation damage. Journal of Physics D, 2795–2803.

Friis, H., Finch, A.A., Williams, C.T., and Hanchar, J.M. (2010) Photoluminescence of zircon ($ZrSiO_4$) doped with REE^{3+} (REE= Pr, Sm, Eu, Gd, Dy, Ho, Er). Physics and Chemistry of Minerals, 37, 333–342.

Gaft, M., Panczer, G., Reisfeld, R., and Uspensky, E. (2001) Laser-induced time-resolved luminescence as a tool for rare-earth element identification in minerals. Physics and Chemistry of Minerals, 28, 347–363.

Geisler, T., Trachenko, K., Ríos, S., Dove, M.T., and Salje, E.K.H. (2003a) Impact of self-irradiation damage on the aqueous durability of zircon ($ZrSiO_4$): implications for its suitability as a nuclear waste form. Journal of Physics: Condensed Matter, 15, 597–605.

Geisler, T., Pidgeon, R.T., Kurtz, R., van Bronswijk, W., and Schleicher, H. (2003b) Experimental hydrothermal alteration of partially metamict zircon. American Mineralogist, 88, 1496–1513.

Geisler, T., Burakov, B., Zirlin, V., Nikolaeva, L., and Pöml, P. (2005) A Raman spectroscopic study of high-uranium zircon from the Chernobyl "lava". European Journal of Mineralogy, 17, 883–894.

Götze, J. (2000) Cathodoluminescence microscopy and spectroscopy in applied mineralogy. Freiberger Forschungsheft C 485, TU Bergakademie Freiberg, 128 p.

——— (2002) Potential of cathodoluminescence (CL) microscopy and spectroscopy for the analysis of minerals and materials. Analytical and Bioanalytical Chemistry, 374, 703–708.

Götze, J., Kempe, U., Habermann, D., Nasdala, L., Neuser, R.D., and Richter, D.K. (1999) High-resolution cathodoluminescence combined with SHRIMP ion probe measurements of detrital zircons. Mineralogical Magazine, 63, 179–187.

Götze, J., Schertl, H.P., Neuser, R.D., Kempe, U., and Hanchar, J.M. (2013) Optical microscope-cathodoluminescence (OM–CL) imaging as a powerful tool to reveal internal textures of minerals. Mineralogy and Petrology, 107, 373–392.

Hanchar, J.M., and Miller, C.F. (1993) Zircon zonation patterns as revealed by cathodoluminescence and backscattered electron images: implications for interpretation of complex crustal histories. Chemical Geology, 110, 1–13.

Hanchar, J.M., and Rudnick, R.L. (1995) Revealing hidden structures: the application of cathodoluminescence and back-scattered electron imaging to dating zircons from lower crustal xenoliths. Lithos, 36, 289–303.

Hanchar, J.M., Finch, R.J., Hoskin, P.W.O., Watson, E.B., Cherniak, D.J., and Mariano, A.M. (2001) Rare earth elements in synthetic zircon: part 1. Synthesis, and rare earth element and phosphorus doping. American Mineralogist, 86, 667–680.

Harangi, S. (2001) Neogene to Quarternary volcanism of the Carpathian-Pannonian region—a review. Acta Geologica Hungarica, 44, 223–258.

Holland, H.D., and Gottfried, D. (1955) The effect of nuclear radiation on the structure of zircon. Acta Crystallographica, 8, 291–300.

Jazmati, A.K., and Townsend, P.D. (2000) Photoluminescence from RE doped BGO waveguides. Nuclear Instruments and Methods in Physics Research Section B: Beam Interactions with Materials and Atoms, 166, 597–601.

Karali, T., Can, N., Townsend, P.D., Rowlands, A.P., and Hanchar, J.M. (2000) Radioluminescence and thermoluminescence of rare earth element and phosphorus-doped zircon. American Mineralogist, 85, 668–681.

Kempe, U., and Götze, J. (2002) Cathodoluminescence (CL) behaviour and crystal chemistry of apatite from rare-metal deposits. Mineralogical Magazine, 66, 151–172.

Kempe, U., Gruner, T., Nasdala, L., and Wolf, D. (2000) Relevance of cathodoluminescence for interpretation of U-Pb zircon ages (with an example of application to a study of zircons from the Saxonian Granulite Complex, Germany). In M. Pagel, V. Barbin, P. Blanc, and D. Ohnenstetter, Eds., Cathodoluminescence in Geosciences, p. 415–455. Springer, Berlin.

Lenz, C., Talla, D., Ruschel, K., Skoda, R., Götze, J., and Nasdala, L. (2013) Factors affecting the Nd^{3+} (REE^{3+}) luminescence of minerals. Mineralogy and Petrology, 107, 415–428.

MacRae, C.M., Wilson, N.C., Torpy, A., and Davidson, C.J. (2012) Hyperspectral cathodoluminescence imaging and analysis extending from ultraviolet to near infrared. Microscopy and Microanalysis, 18, 1239–1245.

MacRae, C.M., Wilson, N.C., and Torpy, A. (2013) Hyperspectral cathodoluminescence. Mineralogy and Petrology, 107, 429–440.

Mariano, A.N. (1989) Cathodoluminescence emission spectra of rare earth element activators in minerals. In B.R. Lipin and G.A. McKay, Eds., Geochemistry and Mineralogy of Rare Earth Elements, p. 339–348. Reviews in Mineralogy, 21, Mineralogical Society of America, Chantilly, Virginia.

Marfunin, A.S. (1979) Spectroscopy, Luminescence, and Radiation Centers in Minerals, 352 p. Springer, Berlin.

Mathieu, R., Zetterström, L., Cuney, M., Gauthier-Lafaye, F., and Hidaka, H. (2001) Alteration of monazite and zircon and lead migration as geochemical tracers of fluid paleocirculations around the Oklo–Okélobondo and Bangombé natural nuclear reaction zones (Franceville basin, Gabon). Chemical Geology, 171, 147–171.

McLelland, J., Morrison, J., Selleck, B., Cunningham, B., Olson, C., and Schmidt,

K. (2001) Hydrothermal alteration of late- to post-tectonic Lyon Mountain granitic gneiss, Adirondack Highlands, New York: Origin of quartz-sillimanite segregations, quartz-albite lithologies, and associated Kiruna-type low-Ti Fe-oxide deposits. Journal of Metamorphic Geology, 19, 1–19.

Mitchell, D.R.G., and Day, R.A. (1998) Electron channelling contrast imaging of defect structures in neutron irradiated aluminium. Scripta Materialia, 39, 923–930.

Morrison, D.A., Davis, D.W., Wooden, J.L., Bogard, D.D., Maczuga, D.E., Phinney, W.C., and Ashwal, L.D. (1985) Age of the Mulcahy Lake intrusion, northwest Ontario, and implications for the evolution of greenstone-granite terraines. Earth and Planetary Science Letters, 73, 306–316.

Murakami, T., Chakoumakos, B.C., Ewing, R.C., Lumpkin, G.R., and Weber, W.J. (1991) Alpha-decay event damage in zircon. American Mineralogist, 76, 1510–1532.

Nasdala, L., Wolf, D., and Irmer, G. (1995) The degree of metamictization in zircon: a Raman spectroscopic study. European Journal of Mineralogy, 7, 471–478.

Nasdala, L., Wenzel, M., Vavra, G., Irmer, G., Wenzel, T., and Kober, B. (2001) Metamictisation of natural zircon: accumulation versus thermal annealing of radioactivity-induced damage. Contributions to Mineralogy and Petrology, 141, 125–144.

Nasdala, L., Lengauer, C.L., Hanchar, J.M., Kronz, A., Wirth, R., Blanc, P., Kennedy, A.K., and Seydoux-Guillaume, A.-M. (2002) Annealing radiation damage and the recovery of cathodoluminescence. Chemical Geology, 191, 121–140.

Nasdala, L., Reiners, P.W., Garver, J.I., Kennedy, A.K., Stern, R.A., Balan, E., and Wirth, R. (2004a) Incomplete retention of radiation damage in zircon from Sri Lanka. American Mineralogist, 89, 219–231.

Nasdala, L., Götze, J., Hanchar, J.M., Gaft, M., and Krbetschek, M.R. (2004b) Luminescence techniques in Earth sciences. In A. Beran and E. Libowitzky, Eds., Spectroscopic Methods in Mineralogy, 6, 43–91. EMU Notes in Mineralogy, Eötvös University Press, Budapest.

Nasdala, L., Kronz, A., Hanchar, J.M., Tichomirowa, M., Davis, D.W., and Hofmeister, W. (2006) Effects of natural radiation damage on back-scattered images of single crystals of minerals. American Mineralogist, 91, 1739–1746.

Nasdala, L., Hofmeister, W., Norberg, N., Martinson, J.M., Corfu, F., Dörr, W., Karno, S.L., Kennedy, A.K., Kronz, A., Reiners, P.W., and others. (2008) Zircon M257—A homogeneous natural reference material for the ion microprobe U-Pb analysis of zircon. Geostandards and Geoanalytical Research, 32, 247–265.

Nasdala, L., Beyssac, O., Schopf, J. W., and Bleisteiner, B. (2012) Application of Raman-based images in the Earth sciences. In A. Zoubir, Ed., Raman Imaging—Techniques and applications, 145–187. Springer Series in Optical Sciences, 168, Springer, Berlin.

Nasdala, L., Grambole, D., and Ruschel, K. (2013) Review of effects of radiation damage on the luminescence emission of minerals, and the example of He-irradiated CePO$_4$. Mineralogy and Petrology, 107, 441–454.

Nicholas, J.V. (1967) Origin of the luminescence in natural zircon. Nature, 215, 1476.

Ollier, N., Concas, G., Panczer, G., Champagnon, B., and Charpentier, T. (2003) Structural features of a Eu^{3+} doped nuclear glass and gels obtained from glass leaching. Journal of Non-Crystalline Solids, 328, 207–214.

Pabst, A. (1952) The metamict state. American Mineralogist, 37, 137–157.

Palenik, C.S., Nasdala, L., and Ewing, R.C. (2003) Radiation damage in zircon. American Mineralogist, 88, 770–781.

Panczer, G., De Ligny, D., Mendoza, C., Gaft, M., Seydoux-Guillaume, A., and Wang, X. (2012) Raman and fluorescence. In J. Dubessy, M.-C. Caumon, and F. Rull, Eds., Applications of Raman Spectroscopy to Earth Sciences and Cultural Heritage, 12, p. 61–82. EMU Notes in Mineralogy, Eötvös University Press, Budapest.

Poller, U., Huth, J., Hoppe, P., and Williams, I.S. (2001) REE, U, Th, and Hf distribution in zircon from Western Carpathian Variscan granitoids: A combined cathodoluminescence and ion microprobe study. American Journal of Science, 301, 858–876.

Rakovan, J., and Reeder, R.J. (1996) Intracrystalline rare earth element distributions in apatite: surface structural influences on incorporation during growth. Geochimica et Cosmochimica Acta, 60, 4435–4445.

Reisfeld, R., and Jørgensen, C.H. (1977) Lasers and Excited States of Rare Earths. Inorganic Chemistry Concepts, 1, Springer, Berlin.

Reisfeld, R., Zigansky, E., and Gaft, M. (2004) Europium probe for estimation of site symmetry in glass films, glasses and crystals. Molecular Physics, 102, 1319–1330.

Rémond, G., Cesbron, F., Chapoulie, R., Ohnenstetter, D., Roques-Carmes, C., and Schoverer, M. (1992) Cathodoluminescence applied to the microcharacterization of mineral materials: a present status in experimentation and interpretation. Scanning Microscopy, 6, 23–68.

Ríos, S., Salje, E.K., Zhang, M., and Ewing, R.C. (2000) Amorphization in zircon: evidence for direct impact damage. Journal of Physics: Condensed Matter, 12, 2401–2412.

Rubin, J.N., Henry, C.D., and Price, J. G. (1989) Hydrothermal zircons and zircon overgrowths, Sierra Blance Peaks, Texas. American Mineralogist, 74, 865–869.

Ruschel, K., Nasdala, L., Rhede, D., Wirth, R., Lengauer, C.L., and Libowitzky, E. (2010) Chemical alteration patterns in metamict fergusonite. European Journal of Mineralogy, 22, 425–433.

Skinner, J., and Moerner, W. (1996) Structure and dynamics in solids as probed by optical spectroscopy. Journal of Physical Chemistry, 100, 13251–13262.

Ternane, R., Ferid, M., Panczer, G., Trabelsi-Ayadi, M., and Boulon, G. (2005) Site-selective spectroscopy of Eu^{3+}-doped orthorhombic lanthanum and monoclinic yttrium polyphosphates. Optical Materials, 27, 1832–1838.

Törnroos, R., (1985) Metamict zircon from Mozambique. Bulletin of the Geological Society of Finland, 57, 181–195.

Van Es, H.J., Vainshtein, D.I., Rozendaal, A., Donoghue, J.F., De Meijer, R.J., and Den Hartog, H.W. (2002) Thermoluminescence of ZrSiO$_4$ (zircon): A new dating method?. Nuclear Instruments and Methods in Physics Research Section B: Beam Interactions with Materials and Atoms, 191, 649–652.

Vavra, G. (1990) On the kinematics of zircon growth and its petrogenetic significance: a cathodoluminescence study. Contributions to Mineralogy and Petrology, 106, 90–99.

Vaz, J.E., and Senftle, F.E. (1971) Thermoluminescence study of the natural radiation damage in zircon. Journal of Geophysical Research, 76, 2038–2050.

Wasilewski, P.J., Senftle, F.E., Vaz, J.E., Thorpe, A.N., and Alexander, C.C. (1973) A study of the natural α-recoil damage in zircon by infrared spectra. Radiation Effects, 17, 191–199.

Weber, W.J. (1990) Radiation-induced defects and amorphization in zircon. Journal of Materials Research, 5, 2687–2697.

Wegh, R.T., Meijerink, A., Lamminmäki, R.J., and Hölsä, J. (2000) Extending Dieke's diagram. Journal of Luminescence, 87, 1002–1004.

Wittwer, A., Nasdala, L., Wanthanachaisaeng, B., Bunnag, N., Skoda, R., Balmer, W. A., Giester, G., and Zeug, M. (2013) Mineralogical characterisation of gem zircon from Ratanakiri, Cambodia. In CORALS–2013: Conference on Raman and Luminescence Spectroscopy in the Earth Sciences, Vienna, Austria, July 3–6 (2013) Book of abstracts, p. 115–116. http://www.univie.ac.at/Mineralogie/Corals2013/abstracts.html.

Yang, B., Luff, B. J., and Townsend, P. D. (1992) Cathodoluminescence of natural zircons. Journal of Physics: Condensed Matter, 4, 5617–5624.

Yang, C., Homman, N.O., Johansson, L., and Malmqvist, K.G. (1994) Microcharacterizing zircon mineral grain by ionoluminescence combined with PIXE. Nuclear Instruments and Methods in Physics Research Section B: Beam Interactions with Materials and Atoms, 85, 808–814.

Zhang, M., and Salje, E.K. (2001) Infrared spectroscopic analysis of zircon: Radiation damage and the metamict state. Journal of Physics: Condensed Matter, 13, 3057–3071.

Zhang, M., Boatner, L.A., Salje, E.K., Ewing, R.C., Daniel, P., Weber, W.J., Zhang, Y., and Farnan, I. (2008) Micro-Raman and micro-infrared spectroscopic studies of Pb-and Au-irradiated ZrSiO$_4$: Optical properties, structural damage, and amorphization. Physical Review B, 77(14), 144110.

Appendix A.4

Laser-induced REE^{3+} photoluminescence of selected accessory minerals

– An "advantageous artefact" of Raman spectroscopy

Lenz, C., Nasdala, L., Talla, D., Hauzenberger, C., Seitz, R.,

and Kolitsch, U. (2015)

Chemical Geology (submitted)

Laser-induced REE³⁺ photoluminescence of selected accessory minerals – An "advantageous artefact" in Raman spectroscopy

Christoph Lenz [a,*], Lutz Nasdala [a], Dominik Talla [a,b], Christoph Hauzenberger [c], Roland Seitz [d], Uwe Kolitsch [e]

[a] *Institut für Mineralogie und Kristallographie, Universität Wien, 1090 Wien, Austria*
[b] *Institute of Geological Sciences, Masaryk University, 61137 Brno, Czech Republic*
[c] *Institut für Erdwissenschaften, Karl-Franzens-Universität Graz, 8010 Graz, Austria*
[d] *Horiba Jobin Yvon GmbH, 82008 Unterhaching, Germany*
[e] *Naturhistorisches Museum Wien, 1010 Wien, Austria*

ABSTRACT

We have studied laser-induced photoluminescence of trivalent rare-earth elements (REEs), which are, as analytical artefacts, obtained in Raman spectra of selected accessory minerals. Spectra of natural titanite, monazite–(Ce), xenotime–(Y), and zircon samples from various geological environments were compared with emission spectra of synthetic, flux-grown analogues doped with REEs. This allowed us to identify potentially mistakable bands as either Raman or PL signal, and in the latter case to assign them to certain REE centres. In the samples investigated, various REE centres are excited selectively using 473, 514, 532, 633, and 785 nm laser excitation. Their assignment was verified by photoluminescence-excitation experiments. Luminescence patterns of zircon and titanite vary in dependence of trace-REE concentrations, hence reflecting geochemical growth conditions. Advantages of "REE artefacts" in Raman spectra of accessory minerals are discussed with respect to their application as fingerprint tool and their relevance for the visualisation of mineral textures.

1. Introduction

In the last decades, the use of Raman spectroscopy in the Earth sciences has increased appreciably. This was stimulated, among other reasons, by (i) a number of analytical advantages (including the opportunity to perform micrometre-scale analyses non-destructively and without special sample-preparation needs), (ii) the increased availability of powerful, easy-to-operate, and cost-efficient Raman spectrometer systems, (iii) a growing number of successful applications in virtually all sub-disciplines of the Earth sciences, and (iv) significant improvements in the availability of reliable reference spectra. The most common field of application of Raman spectroscopy is the identification of mineral phases and components of geological samples on the basis of spectral fingerprint-characteristics. Examples include the fields of gemmology (e.g. Fritsch et al., 2004; Bersani and Lottici, 2010; Bersani et al., 2014), archaeometry and cultural heritage (e.g. Edwards et al., 2000; Smith, 2006; Vandenabeele et al., 2006; Ropret et al., 2010), high-pressure petrology (e.g. Korsakov et al., 2005; Stähle et al., 2008; Marschall et al., 2009), planetary mineralogy (e.g. Wang et al., 1995, 2004; Sharma et al., 2003; Popp and Schmitt, 2004; Bozlee et al., 2005; Blacksberg et al., 2010), environmental mineralogy (e.g. Das and Hendry, 2011), palaeontology (e.g. Schopf et al., 2002; Bernard et al., 2007; Chen et al., 2007), biomineralogy (e.g. Li et al., 2013; Pasteris et al., 2014), and many other disciplines. Furthermore, Earth scientists have become increasingly interested in the application of the hyperspectral Raman-mapping technique. The latter is a powerful tool to visualise, among others, the distribution of mineral phases within geological samples, and internal textures within single-crystals of minerals (Nasdala et al., 2004a; Bernard et al., 2008; Nasdala et al., 2012, and references therein).

The reliable interpretation of Raman spectra of geological samples may however be hampered by a range of possible analytical artefacts (for a detailed discussion see Nasdala et al., 2012 and references therein). Potential bias of results is among others

---

[*] Corresponding author:
C. Lenz, Institut für Mineralogie & Kristallographie,
Universität Wien, Althanstr. 14, 1090 Vienna, Austria.
E-mail address: christoph.lenz@univie.ac.at
Tel.: +43 1 4277 53280; *fax:* +43 1 4277 9532.

caused by the fact that in the analysis of minerals, Raman-scattered light is often recorded together with, or even obscured by, laser-induced photoluminescence (PL). The incident laser beam may excite the sample's valence electrons, and PL emissions are then generated through the release of energy in (radiative) electronic transitions. The strength of this artefact is controlled by the presence and concentration of emission centres in the material analysed. Such luminescence centres or activators may include structural defects and/or minor or trace elements incorporated into the crystal structure (e.g., Marfunin, 1979; Blasse and Grabmeier, 1999).

Confusion of Raman bands with PL bands is likely especially if samples contain notable amounts of rare-earth elements (REE) with *4f* electronic configuration (e.g., Panczer et al., 2012). If such REEs are incorporated in crystalline materials, they may cause narrow-line emissions whose widths (0.1–0.3 nm, or a few cm^{-1}, at room temperature) are on the order of typical Raman-band widths. The REE-related emissions are therefore easily mistaken as Raman bands, and vice versa; publications describing the Raman spectrum of REE-bearing minerals should hence be referred to with appropriate caution. To substantiate this rather pessimistic statement, a few examples are quoted here. Zhang et al. (2000) presented a green-laser excitation (Ar^+ 514.5 nm) spectrum of a sample consisting of crystalline ZrO_2 and amorphous SiO_2, which showed Raman bands of ZrO_2 and additional bands in the Raman-shift range 1,000–1,100 cm^{-1}. The latter were assigned by Zhang et al. (2000) to Raman bands of crystalline $ZrSiO_4$ and SiO_2. The red-laser excitation (He-Ne 632.8 nm) Raman spectrum of the very same sample (Nasdala et al., 2004) however only showed ZrO_2 Raman bands. This indicates that the additional bands obtained by Zhang et al. (2000) were green (wavelength 541–546 nm) PL emissions (most likely caused by trace-Er^{3+}; Gaft et al., 2000; Nasdala and Hanchar, 2005). They were recorded unintentionally in the same spectral range as the Raman bands just because green laser-excitation was used in that Raman experiment. Similarly, Xian et al. (2004) failed to recognise that their Raman spectra of zircon (obtained also with green laser excitation) were obscured by Er^{3+} related PL-emissions, and they treated these emissions as Raman bands (see critical discussion by Nasdala and Hanchar, 2005). Dill and Weber (2010) presented "Raman spectra" of fluorite in the Raman-shift range 400–2400 cm^{-1} (note however that fluorite has only one single first-order Raman band at 322 cm^{-1}; Gee et al., 1966), and they assigned by mistake REE-related PL emissions in their spectra to Raman modes. Possible confusion of REE^{3+} emissions with Raman bands has been discussed

critically by McCubbin et al. (2010). These authors pointed out that in Raman spectra of fluorapatite obtained with 532 nm excitation, Sm^{3+} emissions (wavelengths about 650 nm) are recorded with apparent Raman shifts of 3300–3500 cm^{-1}. These emissions therefore may be mistaken easily as O–H stretching bands of structurally bound hydroxyl groups.

Common accessory minerals (including titanite, monazite- and xenotime-group minerals, and zircon) typically incorporate REEs. The accurate assignment of REE signals in PL spectra of geological samples is often challenging, because (i) minerals, which were formed in natural and hence "polluted" geochemical environments, may contain simultaneously a range of REE species; (ii) emissions of several REEs may overlap in steady-state laser-induced PL spectra; and (iii) crystal-field splitting of REE luminescence transitions depends on the local structural environments of the REE cations. The latter may cause varying numbers and exact positions of sublevel bands for particular emissions of a REE, depending on its host mineral (see Lenz et al. 2013, and references therein).

One challenging task for luminescence studies was, and still is, the detection and correct assignment of REEs in different host minerals (Tarashchan, 1978; Waychunas and Tarashchan, 1995; Habermann et al., 1996; Baumer et al., 1997; Reisfeld et al., 1996; Gaft et al., 1999, 2001; Götze et al., 1999a, b; Blanc et al., 2000; Gorobets and Rogojine, 2001; Waychunas, 2002; Nasdala et al., 2004; Richter et al., 2004; Czaja et al. 2008). A comprehensive but perhaps still incomplete overview of mineral species showing REE photoluminescence was given by Gaft et al. (2005). In the past years, the application of time-resolved luminescence spectroscopy – that utilizes the different decay times of luminescence centres – has strongly improved the reliability and sensitivity in detecting REEs in minerals (e.g., Gaft et al., 2001; Gaft, 2003; Gaft et al., 2005). In spite of this progress, reliable interpretation of PL bands of unknown materials requires the availability of reference spectra obtained from synthetic analogues individually doped with the REE under consideration. For zircon, such investigations have been done already by Cesbron et al. (1995), Blanc et al. (2000), Gaft et al. (2000), Karali et al. (2000), Finch et al. (2004) and Friis et al. (2009).

Following the latter concept, this present study addresses PL artefacts in Raman spectra of the accessory minerals titanite, xenotime–(Y), monazite–(Ce), and zircon. This is done by comparing spectra of a series of natural samples with spectra of synthetic analogues doped with a single REE (with REE in the series Pr^{3+} to Tm^{3+}, except Pm^{3+} and Gd^{3+}). These REEs

are known to cause PL emissions in the visible to near infrared (NIR) range of the electromagnetic spectrum (Gaft et al., 2005). In the case of titanite, which is known to contain occasionally notable amounts of chromium (e.g., Higgens and Ribbe, 1976; Fleischer, 1978), synthetic Cr-doped $CaTiSiO_5$ was included in addition. The present paper aims at pointing the readers' attention to possible biases in the interpretation of Raman spectra of REE-containing accessories, but also at emphasizing opportunities of the use of REE-emission characteristics to identify REEs, and to characterize their host minerals/materials.

2. Samples and Experimental

2.1. Samples investigated

Samples investigated in this present study comprise first a suite of natural titanite, monazite–(Ce), xenotime–(Y), and zircon specimens. The latter are provided by collections of the Natural History Museum Vienna, Austria (NHM), the Institute of Mineralogy and Crystallography at the University of Vienna, and the authors. Second, synthetic analogues were produced and studied, either un-doped or doped with one individual REE or Cr (the latter only for titanite).

Natural titanite samples are from Schiedergraben, Felben valley, Hohe Tauern, Salzburg Austria (sample A), a typical alpine cleft-type mineralisation hosted in amphibolites which is well-known for large, greenish titanite crystals (Strasser, 1989); São Geraldo do Araguaia, Pará, Brazil (sample B); the Mt. Painter uranium mining district, Arkaroola region, North Flinders Ranges, Australia (sample C; details on geology may be found in Coats and Blissett, 1971); Gratton Renfrew Co., Ontario, Kanada (sample D), a skarn located in the extensively metamorphosed Grenville Province (e.g., Kennedy et al., 2010); and from the Saranovskii mine (Saranovskoe), Saranovskaya village (Sarany), Gornozavodskii area, Permskaya Oblast', Middle Urals, Russia (sample E), ultrabasic gabbroic to gabbronoritic intrusions in Precambrian schist and quartzite with chromite ore-bodies and diabas gangue with Cr-bearing titanite in voids (see details in Ivanov, 1979 and Voitovich, 1993).

Natural monazite–(Ce) samples are from Braban Farm, Namibia (sample Namon); Itambé, Brazil (sample GM2); and Madagascar (samples VL-1, F6, and Madmon). Detailed information on F6 was published by Fletcher et al. (2010), and Madmon has been described by Schulz et al. (2007). Results of a detailed study on that five monazite–(Ce) samples, including U–Th–Pb ages, Raman spectroscopic and electron probe micro-analysis (EPMA) data, have been published by Ruschel et al. (2010). In addition, a Nd^{3+} PL study of this suite of samples has been published by Lenz et al. (2013).

Natural xenotime–(Y) samples studied here originate from pegmatitic lenses in the Gföhl gneiss near Königsalm, Senftenberg, Waldviertel, Austria (sample A; for details see Niedermayr, 1969); a pegmatite near Novo Horizonte, Bahia,

Brazil (sample B); and a pegmatite near Brindletown, North Carolina, USA (sample "E4947", for details and further description see Talla et al., 2011).

Zircon samples are from an alkaline pegmatite from the Zomba-Malosa complex of the alkaline province in Malawi (sample A; NHM-sample N3848; see e.g., in Woolley and Jones, 1992; Soman et al., 2010 for geological details); gemstone placers in the Ratnapura district, Sri Lanka (samples M144 and N17, for details see Nasdala et al., 2004b); a pegmatoid near Pack, Packalpe, Styria, Austria (sample D; NHM-sample 6521; see locality description in Weiss, 1972); and two placer deposits in Chantanaburi (sample E) and Kanchanaburi (sample F), Thailand.

2.2. Details on sample synthesis

Synthetic monazite–(Ce) and xenotime–(Y) crystals were produced by a flux method using a slow-cooling route with $NaPO_3$ as flux material. Sodium polyphosphate was mixed with the reactants Y_2O_3 (for xenotime) or CeO_2 (for monazite) and one REE_2O_3 (REE = all lanthanoids from Pr to Tm, except Pm^{3+} and Gd). Mixtures were heated in covered platinum crucibles to a peak temperature of 1170 ℃, held for 2 hours and then slowly cooled to 600℃ at a rate of –1.5 ℃ per hour. The samples were left in the furnace to cool down slowly to room temperature. Single-crystals were recovered from the crucibles by dissolving the flux in distilled water, and dried in air. Crystal sizes range from 0.3 to 4 mm.

The sodium-tetraborate flux synthesis route by Mazdab (2009) was adopted to produce synthetic titanite single-crystals. Reducing the cooling rate to half of that proposed by Mazdab (2009) produced comparably large crystals up to 8 mm in size. The REE-doping of $CaTiSiO_5$ crystals was achieved by adding 1 mg of the respective REE_2O_3 oxide to the reactants. In case of Cr-doping, the molar ratio Ca/(Ti+Cr) was chosen to be 1:1. This prevented excess TiO_2 to crystallize as rutile. For sample recovery, the crucible contents were exposed to an aqueous HNO_3 solution (w = 0.2) for three days. The crystals along with the remainders of flux could then be extracted from the crucibles with moderate mechanical effort. More details on the titanite syntheses are reported elsewhere (Nasdala et al., 2014).

Synthesis of zircon crystals (up to 1.5 mm in size) was accomplished by a flux technique similar to that described by Cesbron et al. (1995) and Hanchar et al. (2001). In our synthesis route we combined the evaporation of the highly volatile MoO_3 with a rapid cooling rate. This allowed us to use an alkali-free mixture of 0.53 g ZrO_2, 0.26 g SiO_2 and 10 g MoO_3, thereby preventing the incorporation of Li^+ into the zircon crystals (compare Hanchar et al., 2001). To produce REE-doped $ZrSiO_4$ (REE = Pr to Tm, except Gd), a minor amount of REE_2O_3 was added without any additional charge-compensating chemical species. The temperature path consisted of heating the loosely capped Pt crucibles to 1100 ℃ at a rate of 216 ℃ per hour. Without any soaking interval, the temperature was then reduced to 700 ℃, at a rate of –26.5 ℃ per hour. Afterwards, the furnace was switched off but left closed, to allow samples to cool slowly to room temperature. Crystals were readily extracted from the crucibles (i.e.,

without the need to use any chemical reagents to dissolve the flux) by washing in distilled water and drying in air. Further details on the synthesis route may be found in Lenz et al. (2013).

For Raman, PL-emission spectroscopy (including hyperspectral PL mapping) and chemical analyses, single-crystals were embedded in epoxy, and polished mounts were produced. Polycrystalline, coarse-grained sample powders (ca. 100 mg each; grain size ca. 100–250 μm) were used for PL-excitation spectroscopy.

2.3. Analytical methods

Laser-induced photoluminescence and Raman measurements were carried out at room temperature using three dispersive single-stage spectrometers: a Horiba (Jobin Yvon) LabRam HR Evolution (473 nm, 532 nm, and 633 nm excitation; 600 grooves/mm grating), a Horiba (Jobin Yvon) LabRam HR800 (532 nm, 633 nm, and 785 nm excitation; 600 grooves/mm grating), and a Renishaw RM–1000 (514 nm excitation; 1200 grooves/mm grating). Laser energies were adjusted to about 3–20 mW at the sample surface. All three systems were equipped with a Si-based, Peltier-cooled charge-coupled device (CCD) detector. The two Horiba systems were operated in the confocal mode. Using an Olympus 100× objective (numerical aperture = 0.9), the lateral resolution was on the order of 1 μm, and the depth resolution (with the laser beam focused at the sample surface) was better than 3 μm. The spectral resolution was between 3 cm^{-1} (in the blue range) and 1.5 cm^{-1} (near infrared). The Renishaw system has a quasi-confocal arrangement of the beam path (a confocal slit combined with pixel binning on the CCD). A Leica 20× objective (numerical aperture = 0.4) was used. The spatial resolution is assessed as ca. 4 μm (lateral) and ca. 10–15 μm (depth), respectively. Wavenumber calibration was done using the Rayleigh line and Ne lamp emissions; the wavenumber accuracy was better than 0.5 cm^{-1}. Hyperspectral PL maps were obtained by means of the Horiba Evolution system, using a software-controlled x–y stage. The step width was 3 μm.

Photoluminescence excitation spectra were recorded using a Horiba Fluorolog 3 operated with a xenon lamp (450 W) and 1200 grooves/mm gratings in the excitation and the emission pathway. The spectral resolution was determined at ~1 nm. Wavelength calibration was done using xenon lamp emissions. A photon counting R928P photomultiplier (PMT) detector, operating in the 190 – 860 nm spectral range, was used.

Rare earth elements were determined by laser-ablation inductive-coupled plasma mass-spectrometry (LA–ICP–MS) at the NAWI Graz Central Lab for Water, Minerals and Rocks, University of Graz and Graz University of Technology. The material was ablated by using an ESI NWR 193 laser ablation unit equipped with a 193 nm excimer laser which was pulsed at 9 Hz, 75 μm spot size corresponding to an energy of ~7.8 Jcm^{-2} and then analysed with an Agilent 7500ce quadrupole ICP–MS. Helium was used as carrier gas at ~0.6

l/min flow and data were acquired in time-resolved mode. For each analysis a 30 second gas blank was obtained for background correction, followed by 60 seconds of active laser and a wash out time of 45 seconds. The standard glass NIST610 (Jochum et al., 2011) was used for standardization and drift correction for zircon and titanite while the USGS phosphate standard MAPS–4 was used for monazite and xenotime. The zircon reference standards 91500 (Wiedenbeck et al., 2004) and Plesovice (Sláma et al., 2008) as well as the NIST612 glass (Jochum et al., 2011) were analysed as unknowns to monitor the accuracy of the measurements. The standards could be reproduced within ±10% of the recommended values. Data reduction was performed using silicon as internal standard for zircon and titanite while phosphorus was used as internal standard for monazite and xenotime.

The P_2O_5 concentration in monazite–(Ce) and xenotime–(Y) as well as selected REEs were determined by electron microprobe analysis (EMPA) at the Eugen F. Stumpfl — Electron Microprobe Laboratory, UZAG (University of Graz, Graz University of Technology and University of Leoben). Analytical conditions were 15 kV accelerating high voltage, 10 nA probe current on PCD. Natural REE phosphates, a natural monazite as well as a REE-doped silicate glass were used as calibration standards. Peak and backgrounds were carefully set to avoid any line overlap.

3. Results & Discussion

3.1. Titanite – $CaTiSiO_5$

Results of LA–ICP–MS analysis of trace element concentrations in natural and synthetic titanite samples are quoted in Table 1. Chromium and REE concentrations vary appreciably among the natural samples investigated, depending on sample origin. Samples Tit-B, Tit-C, and Tit-D are characterised by relatively low Cr (< 100 ppm) and elevated REE concentrations (ranging from ca. 1,100 to 16,600 ppm). Titanite sample Tit-A, by contrast, yielded elevated Cr (ca. 160 – 1,930 ppm) and low REE concentrations (<200 ppm); and sample Tit-E was found to be rich in both, Cr and REE (see Table 1). Chromium and other metals, such as Nb, Ta, V, Mn, Mg, Sn, Al, and Fe, are generally considered to be incorporated at the six-fold coordinated Ti-site (Higgens and Ribbe, 1976; Fleischer, 1978), whereas REEs substitute Ca on its large, seven-coordinated site (Hughes et al., 1997). Charge-balance of trivalent REE within the titanite structure is explained by a coupled substitution with Al and Fe (e.g., Che et al., 2013):
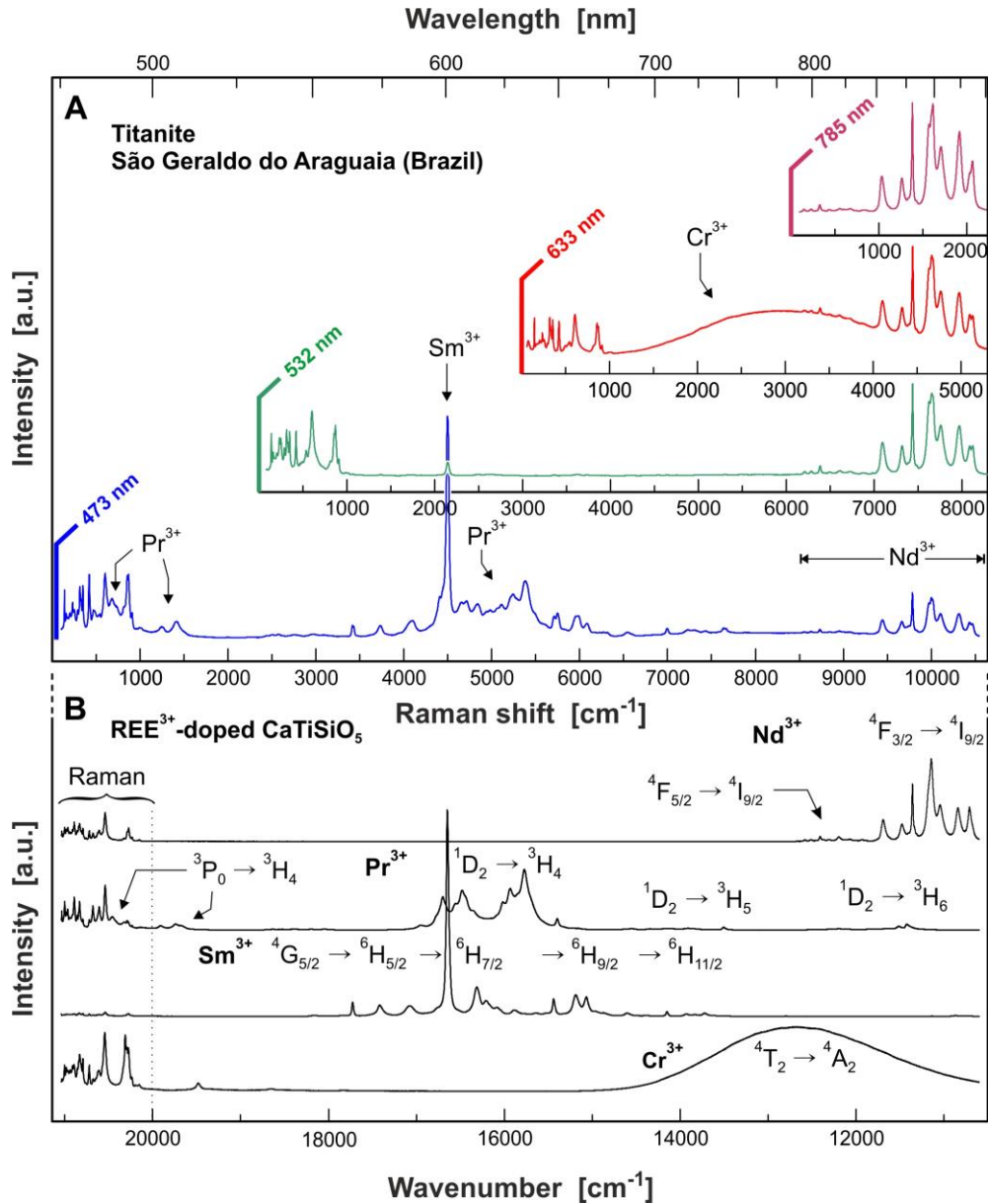
$$Ca^{2+} + Ti^{4+} = REE^{3+} + (Al, Fe)^{3+} \qquad (1)$$
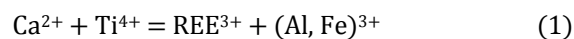
Fig. 1 Raman spectra of titanite from São Geraldo do Araguaia (Brazil) obtained using four different laser excitation-wavelengths (473, 532.1, 632.8, and 785 nm) (**A**) in comparison with laser induced PL spectra (λ_{exc} = 473 nm) of synthetic $CaTiSiO_5$ individually doped with Nd^{3+}, Pr^{3+}, Sm^{3+}, and Cr^{3+} (**B**). As in all following plots, spectra are shown with vertical offset for clarity. Note that all spectra are plotted on the same absolute scale (wavenumber / wavelength); emission lines are hence directly comparable. In subfigure A, individual x-axes are implemented for each individual laser excitation. Assignments of REE^{3+} electronic transitions and Russel-Saunders terms in this figure, and in Figs. 3–6 below, have been extracted from `Dieke´ energy-level diagrams (e.g., Dieke and Crosswhite, 1963; Carnall et al., 1968; Reisfeld and Jørgensen 1977).

Figure 1A shows Raman spectra of sample Tit-B from São Geraldo do Araguaia (Brazil). Spectra were obtained from the same focal spot using four different laser excitation- wavelengths (473, 532, 633, and 785 nm). Photoluminescence spectra of synthetic REE-doped $CaTiSiO_5$ are plotted in Fig. 1B for direct comparison. Narrow-band PL emissions caused by Nd^{3+}, Pr^{3+}, Sm^{3+}, and a broad-band emission of Cr^{3+} (cf. Gaft et al., 2003), predominantly affect Raman spectra of the natural samples investigated (cf. Fig. 1A).

Relative emission intensities of individual REEs depend strongly on the excitation wavelength. The Raman spectra of titanite sample Tit-B obtained using a 473 nm laser-excitation shows emissions of Pr^{3+}, Sm^{3+}, and Nd^{3+}, whereas green excitation (532 nm) excites preferentially the PL of Sm^{3+} and Nd^{3+}, red excitation (633 nm) predominantly Cr^{3+} and Nd^{3+}, and NIR excitation (785 nm) Nd^{3+} only. Spectra obtained with different excitations from the very same micro-area may hence show vast differences in relative intensities of
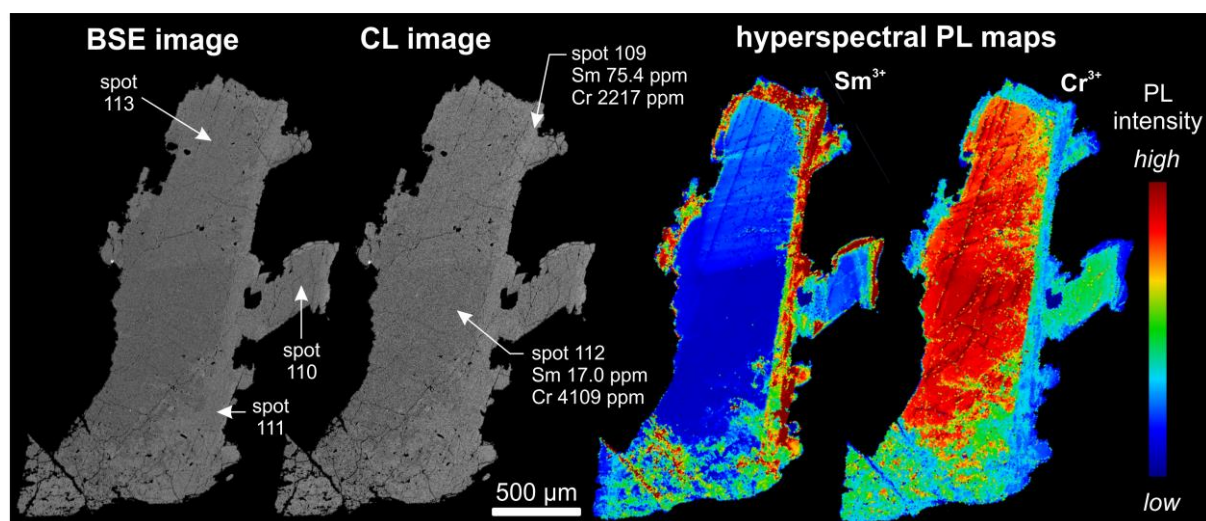
Fig. 2 Series of BSE image, panchromatic CL image, and two hyperspectral PL maps of a chromian titanite from Sarani (Ural Mts., Russia; sample E). The PL maps show colour-coded the intensity of the narrow ~600 nm Sm^{3+} band ($^4G_{5/2} \rightarrow {}^6H_{7/2}$ transition) and the ~ 780 nm Cr^{3+} peak ($^4T_2 \rightarrow {}^4A_2$ broad-band emission), respectively. Locations of the five LA–ICP–MS analysis spots (cf. Table 1) are marked with arrows.

individual REE emissions. These differences are due to strongly energy-dependent excitation efficiencies of various luminescence centres. The latter is supported by Fig. S1 (supplementary materials), which shows PL excitation spectra of a range of synthetic $CaTiSiO_5$ samples doped with different REEs. An overlap of the laser photon-energy with absorption levels of the respective REEs (i.e, preferred excitation or "pumping" of these levels) may result in enhanced luminescence emission. Different absorption levels of Pr^{3+}, Nd^{3+}, and Sm^{3+}, may hence be excited with varying efficiency using different laser excitation-wavelengths (cf. Fig. S1).

Emissions of Nd^{3+} in titanite (between ca. 12,500 and 10,500 cm^{-1}, see Fig. 1) were detected with all laser excitations used in the present study. Under 785 nm excitation, however, Nd^{3+} emissions are exceptionally strong (whereas Raman scattering is weaker under NIR excitation when compared to visible excitation). Therefore, Raman spectra of titanite samples obtained with IR excitation typically are obscured vastly by Nd^{3+} emissions (compare also NIR reference spectra of the RRUFF™ database; Downs, 2006; http://rruff.info/titanite). Another example for Raman spectra being affected by REE emissions may be found in the Romanian Database of Raman Spectroscopy (RDRS; Buzgar et al., 2009). Their titanite spectrum (obtained with green laser excitation) is affected by notable Sm^{3+} photoluminescence (cf. Fig. 1).

Relative emission intensities of individual REEs depend also on REE concentrations present, that is, on the specific geochemical composition of the sample analysed. Titanite sample Tit-A is characterized by exceptionally low REE concentrations and comparably high concentrations of Cr (see Table 1). As a result, PL

spectra of this sample are dominated by the PL of Cr^{3+} only, whereas titanite samples that contain elevated amounts of REEs are dominated by emissions of REE^{3+} (e.g., samples Tit-C and Tit-D, Table 1), or both the emissions of Cr^{3+} and REE^{3+} (sample Tit-E; spectra not shown). Note, however, that very high Cr contents may potentially quench emissions of the REE^{3+}, which has been observed for synthetic, Cr-doped titanite pigments (Nasdala et al., 2014).

Figure 2 presents BSE and CL images of a Cr-bearing titanite sample from Sarany (Ural Mts., Russia; cf. sample Tit-E) in comparison with hyperspectral PL maps. Colour-coded PL maps were produced using the intensity of two different PL centres (Sm^{3+} and Cr^{3+}) as mapping parameters. The emission intensities of Sm^{3+} and Cr^{3+} vary in dependence on their concentrations, respectively. High Sm^{3+} PL intensity is accompanied by elevated Sm concentrations (compare spot 109 in Fig. 2 and Table 2) and high Cr concentrations result in increased Cr^{3+} PL intensities (compare spot 112 in Fig. 2 and Table 2), and vice versa. Note that PL intensities of Sm^{3+} and Cr^{3+} are inversely correlated. This is due to inverse concentrations of these trace elements. The large central interior region has higher Cr than Sm concentrations and, correspondingly, the PL spectrum is dominated by the Cr^{3+}-related broad-band emission. The opposite (i.e., low Cr and high Sm concentration and Sm-dominated PL emission) was observed for the sample's outer area. The latter may indicate a possible alteration or replacement reaction rim (see also the Sm^{3+} PL intensity increase and Cr^{3+} decrease along large internal fractures, particularly recognisable near the bottoms of the PL maps).

3.2. Monazite–(Ce) and xenotime–(Y)

Results of chemical analyses of natural monazite–(Ce) samples investigated in the present study (samples F6, GM2, Mad, Nam and VK-1) were published elsewhere (cf. Table 3 of Ruschel et al., 2010). These five natural samples were found to be homogeneous in terms of chemical composition. They are characterised by generally high concentrations of light rare-earth elements (LREE) – especially of Nd_2O_3 (7.9 - 15.3 wt.%), Sm_2O_3 (1.2 – 5.0 wt.%), Pr_2O_3 (2.5 – 3.8 wt.%) – and variable concentrations of ThO_2 (6.6 – 14.2 wt.%). Both the REE_2O_3 and ThO_2 concentrations are fairly homogeneous on a scale within individual samples but vary appreciably among samples.

Chemical compositions of synthetic $CePO_4$ samples individually doped with Sm, Nd, or Pr, are quoted in Table 2. Concentrations of the respective intended dopant (REE concentrations in the range 0.3–1.5 wt.%) is always clearly higher than concentrations of all other trace REE, with the latter being assigned to impurities in the chemical reagents.

Results of chemical analyses of natural xenotime–(Y) and synthetic YPO_4 samples investigated in this present study are quoted in Table 2, also. Synthetic YPO_4 crystals have dopant concentrations (ranging from 1.5 to 9.0 wt.%) that are appreciably higher than concentrations of all other REEs. Natural xenotime–(Y) samples contain variable amounts of UO_2 and ThO_2 (up to 5.47 wt.% UO_2 in sample Xen-C) and comparably high amounts of HREEs (i.e., Gd, Dy, Ho, Er, and Yb). The preferential incorporation of HREEs in xenotime–(Y) and tetragonal YPO_4, respectively, is assigned to the fact that the $REEO_8$ polyhedron in this mineral structure favours the incorporation of the (smaller) heavy rare-earth elements (HREE: Tb–Lu; Ni et al., 1995).

Figure 3 shows two Raman spectra of a monazite–(Ce) sample from Itambé, Brazil (sample GM2), which are both heavily affected by the PL of REE^{3+} (see Raman reference-spectrum of undoped $CePO_4$ in Fig. 3 for comparison). Typical Raman modes of monazite-type compounds have for instance been discussed by Begun et al. (1981) and Silva et al. (2006). Note that spectra obtained using different lasers are plotted on a relative scale, attaining Raman shifts to be directly comparable. Spectra of REE-doped synthetic $CePO_4$ crystals are shown for comparison. Note that PL emissions of Pr^{3+} and Nd^{3+} strongly mask the Raman signal in the fingerprint spectral range 100–1100 cm^{-1} as observed using blue (473 nm) or NIR laser (785 nm). Similar to titanite, Raman spectra of monazite–(Ce) obtained with NIR laser excitation are typically obscured by the PL of Nd^{3+}. An example is shown in Fig.

3; more examples can be found in the RRUFF™ database (Downs, 2006; http://rruff.info/monazite) where all NIR-excitation spectra of monazite–(Ce) are affected strongly by Nd emission bands. This artefact is assigned to (i) generally high Nd concentrations in natural monazite–(Ce) samples, and (ii) particularly effective excitation of the $^4F_{3/2} \rightarrow {}^4I_{9/2}$ emission by NIR laser light (cf. Fig. S1, supplementary materials).

Comparison of the emission patterns of Nd^{3+} in monazite–(Ce) and titanite exemplifies that a certain REE may result in very different numbers and positions of PL sublevel bands, depending on its host lattice. The principal emission, as well as excitation levels of REE^{3+} (see Fig. S1), appear at similar spectral regions in different host materials; however the crystal-field splitting of the transitions depends strongly on the local crystallographic environment of the REE (compare spectra of various REE^{3+}, i.e., Pr^{3+}, Nd^{3+}, and Sm^{3+} in the monazite–(Ce) vs. titanite structure; Fig. S1).

Raman spectra of a xenotime–(Y) sample from Novo Horizonte (Bahia, Brazil; sample Xen-B in Table 2) are presented in Fig. 4. For Raman band assignments of un-doped synthetic xenotime–(Y) see Giarola et al. (2011); cf. also reference Raman spectrum in Fig. 4. This

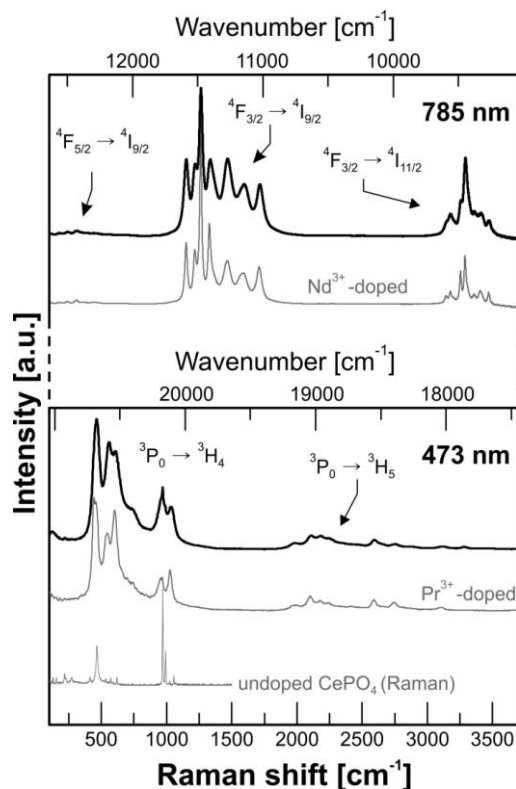**Fig. 3** Raman spectra of monazite–(Ce) from Itambé, Brazil (sample Gm2; bold black graphs) and synthetic $CePO_4$ single crystals (un-doped, Nd^{3+}-doped, and Pr^{3+}-doped; grey graphs). Spectra were obtained using 785 nm (top) and 473 nm laser excitation (bottom). Absolute wavenumbers corresponding to Raman shifts for the particular excitation are shown at the respective top abscissa axis.
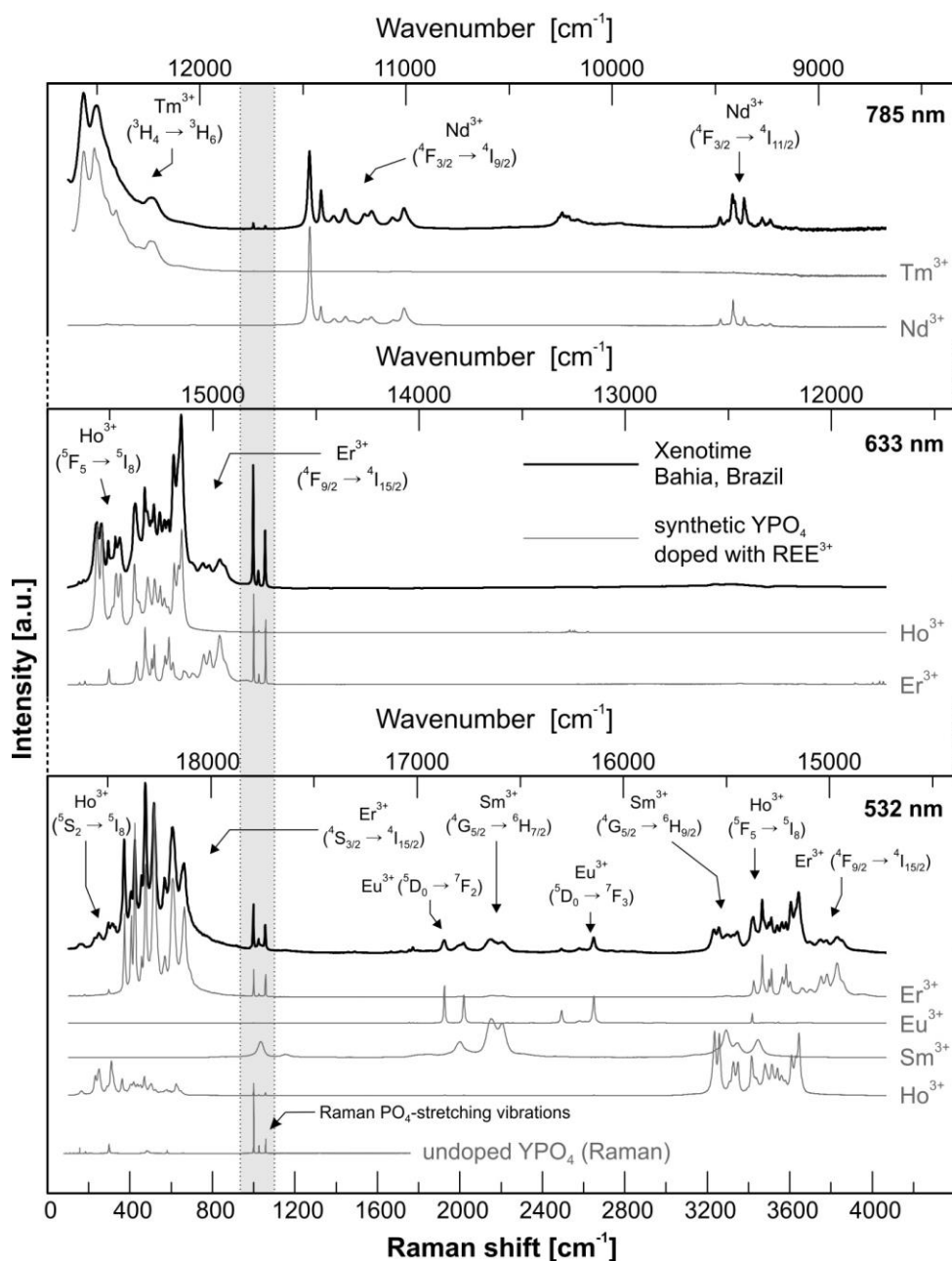
Fig. 4 Raman spectra of xenotime–(Y) from Novo Horizonte (Bahia, Brazil; sample Xen-B) obtained using three different excitation wavelengths (473, 532.1, and 785 nm), shown in comparison with spectra of synthetic REE-doped YPO₄. The Raman-shift region of PO₄ stretching bands is highlighted with a grey bar.

figure shows that, virtually independent of the excitation, the PL of various REE^{3+} centres heavily obscures the Raman signal of the natural xenotime–(Y) sample. The $^5S_2 \rightarrow {}^5I_8$ transition of Ho^{3+} and the $^4S_{3/2} \rightarrow {}^5I_{15/2}$ transition of Er^{3+} superimpose the Raman signal obtained with a 532 nm laser within the spectral range 100–1200 cm^{-1}, and the $^5F_5 \rightarrow {}^5I_8$ transition of Ho^{3+} and the $^4F_{9/2} \rightarrow {}^5I_{15/2}$ transition of Er^{3+} obscure the fingerprint spectral-range of the spectrum obtained under 633 nm excitation. The very same Er^{3+}-related PL is observed in the 532 nm-excitation spectrum at about 3000–4000 cm^{-1}; here it may fake high-shift Raman

signals. The emissions of Ho^{3+} and Er^{3+} are common PL-related artefacts in Raman spectra of natural xenotime-group samples (cf. RRUFF™ database: Downs, 2006; cf. also xenotime spectrum in the Raman database of the Department of Physics and Earth Sciences, University of Parma: https://www.fis.unipr.it/phevix/ramandb.php). Moreover, PL emissions of Sm^{3+} and Eu^{3+} appear between 1300 and 3000 cm^{-1} Raman shift in spectra obtained with 532 nm excitation (Fig. 4). Raman spectra obtained with NIR excitation are heavily affected by Tm^{3+} and Nd^{3+} (cf. 785 nm spectrum in Fig. 4; and NIR reference spectra from the RRUFF™ database). The

excitation efficiency of variable REE centres depends strongly on the excitation wavelength used. This is further demonstrated by PL excitation measurements of selected synthetic YPO_4 mono-doped with REE^{3+} (see Fig. S2; supplementary materials).

Photoluminescence spectra of the natural monazite–(Ce) and xenotime–(Y) samples investigated in the present study are remarkably uniform in terms of their REE^{3+} emission patterns (in contrast to titanite, and zircon discussed below, where appreciable variations among emissions of REEs are observed). Spectra were however found to differ in band widths and absolute intensities of the overall REE emission patterns. The band widths of individual PL bands may be strongly affected by structural disorder, which is reminiscent of the structurally related FWHMs of Raman bands. Note that FWHMs of PL bands increase (and intensities decrease) with increasing structural perturbation as caused by (1) increasing compositional heterogeneity due to the incorporation of heterovalent elements (Ruschel et al., 2010; Lenz et al., 2013) and (2) increasing structural damage accumulated upon self-irradiation due to the incorporation of the radioactive elements Th and U (Nasdala et al., 1995, 2013).

3.3. Zircon

Trace-element concentrations of natural zircon samples and synthetic REE-doped $ZrSiO_4$ determined by LA–ICP–MS analysis are presented in Table 3. Especially the concentrations of the actinides U^{4+} and Th^{4+} were found to vary appreciably (U, 39–7060 ppm; Th, <0.01–663 ppm). These actinide elements substitute for Zr^{4+} in dodecahedral coordination (D_{2d}; Finch et al., 2001). The substitution of (mainly heavy) REE into the structure has been explained primarily by the coupled, xenotime-type substitution (e.g., Hanchar et al., 2001):

$$(REE^{3+}, Y^{3+}) + P^{5+} \rightarrow Zr^{4+} + Si^{4+} \qquad (1)$$
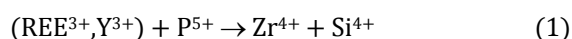
The effect of REE-related PL on Raman spectra of zircon is shown in Fig. 5, for the example of a natural zircon sample from Kanchaburi, Thailand (sample Zir-F). Spectra of synthetic, REE-doped $ZrSiO_4$ crystals are presented for direct comparison. Descriptions of the Raman spectrum of pure zircon (cf. Raman reference-spectrum not affected by REE-PL in Fig. 5) were published for instance by Dawson et al. (1971) and Syme et al. (1977). Similar to xenotime–(Y), Raman spectra of zircon may be obscured strongly by emissions of Tm^{3+} and Nd^{3+} if spectra were recorded using 785 nm laser-excitation. Emissions of Er^{3+} typically interfere with Raman spectra obtained with green excitation (Fig.
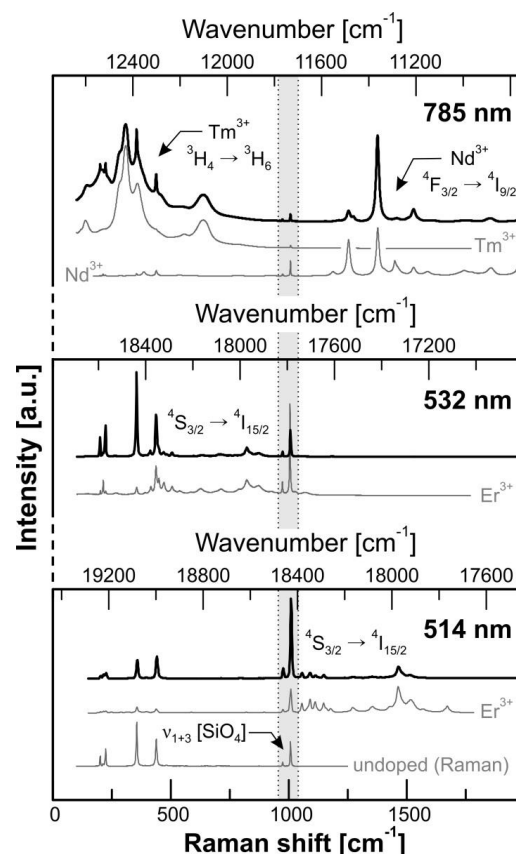
Fig. 5 Raman spectra of zircon from Kanchanaburi, Thailand (bold black graphs; sample A) and synthetic, un-doped and REE-doped $ZrSiO_4$ single crystals (grey graphs). Spectra were obtained using 785 nm, 532.1 nm, and 514.5 nm excitation. The Raman-shift region of SiO_4 stretching bands is highlighted with a grey bar.

5). Note that in the 532 nm excitation and 514 nm excitation spectra shown in Fig. 5, the $^4S_{3/2} \rightarrow {}^4I_{15/2}$ transition of Er^{3+} is observed as group of bands at different relative Raman shifts, but is located at constant absolute wavenumber (see spectra's specific top axes in Fig. 5).

The potential complexity of effects of the sample's chemical composition and structural state on its REE emissions is demonstrated in Figure 6. Spectra of four natural zircon samples are presented (all obtained with 473 nm excitation); these samples show appreciable compositional differences (Table 3) and cover the range from mildly radiation-damaged to metamict. According to our PL observations, most natural zircon samples show an emission pattern similar to that shown in Fig. 6A. The spectrum of a zircon sample from Chantanaburi, Thailand (sample Zir-E) is dominated by Dy^{3+} whereas emissions of Sm^{3+} (for assignment compare the spectrum of the Sm-doped reference in Fig. 6C below) and other REEs are comparably weak. Here, the $^4F_{9/2} \rightarrow {}^6H_{15/2}$ transition of Dy^{3+} (ca. 480 nm wavelength) obscures vastly the Raman-fingerprint spectral range.

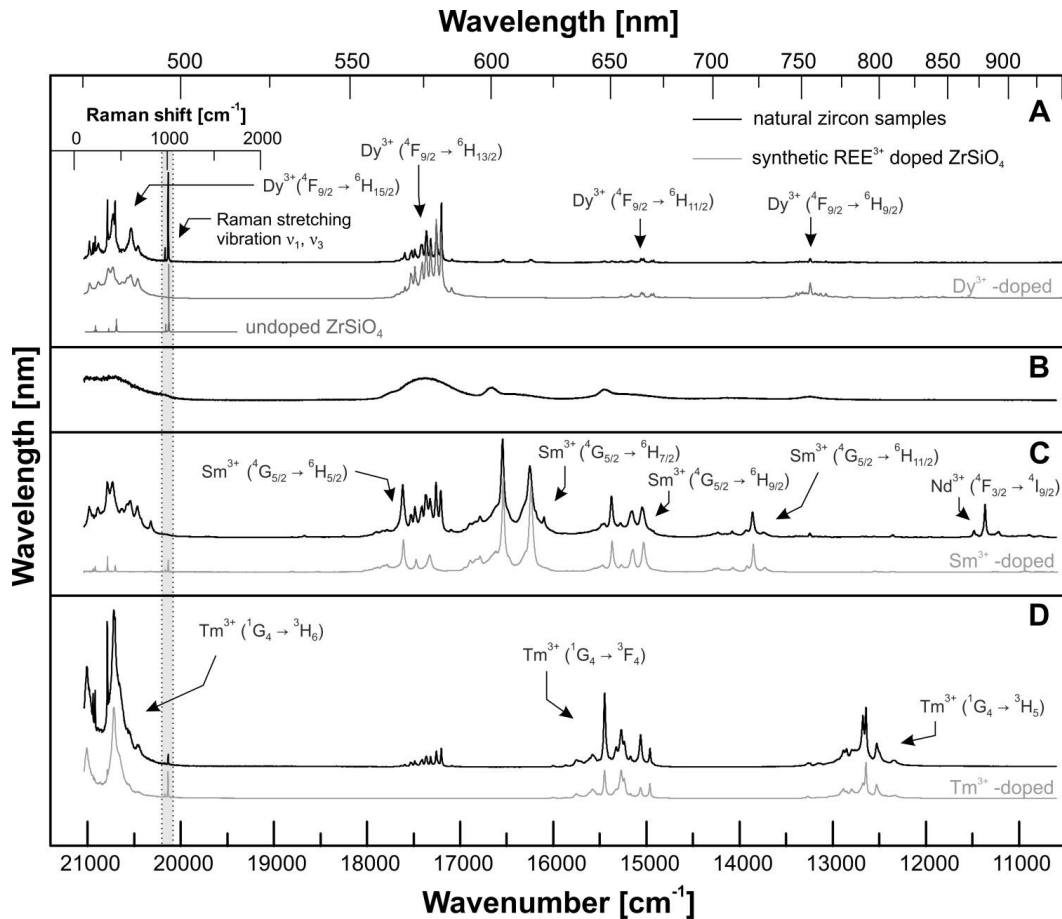**Fig. 6** Laser-induced PL spectra ($\lambda_{exc} = 473$ nm) of zircon samples from Chantanaburi, Thailand (**A**; sample E); Sri Lanka (**B**; sample M144), Mt. Malosa, Malawi (**C**; sample A), and Pack, Styria, Austria (**D**; sample D), shown in comparison with spectra of synthetic, un-doped and REE-doped ZrSiO₄ crystals. The Raman-shift region of SiO₄ stretching bands (see inset abscissa axis) is highlighted with a grey bar.

Figure 6B shows the PL spectrum of a metamict zircon sample from Sri Lanka (sample N17 in Table 3). This spectrum is characterised by electronic transitions of Dy^{3+} and Sm^{3+} as well, however emissions are observed as broad humps. In contrast to PL spectra of the other natural samples and the synthetic references in Fig. 6, REE emissions of sample N17 are not affected anymore by crystal-field splitting, which is due to this sample's amorphous state (see elevated U concentrations in Table 3; compare also X-ray and transmission electron microscopy results of Nasdala et al., 2002). The effect of amorphisation on the PL has been verified in an annealing experiment of Nasdala et al. (2004b). These authors observed that after recrystallization upon dry annealing of zircon N17, splitting of REE transitions into multitudes of Stark's levels was recovered. Recently, it has been demonstrated that emissions of Dy^{3+} and Nd^{3+} in zircon may be used for a luminescence-based spectroscopic quantification of accumulated structural radiation damage (discussed in Lenz et al., 2015).

Figures 6C and 6D demonstrate that deviations from the "common" REE composition may result in significantly different PL spectra that are not dominated by Dy^{3+} alone anymore (compare Fig. 6A). Photoluminescence spectra of zircon samples from the alkaline complex at Mt. Malosa, Malawi (sample A), show relatively intense emissions of Sm^{3+}, Dy^{3+}, and Nd^{3+} (Fig. 5C). This is explained by the fact that in this zircon sample, which contains generally high amounts of REE, the LREE concentrations are higher than that of the HREE (cf. Table 3). The rather untypical PL pattern may hence be considered to reflect the unusual trace-element composition of this sample (for details on the geological setting of the Mt. Malosa alkaline complex see Woolley and Jones, 1992; Soman et al., 2010). Another unusual example is shown in Fig. 5D. This zircon from Pack, Austria (sample Zir–D), is characterised by comparably low concentrations of LREE, Dy, and Ho, whereas it is enriched in the HREEs Er to Lu (cf. Table 3). The PL spectrum is dominated by emissions of Tm^{3+} whereas emissions of Dy^{3+} are of minor intensity. Note that this sample also contains notable amounts of Yb^{3+} and Lu^{3+}, however these REEs are known to have no PL emissions in the visible range (e.g., Reisfeld and Jørgensen 1977), and Er^{3+} is more effectively excited

with 488 nm (Nasdala et al. 2008) or green lasers (cf. Fig. 5, and REE-PL excitation spectra published in Friis et al., 2010).

Both the possible disturbance of Raman spectra by REE emissions and the powerfulness of PL mapping for revealing zoning and other internal heterogeneity, are demonstrated in Fig. 7 by presenting analytical results obtained from a zircon single-crystal from Kanchanaburi, Thailand (sample Zir-F). Figure 7A shows a series of BSE and CL images along with a PL map visualising the intensity distribution of Dy^{3+} emission ($^4F_{9/2} \rightarrow$ $^6H_{15/2}$). This emission overlaps with the Raman signal as shown in Fig. 7B (λ_{exc} = 473 nm). This is noteworthy, however, because Raman maps produced using the intensity of the $\nu_3[SiO_4]$ Raman band may show similar distribution patterns to that observed from neighbouring PL bands of Dy^{3+} (especially if no appropriate background correction is done in the data-reduction process). This may be due to intensity variances as caused by the low – but notable – underlying PL background, and not due to changes of Raman intensities (cf. Fig 7B).

Photoluminescence intensities of Dy^{3+} are very sensitive to minute changes in REE trace-element concentrations. The PL map reveals fine-scaled growth as well as sector zoning in two principal areas, an inner core surrounded by a secondary overgrowth (see Fig. 7A again). This is apparent from crosscut oscillatory-zoning textures, and from PL-intensity differences among both regions. The latter is due to small disparities in Dy concentration; the inner area is slightly enriched in REE and other heavy trace elements such as U and Th (compare bright area in BSE and analyses spots indicated in Fig. 7A). It has been reported that U and Th concentrations vary in close relation to the abundance of overall trace REEs in igneous and metamorphic zircon, and LREEs are predominatly enriched with the incorporation of Ca in alteration rims of zircon crystals (Wopenka et al., 1996; Hoskin and Schaltegger, 2003; Horie et al., 2006; Hoshino et al., 2010). Zircon crystals from metamorphic eclogite-facies rocks, for instance, are characterised by HREE-depleted metamorphic domains which are interpreted to grow with a concurrent formation of REE-consuming garnet
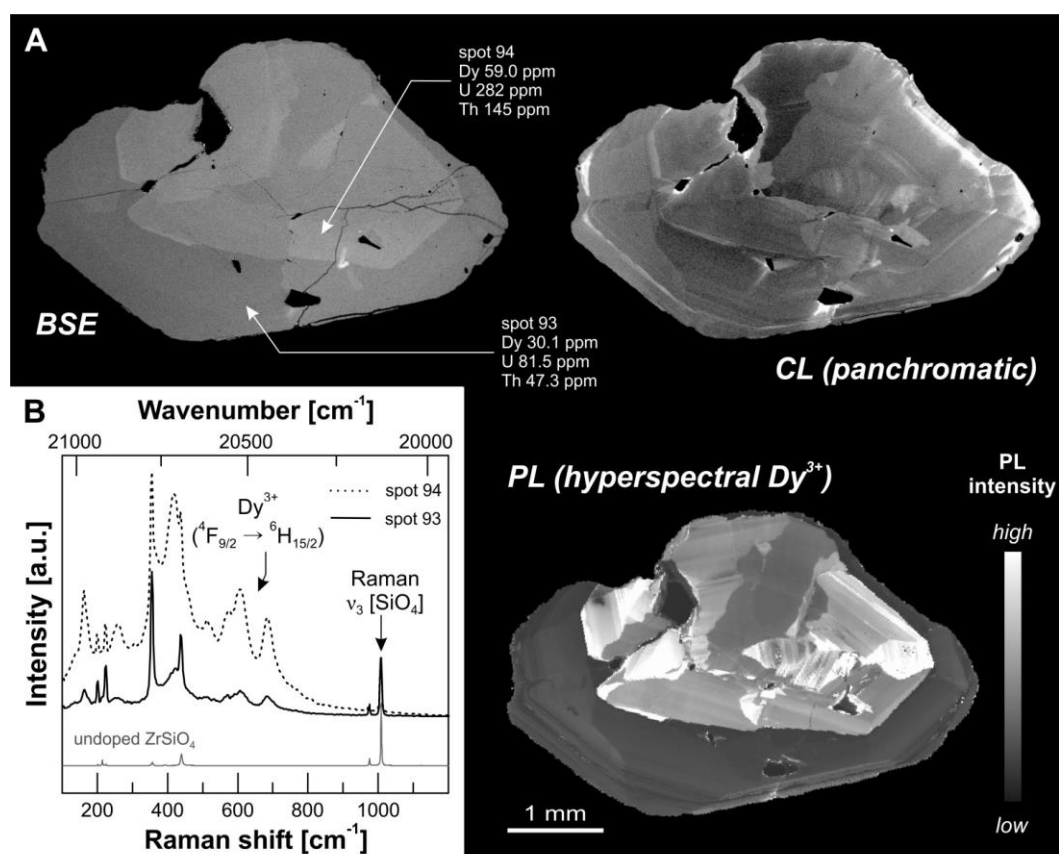
Fig. 7 Series of BSE image, CL image, and hyperspectral PL map (**A**) of a zircon sample from Kanchanaburi, Thailand (sample F). The hyperspectral PL map shows on a grayscale the intensity of the ~20,500 cm⁻¹ Dy^{3+} band ($^4F_{9/2} \rightarrow$ $^6H_{15/2}$ transition). Two spots that were subjected to Raman spectroscopy (λ_{exc} = 473 nm; **B**) and LA–ICP–MS analysis (cf. Table 4) are marked with arrows. Note that Raman bands and Dy^{3+} emissions are excited concomitantly. The latter partially mask the Raman spectrum of zircon (see reference spectrum of un-doped and hence non-luminescent $ZrSiO_4$ for comparison).

under sub-solidus conditions (Rubatto, 2002). Hence, REE distribution patterns as revealed by PL mapping may bear valuable geochemical information important for unravelling the geological history of such samples.

Note, however, that luminescence imaging or mapping is of semi-quantitative nature as luminescence intensity may strongly depend on further variables, such as quenching (Nasdala et al., 2014; Kempe and Götze, 2002) and sensitizing by other elements (e.g., Marfunin, 1979), effects of crystal orientation (e.g., Lenz et al., 2013) and the structural state/crystallinity, e.g. the accumulation of radiation damage due to the incorporation of radioactive U and Th (e.g., Lenz et al., 2015 and references therein). A potential (semi-)quantitative estimation of REE trace elements via luminescence intensity needs a broad range of carefully calibrated analytical conditions, e.g., standard material, system stability, system response, etc. (Barbarand and Pagel, 2001; Habermann, 2002; Richter et al., 2003; Edwards et al., 2007; MacRae et al., 2012, 2013). Xian et al. (2000), for instance, proposed to use absolute intensities of Raman spectral features of zircon to differentiate between rock types of mafic, granitic, and metamorphic origin. These features have been interpreted by Nasdala and Hanchar (2005) to result from PL emissions of trace Er^{3+} incorporated in zircon (cf. Fig. 5, $\lambda_{exc} = 514$ nm). As discussed above, the determination of absolute intensities is difficult, however, without any internal or external calibrations (see also discussion in Nasdala and Hanchar, 2005), but relative intensity variations of specific REE emissions may be visualized without instrumental biases using hyperspectral PL mapping. Spectra from multiple single measurement points were obtained under fairly identical measurement conditions and the crystal orientation remains constant relative to the incident laser if a single crystal is mapped.

4. Summary and conclusions

Steady-state laser-induced photoluminescence of REE^{3+} is a common analytical artefact in Raman spectroscopy of accessory minerals that contain trace amounts of REEs. Intensities of PL emissions in Raman spectra are mainly controlled by (i) the appearance and concentration of the respective PL centre in the sample (cf. Fig. 2) and (ii) the effectivity of the laser photon-energy used for its excitation, i.e., the quantum cross section of the laser and the absorption/excitation levels of the respective REE^{3+} (e.g., Fig. S1 and S2, supplementary materials). The latter is important in so far as specific REE emissions may appear alternatively in dependence of the excitation photon-energy used. If the laser excitation fits with REEs absorption levels, even minute amounts of trace REE may cause well-detectable, narrow PL bands which are potentially mistaken for Raman bands easily. In zircon, for instance, less than 1 ppm Nd (sample Zir-E + Zir-F in Table 3, spectrum shown in Fig. 5) is sufficient to detect measurable emission intensities of Nd^{3+} using a 785 nm laser. Near-infrared lasers were commonly applied to avoid luminescence artefacts due to their comparably low excitation photon-energy, but in particular emissions of Nd^{3+} are excited very effectively via its $^2F_{7/2}$ and $^2F_{5/2}$ absorption levels. We demonstrated that Nd^{3+} emissions strongly interfere with Raman bands in spectra of the four accessory minerals studied. Chen and Stimets (2014) found that the PL of Nd^{3+} ($\lambda_{exc} = 785$ nm) is very common for many other Ca-minerals as well.

In addition to effects of selective excitation as observed by using different laser photon energies, the chemical composition of accessory minerals may strongly affect the PL pattern obtained. Presented examples of titanite and zircon demonstrated that steady-state PL spectra substantially differ with respect to the samples trace-element composition. The relation of Cr to REE concentrations strongly affects the dominance of their emissions in spectra of titanite. The presence of specific REE emissions in PL patterns of zircon varies with relative depletion or enrichment of trace HREE and LREE, respectively (cf. Fig. 6A, C, D). In contrast, the REE-minerals monazite–(Ce) and xenotime–(Y) are characterised by high overall REE concentrations. Relative differences in their concentrations have only minor impact on the PL pattern. The PL spectra of monazite–(Ce) and xenotime–(Y) samples analysed have comparably uniform patterns with respect to the presence of the REE^{3+} emissions identified. They are more significantly affected by the structural disorder as caused by (i) increasing compositional heterogeneity due to the incorporation of heterovalent elements (Ruschel et al., 2010; Lenz et al., 2013) and (ii) increasing structural damage accumulated upon self-irradiation due to the incorporation of the radioactive elements Th and U (Nasdala et al., 2013).

Internal textures of single crystals (based on intensity differences of PL emissions) may be visualised using hyperspectral mapping. As for the example of titanite (from Sarany, Ural Mts., Russia), it was demonstrated that semi-quantitative element distributions of two different PL centres (i.e. Sm^{3+} and Cr^{3+}) were visualised using hyperspectral PL maps. Images obtained from BSE or panchromatic CL do not bear equivalent information (see Fig. 2). An example of

zircon demonstrated that PL intensity maps of REE[3+] may visualise the internal texture of zircon single-crystals (growth and sector zoning). Commonly, CL images are used to visualize internal textures of zircon (e.g., Vavra, 1990; Hanchar and Miller, 1993; Hanchar and Rudnick, 1995; Rakovan and Reeder, 1996; Götze, 2000, 2002; Hoskin and Black, 2000; Rubatto and Gebauer, 2000; Corfu et al., 2003; Götze et al., 2013). They provide valuable information on primary formation and post-growth history. Hyperspectral PL mapping (performed with "Raman" systems using motorized x–y stages) may be used complementary with the advantage to select specific luminescence centres being used as mapping parameter. The opportunity to excite more different PL centres by choosing alternative excitation lasers is advantageous in comparison to CL hyperspectral mapping techniques (cf., Edwards et al., 2007; MacRae, 2013). Figure 7A demonstrates that the hyperspectral PL map of Dy[3+] emission intensities in zircon is particular more sensitive to minute differences in element concentrations than equivalent panchromatic CL images; and is in particular more suited to unravel sector zoning of specific REEs, that is considered to be more common than generally detected (Watson and Liang, 1995).

Note, however, that luminescence imaging or mapping is of semi-quantitative character as the intensity of PL emissions may strongly depend on further variables such as quenching (described for titanite e.g., in Nasdala et al. 2014), sensitizing by other elements (e.g., Kempe and Götze, 2002; Marfunin, 1979) and effects of crystal orientation (e.g., Lenz et al., 2013; and references therein). Luminescence intensities of REE[3+] may also be affected by radiation damage as caused by radioactive decay of U and Th; especially in samples with high U and Th concentrations and elevated geologic ages (e.g., Seydoux-Guillaume et al., 2002; Panczer et al., 2012; Lenz et al., 2015).

Rather independent of the host crystal, emissions of particular REEs are recorded always in the same spectral range. Their fine-splitting however depends strongly on the host mineral, that is, the local structural environment of the REE[3+] ion (crystal-field dependent Stark's splitting; e.g., Burns, 1990). To give an example, appreciable variations of numbers and positions of individual bands related to the emission of Pr^{3+}, Nd^{3+}, and Sm^{3+} in $CaTiSiO_5$ and $CePO_4$ are shown in Fig. S1. This fact is advantageous insofar as knowledge of the fine-splitting in particular host minerals opens up the opportunity to use REE[3+] emissions, similar to Raman spectra, as fingerprint tool in mineral identification. For this, however, comprehensive PL-spectral databases are needed. Examples of quick mineral identification by

luminescence have already been proposed in igneous/metamorphic and sedimentary petrology (Richter et al., 2006, 2008), and gemmological (Bersani et al., 2012; Fritsch et al., 2012) and mineral provenance studies (Andò and Garzanti, 2014). Also, the availability of reliable, highly resolved reference PL spectra provides the opportunity to identify specific REE species in a specific host mineral, even in cases of mineral unknowns whose emissions consist of multiple, strongly interfering REE centres (see e.g., Fig. 3).

Note that not all REE[3+] species present in the samples studied here may have been identified in our spectra. This is because certain centres respond differently to different excitations. For instance, the emission of Sm dominates the 473 nm-spectrum of titanite sample Tit-B whereas this element is hardly detected in the 532 nm-spectrum of the very same sample (Fig. 1A). We therefore cannot exclude the possibility that laser excitations other than used in our study might excite further centres. Future studies addressing this question require systematic PL excitation-emission analysis of compositionally homogeneous, natural samples, similar to that shown, e.g., for selected REEs in synthetic titanite, monazite–(Ce), and xenotime–(Y) in Figs. S1 and S2. Photoluminescence excitation spectra of various REE[3+] species in synthetic zircon have been published by Friis et al. (2010).

Narrow laser-induced REE[3+] emission-bands in Raman spectra are quite easily recognized if they are recorded in spectral ranges that typically do not show Raman bands of minerals (e.g. 1600–2800 cm^{-1} or above 4000 cm^{-1}). Emissions in the Raman-shift range below 1600 cm^{-1}, or in the "hydroxyl stretching range" (ca. 3000–3800 cm^{-1}) are in contrast more easily mistaken as Raman signals. In general, confusion of PL bands with Raman bands may be avoided by performing multiple Raman analyses with different laser excitations. Raman bands must have uniform Raman-shifts in all Raman spectra. Luminescence emissions, in contrast, are characterized by particular photon energies and consequently certain absolute spectral positions; they hence must appear at different apparent Raman shifts (see e.g., Fig. 1 and discussion by Panczer et al., 2012). Nowadays there is a wide range of laser sources available to monitor Raman spectra at many different excitation wavelengths (e.g., Dubessy et al., 2012). To obtain unbiased results, one should attempt to find an excitation that causes least PL artefacts in the Raman spectrum. To provide an example, our Raman spectra of zircon and monazite–(Ce) obtained with 633 nm excitation (not shown) were unaffected by any REE[3+]-related PL in the Raman-fingerprint range.

We encourage operators of Raman systems to compare cautiously their spectra, especially if unknown or unusual "Raman bands" are evident, with published REE luminescence spectra and/or Raman spectra of synthetic analogues. The PL spectra shown in this paper, and further spectra of synthetic REE-doped titanite, monazite–(Ce), xenotime–(Y), and zircon, are available for download from the CSIRO luminescence database (http://www.csiro.au/luminescence).

Acknowledgments

References

Andò, S., Garzanti, E., 2014. Raman spectroscopy in heavy-mineral studies. Geological Society, London, Special Publications 386, p. 395–412.

Baumer, A., Blanc, P., Cesbron, F., Ohnenstetter, D., 1997. Cathodoluminescence of synthetic (doped with rare-earth elements) and natural anhydrites. Chem. Geol. 138, 73–80.

Barbarand, J., Pagel, M., 2001. Cathodoluminescence study of apatite crystals. Am. Mineral. 86, 473–484.

Begun, G. M., Beall, G. W., Boatner, L. A., Gregor, W. J., 1981. Raman spectra of the rare earth orthophosphates. J. Raman. Spectrosc. 11, 273–278.

Bernard, S., Benzerara, K., Beyssac, O., Menguy, N., Guyot, F., Brown Jr, G.E., Goffe, B., 2007. Exceptional preservation of fossil plant spores in high-pressure metamorphic rocks. Earth Planet. Sc. Lett. 262, 257–272.

Bernard, S., Beyssac, O., Benzerara, K., 2008. Raman mapping using advanced line-scanning systems: geological applications. Appl. Spectrosc. 62, 1180–1188.

Bersani, D., Lottici, P. P., 2010. Applications of Raman spectroscopy to gemology. Anal. Bional. Chem. 397, 2631–2646.

Bersani, D., Petriglieri, J. R., Andò, S. & Lottici, P. P., 2012. Identification of impurities in gemological materials by means of photoluminescence using micro-Raman apparatus. In GeoRaman Xth Meeting, June 2012, Nancy, France, p. 263–264.

Bersani, D., Azzi, G., Lambruschi, E., Barone, G., Mazzoleni, P., Raneri, S., Longobardo, U., Lottici, P. P., 2014. Characterization of emeralds by micro-Raman spectroscopy. J. Raman. Spectrosc. 45, 1293–1300.

Blacksberg, J., Rossman, G. R., Gleckler, A., 2010. Time-resolved Raman spectroscopy for in situ planetary mineralogy. Appl. Optics 49, 4951–4962.

Blanc, P., Baumer, A., Cesbron, F., Ohnenstetter, D., Panczer, G., Rémond, G., 2000. Systematic cathodoluminescence spectral analysis of synthetic doped minerals: anhydrite, apatite, calcite, fluorite, scheelite and zircon. In M. Pagel, V.

Barbin, P. Blanc, D. Ohnenstetter (Eds.), Cathodoluminescence in geosciences. Springer Berlin Heidelberg, p. 127-160.

Blasse, G., Grabmaier, B., 1994. Luminescence materials. 248 p., Springer Berlin.

Bozlee, B. J., Misra, A. K., Sharma, S. K., Ingram, M., 2005. Remote Raman and fluorescence studies of mineral samples. Spectrochim. Acta A 61, 2342–2348.

Burns, R.G., 1993. Mineralogical applications of crystal field theory. Cambridge Topics in Mineral Physics and Chemistry, 5, Cambridge University Press.

Buzgar, N., Apopei, A.I., Buzatu, A., 2009. Romanian Database of Raman Spectroscopy (http://rdrs.uaic.ro).

Carnall, W. T., Fields, P. R., Rajnak, K. 1968. Electronic energy levels in the trivalent lanthanide aquo ions. I. Pr^{3+}, Nd^{3+}, Pm^{3+}, Sm^{3+}, Dy^{3+}, Ho^{3+}, Er^{3+}, and Tm^{3+}. J. Chem. Phys. 49, 4424−4442.

Cesbron, F., Blanc, P., Ohnenstetter, D., Rémond, G., 1995. Cathodoluminescence of rare earth doped zircons. I. Their possible use as reference materials. Proceedings of the 13th Pfefferkorn Conference, Scanning Microscopy Suppl. 9, 35–56.

Chakhmouradian, A. R., 2004. Crystal chemistry and paragenesis of compositionally unique (Al-, Fe-, Nb-, and Zr-rich) titanite from Afrikanda, Russia. Am. Mineral. 89, 1752–1762.

Che, X. D., Linnen, R. L., Wang, R. C., Groat, L. A., Brand, A. A., 2013. Distribution of trace and rare earth elements in titanite from tungsten and molybdenum deposits in Yukon and British Columbia, Canada. Can. Mineral. 51, 415–438.

Chen, H., Stimets, R. W., 2014. Fluorescence of trivalent neodymium in various materials excited by a 785 nm laser. Am. Mineral. 99, 332–342.

Chen, J.Y., Schopf, J.W., Bottjer, D.J., Zhang, C.Y., Kudryavtsev, A.B., Tripathi, A.B., Wang, X.Q., Yang, Y.H., Gao, X. & Yang, Y., 2007. Raman spectra of a lower Cambrian ctenophore embryo from southwestern Shaanxi, China. Proceedings of the National Academy of Sciences of the United States of America 104, 6289–6292.

Czaja, M., Bodył, S., Głuchowski, P., Mazurak, Z., Strek, W., 2008. Luminescence properties of rare earth ions in fluorite, apatite and scheelite minerals. J. Alloy. Compd. 451, 290–292.

Coats, R. P., Blissett, A. H., 1971. Regional and economic geology of the Mount Painter province. Geological Survey of South Australia Bulletin, 43, Dept. of Mines, Geol. Survey of South Australia, 426 p.

Corfu, F., Hanchar, J.M., Hoskin, P.W.O., Kinny, P., 2003. Atlas of zircon textures. In J.M. Hanchar, P.W.O. Hoskin (Eds.), Zircon. Reviews in Mineralogy and Geochemistry, 53, Mineralogical Society of America, Chantilly, Virginia, p. 469–500.

Das, S., Hendry, M. J., 2011. Application of Raman spectroscopy to identify iron minerals commonly found in mine wastes. Chem. Geol. 290, 101–108.

Dawson, P., Hargreave, M. M., Wilkinson, G. R., 1971. The vibrational spectrum of zircon ($ZrSiO_4$). J. Phys. C. Solid. State. 4, 240.

Dieke, G. H., Crosswhite, H. M., 1963. The spectra of the doubly

and triply ionized rare earths. Appl. Optics 2, 675–686.

Dill, H. G., Weber, B., 2010. Accessory minerals of fluorite and their implication regarding the environment of formation (Nabburg–Wölsendorf fluorite district, SE Germany), with special reference to fetid fluorite ("Stinkspat"). Ore Geol. Rev. 37, 65–86.

Downs, R. T., 2006. The RRUFF Project: an integrated study of the chemistry, crystallography, Raman and infrared spectroscopy of minerals. Program and Abstracts of the 19th General Meeting of the International Mineralogical Association in Kobe, Japan. O03-13.

Dubessy, J., Caumon, M. C., Rull, F., Sharma, S., 2012. Instrumentation in Raman spectroscopy: elementary theory and practice. In J. Dubessy, M.-C. Caumon, F. Rull (Eds.), Raman spectroscopy applied to Earth sciences and cultural heritage, EMU Notes in Mineralogy, 12, European Mineralogical Union and Mineralogical Society of Great Britain and Ireland, London, p. 83–172.

Edwards, H. G. M., Newton, E. M., Russ, J., 2000. Raman spectroscopic analysis of pigments and substrata in prehistoric rock art. J. Mol. Struct. *550*, 245–256.

Edwards, P. R., Martin, R. W., Lee, M. R., 2007. Combined cathodoluminescence hyperspectral imaging and wavelength dispersive X-ray analysis of minerals. Am. Mineral. 92, 235–242.

Finch, R.J., Hanchar, J.M., Hoskin, P.W.O., Burns, P.C., 2001. Rare-earth elements in synthetic zircon: Part 2. A single-crystal X-ray study of xenotime substitution. Am. Mineral. 86, 681–689.

Finch, A.A., Garcia-Guinea, J., Hole, D.E., Townsend, P.D., Hanchar, J.M., 2004. Ionoluminescence of zircon: rare earth emissions and radiation damage. J. Phys. D. Appl. Phys. 37, 2795–2803.

Fletcher, I. R., McNaughton, N. J., Davis, W. J., Rasmussen, B., 2010. Matrix effects and calibration limitations in ion probe U–Pb and Th–Pb dating of monazite. Chem. Geol. 270, 31–44.

Friis, H., Finch, A. A., Williams, C. T., Hanchar, J. M., 2010. Photoluminescence of zircon (ZrSiO4) doped with REE[3+] (REE= Pr, Sm, Eu, Gd, Dy, Ho, Er). Phys. Chem. Miner. 37, 333–342.

Fleischer, M., 1978. Relation of the relative concentrations of lanthanides in titanite to type of host rocks. Am. Mineral. 63, 869–873.

Fritsch, E., Rondeau, B., Hainschwang, T., Karampelas, S., 2012. Raman spectroscopy applied to Gemmology. In J. Dubessy, M.-C. Caumon, F. Rull (Eds.), Raman spectroscopy applied to Earth Sciences and cultural heritage. EMU Notes in Mineralogy 12, European Mineralogical Union and Mineralogical Society of Great Britain and Ireland, London, p. 455-490.

Gaft, M., Reisfeld, R., Panczer, G., Uspensky, E., Varrel, B., Boulon, G., 1999. Luminescence of Pr[3+] in minerals. Opt. Mater. 13, 71–79.

Gaft, M., Panczer, G., Reisfeld, R., Shinno, I., 2000. Laser-induced luminescence of rare-earth elements in natural zircon. J. Alloy. Compd. 300, 267–274.

Gaft, M., Panczer, G., Reisfeld, R., Uspensky, E., 2001. Laser-induced time-resolved luminescence as a tool for rare-earth element identification in minerals. Phys. Chem. Miner. 28, 347–363.

Gaft, M., Nagli, L., Reisfeld, R., Panczer, G., 2003. Laser-induced time-resolved luminescence of natural titanite CaTiOSiO4. Opt. Mater. 24, 231–241.

Gaft, M., Reisfeld, R., Panczer, G., 2005. Modern luminescence spectroscopy of minerals and materials. Springer, 356 p.

Gee, A. R., O'Shea, D. C., Cummins, H. Z., 1966. Raman scattering and fluorescence in calcium fluoride. Solid State Commun. 4, 43–46.

Giarola, M., Sanson, A., Rahman, A., Mariotto, G., Bettinelli, M., Speghini, A., Cazzanelli, E., 2011. Vibrational dynamics of YPO4 and ScPO4 single crystals: An integrated study by polarized Raman spectroscopy and first-principles calculations. Phys. Rev. B 83, 224302.

Götze, J., Kempe, U., Habermann, D., Nasdala, L., Neuser, R. D., Richter, D. K., 1999a. High-resolution cathodoluminescence combined with SHRIMP ion probe measurements of detrital zircons. Mineral. Mag. 63, 179–179.

Götze, J., Habermann, D., Neuser, R. D., Richter, D. K., 1999b. High-resolution spectrometric analysis of rare earth elements-activated cathodoluminescence in feldspar minerals. Chem. Geol. 153, 81–91.

Götze, J. (2000) Cathodoluminescence microscopy and spectroscopy in applied mineralogy. Freiberger Forschungshefte C485, TU Bergakademie Freiberg, 128 p.

Götze, J. (2002) Potential of cathodoluminescence (CL) microscopy and spectroscopy for the analysis of minerals and materials. Anal. Bioanal. Chem. 374, 703–708.

Götze, J., Schertl, H. P., Neuser, R. D., Kempe, U., Hanchar, J. M., 2013. Optical microscope-cathodoluminescence (OM–CL) imaging as a powerful tool to reveal internal textures of minerals. Miner. Petrol. 107, 373–392.

Gorobets, B., & Rogojine, A. (2001) Luminescence spectra of minerals. Reference book. All-Russia Institute of Mineral Resources, Moscow, 300 p.

Habermann, D., Neuser, R. D., Richter, D. K., 1996. REE-activated cathodoluminescence of calcite and dolomite: high-resolution spectrometric analysis of CL emission (HRS-CL). Sediment. Geol. 101, 1–7.

Habermann, D., 2002. Quantitative cathodoluminescence (CL) spectroscopy of minerals: possibilities and limitations. Miner. Petrol. 76, 247–259.

Hanchar, J.M., Miller, C.F., 1993. Zircon zonation patterns as revealed by cathodoluminescence and backscattered electron images: implications for interpretation of complex crustal histories. Chem. Geol. 110, 1–13.

Hanchar, J.M., Rudnick, R.L., 1995. Revealing hidden structures: the application of cathodoluminescence and back-scattered electron imaging to dating zircons from lower crustal xenoliths. Lithos 36, 289–303.

Hanchar, J. M., Finch, R. J., Hoskin, P. W., Watson, E. B., Cherniak, D. J., Mariano, A. N., 2001. Rare earth elements in synthetic zircon: Part 1. Synthesis, and rare earth element and phosphorus doping. Am. Mineral. 86, 667–680.

Higgins, J. B., Ribbe, P. H., 1976. The crystal chemistry and space groups of natural and synthetic titanites. Am. Mineral. 61, 878–888.

Horie, K., Hidaka, H., Gauthier-Lafaye, F., 2006. Elemental distribution in zircon: Alteration and radiation-damage effects. Phys. Chem. Phys. Chem Earth 31, 587–592.

Hoshino, M., Kimata, M., Nishida, N., Shimizu, M., Akasaka, T., 2010. Crystal chemistry of zircon from granitic rocks, Japan: genetic implications of HREE, U and Th enrichment. Neues Jb. Miner. Abh. 187, 167–188.

Hoskin, P. W. O., Black, L. P., 2000. Metamorphic zircon formation by solid-state recrystallization of protolith igneous zircon. J. Metamorph. Geol. 18, 423–439.

Hoskin, P. W., Schaltegger, U., 2003. The composition of zircon and igneous and metamorphic petrogenesis. Reviews in Mineralogy and Geochemistry, 53, Mineralogical Society of America, Chantilly, Virginia, p. 27–62.

Hughes, J. M., Bloodaxe, E. S., Hanchar, J. M., & Foord, E. E. (1997). Incorporation of rare earth elements in titanite: Stabilization of the A2/a dimorph by creation of antiphase boundaries. Am. Mineral. 82, 512–516.

Ivanov, O. K. (1979): Chromium-containing sphene. *Zapiski Vsesoyuznogo Mineralogicheskogo Obshchestva 108*, 600–601 (in Russian).

Jochum, K.P., Weis, U., Stoll, B., Kuzmin, D., Yang, Q., Raczek, I., Jacob, D.E., Stracke, A., Birbaum, K., Frick, D.A., Günther, D., Enzweiler, J., 2011. Determination of reference values for NIST SRM 610–617 glasses following ISO guidelines. Geostand. Geoanal. Res. 35, 397–429.

Karali, T., Can, N., Townsend, P. D., Rowlands, A. P., Hanchar, J. M., 2000. Radioluminescence and thermoluminescence of rare earth element and phosphorus-doped zircon. Am. Mineral. 85, 668–681.

Kempe, U., Götze, J., 2002. Cathodoluminescence (CL) behaviour and crystal chemistry of apatite from rare-metal deposits. Miner. Mag. 66, 151–172.

Kennedy, A. K., Kamo, S. L., Nasdala, L., Timms, N. E., 2010. Grenville skarn titanite: potential reference material for SIMS U–Th–Pb analysis. Can. Mineral. 48, 1423–1443.

Korsakov, A. V., Vandenabeele, P., Theunissen, K., 2005. Discrimination of metamorphic diamond populations by Raman spectroscopy (Kokchetav, Kazakhstan). Spectrochim. Acta A 61, 2378–2385.

Lenz, C., Talla, D., Ruschel, K., Škoda, R., Götze, J., Nasdala, L., 2013. Factors affecting the Nd^{3+} (REE^{3+}) luminescence of minerals. Miner. Petrol. 107, 415–428.

Lenz, C. Nasdala, L., 2015. A photoluminescence study of REE^{3+} emissions in radiation damaged zircon. Am. Mineral. (in press).

Li, Z., Pasteris, J. D., Novack, D., 2013. Hypermineralized whale rostrum as the exemplar for bone mineral. Connect. Tissue Res. 54, 167–175

Marfunin, A.S. (1979). Spectroscopy, luminescence, and radiation centers in minerals, Springer, Berlin, Heidelberg, New York, 352 p.

MacRae, C. M., Wilson, N. C., Torpy, A., Davidson, C. J., 2012. Hyperspectral cathodoluminescence imaging and analysis extending from ultraviolet to near infrared. Microsc. Microanal. 18, 1239.

MacRae, C.M., Wilson, N.C., Torpy, A., 2013. Hyperspectral cathodoluminescence. Miner. Petrol. 107, 429–440.

Marschall, H.R., Korsakov, A.V., Luvizotto, G.L., Nasdala, L.,

Ludwig, T., 2009. On the occurrence and boron isotopic composition of tourmaline in (ultra)high-pressure metamorphic rocks. J. Geol. Soc. London 166, 811–823.

Mazdab, F. K. (2009). Characterization of flux-grown trace-element-doped titanite using the high-mass-resolution ion microprobe (SHRIMP–RG). Can. Mineral. 47, 813–831.

McCubbin, F. M., Steele, A., Nekvasil, H., Schnieders, A., Rose, T., Fries, M., Carpenter, P.K., Jolliff, B. L., 2010. Detection of structurally bound hydroxyl in fluorapatite from Apollo mare basalt 15058, 128 using TOF-SIMS. Am. Mineral. 95, 1141–1150.

Nasdala, L., Irmer, G., Wolf, D. (1995). The degree of metamictization in zircon: a Raman spectroscopic study. Eur. J. Mineral. 7, 471–478.

Nasdala, L., Smith, D.C., Kaindl, R., Ziemann, M., 2004a. Raman spectroscopy: Analytical perspectives in mineralogical research. In A. Beran and E. Libowitzky (Eds.), Spectroscopic methods in mineralogy, EMU Notes in Mineralogy, 6, European Mineralogical Union, p. 281–343.

Nasdala, L., Reiners, P. W., Garver, J. I., Kennedy, A. K., Stern, R. A., Balan, E., Wirth, R., 2004b. Incomplete retention of radiation damage in zircon from Sri Lanka. Am. Mineral. 89, 219–231.

Nasdala, L., Hanchar, J.M., 2005. Comment on: Application of Raman spectroscopy to distinguish metamorphic and igneous zircon (Xian et al., Anal. Lett. 2004, v. 37, p. 119). Anal. Lett. 38, 727–734.

Nasdala, L., Hofmeister, W., Norberg, N., Martinson, J. M., Corfu, F., Dörr, W., Kamo, S.L., Kennedy, A.K., Krons, A., Reiners, P.W., Frei, D., Kosler, J., Wan, Y., Götze, J., Häger, T., Kröner, A., Valley, J. W., 2008. Zircon M257 – a homogeneous natural reference material for the ion microprobe U-Pb Analysis of zircon. Geostand. Geonal. Res. 32, 247–265.

Nasdala, L., Beyssac, O., Schopf, J.W., Bleisteiner, B., 2012. Application of Raman-based images in the Earth sciences. In A. Zoubir (Ed.), Raman imaging – Techniques and applications, Springer Series in Optical Sciences, 168, Springer, Berlin, Heidelberg, p. 145–187.

Nasdala, L., Grambole, D., Ruschel, K., 2013. Review of effects of radiation damage on the luminescence emission of minerals, and the example of He-irradiated $CePO_4$. Miner. Petrol. 107, 441–454.

Nasdala, L., Stoyanova Lyubenova, T., Gaft, M., Wildner, M., Diegor, W., Petautschnig, C., Talla, D., Lenz, C., 2014. Photoluminescence of synthetic titanite-group pigments: A rare quenching effect. Chem. Erde-Geochem. 74, 419–424.

Ni, Y., Hughes, J. M., Mariano, A. N., 1995. Crystal chemistry of the monazite and xenotime structures. Am. Mineral. 80, 21–26.

Niedermayr, G. (1969): Der Pegmatit von der Köngsalm, Niederösterreich. Ann. Naturhistor. Mus. Wien 78, 49–54

Panczer, G., De Ligny, D., Mendoza, C., Gaft, M., Seydoux-Guillaume, A., Wang, X., 2012. Raman and fluorescence. In J. Dubessy, M.-C. Caumon, F. Rull (Eds.), Raman Spectroscopy applied to Earth sciences and cultural heritage. EMU Notes in Mineralogy 12, European Mineralogical Union, p. 61–82

Pasteris, J. D., Yoder, C. H., Wopenka, B., 2014. Molecular water in nominally unhydrated carbonated hydroxylapatite: The

key to a better understanding of bone mineral. Am. Mineral. 99, 16–27.

Rakovan, J., Reeder, R. J., 1996. Intracrystalline rare earth element distributions in apatite: Surface structural influences on incorporation during growth. Geochim Cosmochim Ac. 60, 4435-4445.

Reisfeld, R., Jørgensen, C. K., 1977. Chemical Bonding and Lanthanide Spectra. In R. Reisfeld and C.K. Jørgensen (Eds.) Lasers and Excited States of Rare Earths. Springer Berlin Heidelberg, p. 123–156.

Reisfeld, R., Gaft, M., Boulon, G., Panczer, C., Jørgensen, C. K., 1996. Laser-induced luminescence of rare-earth elements in natural fluor-apatites. J. Lumin. 69, 343–353.

Richter, D. K., Götte, T., Götze, J., Neuser, R. D., 2003. Progress in application of cathodoluminescence (CL) in sedimentary petrology. Miner Petrol 79, 127–166.

Richter, D. K., Gotte, T., Niggemann, S., Wurth, G., 2004. REE^{3+} and Mn^{2+} activated cathodoluminescence in lateglacial and holocene stalagmites of central europe: evidence for climatic processes?. Holocene 14, 759–768.

Richter, D. K., Krampitz, H., Görgen, P., Götte, T., Neuser, R. D., 2006. Xenotime in the lower buntsandstein of central europe: evidence from cathodoluminescence investigation. Sediment. Geol. 183, 261–268.

Richter, D. K., Görgen, P., Götte, T., 2008. Monazite cathodoluminescence – A new tool for heavy mineral analysis of siliciclastic sedimentary rocks. Sediment. Geol. 209, 36–41.

Ropret, P., Miliani, C., Centeno, S. A., Tavzes, Č., Rosi, F., 2010. Advances in Raman mapping of works of art. J. Raman Spectrosc. 41, 1462–1467.

Rubatto, D., Gebauer, D., 2000. Use of cathodoluminescence for U-Pb zircon dating by ion microprobe: some examples from the Western Alps. In M. Pagel, V. Barbin, P. Blanc, D. Ohnenstetter (Eds.), Cathodoluminescence in geosciences. Springer Berlin Heidelberg, p. 373–400.

Rubatto, D. (2002). Zircon trace element geochemistry: partitioning with garnet and the link between U–Pb ages and metamorphism. Chem. Geol. 184, 123–138.

Ruschel, K., Nasdala, L., Kronz, A., Hanchar, J. M., Többens, D. M., Škoda, R., Finger, F., Möller, A., 2012. A Raman spectroscopic study on the structural disorder of monazite–(Ce). Miner. Petrol. 105, 41–55.

Schopf, J. W., Kudryavtsev, A. B., Agresti, D. G., Wdowiak, T. J., Czaja, A. D., 2002. Laser–Raman imagery of Earth's earliest fossils. Nature 416, 73–76.

Schulz, B., Brätz, H., Bombach, K., Krenn, E., 2007. In situ Th-Pb dating of monazite by 266 nm laser ablation and ICP-MS with a single collector, and its control by EMP analysis. Z. geol. Wiss. Berlin 35, 377–392.

Seydoux-Guillaume, A. M., Wirth, R., Nasdala, L., Gottschalk, M., Montel, J. M., and Heinrich, W., 2002. An XRD, TEM and Raman study of experimentally annealed natural monazite. Phys. Chem. Miner. 29, 240–253.

Sharma, S. K., Lucey, P. G., Ghosh, M., Hubble, H. W., Horton, K. A., 2003. Stand-off Raman spectroscopic detection of minerals on planetary surfaces. Spectrochim. Acta A 59, 2391–2407.

Silva, E. N., Ayala, A. P., Guedes, I., Paschoal, C. W. A., Moreira, R. L., Loong, C. K., Boatner, L. A., 2006. Vibrational spectra of monazite-type rare-earth orthophosphates. Opt. Mater. 29, 224–230.

Sláma, J., Košler, J., Condon, D. J., Crowley, J. L., Gerdes, A., Hanchar, J. M., Horstwood, M.S.A., Morris, G.A., Nasdala, L., Norberg, N., Schaltegger, U., Schoene, B., Tubrett, M.N., Whitehouse, M. J., 2008. Plešovice zircon – a new natural reference material for U–Pb and Hf isotopic microanalysis. Chem. Geol. 249, 1–35.

Smith, D. C., 2006. A review of the non-destructive identification of diverse geomaterials in the cultural heritage using different configurations of Raman spectroscopy. Geological Society, London, Special Publications 257, 9–32.

Soman, A., Geisler, T., Tomaschek, F., Grange, M., Berndt, J., 2010. Alteration of crystalline zircon solid solutions: a case study on zircon from an alkaline pegmatite from Zomba–Malosa, Malawi. Contrib. Mineral. Petr. 160, 909–930.

Stähle, V., Altherr, R., Koch, M., Nasdala, L., 2008. Shock-induced growth and metastability of stishovite and coesite in lithic clasts from suevite of the Ries impact crater (Germany). Contrib. Mineral. Petr. 155, 457–472.

Strasser, A., 1989. Die Minerale Salzburgs. Author's publishing, Salzburg, Austria, 348 p.

Syme, R. W. G., Lockwood, D. J., Kerr, H. J., 1977. Raman spectrum of synthetic zircon ($ZrSiO_4$) and thorite ($ThSiO_4$). J. Phys. C 10, 1335.

Talla, D., Beran, A., Škoda, R., Losos, Z., 2011. On the presence of OH defects in the zircon-type phosphate mineral xenotime, $(Y,REE)PO_4$. Am. Mineral. 96, 1799–1808.

Tarashchan, A., 1978. Luminescence of minerals. Naukova Dumka, Kiev, 296 p.

Vandenabeele, P., Edwards, H. G., Moens, L., 2007. A decade of Raman spectroscopy in art and archaeology. Chem. Rev. 107, 675–686.

Van Es, H. J., Vainshtein, D. I., Rozendaal, A., Donoghue, J. F., De Meijer, R. J., Den Hartog, H. W., 2002. Thermoluminescence of $ZrSiO_4$ (zircon): A new dating method?. Nucl. Instrum. Meth. B 191, 649–652.

Vavra, G., 1990. On the kinematics of zircon growth and its petrogenetic significance: a cathodoluminescence study. Contrib. Mineral. Petr. 106, 90–99.

Vaz, J. E., Senftle, F. E., 1971. Thermoluminescence study of the natural radiation damage in zircon. J. Geophys. Res. 76, 2038–2050.

Voitovich, V. S., 1993. Genesis of the Sarany chromite deposit. Otechestvennaya Geologiya 1993, 32–37 (in Russian).

Waychunas, G. A., 2002. Apatite luminescence. Reviews in mineralogy and geochemistry, 48, Mineralogical Society of America, Chantilly, Virginia, p. 701–742.

Waychunas, G.A., Tarashchan, A., 1995. Luminescence of Minerals — Interpretation of the luminescence spectra in terms of band theory, crystal field theory, sensitization and quenching. Advanced Mineralogy 2, Springer-Verlag, p. 124–135.

Wang, A., Jolliff, B. L., Haskin, L. A., 1995. Raman spectroscopy as a method for mineral identification on lunar robotic exploration missions. J. Geophys. Res-Planet. 100, 21189–21199.

Wang, A., Kuebler, K., Jolliff, B., Haskin, L. A., 2004. Mineralogy of a Martian meteorite as determined by Raman spectroscopy. J. Raman Spectrosc. 35, 504–514.

Watson, E. B., Liang, Y., 1995. A simple model for sector zoning in slowly grown crystals: Implications for growth rate and lattice diffusion, with emphasis on accessory minerals in crustal rocks. Am. Mineral. 80, 1179–1187.

Weiss, A., 1972. Zirkonvorkommen im Raume Köflach-Pack. Mitteilungsblatt - Abteilung für Mineralogie am Landesmuseum Joanneum, 23–24.

Wiedenbeck, M., Hanchar, J. M., Peck, W. H., Sylvester, P., Valley, J., Whitehouse, M., Kronz, A., Morishita, Y., Nasdala, L., Fiebig, J., Franchi, I., Girard, J.-P., Greenwood, R.C., Hinton, R., Kita, N., Mason, P.R.D., Norman, M., Ogasawara, M., Piccoli, P.M., Rhede, D., Satoh, H., Schulz-Dobrick, B., Skår, O., Spicuzza, MJ., Terada, K., Tindle, A., Togashi, S., Vennemann, T., Xie, Q., Zheng, Y.F., 2004. Further characterisation of the 91500 zircon crystal. Geostand. Geoanal. Res. 28, 9–39.

Wopenka, B., Jolliff, B. L., Zinner, E., Kremser, D. T., 1996. Trace element zoning and incipient metamictization in a lunar zircon: application of three microprobe techniques. Am. Mineral. 81, 902–912.

Woolley, A. R., Jones, G. C., 1992. The alkaline/peralkaline syenite-granite complex of Zomba-Malosa, Malawi: mafic mineralogy and genesis. J. Afr Earth Sci. 14, 1–12.

Xian, W. S., Sun, M., Malpas, J., Zhao, G. C., Zhou, M. F., Ye, K., Liu, J. B., Phillips, D. L., 2004. Application of Raman spectroscopy to distinguish metamorphic and igneous zircons. Anal. Lett. 37, 119–130.

Yang, C., Homman, N. O., Johansson, L., Malmqvist, K. G., 1994. Microcharacterizing zircon mineral grain by ionoluminescence combined with PIXE. Nucl. Instrum. Meth. B 85, 808–814.

Zhang, M., Salje, E. K., Farnan, I., Graeme-Barber, A., Daniel, P., Ewing, R. C., Clark, A.M., Leroux, H., 2000. Metamictization of zircon: Raman spectroscopic study. J. Phys-Condens. Mat. 12, 1915.

Table 1. Chromium and REE concentrations of natural titanite samples and synthetic REE-doped $CaTiSiO_5$ as determined by LA–ICP–MS analysis.

| Sample | Tit-A | | | | | Tit-B | | | | Tit-C | | | Tit-D | | | Tit-E | | | | |
| Description | Schiedergraben, Felbertal, Salzburg, Austria | | | | | São Geraldo do Araguaia, Brazil | | | | Mt. Painter, Australia | | | Gratan, Ontario, Kanada | | | Sarany, Ural Mts., Russia | | | | |
Spot	124	125	126	127	128	120	121	122	123	117	118	119	114	115	116	109	110	111	112	113
Cr (ppm)	1930	1933	351	166	284	55.45	64.0	43.3	47.9	45.1	42.7	43.5	24.34	23	23.1	2217	3142	2407	4109	3906
Y (ppm)	373	335	128	15.9	50.44	190	202	361	193	10660	10980	10842	1549	1526	1524	343	192	586	52.5	148
La (ppm)	0.01	0.02	0.10	<0.01	<0.01	85.5	97.8	64.5	52.6	906	927	918	498	497	514	95.3	50.7	51.3	14.4	44.2
Ce (ppm)	0.16	0.21	0.21	0.02	0.05	449	476	410	333	5322	5436	5323	2286	2311	2392	538	292	338	95.9	255
Pr (ppm)	0.08	0.09	0.07	0.01	0.02	74.6	74.5	83.5	60.0	1064	1075	1090	381	381	392	74.3	40.64	67.3	15.8	39.2
Nd (ppm)	1.12	1.01	0.70	0.10	0.36	345	338	452	298	5496	5627	5685	1816	1802	1829	312	172	363	74.7	170
Sm (ppm)	2.40	2.45	1.38	0.23	0.62	75.4	75.5	129	73.4	1647	1703	1707	424	435	431	75.4	43.9	131	16.9	37.1
Eu (ppm)	1.24	1.12	0.94	0.15	0.51	41.3	35.6	59.9	41.9	134	137	140	86.6	91.3	87.7	61.8	36.2	81.0	13.0	27.5
Gd (ppm)	10.2	9.49	4.86	0.68	1.92	69.4	69.9	123	68.5	1679	1709	1737	354	370	355	83.2	47.7	145	15.7	38.0
Tb (ppm)	3.88	3.63	1.58	0.21	0.62	8.51	8.67	16.3	8.19	310	314	319	55.7	56.9	54.7	12.4	7.29	23.7	2.26	5.78
Dy (ppm)	46.5	42.8	16.7	2.21	6.36	42.6	44.3	85.2	42.2	2084	2089	2150	345	348	335	74.5	44.1	143	12.9	34.8
Ho (ppm)	13.8	12.7	4.77	0.56	1.74	7.14	7.37	14.0	7.13	402	413	416	65.8	64.9	63.1	13.2	7.59	23.5	2.17	6.13
Er (ppm)	52.0	47.2	17.1	1.89	6.33	17.7	18.5	34.4	17.8	1190	1224	1222	182	180	175.5	31.6	18.3	52.5	4.89	14.4
Tm (ppm)	7.89	7.17	2.62	0.30	0.94	2.17	2.29	4.10	2.20	171	176	175	23.8	23.7	22.8	3.66	2.04	5.79	0.54	1.65
Yb (ppm)	48.7	44.0	16.9	1.87	6.37	13.6	14.8	23.3	13.5	1076	1112	1113	133	135	131	19.3	11.0	28.2	2.82	8.63
Lu (ppm)	5.29	4.87	2.00	0.19	0.75	1.75	1.94	2.41	1.72	121	125	128	13.6	13.7	13.4	1.56	0.85	1.97	0.22	0.70
LREE (ppm)	15.2	14.4	8.26	1.18	3.48	1140	1167	1321	927	16247	16615	16599	5845	5886	6001	1240	683	1178	246	612
HREE (ppm)	178	162	61.6	7.23	23.11	93.4	97.9	180	92.8	5355	5453	5522	818	822	795	156	91.1	279	25.8	72.1
REE total (ppm)	193	177	69.9	8.41	26.59	1234	1265	1501	1020	21602	22068	22121	6664	6709	6797	1396	774	1456	272	684

Table 1 (continued).

Sample	Tit-Sm			Tit-Pr			Tit-Nd			Titn-Eu		
Description	synthetic Sm-doped CaTiSiO$_5$			synthetic Pr-doped CaTiSiO$_5$			synthetic Nd-doped CaTiSiO$_5$			synthetic Eu-doped CaTiSiO$_5$		
Spot	97	98	99	100	101	102	103	104	105	106	107	108
Cr (ppm)	1.56	1.76	1.39	6.97	6.05	6.15	2.23	2.30	2.50	3.31	3.25	3.46
Y (ppm)	0.31	0.36	0.38	23.6	22.3	23.0	0.10	0.06	0.07	0.44	0.41	0.42
La (ppm)	0.02	0.02	0.02	0.02	0.03	0.02	0.02	0.02	0.01	0.02	0.02	0.01
Ce (ppm)	0.03	0.04	0.03	0.58	0.07	0.08	0.05	0.03	0.03	0.05	0.06	0.04
Pr (ppm)	<0.01	<0.01	0.01	171	175	169	0.01	0.01	0.01	0.05	0.04	0.05
Nd (ppm)	0.05	0.02	0.03	1.18	0.69	0.63	306	205	204	0.08	0.06	0.07
Sm (ppm)	421	406	402	<0.03	<0.03	<0.03	<0.03	<0.03	<0.03	<0.03	<0.03	<0.03
Eu (ppm)	<0.01	<0.01	0.01	0.02	0.02	0.02	<0.01	<0.01	0.01	199	190.79	192
Gd (ppm)	<0.03	<0.03	<0.03	2.74	2.64	2.67	<0.03	<0.03	<0.03	<0.03	<0.03	<0.03
Tb (ppm)	<0.01	<0.01	<0.01	0.01	0.01	<0.01	0.08	0.06	0.06	<0.01	<0.01	<0.01
Dy (ppm)	0.25	0.21	0.22	0.47	0.42	0.48	0.04	0.04	0.04	0.04	0.04	0.03
Ho (ppm)	0.05	0.05	0.05	<0.01	<0.01	<0.01	<0.01	<0.01	<0.01	<0.01	<0.01	<0.01
Er (ppm)	0.10	0.09	0.08	<0.01	0.01	<0.01	0.13	0.09	0.07	<0.01	<0.01	<0.01
Tm (ppm)	0.01	0.01	0.01	1.02	1.02	1.01	<0.01	<0.01	<0.01	0.03	0.02	0.02
Yb (ppm)	<0.02	<0.02	<0.02	<0.02	<0.02	<0.02	<0.02	<0.02	<0.02	<0.02	0.02	<0.02
Lu (ppm)	<0.01	<0.01	<0.01	<0.01	<0.01	<0.01	<0.01	<0.01	<0.01	<0.01	<0.01	<0.01
LREE (ppm)	421	406	402	175	178	172	306	205	204	199	191	192
HREE (ppm)	0.41	0.36	0.36	1.50	1.46	1.49	0.25	0.19	0.18	0.07	0.08	0.06
REE total (ppm)	421	406	402	177	189	173	306	205	204	199	191	192

Table 2 Chemical composition of chemically homogeneous, synthetic REE-doped CePO₄, YPO₄, and natural xenotime samples as determined by EMPA and LA–ICP–MS analyses.

	ThO₂	UO₂	Y₂O₃	La₂O₃	Ce₂O₃	Pr₂O₃	Nd₂O₃	Sm₂O₃	Eu₂O₃	Gd₂O₃	Tb₂O₃	Dy₂O₃	Ho₂O₃	Er₂O₃	Tm₂O₃	Yb₂O₃	Lu₂O₃	P₂O₅
Sample Mz-Sm (synthetic Sm-doped CePO₄)																		
	0.05 ppm	<0.01 ppm	337 ppm	1.46 ppm	70.12 wt.%	2.92 ppm	1.86 ppm	1.53 wt.%	16.8 ppm	1863 ppm	38.1 ppm	24.8 ppm	3.51 ppm	6.67 ppm	0.77 ppm	0.32 ppm	0.01 ppm	30.64 wt.%
Sample Mz-Nd (synthetic Nd-doped CePO₄)																		
	0.02 ppm	<0.01 ppm	4.44 ppm	1.21 ppm	71.73 wt.%	3.22 ppm	3316 ppm	0.11 ppm	1.16 ppm	1858 ppm	39.6 ppm	3.00 ppm	0.54 ppm	1.74 ppm	0.26 ppm	0.28 ppm	0.01 ppm	30.76 wt.%
Sample Mz-Pr (synthetic Pr-doped CePO₄)																		
	0.04 ppm	<0.01 ppm	60.6 ppm	3.80 ppm	70.70 wt.%	1.39 wt%	12.4 ppm	0.08 ppm	1.10 ppm	2110 ppm	36.9 ppm	1.75 ppm	0.03 ppm	0.03 ppm	<0.01 ppm	0.28 ppm	0.01 ppm	30.66 wt.%
Sample Xen-Eu (synthetic Eu-doped YPO₄)																		
	0.53 ppm	<0.01 ppm	59.33 wt.%	0.12 ppm	516 ppm	0.03 ppm	3.72 ppm	0.05 ppm	1.39 wt.%	1.15 ppm	0.03 ppm	0.16 ppm	84.1 ppm	0.24 ppm	20.4 ppm	0.04 ppm	0.01 ppm	37.79 wt.%
Sample Xen-Sm (synthetic Sm-doped YPO₄)																		
	<0.01 ppm	<0.01 ppm	55.40 wt.%	3.65 ppm	29.0 ppm	4.55 ppm	31.3 ppm	5.20 wt.%	2.51 ppm	2.49 ppm	61.2 ppm	422 ppm	10.0 ppm	23.6 ppm	2.2 ppm	5.89 ppm	0.73 ppm	38.20 wt.%
Sample Xen-Tm (synthetic Tm-doped YPO₄)																		
	0.14 ppm	<0.01 ppm	57.73 wt.%	0.11 ppm	11.7 ppm	0.01 ppm	5.34 ppm	0.04 ppm	0.26 ppm	0.07 ppm	0.04 ppm	0.29 ppm	1360 ppm	0.52 ppm	2.65 wt.%	0.22 ppm	0.01 ppm	38.50 wt.%
Sample Xen-Nd (synthetic Nd-doped YPO₄)																		
	0.01 ppm	0.04 ppm	57.04 wt.%	4.73 ppm	39.9 ppm	11.2 ppm	3.37 wt.%	3.12 ppm	2.04 ppm	1.89 ppm	253 ppm	12.0 ppm	195 ppm	20.2 ppm	0.94 ppm	5.64 ppm	1.06 ppm	38.32 wt.%
Sample Xen-Er (synthetic Er-doped YPO₄)																		
	<0.01 ppm	<0.01 ppm	54.42 wt.%	1.56 ppm	14.3 ppm	3.04 ppm	23.0 ppm	229 ppm	0.21 ppm	1.64 ppm	33.4 ppm	76.5 ppm	2.04 ppm	8.88 wt.%	4.54 ppm	6.83 ppm	1.31 ppm	38.01 wt.%
Sample Xen-Dy (synthetic Dy-doped YPO₄)																		
	<0.01 ppm	<0.01 ppm	54.01 wt.%	2.83 ppm	19.9 ppm	4.20 ppm	28.0 ppm	2.63 ppm	0.93 ppm	1.98 ppm	321 ppm	8.00 wt.%	4.29 ppm	16.1 ppm	1.24 ppm	6.43 ppm	1.35 ppm	38.01 wt.%
Sample Xen-Ho (synthetic Ho-doped YPO₄)																		
	<0.01 ppm	<0.01 ppm	53.9 wt.%	1.83 ppm	11.3 ppm	3.36 ppm	24.6 ppm	9.7 ppm	243 ppm	2.43 ppm	8.25 ppm	21.7 ppm	8.51 wt.%	42.1 ppm	2.54 ppm	15.0 ppm	1.69 ppm	38.00 wt.%

Element oxide concentrations*

* Data collected by means of EMPA analyses are quoted in wt.%; those by means of LA–ICP–MS are quoted in ppm.

Table 2 continued.

								Element oxide concentrations*									
ThO$_2$	UO$_2$	Y$_2$O$_3$	La$_2$O$_3$	Ce$_2$O$_3$	Pr$_2$O$_3$	Nd$_2$O$_3$	Sm$_2$O$_3$	Eu$_2$O$_3$	Gd$_2$O$_3$	Tb$_2$O$_3$	Dy$_2$O$_3$	Ho$_2$O$_3$	Er$_2$O$_3$	Tm$_2$O$_3$	Yb$_2$O$_3$	Lu$_2$O$_3$	P$_2$O$_5$
Sample Xen-A (Königsalm, Senftenberg, Austria; pegmatite)																	
3040 ppm	6730 ppm	43.34 wt.%	109 ppm	1092 ppm	540 ppm	0.45 wt.%	0.45 wt%	190 ppm	2.05 wt.%	0.59 wt.%	5.31 wt.%	1.7 wt.%	4.60 wt.%	0.85 wt.%	4.67 wt.%	1.08 wt.%	35.39 wt.%
Sample Xen-B (Novo Horizonte, Bahia, Brasilia; pegmatite)																	
1450 ppm	184 ppm	46.30 wt.%	1.74 ppm	32.7 ppm	40.7 ppm	1272 ppm	6408 ppm	4090 ppm	2.91 wt.%	9885 ppm	5.51 wt.%	1.9 wt.%	4.10 wt.%	6688 ppm	2.80 wt.%	3175 ppm	36.10 wt.%
Sample Xen-C (Brindletown, North Carolina, USA; pegmatite)																	
6013 ppm	5.47 wt.%	39.74 wt.%	107 ppm	985 ppm	490 ppm	5754 ppm	7789 ppm	707 ppm	2.01 wt.%	7592 ppm	4.63 wt.%	1.8 wt.%	4.67 wt.%	0.89 wt.%	5.45 wt.%	1.31 wt.%	33.30 wt.%

* Data collected by means of EMPA analyses are quoted in wt.%; those by means of LA–ICP–MS are quoted in ppm.

Table 3. Trace-element concentrations of natural zircon samples and synthetic REE–doped ZrSiO$_4$ as determined by LA–ICP–MS analysis

Sample no. Description	Zir-A Mt. Malosa, Malawi; alkaline pegmatite		M144* Ratnapura, Sri Lanka; gem gravel			N17* Ratnapura, Sri Lanka; gem gravel		Zir-D Pack, Styria, Austria pegmatite			Zir-E Chantanaburi, Thailand gem gravel			Zir-F Kanchanaburi, Thailand gem gravel			
Spot No.	63	64	69	70	71	72	73	74	75	76	90	91	92	93	94	95	96
U (ppm)	130	103	421	424	428	6510	7060	166	71.2	17.9	40.8	38.8	50.1	81.5	282	319	248
Th (ppm)	663	308	135	138	136	334	368	0.01	0.01	<0.01	15.3	19.7	26.2	47.3	145	188	134
Mo (ppm)	0.61	0.62	0.65	0.68	0.69	0.63	0.62	0.62	0.64	0.56	0.64	0.69	0.72	0.64	0.71	0.68	0.63
Y (ppm)	8350	13800	122	121	122	234	245	310	156	270	187	273	361	407	858	654	864
La (ppm)	560	52.5	0.01	<0.01	0.01	0.02	0.02	<0.01	<0.01	<0.01	<0.01	0.01	<0.01	<0.01	<0.01	<0.01	<0.01
Ce (ppm)	5860	1880	3.49	3.36	3.30	5.04	5.63	<0.01	<0.01	<0.01	0.86	0.89	1.03	4.86	6.86	7.81	7.40
Pr (ppm)	860	146	0.05	0.05	0.05	0.35	0.41	<0.01	<0.01	<0.01	0.01	0.05	0.05	0.02	0.03	0.05	0.04
Nd (ppm)	3570	998	0.71	0.70	0.73	5.89	7.14	<0.03	<0.03	<0.03	0.27	0.83	1.09	0.25	0.50	0.63	0.51
Sm (ppm)	810	554	1.11	1.11	1.10	22.4	25.2	<0.03	<0.03	<0.03	0.58	2.00	2.69	0.82	1.34	1.41	1.48
Eu (ppm)	53.0	47.7	0.26	0.23	0.30	0.01	0.01	0.01	<0.01	<0.01	0.54	1.45	1.90	0.36	0.16	0.23	0.20
Gd (ppm)	705	808	3.66	3.80	3.68	96.2	103	0.06	0.04	0.03	3.91	9.27	11.5	5.21	9.10	8.28	9.45
Tb (ppm)	125	179	0.97	0.97	0.95	21.9	23.2	0.07	0.03	0.03	1.53	3.09	3.91	2.17	4.03	3.49	4.19
Dy (ppm)	928	1500	10.7	10.6	10.5	99.2	106	3.20	1.34	1.84	19.5	33.3	43.0	30.1	59.0	49.3	60.8
Ho (ppm)	228	385	3.78	3.70	3.73	7.15	7.54	5.11	2.59	4.28	6.71	10.3	12.9	12.5	24.7	19.6	24.9
Er (ppm)	874	1580	17.9	17.8	17.8	4.57	4.80	97.2	53.7	103	29.3	42.2	52.8	68.3	138	104	136
Tm (ppm)	163	293	3.76	3.85	3.81	0.13	0.12	52.5	29.6	66.4	5.77	7.63	9.77	16.5	33.2	24.7	33.0
Yb (ppm)	1340	2500	36.9	35.5	36.1	0.32	0.35	846	492	1250	47.8	62.9	78.0	164	343	252	340
Lu (ppm)	174	320	6.41	6.45	6.29	0.06	0.06	203	124	362	7.96	9.69	12.1	32.2	67.2	46.9	65.2
LREE (ppm)	12400	4490	9.19	9.25	9.18	130	142	0.07	0.04	0.04	6.17	14.5	18.2	11.5	17.9	18.4	19.1
HREE (ppm)	3840	6750	80.4	78.8	79.1	133	142	1210	703	1780	119	169	212	326	667	500	665
REE total (ppm)	16300	11200	89.6	88.0	88.3	263	284	1210	703	1780	125	184	231	337	687	519	684

* for detailed sample description see Nasdala et al. (2004)

Table 3 (continued).

Sample no.	Ho–0.8		Tm–0.8		Nd–0.8		Sm–2		Dy–0.2
Description	synthetic Sm-doped ZrSiO₄		synthetic Tm-doped ZrSiO₄		synthetic Nd-doped ZrSiO₄		synthetic Sm-doped ZrSiO₄		Dy-doped ZrSiO₄
Spot No.	77	78	79	80	81	82	83	84	87
U (ppm)	0.04	0.05	0.07	0.04	0.06	0.10	0.08	0.04	0.16
Th (ppm)	0.01	0.02	0.02	0.04	0.07	0.18	0.01	<0.01	0.01
Mo (ppm)	304	939	4650	1700	505	14700	1480	49	4920
Y (ppm)	0.06	0.10	0.07	0.11	0.49	1.11	0.09	0.13	1940
La (ppm)	<0.01	<0.01	0.01	<0.01	<0.01	<0.01	<0.01	<0.01	0.02
Ce (ppm)	<0.01	<0.01	0.01	0.02	0.01	0.08	<0.01	<0.01	0.01
Pr (ppm)	<0.01	<0.01	<0.01	<0.01	<0.01	<0.01	<0.01	<0.01	0.47
Nd (ppm)	<0.03	<0.03	<0.03	0.03	11.6	109	<0.03	<0.03	16.7
Sm (ppm)	<0.03	<0.03	<0.03	<0.03	<0.03	<0.03	109	146	0.68
Eu (ppm)	<0.01	<0.01	<0.01	<0.01	<0.01	<0.01	<0.01	<0.01	0.01
Gd (ppm)	0.03	0.08	0.06	0.17	0.07	0.15	0.08	0.07	0.20
Tb (ppm)	<0.01	<0.01	<0.01	<0.01	0.01	0.03	<0.01	<0.01	0.02
Dy (ppm)	0.02	<0.02	<0.02	<0.02	0.23	0.54	0.07	0.11	12000
Ho (ppm)	561	905	0.10	0.15	0.13	0.26	0.14	0.20	0.10
Er (ppm)	0.08	0.10	0.15	0.20	<0.02	0.06	0.04	0.04	0.03
Tm (ppm)	0.16	0.25	1070	1310	<0.01	<0.01	0.01	0.01	0.01
Yb (ppm)	0.03	0.06	0.04	<0.02	0.03	0.06	0.02	0.03	0.23
Lu (ppm)	<0.01	<0.01	<0.01	<0.01	<0.01	<0.01	<0.01	<0.01	0.10
LREE (ppm)	0.04	0.08	0.08	0.24	11.7	109	109	147	18.1
HREE (ppm)	562	906	1070	1320	0.39	0.95	0.28	0.40	12000
REE total (ppm)	562	906	1070	1320	12.1	110	109	147	12000

Supplementary materials
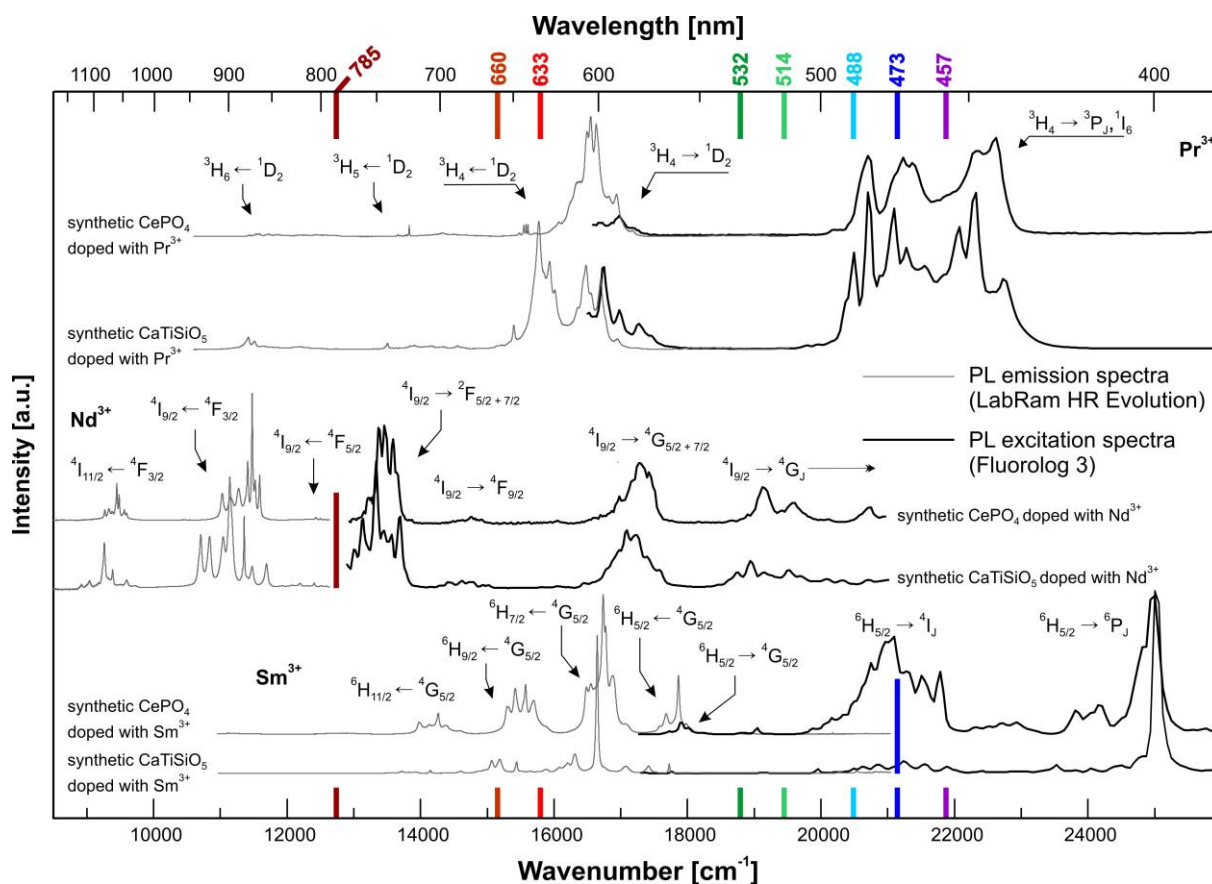
Fig. S1 Photoluminescence excitation and emission spectra of synthetic $CaTiSiO_5$ and $CePO_4$ individually doped with Pr^{3+}, Nd^{3+}, and Sm^{3+}. Excitation spectra were recorded using the intensity of an emissive level while the sample was illuminated with the light of photon energy being continuously scanned through the UV to visible spectral range (emission level used: $CaTiSiO_5$ – Pr^{3+} near 633, Nd^{3+} near 810, and Sm^{3+} near 600 nm; $CePO_4$ – Pr^{3+} near 723, Nd^{3+} near 810 and Sm^{3+} near 700 nm). Laser-induced PL emission spectra were obtained using 473 nm laser to excite Pr^{3+} and Sm^{3+}, and a 785 nm laser to excite the PL of Nd^{3+} doped materials. Further typical laser excitation-wavelengths used in Raman spectroscopy are indicated; an overlap of laser-excitation photon-energy with respective REE^{3+} absorptions levels potentially results in excitation of PL emissions, which may interfere with Raman signals. Note that spectra are normalized; absolute intensity maxima of stacked spectra are not to scale. Assignments of REE^{3+} electronic transitions and Russel-Saunders terms have been extracted from `Dieke´ energy-level diagrams (e.g., Dieke and Crosswhite, 1963; Carnall et al., 1968; Reisfeld and Jørgensen 1977).
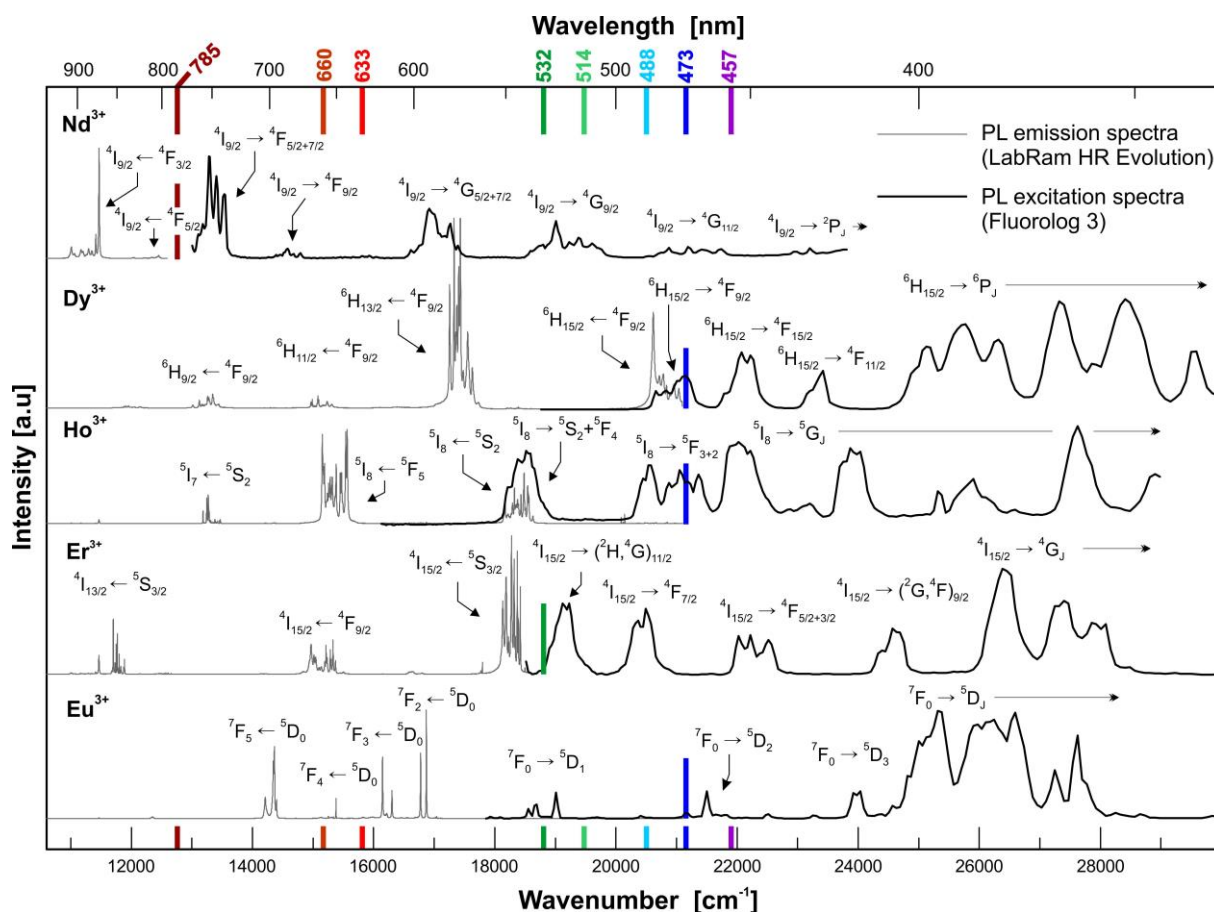
Fig. S2 Photoluminescence excitation and emission spectra of synthetic YPO_4 individually doped with Nd^{3+}, Dy^{3+}, Ho^{3+}, Er^{3+} and Eu^{3+}. Excitation spectra were recorded using the intensity of an emissive level while the sample was illuminated with the light of photon energy being continuously scanned through the UV to visible spectral range (emission level used: $CaTiSiO_5$ – Nd^{3+} near 810, Dy^{3+} near 570, Ho^{3+} near 656, Er^{3+} near 550, and Eu^{3+} near 592 nm). Laser-induced PL emission spectra were obtained using a 473 nm laser to excite Dy^{3+}, Ho^{3+} and Eu^{3+}; a 532 nm laser to excite Er^{3+}; a 785 NIR-laser for Nd^{3+} doped YPO_4. Further typical laser excitation-wavelengths used in Raman spectroscopy are indicated; an overlap of laser-excitation photon-energy with respective REE^{3+} absorptions levels potentially results in excitation of PL emissions, which may interfere with Raman signals. Note that spectra are normalized; absolute intensity maxima of stacked spectra are not to scale. Assignments of REE^{3+} electronic transitions and Russel-Saunders terms have been extracted from `Dieke´ energy-level diagrams (e.g., Dieke and Crosswhite, 1963; Carnall et al., 1968; Reisfeld and Jørgensen 1977).

Appendices B – selected conference abstracts

Orientation-dependent REE photoluminescence of zircon, xenotime and monazite

C. Lenz, D. Talla, L. Nasdala; Institut für Mineralogie & Kristallographie, Universität Wien, Althanstr. 14, A-1090 Wien

Introduction

In Earth sciences, the Rare Earth Elements (REE) distribution in different minerals is used to trace geochemical signatures of formation processes and their genetic implications. One challenging task in REE spectroscopy of the last decades was the detection of different REE in different mineral hosts by luminescence methods [1]. It has become commonplace to interpret REE luminescence by evaluating the Stark level splitting caused by the crystal field interaction [2]. The presence of REE ions at more than one non-equivalent structural positions and semi-quantitative suggestion on rare-earth content is supposed [3-6], however, without regarding the orientation-dependence of REE emissions [7], which is often neglected and insufficiently investigated on synthetic analogue.

Methods & Samples

We have studied REE mono-doped single-crystals of zircon ($ZrSiO_4$), xenotime (YPO_4) and monazite ($CePO_4$) synthesized with Mo flux technique. Common REE in minerals are chosen as dopants (Dy^{3+}, Sm^{3+}, Ho^{3+}, Tb^{3+}, Eu^{3+}, Er^{3+}). Steady-state photoluminescence (PL) and Raman spectra were obtained in quasi back-scattering geometry using a Renishaw RM1000 system with the 488 nm Ar^+ emission line. Oriented measurements of polished sections parallel to the crystallographic c-axis were made.

Results & Diskussion

The luminescence of REEs is characterized by specific transitions between different spin-orbit coupled spectral levels which are well studied [8]. These states are further splitted in crystalline materials by the crystal field interaction (Stark sublevels). The luminescence of REE is dependent on both the type of REE incorporated and the symmetry of the REE-substituted crystallographic cation-site. Our results show that the crystal orientation has a strong influence on the REE photoluminescence with respect to the polarization of the laser. Generally, the luminescence intensity strongly increases with polarization direction of the laser parallel to the optical axis (crystallographic c-axis within tetragonal structures of zircon and xenotime). In various cases intensity ratios between bands change drastically, peak positions are moved, or whole sets of bands disappear as is exemplary shown for transitions of Eu^{3+}, Ho^{3+} and Dy^{3+} in xenotime (Fig. 1).
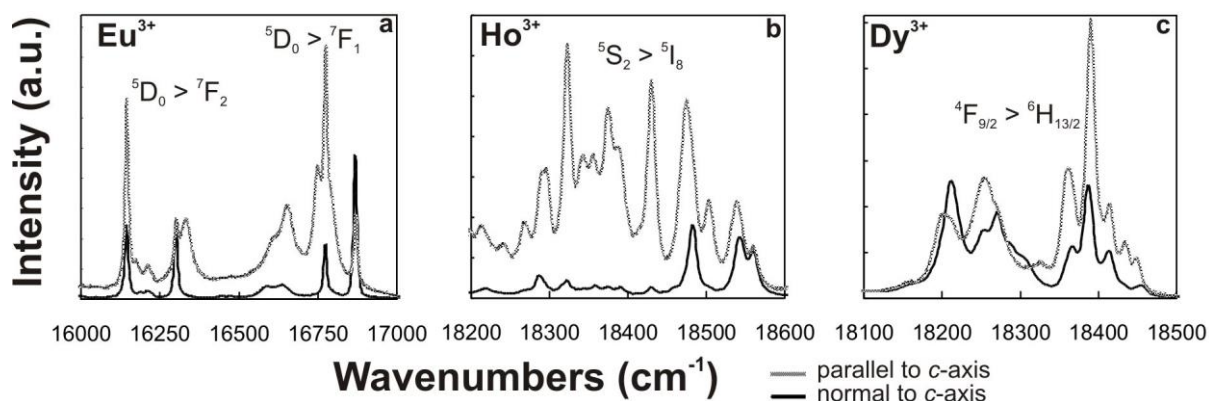

Fig. 1 PL spectra of xenotime single-crystals doped with Eu^{3+} (a) Ho^{3+} (b) and Dy^{3+} (c). Samples were measured with the electric field vector of the incident beam of light oriented parallel or normal to the crystallographic c-axis.

1. Gaft, M., R. Reisfeld, and G. Panczer, *Luminescence spectroscopy of minerals and materials*. 2005: Springer Verlag.
2. Reisfeld, R., E. Zigansky, and M. Gaft, *Europium probe for estimation of site symmetry in glass films, glasses and crystals.* Molecular Physics, 2004. **102**(11): p. 1319–1330.
3. Dexpert-Ghys, J., R. Mauricot, and M. Faucher, *Spectroscopy of Eu^{3+} ions in monazite type lanthanide orthophosphates LnPO4, Ln= La or Eu.* Journal of luminescence, 1996. **69**(4): p. 203–215.
4. Czaja, M., et al., *Luminescence properties of Pr^{3+} and Sm^{3+} ions in natural apatites.* Physics and Chemistry of Minerals, 2009: p. 1-9.
5. Barbin, V., J.P. Jouart, and T. D'Almeida, *Cathodoluminescence and laser-excited luminescence spectroscopy of Eu^{3+} and Eu^{2+} in synthetic CaF_2: a comparative study.* Chemical Geology, 1996. **130**(1-2): p. 77–86.
6. Friis, H., et al., *Photoluminescence of zircon (ZrSiO4) doped with REE^{3+} (REE = Pr, Sm, Eu, Gd, Dy, Ho, Er).* Physics and Chemistry of Minerals, 2009. **37**(6): p. 333–342.
7. Owen, J.J., A.K. Cheetham, and R.A. McFarlane, *Orientation-dependent fluorescence studies and spectroscopic analysis of doped barium yttrium fluoride upconversion laser crystals ($BaY_{2-x-y}Yb_xTm_yF_8$).* JOSA B, 1998. **15**(2): p. 684–693.
8. Dieke, G.H., *Spectra Energy Levels of Rare Earth Ions in Crystals*. 1968, New York: Wiley Interscience.

Orientation dependence of REE³⁺ photoluminescence spectra and a possible artefact

Reissner, C., Lenz, C.*, Nasdala, L.

Institut für Mineralogie und Kristallographie, Universität Wien,
Althanstraße 14,1090 Wien, Austria
*e-mail: christoph.lenz@univie.ac.at

Quantifications of rare earth elements (REEs) from emission intensities have been proposed for several minerals (Barbarand & Pagel 2001; Habermann 2002; MacRea et al. 2012). A potential semi-quantitative estimation of trace elements via luminescence intensity requires to consider and maintain a broad range of carefully calibrated conditions, including reliable standard materials, system stability, and system response (Cesbron et al. 1995, Barbarand and Pagel 2001). Even though being a well-known luminescence phenomenon (Owen et al. 1998; Barbarand and Pagel 2001; Finch et al. 2003), the orientation-dependence of REE³⁺ emissions is often neglected, which may result in biased conclusions.

As an example, we have studied the orientation-dependence of the photoluminescence (PL) emission of trace Nd^{3+} ($^4F_{3/2} \rightarrow {}^4I_{9/2}$ electronic transition) in synthetic xenotime–(Y). Our results reconfirm that the emission intensity depends strongly on the direction of the emitted light being analysed. Especially in PL, the intensities observed are further affected by the polarisation of the incident laser beam. Figure 1 demonstrates effects of the orientation of electric field vector (E) relative to crystallographic directions. First, changing the polarisation direction of the laser beam causes the intensity of the luminescence bands to vary appreciably (Fig. 1a). Second, by placing a polarisation filter in the emission pathway it can be demonstrated that the luminescence emission itself is polarised (Fig. 1b). To avoid potentially biased interpretations, such effects need to be considered in discussing PL intensities.
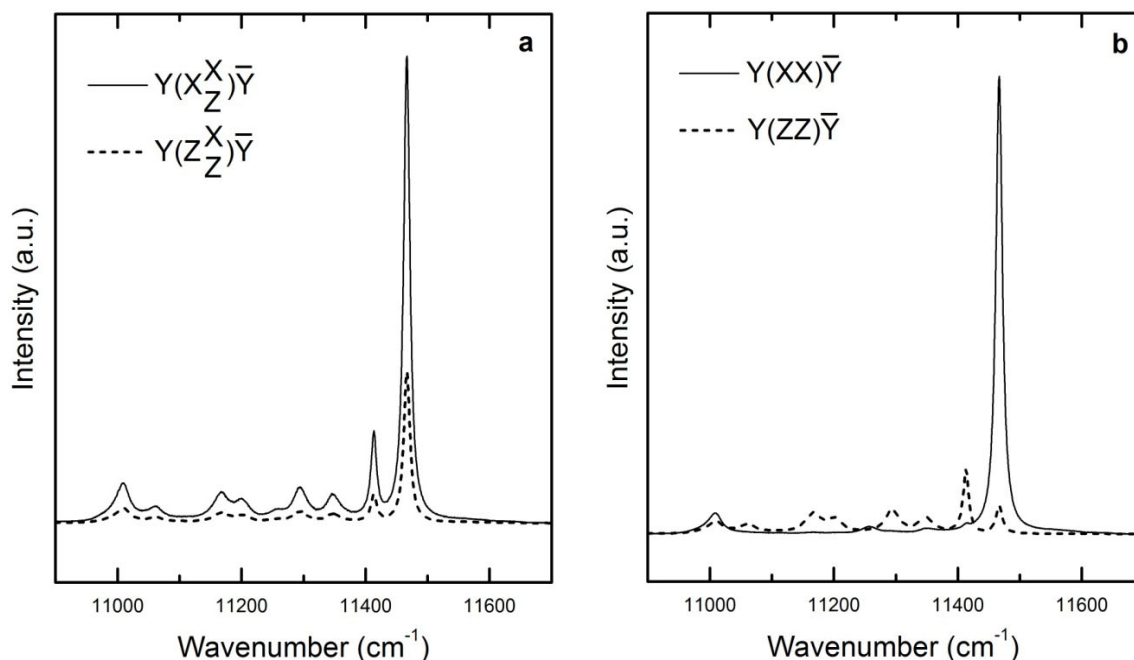

Fig. 1. *Orientation-dependence of the laser-induced PL (532 nm excitation) of Nd^{3+} ($^4F_{3/2} \rightarrow {}^4I_{9/2}$) in synthetic Nd^{3+}-doped YPO_4 (xenotime; $I4_1/amd$). Two examples are presented for how the polarization of the incident laser beam (**a**) and the polarisation of the emitted light analysed (**b**) affect intensities. Experimental geometries are reported using the so-called Porto notation (Damen et al. 1966).*
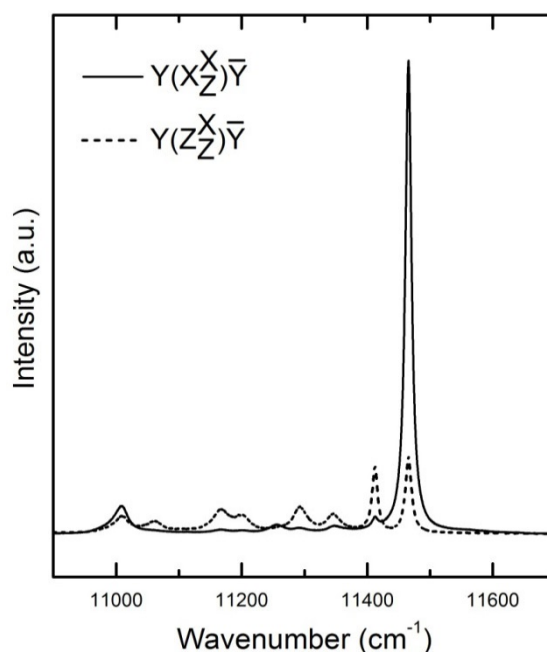
87

Fig. 2. *Photoluminescence emissions of Nd^{3+} ($^4F_{3/2} \rightarrow {}^4I_{9/2}$) in synthetic Nd-doped, xenotime-structured YPO_4 (532 nm excitation). Spectra were obtained without polarisation filter and 1800 lines/mm grid.*

In addition to the orientation dependence described above, we noticed a hitherto unrecognised possible artefact that is caused by the grating in the optical pathway. The intensity ratios of Nd^{3+} luminescence emission bands near 880 nm wavelength vary appreciably, depending on the grating used. The pairs of spectra shown in Figs. 1a and 2 were obtained under identical geometries and conditions (same Horiba LabRAM–HR800 spectrometer, objective, laser power, accumulation time, measurement point, etc.), however with different gratings. The spectra pair shown in Fig. 1a was recorded with a grating with 600 lines/mm whereas a grating with 1800 lines/mm was used for the spectra pair shown in Fig. 2. Most remarkably, spectra obtained with the 600 lines/mm grid and an analyser in the optical pathway (Fig. 1b) are very similar to spectra observed with the 1800 lines/mm grid but without any analyser. This observation may indicate that the 1800 lines/mm grating acts similar to a polariser, perhaps due to high refracting angles in the near-infrared spectral range.

References:

Barbarand J, Pagel M (2001) Cathodoluminescence study of apatite crystals. Am Mineral 86:473–484

Cesbron F, Blanc P, Ohnenstetter D, Rémond G (1995) Cathodoluminescence of rare earth doped zircons. I. Their possible use as reference materials. Scanning Microsc Suppl 9:35–56

Damen TC, Porto SPS, Tell B (1966) Raman effect in zinc oxide. Phys Rev 142:570–574

Finch A, Hole D, Townsend P (2003) Orientation dependence of luminescence in plagioclase. Phys Chem Miner 30:373–381

Habermann D (2002) Quantitative cathodoluminescence (CL) spectroscopy of minerals: possibilities and limitations. Miner Petrol 76:247–259

Lenz C, Talla D, Ruschel K, Škoda R, Götze J, Nasdala L (2013) Factors affecting the Nd^{3+} (REE^{3+}) luminescence of minerals. Miner Petrol (published online: DOI 10.1007/s00710-013-0286-2)

MacRea CM, Wilson NC, Torpy A, Davidson CJ (2012) Hyperspectralcathodoluminescence imaging and analysis extending from ultraviolet to near infrared. Microsc Microanal 18:1239–1245

Owen JJ, Cheetham AK, McFarlane RA (1998) Orientation-dependent fluorescence studies and spectroscopic analysis of doped barium yttrium fluoride upconversion laser crystals ($BaY_{2-x-y}Yb_xTm_yF_8$). J Opt Soc Am B 15:684–693

88

Biological controls on oxygenation in the Neoproterozoic and Paleozoic

TIMOTHY M. LENTON[1]

[1]University of Exeter, Exeter, UK, t.m.lenton@exeter.ac.uk

The deep oceans were finally oxygenated during the Late Neoproterozoic, and this is widely attributed to a rise in atmospheric oxygen. However, existing data suggests there followed a de-oxygenation of the ocean across the Precambrian-Cambrian boundary. Only later in the Paleozoic did the deep ocean recover a fully oxygenated state. What biogeochemical mechanisms could explain these changes?

It is hypothesised that increases in phosphorus weathering, either due to greening of the land [1] or the aftermath of glaciations [2], fuelled organic carbon burial and thus a Neoproterozoic increase in atmospheric oxygen. However, sustained changes in silicate weathering flux are prevented by the well-known regulator of atmospheric CO_2 and temperature. Thus, increases in phosphorus weathering can only be sustained long enough to affect atmospheric oxygen if there is selective weathering of phosphorus relative to bulk rock (by biology) [1], or a shift in the balance of CO_2 sinks from seafloor weathering to continental weathering [3].

Hence it is worth considering if the Neoproterozoic oxygenation of the ocean could have happened without a rise in atmospheric oxygen. A possible scenario invokes the evolution of eukaryotes in the surface ocean producing larger particles that sank faster [4]. This would have shifted oxygen demand away from the bottom waters of continental shelves (where the majority of phosphorus burial and recycling occurs) to greater depth. Oxygenation of the shelves would have increased the efficiency phosphorus removal from the ocean (in organic matter and adsorbed to iron oxyhydroxides) thus lowering global productivity and lowering oxygen demand in the deep ocean, oxygenating it. The net effect on organic carbon burial is uncertain because less export production was counteracted by faster sinking to sediments.

The subsequent early Paleozoic de-oxygenation of the ocean could be explained by the evolution of animal bioturbation lowering the C/P burial ratio of organic matter in sediments and thus lowering atmospheric oxygen [5].

The later rise of land plants, selectively weathering phosphorus and producing recalcitrant high C/P biomass, increased organic carbon burial and atmospheric oxygen, finally producing a persistent oxygenation of the ocean.

[1] Lenton & Watson (2004) *GRL* **31**, L05202. [2] Planavsky *et al..* (2010) *Nature* **467**, 1088-90. [3] Mills *et al..* (submitted). [4] Logan *et al..* (1995) *Nature* **376**, 53-6. [5] Boyle *et al..* (submitted).

Orientation-dependent REE[3+] luminescence: a possible artifact in luminescence imaging

C. LENZ[1]*, C. REISSNER[1], D. TALLA[1,2] AND L. NASDALA[1]

[1] Institut für Mineralogie und Kristallographie, Universität Wien, Althanstraße 14, 1090 Wien, Austria (*correspondence: christoph.lenz@univie.ac.at)
[2] Institute of Geological Sciences, Masaryk University, Kotlářská 2, 61137 Brno, Czech Republic

Luminescence imaging is a sensitive tool for revealing internal zoning patterns of crystals and other geological samples, especially for species containing rare-earth elements (REE[3+]) [1,2]. In addition to the traditional direct imaging methods, the hyperspectral mapping technique is used increasingly for this [3]. Quantifications of REEs from emission intensities have been proposed for several minerals [3–5]. Note, however, that the orientation-dependence of REE[3+] emissions is often neglected by Earth scientists [4], even though the phenomenon is well known [5,6].
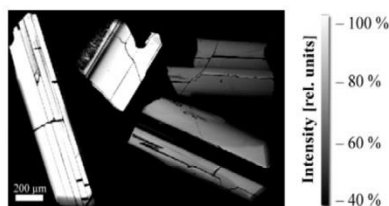

Figure 1: PL map (532 nm excitation with N–S polarisation) of the emission of Nd^{3+}, showing clear intensity differences among chemically uniform but randomly oriented crystals.

As an example, we have studied the orientation-dependence of the $^4F_{3/2} \rightarrow {}^4I_{9/2}$ emission of trace Nd^{3+} in zircon and xenotime–(Y) and their synthetic analogues. We found once again that the emission intensity depends strongly on the direction of the emitted light being analysed (CL and PL). In PL, the intensities observed are further affected by the polarisation of the incident laser beam relative to the crystal (compare Fig. 1).

[1] Götze (2002) *Anal Biaanal Chem* **374**:703–708. [2] Hanchar & Miller (1993) *Chem Geol* **110**:1–13. [3] MacRea *et al..* (2012) *Microsc Microanal* **18**:1239–1245. [4] Habermann (2002) *Miner Petrol* **76**:247–259. [5] Barbarand & Pagel (2001) *Am Mineral* **86**:473–484. [6] Finch *et al..* (2003) *Phys Chem Miner* **30**:373–38.

ION AND ELECTRON IRRADIATION – TOOLS TO STUDY RADIATION DAMAGE IN MINERALS

L. Nasdala [1], _C. Lenz_ [1], _A. Artač_ [1], _S. Akhmadaliev_ [2], _T. Váczi_ [3], _G. Habler_ [4], _R. Abart_ [4]

[1] Institut für Mineralogie und Kristallographie, Universität Wien, Vienna, Austria; lutz.nasdala@univie.ac.at, christoph.lenz@univie.ac.at, andreas.artac@univie.ac.at

[2] Institut für Ionenstrahlphysik und Materialforschung, Helmholtz-Zentrum Dresden-Rossendorf, Dresden, Germany; c.akhmadaliev@hzdr.de

[3] Department of Mineralogy, Eötvös Loránd University, Budapest, Hungary; vaczitamas@caesar.elte.hu

[4] Department für Lithosphärenforschung, Universität Wien, Vienna, Austria; gerlinde.habler@univie.ac.at, rainer.abart@univie.ac.at

The long-term impact of natural radioactivity may cause severe structural damage in minerals. This damage is created mainly by the nuclear interaction (atomic "knock-ons") of high-energy corpuscles with lattice atoms. In minerals incorporating instable nuclei (U and Th) in their lattice, damage is caused mainly by recoils of heavy daughter nuclei upon emission of an alpha particle [1–3], which generate nm-sized defect clusters. Non-radioactive minerals can also become damaged, through alpha irradiation from adjacent phases [4,5]. With progressive damage accumulation, minerals may finally be transformed to a so-called "metamict", amorphous state [6].

Radiation-damaged minerals are important objects in geochemistry and geochronology, and their investigation has increased appreciably over the past two decades, stimulated by the potential use of mineral-like ceramics as waste forms for the immobilisation of spent nuclear fuel and other radioactive waste [7–10]. The damage accumulation is associated with changes of physical properties and a general decrease of the chemical durability. Radiation-damaged minerals are hence more susceptible to alteration [11,12] and the loss of radioisotopes, which may bias results of chemical and isotopic age determinations [13–15]. Better understanding of radiation damage and associated property changes therefore helps to avoid biased age data, and to interpret the post-growth history of minerals. For this, however, an improved quantitative knowledge of radiation effects is needed.

Attempted quantifications of irradiation effects based on the study of naturally radiation-damaged minerals are often biased, because of the insufficiently known thermal (and hence annealing) history of natural samples. This problem may be overcome by studying minerals that were ion-irradiated in the laboratory.

This plenary lecture starts with an introductory overview of effects of corpuscular radiation in minerals. It characterises "metamictisation" of U- and Th-bearing minerals as a process of long-term accumulation mainly of alpha-recoil clusters, which however occurs only if damage does not undergo thermal annealing [16]. A number of examples for experimental studies are presented.

Helium irradiation (and subsequent thermal treatment) was done to study radio-colouration of diamond and cordierite. Cordierite shows orange-yellow radiocolouration (in natural samples typically around inclusions of monazite and zircon) when being mildly radiation-damaged, whereas at elevated stages of structural destruction colouration reversal is observed (a phenomenon which is also known from sheet silicates [17]). Diamond, in contrast, was not found to show any colouration reversal but yielded a direct correlation of the intensity of green surface stains with the degree of damage [5]. Experimental He irradiation was also applied to investigate phenomena of defect luminescence in various minerals including zircon, monazite, and diamond. It was found that defect luminescence is only observed at very low defect densities and then suppressed already at relatively moderate defect densities. For example, the greenish-yellow defect photoluminescence of irradiated diamond after heat treatment (due to the thermal formation of H3 defects) was observed at defect densities in the approximate range 0.000006–0.003 dpa (average of atomic displacements per lattice atom) [5]. The yellow defect luminescence of zircon was observed by [18] in the approximate range 0.00005–0.003 dpa. This result indicates that in heavy-mineral concentrates observed under UV illumination, strongly yellowish luminescing zircon grains are merely mildly radiation-damaged and hence potentially more suitable for U–Th–Pb geochronology. In the same study [18] it was also

observed that He-irradiation of mildly to strongly radiation-damaged zircon always resulted in an increase of the structural damage. Alpha-assisted annealing of alpha-recoil damage (which has been observed by [19] for initially damaged phosphate minerals irradiated with He ions) is therefore probably insignificant for natural zircon.

Electron-irradiation experiments of polished sample mounts containing zircon showed that the impact of the electron beam in the EPMA (electron probe micro-analyser) does not create additional damage but causes moderate structural recovery. The extent of the recovery depends on the magnitude of the beam-treatment, i.e. it increases both with increasing irradiation time and enhanced beam current.

We finally present first results of heavy-ion irradiations of thin lamellae that were produced using the focused ion beam (FIB) technique (Fig. 1). Based on results of Monte Carlo simulations using the SRIM (the Stopping and Range of Ions in Matter, [20]) code, the thicknesses of these lamellae were adjusted carefully according to the penetration depths of the MeV Au ions irradiated (Fig. 2a). On the one hand, this ensures that the irradiated samples contain the majority of the structural damage produced, which is a presumption for quantitative estimates. On the other hand, irradiated samples will not contain any un-irradiated volumes, whose presence is likely to bias the analytical results (compare [21]). The broadening of spectroscopic signals (emissions of centres related to rare-earth elements, and vibrational modes; Fig. 2b) will provide potentially, after proper calibration, an in-situ measure of radiation damage in accessory minerals in geological samples.
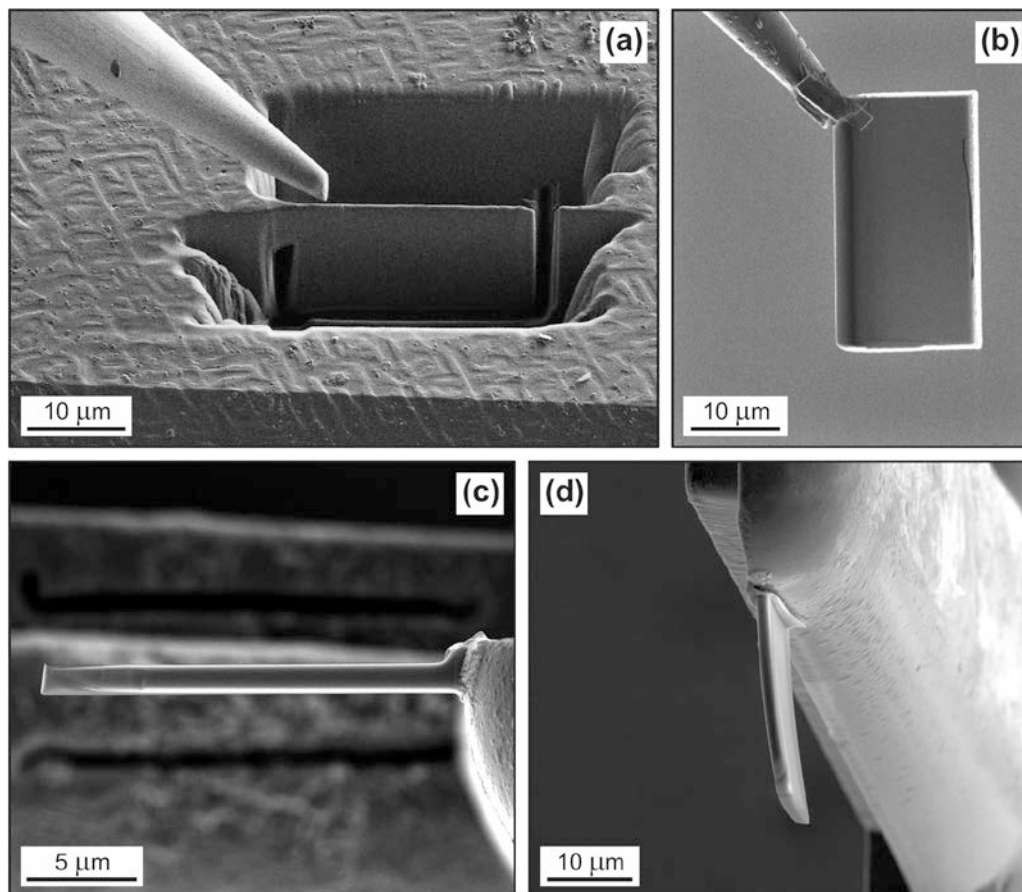

Figure 1: Scanning electron microscope (SEM) images visualising the preparation of thin lamellae. (a) Surface of a synthetic crystal. A thin "wall" of sample material was produced by FIB sputtering two rectangular trenches in close vicinity. After sample tilt, the "wall" is then cut free (see <2 μm wide "trenches"). (b) Lamella attached to the tip of a micro-manipulator needle. (c) A 1.3 μm thick, plane-parallel lamella after final thinning at low ion-beam current. The lamella is attached to a Cu sample holder (right margin) by Pt deposition. (d) Lamella after irradiation with MeV Au ions (note the slight bending due to the build-up of internal stress).
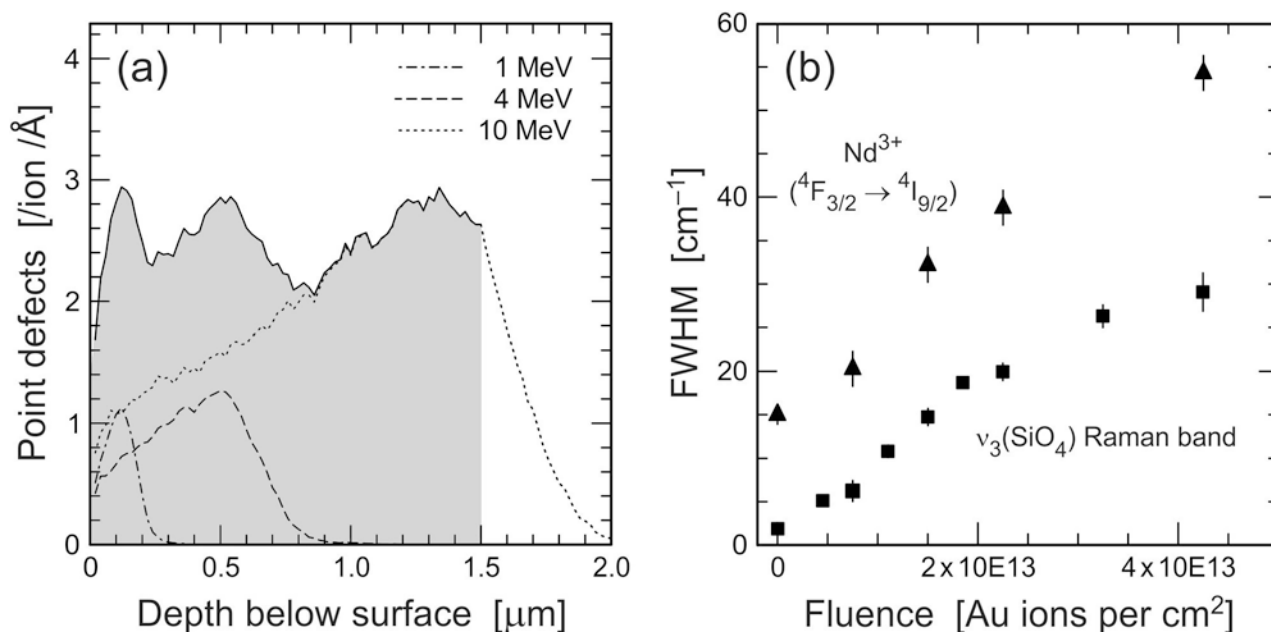
Figure 2: Irradiation of FIB foils used to quantify irradiation effects. (a) Depth distribution of point defects created by the triple irradiation of a $ZrSiO_4$ target with 1 MeV (15.6 %), 4 MeV (21.9 %), and 10 MeV (62.5 %) Au ions, as predicted by Monte Carlo simulations using SRIM [20]. Solid graph = sum (i.e., total defects). Individual fluences (cf. percentages above) were chosen in order to create a more or less homogeneous defect density in the ~1.5 μm thick target. (b) Broadening of the ~11.350 cm^{-1} emission band of Nd^{3+} (triangles), and the main, B_{1g}-type ~1008 cm^{-1} Raman band, observed from Au-irradiated FIB lamellae of zircon.

References:
[1] P.J. Wasiliewski, F.E. Senftle, J.E. Vaz, A.N. Thorpe, C.C. Alexander C.C., Radiat. Eff. 17 (1973) 191–199.
[2] W.J. Weber, R.C. Ewing, L.M. Wang, J. Mater. Res. (1994) 688–698.
[3] R. Devanathan, L.R. Corrales, W.J. Weber, A. Chartier, C. Meis, Nucl. Instr. Meth. Phys. Res. B, 250 (2006) 46–49.
[4] D.C. Pal, Curr. Sci. India 87 (2004) 662–667.
[5] L. Nasdala, D. Grambole, M. Wildner, A.M. Gigler, T. Hainschwang, A.M. Zaitsev, J.W. Harris, J. Milledge, D.J. Schulze, W. Hofmeister, W.A. Balmer, Contrib. Mineral. Petrol. 165 (2013) 843–861.
[6] R.C. Ewing, Nucl. Instr. Meth. Phys. Res. B 91 (1994) 22–29.
[7] B. Omelyanenko, T. Livshits, S. Yudintsev, B. Nikonov, Geol. Ore Deposit. 49 (2007) 173–193.
[8] W.J. Weber, A. Navrotsky, S. Stefanovsky, E.R. Vance, E. Vernaz, E., MRS Bull. 34 (2009) 46–53.
[9] J.M. Montel, C. R. Geosci. 343 (2011) 230–236.
[10] R. Ewing, W.J. Weber, in L.R. Morss, N. M. Edelstein, and J. Fuger, J., Eds. (2011) The Chemistry of the Actinide and Transactinide Elements, 6, Springer, Netherlands, p. 3813–3887.
[11] K. Horie, H. Hidaka, F. Gauthier-Lafaye, Phys. Chem. Earth 31 (2006) 587–592.
[12] C. Lenting, T. Geisler, A. Gerdes, E. Kooijman, E.E. Scherer, A. Zeh, Am. Mineral. 95 (2010) 1343–1348.
[13] P. Goncalves, M.L. Williams, M.J. Jercinovic, Am. Mineral. 90 (2005) 578–585.
[14] Y.D. Kuiper, Am. Mineral. 90 (2005) 586–591.
[15] L. Nasdala, J.M. Hanchar, D. Rhede, A.K. Kennedy, T. Váczi, Chem. Geol. 269 (2010) 290–300.
[16] L. Nasdala, M. Wenzel, G. Vavra, G. Irmer, T. Wenzel, B. Kober, Contrib. Mineral. Petrol. 141 (2001) 125–144.
[17] C. Moazed, R. Overbey, R.M. Spector, Nature 258 (1977) 315–317.
[18] L. Nasdala, D. Grambole, J. Götze, U. Kempe, T. Váczi, Contrib. Mineral. Petrol. 161 (2010) 777–789.
[19] S. Ouchani, J.-C. Dran, J. Chaumont, Nucl. Instrum. Methods B 132 (1997) 447–451.
[20] J.F. Ziegler, J.P. Biersack, U. Littmark, The stopping and range of ions in solids, 1985, Pergamon, New York.
[21] L. Nasdala, R. Grötzschel, S. Probst, B. Bleisteiner, Can. Mineral. 48 (2010) 351–359.

Heavy ion irradiation induced damage in monazite-(Ce), CePO$_4$

Andreas Artač* [1], Christoph Lenz [1], Shavkat Akhmadaliev [2], Gerlinde Habler [3], Lutz Nasdala [1]

(1) Institut für Mineralogie und Kristallographie, Althanstraße 14 (UZA 2), 1090 Vienna, Austria
(2) Helmholtz-Zentrum Dresden-Rossendorf, Bautzner Landstraße 400, 01314 Dresden, Germany
(3) Departement of Lithospheric Research, Althanstraße 14 (UZA 2), 1090 Vienna, Austria

The process of irradiation induced amorphisation in inorganic materials is controversially discussed in literature [1, 2]. The purpose of the present research is a better quantification of how much of irradiation causes how much of damage. This is still an important issue for Earth and material sciences (e.g., interpretation of geochronological data, and potential use of minerals as nuclear waste form) [3]. In the present project several FIB foils of a natural and a synthetic monazite crystal were prepared and irradiated with different fluences of heavy ions (Au). Four foils per sample were irradiated with fluences ranging from 7.5×10^{12} to 4.25×10^{13} ions/cm².

Raman spectroscopic measurements were done to estimate the amount of radiation damage [2]. Furthermore laser-induced photoluminescence spectra of the same samples were obtained. With both methods, notable increases of width of spectroscopic signals in dependence of the irradiation dose were observed. This correlation can be used to potentially estimate structural damage caused by ion irradiation.
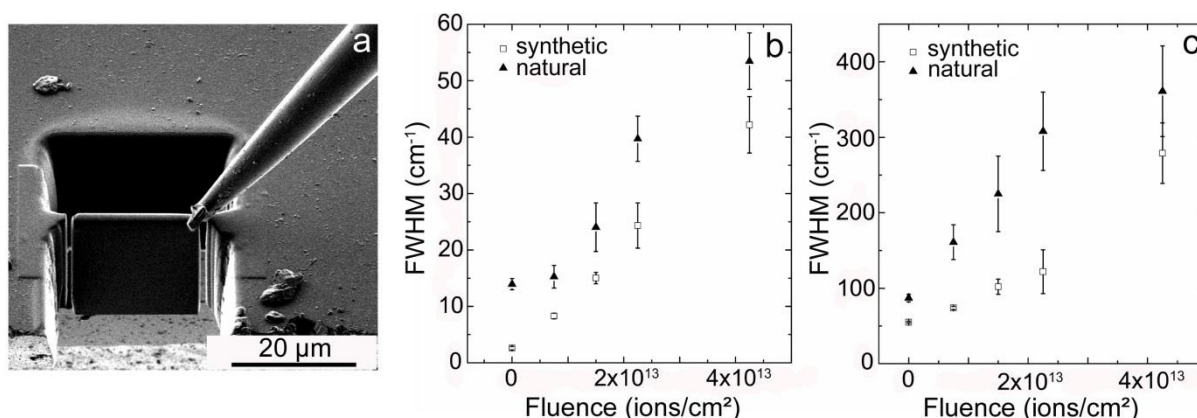

Figure 1: (a) Ion-beam image of a cut-out FIB-foil of synthetic monazite-(Ce) attached to the tip of a micromanipulator. (b) Plot of Raman band width of the symmetric stretching band of monazite-(Ce) at ~970 cm^{-1} against ion fluence. (c) Plot of Nd^{3+} ($^2F_{3/2} \rightarrow {}^4I_{9/2}$) PL band (sub-level at ca. 11030 cm^{-1}) of monazite-(Ce) against ion fluence.

[1] Nasdala, L., M. Wenzel, et al. (2001). "Metamictisation of natural zircon: accumulation versus thermal annealing of radioactivity-induced damage (Vol 141, Pg 125, 2001)." Contributions to Mineralogy and Petrology 143(6): 767-768.
[2] Nasdala, L., G. Irmer, et al. (1995). "The Degree of Metamictization in Zircon - a Raman-Spectroscopic Study." European Journal of Mineralogy 7(3): 471-478.
[3] Montel, J. M. (2011). "Minerals and design of new waste forms for conditioning nuclear waste." Comptes Rendus Geoscience 343(2-3): 230-236.

* Contact: andreas.artac@univie.ac.at

Quantitative estimation of radiation-induced defect accumulation in zircon ($ZrSiO_4$) – A REE^{3+} photoluminescence and Raman spectroscopic approach

Christoph Lenz[1], Andreas Artac[1], Shavkat Akhmadaliev[2] and Lutz Nasdala[1]

[1] Institut für Mineralogie und Kristallographie, Universität Wien, Althanstraße 14, 1090 Vienna, Austria
[2] Helmholtz-Zentrum Dresden-Rossendorf, Bautzner Landstraße 400, 01314 Dresden, Germany

We present first results of a comparative study addressing effects of radiation-induced damage in two types of sample, namely, (i) natural zircon that has experienced long-term self-irradiation due to the radioactive decay of trace-U and -Th, and (ii) samples irradiated with heavy ions. The objective is to provide REE^{3+} laser-induced photoluminescence (PL) and Raman spectroscopic estimates of irradiation-induced damage for zircon samples of unknown geothermal history.

The full-width-at-half-maximum (FWHM) of certain PL sublevel bands of trace REE^{3+}, and the $\nu_3[SiO_4]$ Raman band, are used to estimate the radiation damage present. Complementary to results of [1], it has been found that the FWHMs of REE^{3+}-related PL bands relate closely to the effective time-integrated α–dose of well-characterised natural zircon samples. Hence, PL of REE^{3+} may be used for the quantitative estimation of radiation damage, in addition to the already well-established Raman-based approach. Further, we compare naturally radiation-damaged zircon with ion-irradiated material. For this purpose, well-crystalline, gem-quality zircon from Ratanakiri (Cambodia) was annealed, and thin foils (1.5 µm thickness) – prepared with the focused ion beam (FIB) technique – were irradiated with Au-ions (Fig. 1).
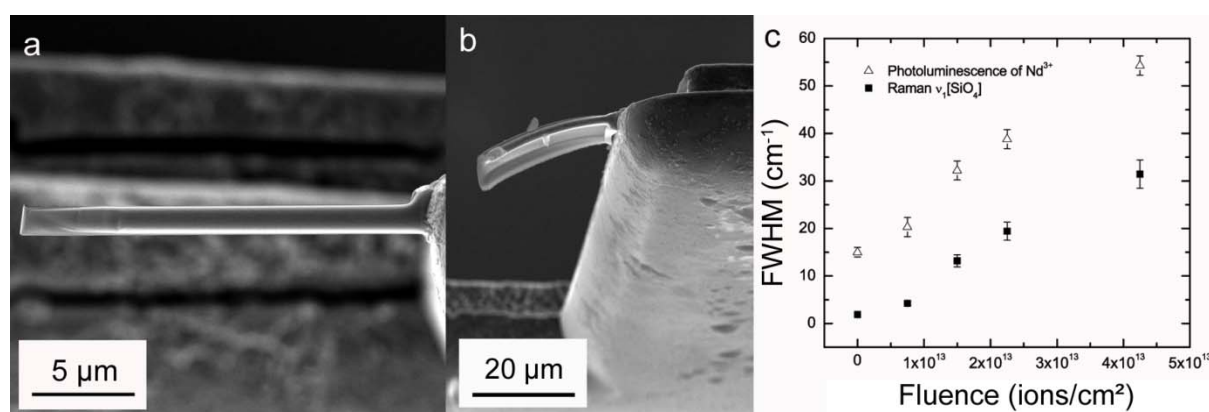

Fig.1 Zircon irradiation with Au ions: Lamellae were prepared with the FIB technique (**a**) and irradiated. Radiation damage causes volume swelling (**b**) and an increase of spectroscopic band widths (**c**). The FWHM of the PL emission of trace Nd^{3+} ($^4F_{3/2} \rightarrow {}^4I_{9/2}$) and the Raman $\nu_3[SiO_4]$ mode were found to be well suitable to estimate the radiation damage created.

[1] Nasdala, L., et al. (2001) Metamictisation of natural zircon: Accumulation versus thermal annealing of radioactivity-induced damage. Contributions to Mineralogy and Petrology 141, 125–144.

Luminescence database - an update

N. C. Wilson[1], C. M. MacRae[1], A. Torpy[1], M. Gaft[2], J. Götze[3], C. Lenz[4], L. Nasdala[4], J. M. Hanchar[5], and G. Barmarin[6]

[1]CSIRO Process Science and Engineering, Box 312, Clayton, VIC, 3169, Australia.
[2]Laser Distance Spectrometry Ltd., Petah Tikva, Israel
[3]Institut für Mineralogie, Technische Universität Bergakademie Freiberg, Germany
[4]Institut für Mineralogie und Kristallographie, Universität Wien, Austria
[5]Department of Earth Sciences, Memorial University of Newfoundland, St. John's, Canada
[6]www.fluomin.org/uk/accueil.php
Corresponding Author's e-mail address: nick.wilson@csiro.au

The luminescence database [1] was developed to provide a quick reference for identifying peaks in luminescence spectra, in similar fashion to KLM lines for x-rays or the RRUFF database for Raman lines. In the case of KLM lines, the characteristic x-ray energies are largely unaffected by bonding and so a table is relatively easy to compile. However, for luminescence the case is more complex, with the emission being sensitive to both material composition and structure of the host lattice. This complexity arises due to the luminescence signal being generated from a set of bonding influenced states such as conduction to valence band transitions, defect states and phonon modes [2]. Luminescence emission is generally grouped into intrinsic and extrinsic types, with intrinsic luminescence being native to the host material and extrinsic emission attributed to the presence of trace element impurities. These complications require the database to record not only the emitter of the line, but the host material in which it resides.

The initial database, generated from a literature survey of papers containing well characterized luminescence data, comprised over 70 minerals and a smaller number of synthetic materials, including semiconductors. With multiple entries for each structure, the database recorded over 1150 lines and bands, detailing the mineral name, associated chemical formula, charge on the ion or classification as intrinsic or extrinsic, and wavelength of energy of line observed. Wherever possible the sample temperature at which the emission line was recorded was included, as well as the technique used to excite and the instrument used to collect the luminescence. This was recorded as both temperature and polarisation effects can occur in a number of minerals/materials that lead to changes in relative peak intensity with wavelength. The publication reference for all entries was also noted so that further experimental and sample details can be examined. The database currently contains over 2700 lines.

The database was made public as a community resource available through the internet (http://www.csiro.au/luminescence/) and embedded within the freely available OpticalFit [3] software (Fig. 1). OpticalFit is a Windows-compatible software package for spectral fitting and peak deconvolution, and allows the database entries to be overlaid onto the spectra to aid in identification by choosing from a drop down list of structures, chemical formula and lines. In addition to recording line energies for particular minerals, the database now includes reference spectra generated using a number of techniques. This information greatly enhances the utility of the database, as it enables relative peak heights and efficiency of luminescence to be provided to the researcher.

Submissions to the database from the wider community have been welcomed, and since its inception, the database has grown considerably in size. M. Gaft, J. Götze, L. Nasdala, C. Lenz and J. M. Hanchar

have most recently supplied collections of reference spectra and associated peak assignment collected across a wide range of minerals, both natural and synthetic, along with a set of related references detailing the samples and collection conditions. G. Barmarin, who has compiled a collection of luminescent minerals [4] and associated photoluminescence spectra, has contributed a large number of specimens from which we have collected cathodoluminescence (CL) reference spectra. Spectra from rutile and haematite, which are not normally thought of as CL active have also been included. We have been optimizing the collection of CL signals [5] from very weak emitters through hyper-spectral mapping and are growing the database to include reference spectra from such materials.

References:

[1] C.M. MacRae and N. C. Wilson, "Luminescence Database I - Minerals and Materials", Microscopy and Microanalysis, 14, 184-204, (2008)
[2] A. S. Marfunin, Spectroscopy, Luminescence and Radiation Centers in Minerals (Springer-Verlag, Berlin Heidelberg New York, ed. 1979).
[3] http://www.csiro.au/luminescence/opticalfit/index.html
[4] http://www.fluomin.org/uk/accueil.php
[5] N.C. Wilson, C.M. MacRae, and A. Torpy, Weak signal cathodoluminescence mapping, AMAS XII, Sydney 2013, p48-49
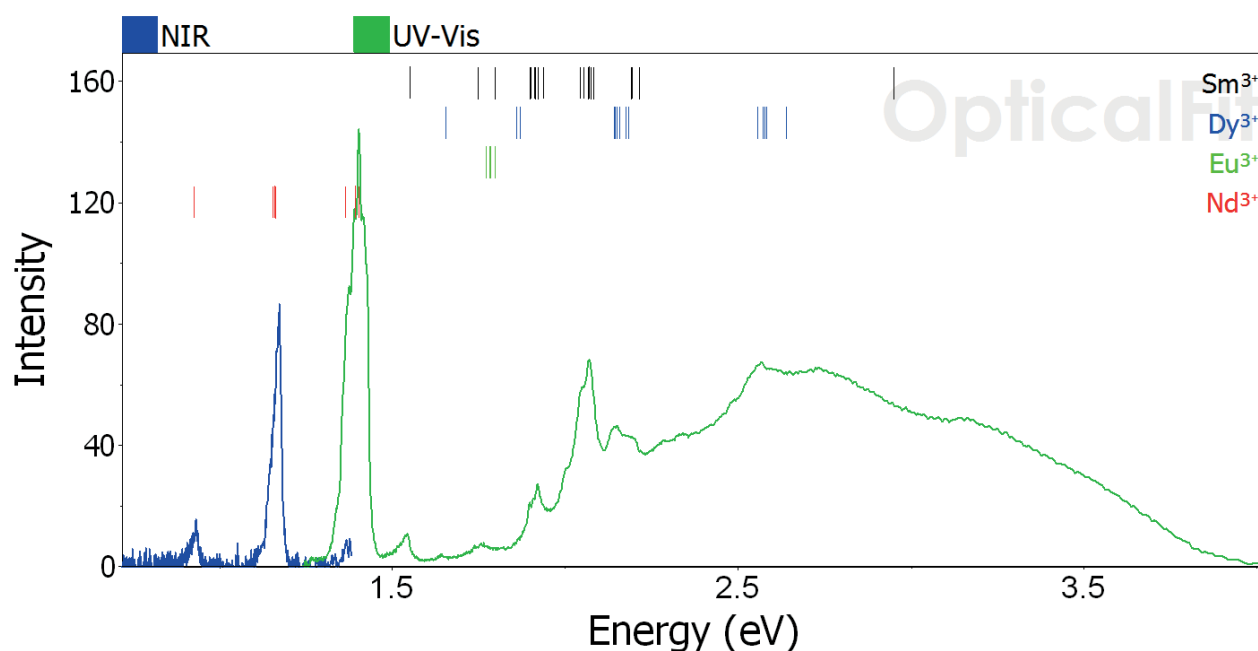

Figure 1 Optical fit showing a combined optical and near infra-red spectrum from an apatite sample. Colored vertical lines show database entries for Sm, Dy, Eu and Nd.

Curriculum vitae

Dipl.-Min. Christoph Lenz

Institut für Mineralogie und Kristallographie, Universität Wien

Althanstr. 14, 1090 Wien, Österreich (Austria)

christoph.lenz@univie.ac.at

http://www.univie.ac.at/Mineralogie/lenz_engl.htm

2004 – 2007 Study of mineralogy (equivalent to BSc.) at the Technical University Bergakademie Freiberg, Institute of Mineralogy; Mentors: D. Wolf / G. Heide

2007 – 2010 Advanced studies (equivalent to MSc.) with focus on "Technical Mineralogy" at the Technical University Bergakademie Freiberg; Mentors: G. Heide, J. Götze

2009 – 2010 Diploma thesis about the topic: „Correlation between atomic M-O distance and cathodoluminescence of selected carbonate minerals"; Mentor: J. Götze

since 2010 PhD (Prae-Doc scientific assistant) at the Institute of Mineralogy and Crystallography, University of Vienna; PhD topic: "Luminescence of lanthanoides (Rare-earth elements, REE) – Probes of structural variations in minerals" Supervisor: Lutz Nasdala

Christoph Lenz

List of publications

Peer-reviewed articles

Lenz, C., Nasdala, L., Talla, D., Hauzenberger, C., Seitz, R., Kolitsch, U. (2015): *Laser-induced REE^{3+} photoluminescence of selected accessory minerals – An "advantageous artefact" in Raman spectroscopy*. Chemical Geology (submitted).

Wierzbicka-Wieczorek, M., Göckeritz, M., Kolitsch, U., **Lenz, C.**, and Giester, G., (2015): *Two structure types based on the Si_6O_{15} rings: synthesis and structural and spectroscopic characterisation of $Cs_{1.86}K_{1.14}DySi_6O_{15}$ and $Cs_{1.6}K_{1.4}SmSi_6O_{15}$*. European Journal of Inorganic Chemistry (submitted).

Lenz, C., Nasdala, L. (2015): *A photoluminescence study of REE^{3+} emissions in radiation-damaged zircon*. American Mineralogist (in press).

Wierzbicka-Wieczorek, M., Göckeritz, M., Kolitsch, U., **Lenz, C.**, and Giester, G., (2015): *Crystallographic and spectroscopic investigations on nine metal–rare-earth silicates with the apatite structure type.* European Journal of Inorganic Chemistry, DOI:10.1002/ejic.201403070. (http://dx.doi.org/10.1002/ejic.201403070)

Nasdala, L., Lyubenova, T.S., Gaft, M., Wildner, W., Diegor, W., Petautschnig, C., Talla, D., **Lenz, C.** (2014): *Photoluminescence of synthetic titanite-group pigments: A rare quenching effect*. Chemie der Erde – Geochemistry, 74, 419–424. (http://www.sciencedirect.com/science/article/pii/S0009281914000348)

Wierzbicka-Wieczorek, M., **Lenz**, C., Giester, G. (2013): *Flux synthesis and structural and spectroscopic characterization of a cobalt europium trisilicate*. European Journal of Inorganic Chemistry, 19, 3405–3411. (http://onlinelibrary.wiley.com/doi/10.1002/ejic.201300018/abstract)

Lenz, C., Talla, D., Ruschel, K., Skoda, R., Götze, J. & Nasdala, L. (2013): *Factors affecting the Nd^{3+} (REE^{3+}) luminescence of minerals*. Mineralogy and Petrology, 107, 415–428. (http://link.springer.com/article/10.1007/s00710-013-0286-2)

Conference abstracts

Wierzbicka-Wieczorek, M., Göckeritz, M., Kolitsch, U., **Lenz, C.**, Giester, G. (2014): *Crystal structures and photoluminescencet properties of the disilicates $K_3P_3(Si_2O_7)$, $K_{2.40}Rb_{0.60}Pr(Si_2O_7)$ and $K_{2.84}Rb_{0.16}Sm(Si_2O_7)$*. 92nd Annual Meeting DMG, Jena, Germany, September, 2014. Programme and abstracts, p. 107.

Nasdala, L., **Lenz, C.**, Artač, A., Akhmadaliev, S., Váczi, T., Habler, G. & Abart, R. (2014): Ion and electron irradiation - Tools to study radiation damage in Minerals. XVIII. International Conference on Crystal Chemistry, X-Ray Diffraction and Spectroscopic Studies of Minerals, Ekaterinburg, Russia, October, 2014. Book of Abstracts, p. 125–127.

Artac, A., Jachs, B., **Lenz, C.**, Akhmadaliev, S., Habler, G., Talla, D., Nasdala, L. (2014): *Surface swelling and spectroscopic investigations of Au-irradiated monazite–(Ce) crystals.* 19th International Conference on Ion Beam Modification of Materials, Leuven, Belgium, September 2014. Book of Abstracts, p. PB 64.

Lenz, C., Artač, A., Akhmadaliev, S., Nasdala, L. (2014): *Quantitative estimation of radiation-induced defect accumulation in zircon (ZrSiO$_4$) – A REE^{3+} photoluminescence and Raman spectroscopic approach.* 92nd Annual Meeting DMG, Jena, Germany, September, 2014. Programme and Abstracts, p. 341.
(http://www.univie.ac.at/Mineralogie/docs/Abstract_DMG2014_Lenz.pdf)

Wierzbicka-Wieczorek, M., Göckeritz, M., Kolitsch, U., Lenz, C., Giester, G. (2014): *(Cs,K)$_3$DySi$_6$O$_{15}$: a novel framework structure type based on Si$_6$O$_{15}$ rings.* 21st General Meeting of the International Mineralogical Association (IMA), Gauteng, South Africa, September, 2014. Book of Abstracts, p. 321.

Artač, A., **Lenz, C.**, Akhmadaliev, S., Habler, G., Nasdala, L. (2014): *Heavy-ion irradiation damage in monazite–(Ce), CePO$_4$.* 12th Europhysical Conference on Defects in Insulating Materials (EURODIM), University of Kent, Canterbury, UK, July, 2014.

Wilson, N.C., MacRae, C.M., Torpy, A., Gaft, M., Götze, J., Nasdala, L., **Lenz, C.**, Hanchar, J.M., Barmarin, G. (2014): Luminescence database – an update. MSA Microscopy & Microanalysis, Hartford, CT, U.S.A., August, 2014. Microscopy and Microanalysis 20 (Supplement 3), p. 916.

Lenz, C., Nasdala, L. (2014): *Estimation of radiation-induced defect accumulation with REE^{3+} luminescence spectroscopy in zircon.* 12th Europhysical Conference on Defects in Insulating Materials (EURODIM 2014), University of Kent, Canterbury, UK, July, 2014.
(http://www.univie.ac.at/Mineralogie/docs/Eurodim2014_LENZ.pdf)

Lenz, C., Nasdala, L. (2013): *Potential estimation of radiation-induced structural disorder with REE^{3+} luminescence spectroscopy.* MinPet2013, Graz, Austria, September 2013. Mitteilungen der Österreichischen Mineralogischen Gesellschaft, 159, p. 88.
(http://www.univie.ac.at/Mineralogie/docs/Abstract_Lenz - MinPet2013.pdf)

Lenz, C., Reissner, C., Talla, D., Nasdala, L. (2013): *Orientation-dependent REE^{3+} luminescence: A possible artefact in luminescence imaging.* Goldschmidt 2013, Florence, Italy, August, 2013. Mineralogical Magazine, 77, 1226. Mineralogical Magazine, 77(5), p. 1586.
(http://goldschmidt.info/2013/abstracts/finalPDFs/1586.pdf)

Wierzbicka-Wieczorek, M., **Lenz, C.**, Giester, G. (2013): *Photoluminescent properties of lanthanide-doped sorosilicates.* Conference on Raman and Luminescence Spectroscopy in the Earth Sciences (CORALS–2013), Wien, Austria, July 2013. Book of Abstracts, p. 111–112.
(http://www.univie.ac.at/Mineralogie/Corals2013/docs/CORALS_Wierzbicka-Wieczorek.pdf)

Wanthanachaiseng, B., Bunnag, N., Sutthirat, C., Atichat, W., Ounorn, P., Sripoonjan, T., **Lenz, C.**, Nasdala, L. (2013): *Investigation of Be-treated sapphire by luminescence spectroscopy.* Conference on Raman and Luminescence Spectroscopy in the Earth Sciences (CORALS–2013), Wien, Austria, July 2013. Book of Abstracts, p.109–110.
(http://www.univie.ac.at/Mineralogie/Corals2013/docs/CORALS_Wanthanachaisaeng.pdf)

Reissner, C., **Lenz. C.**, Nasdala, L. (2013): *Orientation dependence of REE^{3+} photoluminescence spectra and a possible artifact*. Conference on Raman and Luminescence Spectroscopy in the Earth Sciences (CORALS–2013), Wien, Austria, July 2013. Book of Abstracts, p. 87–88.
(http://www.univie.ac.at/Mineralogie/Corals2013/docs/CORALS_Reissner.pdf)

Škoda, R., Novák, M., Havránek, V., **Lenz**, C. (2013) *Solid solutions between silicate and phosphate minerals of the olivine structure type: Example from Pøibyslavice metagranite, Czech Republic*. GAC–MAC Joint annual meeting, Winnipeg, Canada, 2013. Program with abstracts, p. 178.

Lenz, C., Ruschel, K., Kronz, A., Talla, D., Škoda, R., and Nasdala, L. (2012): *A Nd^{3+} luminescence spectroscopic study on the structural disorder of monazite-(Ce)*. 1st European Mineralogical Conference (EMC2012), Frankfurt, Germany, September 2012. Vol. 1, EMC2012–458.
(http://meetingorganizer.copernicus.org/EMC2012/EMC2012-458.pdf)

Petautschnig, C., Götze, J., **Lenz**, C., Nasdala, L. and Rericha, A. (2012): *Micro-Raman spectroscopy of annealed Mali onyx agate and man-made analogues*. X[th] GeoRaman Conference, Nancy, France, June, 2012. Book of Abstracts, p. 261–262.

Lenz, C., Petautschnig, C., Akhmadaliev, S., Hanf, D., Talla, D., Nasdala, L. (2012): *Combined Raman and photoluminescence spectroscopic investigation of He-irradiation effects in monazite*. European Geosciences Union General Assembly, Wien, Austria, April, 2012. Geophysical Research Abstracts Vol. 14, EGU2012–11138.
(http://meetingorganizer.copernicus.org/EGU2012/EGU2012-11138.pdf)

Lenz, C., Talla, D., Nasdala, L. (2011): *Orientation-dependent REE photoluminescence of zircon, xenotime and monazite*. DGK–DMG–ÖMG Joint Meeting, Salzburg, Austria, September, 2011. Zeitschrift für Kristallographie, Supplement 3, p. 139–140.

Lenz, C., Götze, J. (2011): *Manganese-activated cathodoluminescence of selected carbonate minerals*. Conference on Micro-Raman and Luminescence Studies in the Earth and Planetary Sciences (CORALS-20111), Madrid, Spain, May, 2011. 54. LPI Contribution No. 1616, Lunar and Planetary Institute, Houston.

Danksagung

Zuvorderst danke ich meinem Doktorvater Lutz Nasdala. Seinem unermüdlichen und engagierten Einsatz ist die Entstehung und Verwirklichung dieser Arbeit zu verdanken. Er ermöglichte mir aufschlussreiche Einblicke in den Wissenschaftsbetrieb und vermittelte mir akkurates, wissenschaftliches Denken und Arbeiten, sowie Stil und Ausdrucksform beim Erstellen von wissenschaftlichen Publikationen. Darüber hinaus danke ich ihm für die die Förderung vieler externer Labor- und Konferenzbesuche, sowie für die fortwährende konstruktive Zusammenarbeit während meiner Dissertation.

Allen Mitarbeitern des Instituts für Mineralogie & Kristallographie der Universität Wien danke ich für die einladende, fruchtbare Arbeitsatmosphäre und ihrer Unterstützung meiner Arbeit. Viele Ideen und Anregungen erhielt ich in unzähligen Gesprächen und Diskussionen. Ich danke Domenik Talla für seinen beharrlichen Einsatz bei diversen Syntheseversuchen, Manfred Wildner und Eugen Libowitzky für ihre beherzte Vermittlung der optischen Spektroskopie, sowie vielen weiteren geschätzten Kollegen für Erkenntnisse aus ihren Lehrinhalten. Den Mitarbeitern der Werkstätte bin ich zu besonderem Dank verpflichtet, insbesondere Andreas Wagner für seine exzellente Probenpräparation, als auch Thomas Rosen und Wolfgang Prosche für ihre stete Einsatzbereitschaft und ihren technischen Problemlösungen. Wolfgang Zirbs und den Mitarbeiterinnen des Sekretariats danke ich für Abhilfe bei allfälligen technischen und administrativen Tätigkeiten. Ebenso danke ich der Kollegin Maria Wierzbicka-Wieczorek, den ehemaligen Doktoranden Katja Ruschel und Christian Petautschnig, den Doktoranden Manuela Zeug und Andreas Artač, sowie den Studentinnen Claudia Reissner und Astrid Witwer, für die stets heitere und unkomplizierte Zusammenarbeit an gemeinsamen Projekten.

Darüber hinaus bedanke ich mich bei Gerlinde Habler für ihre Ausdauer und Unterstützung bei der FIB-Probenpräparation, Shavkat Akhmadaliev und Daniel Hanf für ihre Betreuung am Ionenstrahlzentrum Dresden-Rossendorf, meinem Diplomarbeitsbetreuer Jens Götze für die andauernde wissenschaftliche Zusammenarbeit, Uwe Kolitsch für die Bereitstellung vieler Proben, sowie den Kollegen Radek Skoda und Christoph Hauzenberger für zahlreiche chemische Analysen.

Meiner Familie, Sophia, und vielen Freunden möchte ich für die stete Unterstützung während meines Doktorats danken. Aus ihrem Interesse an meiner Arbeit und ihrer andauernden Ermutigung entsprang viel Motivation und Ausdauer. Diese Arbeit widme ich meiner Urgroßmutter Elfriede Berg; sie hat mich in jungen Jahren auf eine Reise mitgenommen, der ich seither treu geblieben bin.

Nimm an die Weisheit, denn sie ist besser als Gold; und Verstand haben ist edler als Silber.

(Sprüche 16,16)